Measurement of the top quark pair production cross section with $\sqrt{s} = 7$ TeV of pp collisions at LHC with b-tagging in the dilepton final state with the ATLAS detector

CERN-THESIS-2013-177
21/05/2013

DISSERTATION
Presented in Fulfillment of the Requirements
for the Degree of Doctor of Science
in the Graduate School of Osaka University

Minoru Hirose
Osaka University

May, 2012

Abstract

We report on the measurement of the production cross section of the top quark pair in pp collision with $\sqrt{s} = 7$ TeV at LHC using 4.7 fb^{-1} of data taken in the ATLAS detector. The production cross section is one of the most basic properties of top quark and needed to be well understood to test the standard model of particle physics and to prepare for the future LHC physics program. The measurement is performed using the information of the b-quark jet tagging algorithm. We obtain the following cross sections in the three dilepton final states and the combined channel:

$$\begin{aligned}
\sigma_{t\bar{t}} &= 167 \pm 6(\text{stat.})^{+25}_{-19}(\text{syst.}) \pm 3(\text{lumi.}) \text{ pb (ee)}, \\
\sigma_{t\bar{t}} &= 178 \pm 4(\text{stat.})^{+15}_{-11}(\text{syst.}) \pm 3(\text{lumi.}) \text{ pb } (\mu\mu), \\
\sigma_{t\bar{t}} &= 173 \pm 3(\text{stat.})^{+16}_{-14}(\text{syst.}) \pm 3(\text{lumi.}) \text{ pb (e}\mu), \text{ and} \\
\sigma_{t\bar{t}} &= 177 \pm 2(\text{stat.})^{+14}_{-11}(\text{syst.}) \pm 3(\text{lumi.}) \text{ pb (Combined)},
\end{aligned}$$

where (stat.), (syst.), and (lumi.) are the uncertainties from statistics, systematics other than the luminosity measurement, and the luminosity measurement, respectively. The results are consistent with the approximate NNLO prediction, $166.78^{+17.3}_{-18.4}$ pb. This measurement is the most precise cross section measurement in the dilepton final state in the ATLAS experiment.

Contents

1 Introduction **1**
- 1.1 Top quark physics . . . 1
  - 1.1.1 Importance of the top quark . . . 1
- 1.2 Phenomenology of the top quark physics . . . 4
  - 1.2.1 Production of the top quark . . . 4
  - 1.2.2 Decay of the top quark . . . 9
  - 1.2.3 Top quark signature in the hadron collider . . . 10
- 1.3 Measurement of the production cross section . . . 11
- 1.4 Past measurements . . . 12
  - 1.4.1 Before the discovery of the top quark . . . 12
  - 1.4.2 Measurements at Tevatron . . . 12
  - 1.4.3 Measurements at LHC . . . 13
- 1.5 Measurement technique . . . 14
  - 1.5.1 Principle of the measurement . . . 14

2 The Large Hadron Collider **16**
- 2.1 Advantages of the proton-proton collider . . . 16
- 2.2 The LHC injector chain . . . 17
  - 2.2.1 The proton pre-injectors . . . 17
  - 2.2.2 SPS as the LHC injector . . . 19
- 2.3 The LHC main ring . . . 20
  - 2.3.1 Magnets . . . 20

3 The ATLAS experiment **24**
- 3.1 ATLAS coordinate system . . . 25
- 3.2 Magnets . . . 25
- 3.3 Inner tracker . . . 28
  - 3.3.1 Pixel detector . . . 28
  - 3.3.2 SemiConductor Tracker . . . 30
  - 3.3.3 Transition Radiation Tracker . . . 33
- 3.4 Calorimeters . . . 34
  - 3.4.1 Electromagnetic calorimeter . . . 34
  - 3.4.2 Hadron calorimeter . . . 36
- 3.5 Muon spectrometer . . . 37
  - 3.5.1 Monitored Drift Tube . . . 37
  - 3.5.2 Cathode Strip Chamber . . . 39
  - 3.5.3 Resistive Plate Chamber . . . 40
  - 3.5.4 Thin Gap Chamber . . . 41
- 3.6 Forward detectors . . . 42

3.6.1 LUCID . . . 42
3.6.2 Beam Condition Monitor . . . 42
3.7 Trigger and the data acquisition system . . . 43
3.7.1 Level-1 trigger . . . 43
3.7.2 High-Level Trigger . . . 46
3.8 ATLAS computing system . . . 46

4 Data samples **47**
4.1 Collision data . . . 47
4.1.1 Luminosity determination . . . 48
4.1.2 Data taking period, trigger setup and data stream . . . 51
4.2 Monte Carlo samples . . . 52
4.2.1 Common setting for all Monte Carlo samples . . . 52
4.2.2 List of the MC samples . . . 54
4.2.3 Signal Monte Carlo sample . . . 55
4.2.4 Background Monte Carlo samples . . . 55
4.2.5 Top quark pair samples for systematics . . . 56

5 Event reconstruction **58**
5.1 Charged track . . . 58
5.2 Interaction vertex . . . 59
5.3 Electron . . . 59
5.4 Muon . . . 63
5.5 Jet . . . 65
5.6 Missing transverse energy . . . 72
5.7 Identification of the b-quark jet . . . 74

6 b-tagging efficiency **80**
6.1 Control sample of the b-quark jets . . . 80
6.2 Tag counting method . . . 80
6.3 Event selection . . . 82
6.4 Estimate of the top quark pair acceptance . . . 82
6.5 Estimate of backgrounds . . . 82
6.5.1 W+jets backgrounds . . . 83
6.5.2 Fake lepton backgrounds . . . 84
6.5.3 Other backgrounds . . . 89
6.6 Distributions in background enhanced regions . . . 89
6.7 Yields and distributions in the signal region . . . 91
6.8 Determination of the flavor fraction . . . 95
6.9 Simultaneous fitting for data . . . 96
6.10 Validation of the tag counting method . . . 96
6.11 Systematic uncertainties . . . 97
6.11.1 Integrated luminosity . . . 101
6.11.2 W+jets background estimate . . . 101
6.11.3 Fake lepton background . . . 101
6.11.4 Fake lepton background distribution shape . . . 101
6.11.5 Jet related uncertainties . . . 101
6.11.6 Lepton related uncertainties . . . 102
6.11.7 Mis-tagging efficiency for the b-tagging . . . 103

6.11.8 Missing transverse energy uncertainty . . . 104
6.11.9 Heavy flavor fraction . . . 104
6.11.10 Generator, parton shower modeling . . . 104
6.11.11 Initial and final state radiation . . . 104
6.11.12 MC statistics . . . 104
6.12 Result . . . 105

7 Measurement of the production cross section 106
7.1 Event selection . . . 106
7.1.1 Cut values . . . 109
7.1.2 Remaining events expected by the MC samples . . . 110
7.2 Signal acceptance . . . 113
7.3 Background estimation . . . 124
7.3.1 Fake lepton backgrounds . . . 126
7.3.2 The events with Z/γ^* which decays into ee or $\mu\mu$ . . . 127
7.3.3 Other backgrounds . . . 131
7.4 Validation of background estimation . . . 135
7.5 Signal region . . . 140
7.6 Cross section measurement . . . 142

8 Discussion 151

9 Conclusion 157

Bibliography 159

List of Figures

1.1 The Feynman diagram of fermion one-loop contribution to the Higgs boson. . . . 2
1.2 All particles in the standard model and their superpartners. 4
1.3 Example of the gluino ($\tilde{g}$) decay into the final state with the top quark. The particle χ in the diagrams are chargino or neutralino which are fermionic superpartner predicted in SUSY. 5
1.4 The $t\bar{t}$ production process at the lowest order in hadron colliders. The top (bottom) shows quark-antiquark annihilation (the gluon fusion). 6
1.5 The covered fractional energy x and Q^2 range to measure the PDFs by the experiments in HERA, Tevatoron and the fixed target experiments. The ordinal energy range for the physics explored by the ATLAS and the CMS experiments is shown as the red box. 8
1.6 The distributions of x times the parton distributions $f(x, Q^2)$ for $Q^2 = 10$ and 10^4 GeV^2 with its uncertainty using the MSTW 2008 NNLO parametrization [8]. The one for gluon is scaled down by factor 10. 8
1.7 The decay channels of top quark pair 11
1.8 Summary of the $\sigma_{t\bar{t}}$ measurement with $p\bar{p}$ collisions at $\sqrt{s} = 1.96$ TeV [18]. The red (blue) bar in each point show the statistical (total) uncertainty. 13
1.9 Summary of the $\sigma_{t\bar{t}}$ measurements with $\sqrt{s} = 7$ TeV at the ATLAS and the CMS experiments [21, 22, 23, 24, 25, 26]. 14

2.1 CERN accelerator complex [32]. PSB is indicated as 'BOOSTER'. 18
2.2 Duoplasmatron proton ion source [34]. 18
2.3 The cross-section of cryodipole (lengths in mm) [27]. 21
2.4 Magnet system near the interaction point for the ATLAS experiment, IP1, shown on the left side of the figure. The length in the figure is given in meters. Q1, Q2 and Q3 are the final focusing quadrupole magnet triplets to provide high luminosity collisions at the interaction point [27]. 21
2.5 Cross section of the D2 cryodipole [27]. 22
2.6 Cross section of the MXQA insertion quadrupole [28]. 23

3.1 The full ATLAS detector [37]. 24
3.2 The ATLAS coordinate system. The azimuthal angle ϕ is measured from the positive x-axis. The polar angle θ is measured from the positive z-axis. The pseudorapidity $\eta = \pm 1, \pm 2$ and ± 3 are indicated in blue lines on the right plots. 25
3.3 Geometry of the ATLAS magnets. The eight barrel toroid coils and two eight endcap toroid coils (red rectangles) are around the solenoid winding (blue cylinder) [38]. 26
3.4 The magnetic field strength along the beam direction (left) and the radial component of the magnetic field (right) as a function of r and z [39]. 27

3.5 Integrated field strength by the toroidal magnets as a function of pseudorapidity [38]. . . . 27
3.6 The cut-away image of the inner tracker [40]. . . . 28
3.7 The ATLAS pixel detector module [41]. . . . 29
3.8 The pixel support structure [42]. . . . 29
3.9 RMS of residuals in the ϕ direction (left) and the z direction (right) as a function of the track incident angle [43]. The residual is measured by taking the difference between the estimated hit position using the reconstructed track and the actual hit position on the module. The hit position is estimated by using two algorithms, one taking the center of the cluster of hit pixels (red circle) and the other considering the amount of deposit charges (triangle). . . . 30
3.10 The ATLAS SCT module [44] 31
3.11 The layout of the ATLAS inner tracker [44]. The distances are given in mm. . . . 31
3.12 The residual in the ϕ direction for the barrel region (left) and the end-cap region (right). The data reconstructed with different detector alignment setting are plotted in blue circles and black boxes. The distribution of MC is also shown in red circles. . . . 32
3.13 The hit efficiency for the SCT barrel module [46]. Each bin corresponds to the sensors for inside or outside of each module on each detector layer. The efficiency is shown for two different types of tracks, SCT stand-alone tracks which are the tracks reconstructed with only the hit information in SCT and inner tracker combined tracks. . . . 32
3.14 The residual distribution in the ϕ direction for the TRT barrel (left) and end-cap (right) detecter. The single gaussian fitting is performed to extract the width [47]. 33
3.15 The pion mis-identification probability by TRT with the requirement of the electron selection efficiency of 90 % [47]. . . . 33
3.16 The layout of the ATLAS calorimeters [48] 34
3.17 The accordion-shaped lead-LAr sampling calorimeter [49]. The honeycomb spacers position the electrodes between the lead absorber plates. . . . 35
3.18 The readout granularity of the EM calorimeter [50] 35
3.19 Detector design of TileCal. The signal from the sampling scintillator is read out by the photo multiplier tubes through the wave length shifting fiber. . . . 37
3.20 Side view of one quadrant of the muon spectrometer (Top) and Transverse view of the spectrometer (bottom) [38]. . . . 38
3.21 Schematic drawing of an MDT chamber [38]. There are eight layers rather than six layers for the innermost station to improve a pattern recognition capability. . . . 39
3.22 Cutaway view of a single CSC layer [38] 40
3.23 Mechanical structure of an RPC chamber [38] 40
3.24 Schematic cross-section of a triplet (left) and of a doublet of TGC. The width of the gas gap is shown enlarged [38]. . . . 41
3.25 The LUCID detector is installed between the beam pipe and the conical support tube of the beam pipe [51]. . . . 42
3.26 The cross section of LUCID at the front of the detector ($z = \pm 16.98$ m) [51]. . . . 43
3.27 Block diagram of the ATLAS trigger and data acquisition systems. In this figure, the event rate is written as 200 Hz, which is the design value. However, data were taken with 400 Hz in the 2011 operation [41]. . . . 44
3.28 Calorimeter clusters used in the L1 calorimeter trigger system. One trigger tower is defined as the size in η-ϕ plane of $\Delta\eta \times \Delta\phi = 0.1 \times 0.1$ in most parts. It is larger at the forward region [41]. . . . 45

3.29 Level-1 muon trigger scheme [38]. 45

4.1 The luminosity weighted data taking efficiency per day [52]. 47
4.2 The integrated delivered luminosity from LHC and the recorded luminosity with the ATLAS detector in 2011 [52]. 48
4.3 The distribution of the mean number of interactions per bunch crossing in 2011 [52]. The red (blue) shows for data taken before (after) the september technical shutdown where β^* was reduced from 1.5 m to 1.0 m. 53

5.1 The idea of the tag and probe method using Z bosons 61
5.2 Example of the electron trigger efficiency and its scale factor as a function of the electron η. The shaded band in the bottom plot indicates the uncertainty. This efficiency is evaluated at the electron transverse energy of 50 GeV. 62
5.3 Example of the electron selection efficiency and its scale factor. Selection efficiency includes the reconstruction, the `tight++` selection and the isolation requirement. The shaded band in the bottom plot indicates the uncertainty. This efficiency is evaluated at the electron transverse energy of 50 GeV. 63
5.4 The efficiency and the scale factor of the muon selection. The selection efficiency contains reconstruction and isolation efficiency. The shaded band indicates the uncertainty. This efficiency is evaluated at the muon transverse energy of 50 GeV. 65
5.5 The muon trigger efficiency measured in data in the η-ϕ plane. The low efficiency region at $\phi \sim -1.8$ is due to the ATLAS support structure. 66
5.6 The muon trigger efficiency and the scale factors between data and MC. This efficiency is evaluated at the muon transverse energy of 50 GeV. The discrepancy between data and MC in the barrel region, $|\eta| < 1.05$, is caused by hardware problems in RPC. 66
5.7 Invariant mass reconstructed from di-muon. For MC, the distribution is made before applying the muon momentum smearing. 67
5.8 The jet shape in the y (rapidity)-ϕ plane for the SISCone (left) and the anti-k_t (right) algorithm [85]. SISCone is one of the cone-type algorithms and is shown to see the shape difference between the algorithms. 68
5.9 Images of the principle of the JES measurement in the γ+jets and the Z+jets analysis. Momentum in the transverse direction must be conserved. 69
5.10 The mean P_{T} balance, $P_{\mathrm{T}}^{\mathrm{jet}}/P_{\mathrm{T}}^{\gamma}$, as a function of the P_{T} of the reference photon measured in the γ+jets analysis. The bottom plot shows the data-to-MC ratio [86]. 69
5.11 Data-to-MC ratio of the mean P_{T} balance as a function of the P_{T} of the Z boson measured in the Z+jets analysis. Dashed lines show the $-1\%, -2\%$ and -5% shifts [87]. 70
5.12 Summary of the uncertainty for JES measured in the γ+jets analysis [86] 70
5.13 Summary of the uncertainty for JES measured in the Z+jets analysis [87] 71
5.14 The schematic image of JVF. Jet1 is a jet originating from a pileup vertex. Jet2 and Jet3 come from PV. Tracks from PV (the pileup vertex) are indicated in the blue (red) lines. JVF of Jet1 (JVF_1) is zero because there is no matched tracks associated to PV. For Jet3, JVF equals to unity because all the associated tracks comes from PV. On the other hand, Jet2 originally coming from PV have an associated track from the pileup vertex. Therefore, JVF_2 should be smaller than unity. 72

5.15 The efficiency of the selection based on the JVF requirement for the hard scattered jet as a function of jet P_{T} together with its scale factor $\varepsilon_{\mathrm{data}}/\varepsilon_{\mathrm{MC}}$. The shaded band in the bottom plot indicates the uncertainty. 73
5.16 $E_{\mathrm{T}}^{\mathrm{miss}}$ resolution as a function of the total energy sum in the event [89]. 74
5.17 Schematics of the signed impact parameters (d_0 for the r-ϕ plane, z_0 for the r-z plane). The track labeled with 'trk 1' crosses the jet axis at the side which the jet is toward. In this case, the sign of the impact parameter is defined as positive. The track indicated as 'trk 2' traverses the jet axis at the opposite side. The sign of the impact parameter is negative in this case. 75
5.18 The normalized signed transverse impact parameter for b-, c- and light-jets obtained with MC [90] 76
5.19 The image of the b- and c-hadron cascade decay 77
5.20 The normalized secondary vertex mass distribution for b-, c- and light-jets obtained with MC [93] 78
5.21 The distribution of the difference of the mass reconstructed by $K^-\pi^+\pi^+$ and by $K^-\pi^+$ [94] 79

6.1 The acceptance of the e+jets channel (left) and the μ+jets channel (right) to the true e+jets and μ+jets events in the MC@NLO MC sample. 83
6.2 The measured efficiency for real loose leptons to pass the tight lepton requirements as a function of the lepton P_{T}, η and the number of jets in the event. . . . 86
6.3 $E_{\mathrm{T}}^{\mathrm{miss}}$ (left) and the jet multiplicity (right) distributions after requiring the selection to enhance QCD multi-jet events for the e+jets (top) and the μ+jets (bottom). $E_{\mathrm{T}}^{\mathrm{miss}}$ (the jet multiplicity) cut is not applied for the illustration purpose. The required cut positions are indicated in the red doted lines. 87
6.4 $\varepsilon_{\mathrm{fake}}$ as a function of lepton P_{T} (top left), lepton eta (top right), the jet multiplicity in the event (bottom left) and the leading jet P_{T} (bottom right). 88
6.5 The lepton P_{T}, $M_{\mathrm{T}}(W)$ and the jet multiplicity distributions in the W+jets enhanced region for e+jets (left) and μ+jets (right) channels. The last bin contains overflowing events. The uncertainties considered here are the estimated numbers of fake leptons and W+jets events, the theoretical cross section uncertainties for $t\bar{t}$, Z/γ^*, di-boson and the single top production and MC statistics. 90
6.6 The lepton P_{T}, η, and the b-tagged jet multiplicity distributions in the fake lepton enhanced region for e+jets (left) and μ+jets (right) channels. The last bin in the top and bottom plots contains overflowing events. The uncertainties considered here are the estimated numbers of fake leptons and W+jets events, the theoretical cross section uncertainties for $t\bar{t}$, Z/γ^*, di-boson and the single top production and MC statistics. 92
6.7 The lepton P_{T} and $E_{\mathrm{T}}^{\mathrm{miss}}$ distributions in the signal region for e+jets (left) and μ+jets (right) channels. The last bin contains overflowing events. The uncertainties considered here are the estimated numbers of fake leptons and W+jets events, the theoretical cross section uncertainties for $t\bar{t}$, Z/γ^*, di-boson and the single top production and MC statistics. 93
6.8 The jet multiplicity, P_{T} and b-tagged jet multiplicity in the signal region for e+jets (left) and μ+jets (right) channels. The last bin contains overflowing events. The uncertainties considered here are the estimated numbers of fake leptons and W+jets events, the theoretical cross section uncertainties for $t\bar{t}$, Z/γ^*, di-boson and the single top production and MC statistics. 94

6.9 Left : The log-likelihood distribution in the $\sigma_{t\bar{t}}$ and ε_b plane. For the later use to estimate the error from the likelihood by using Wilks theorem, $-2\ln L$ is shown. Expected value in MC is indicated in the triangle and the best fit point, the minimum of $-2\ln L$, in the circle. Right : the number of b-tagged jets distribution for e+jets and μ+jets channels. Blue histogram shows the estimated shape obtained with using the predicted $\sigma_{t\bar{t}}$ and ε_b in MC. The magenta shows the shape for the best fit result. The points shows the distribution obtained from data. 96
6.10 The result of the pseudo experiments with the input $\sigma_{t\bar{t}} = 164$ pb and $\varepsilon_b = 85$ %. The black histograms are the Pseudo Experiment results. The red line shows the result of the Gaussian fitting. The outputs of the Gaussian fitting are shown as 'Mean' and 'Sigma' inside the plots. 97
6.11 The linearity of the $\sigma_{t\bar{t}}$ measurement for all the input combinations. Horizontal bars indicate the extracted $\sigma_{t\bar{t}}$ by the pseudo experiments against each input value. The red line shows the line of (Output $\sigma_{t\bar{t}}$) = (Input $\sigma_{t\bar{t}}$). 98
6.12 The linearity of the ε_b measurement for all the input combinations. Horizontal bar indicate the extracted ε_b by the pseudo experiments against each input value. The red line shows the line of (Output ε_b) = (Input ε_b). 99
6.13 The width of the pull distributions for each combination of the inputs. The left plot shows the one for the $\sigma_{t\bar{t}}$ measurement, and the right one for the ε_b measurement. 100
6.14 The result of 10000 trials of the likelihood fitting with varying the fake lepton distribution shape. The relative difference of the fitting results from the nominal fitting result are plotted. The plot on the left is for the cross section measurement and the right one for the b-tagging efficiency measurement. The widths of distribution are extracted by the gaussian fitting. 102

7.1 Invariant mass of dilepton system in $t\bar{t}$ and $Z/\gamma^* \to ee/\mu\mu$ events. 107
7.2 $E_{\mathrm{T}}^{\mathrm{miss}}$ distribution in $t\bar{t}$, $Z/\gamma^* \to ee/\mu\mu$ and $Z/\gamma^* \to \tau\tau$ events. 108
7.3 H_{T} distribution in $t\bar{t}$ and $Z/\gamma^* \to \tau\tau$ events. 108
7.4 The jet multiplicity distribution in $t\bar{t}$, $Z/\gamma^* \to \ell\ell$ and di-boson events. 109
7.5 The b-tagged jet multiplicity distribution in $t\bar{t}$, $Z/\gamma^* \to \ell\ell$ and di-boson events. . 110
7.6 The expected uncertainties of the cross section measurement in the ee and $\mu\mu$ channels with different combinations of the selection threshold. 110
7.7 The expected uncertainties of the cross section measurement in the $e\mu$ channel with a different H_{T} threshold. 111
7.8 The comparison of the number of jets distribution among the samples with different JES. The bottom plot in each figure shows the difference from the nominal sample for JES $+1\sigma$ (red) and for JES -1σ (blue) cases. 115
7.9 The comparison of the $E_{\mathrm{T}}^{\mathrm{miss}}$ distribution among the samples with different JES. The bottom plot in each figure shows the difference from the nominal sample for JES $+1\sigma$ (red) and for JES -1σ (blue) cases. 116
7.10 The acceptance at each selection step of the sample with various JES for the ee (top left), the $\mu\mu$ (top right) and the $e\mu$ (bottom) channel. The bottom plot in each figure shows the relative difference from the nominal JES sample. The red (blue) points show the sample with shifted JES by $+1$ (-1) sigma. 117

7.11 The acceptance at each selection step for the MC sample generated with the MC@NLO generator and the POWHEG generator for the ee (top left), the $\mu\mu$ (top right) and the $e\mu$ (bottom) channel. Bottom part of each plot shows the relative acceptance difference between the two samples. 119
7.12 Distributions of jet multiplicity after requiring two selected electrons for various MC samples. Bottom plots shows the difference between the samples of interest to estimate the systematic uncertainty, *i.e.* (POWHEG+HERWIG)-(MC@NLO+HERWIG) in magenta, (POWHEG+HERWIG)-(POWHEG+PYTHIA) in light blue, (More ISR/FSR)-(MC@NLO) in red, (Less ISR/FSR)-(MC@NLO) in blue. 120
7.13 Distributions of the jet multiplicity after requiring two selected muons for various MC samples. Bottom plots shows the difference between the samples of interest to estimate the systematic uncertainty, *i.e.* (POWHEG+HERWIG)-(MC@NLO+HERWIG) in magenta, (POWHEG+HERWIG)-(POWHEG+PYTHIA) in light blue, (More ISR/FSR)-(MC@NLO) in red, (Less ISR/FSR)-(MC@NLO) in blue. 121
7.14 Distributions of the jet multiplicity after requiring a selected electron and a selected muon for various MC samples. Bottom plots shows the difference between the samples of interest to estimate the systematic uncertainty, *i.e.* (POWHEG+HERWIG)-(MC@NLO+HERWIG) in magenta, (POWHEG+HERWIG)-(POWHEG+PYTHIA) in light blue, (More ISR/FSR)-(MC@NLO) in red, (Less ISR/FSR)-(MC@NLO) in blue. 121
7.15 The acceptance at each selection step for the MC sample generated with the POWHEG generator interfaced with PYTHIA and HERWIG for the parton shower modeling for the ee (top left), the $\mu\mu$ (top right) and the $e\mu$ (bottom) channel. Bottom part of each plot shows the relative acceptance difference between two samples. 122
7.16 Distributions of the track multiplicity after requiring two selected electrons for various MC samples. Bottom plots shows the difference between the samples of interest to estimate the systematic uncertainty, *i.e.* (POWHEG+HERWIG)-(MC@NLO+HERWIG) in magenta, (POWHEG+HERWIG)-(POWHEG+PYTHIA) in light blue, (More ISR/FSR)-(MC@NLO) in red, (Less ISR/FSR)-(MC@NLO) in blue. 123
7.17 Distributions of the track multiplicity after requiring two selected muons for various MC samples. Bottom plots shows the difference between the samples of interest to estimate the systematic uncertainty, *i.e.* (POWHEG+HERWIG)-(MC@NLO+HERWIG) in magenta, (POWHEG+HERWIG)-(POWHEG+PYTHIA) in light blue, (Sample with more ISR/FSR)-(MC@NLO) in red, (Sample with less ISR/FSR)-(MC@NLO) in blue. 123
7.18 Distributions of the track multiplicity after requiring a selected electron and a selected muon for various MC samples. Bottom plots shows the difference between the samples of interest to estimate the systematic uncertainty, *i.e.* (POWHEG+HERWIG)-(MC@NLO+HERWIG) in magenta, (POWHEG+HERWIG)-(POWHEG+PYTHIA) in light blue, (More ISR/FSR)-(MC@NLO) in red, (Less ISR/FSR)-(MC@NLO) in blue. 124
7.19 The acceptance at each selection step for the MC sample generated with increased or decreased ISR/FSR for the ee (top left), the $\mu\mu$ (top right) and the $e\mu$ (bottom) channel. Bottom part of each plot shows the relative acceptance difference between the two samples. 125

7.20 The distributions of data on $E_{\mathrm{T}}^{\mathrm{miss}}$ and $M_{\ell\ell}$ plane for the ee (left) and the $\mu\mu$ (right) channel. The control region (CR) and the signal region (SR) is indicated by the yellow and red box, respectively. 127
7.21 The distributions of $E_{\mathrm{T}}^{\mathrm{miss}}$ for the Z+2jets in the ee (left) and the $\mu\mu$ channel with MC samples. The black, red, blue and green histograms show the one with the nominal jet calibration (Nominal), with the JES scaled up and down (JES $\pm1\sigma$) and with the smeared jet energy (JER), respectively. The bottom plots show the difference from the nominal for the case of JES $\pm1\sigma$ and JER with the same color convention. 130
7.22 The CR dependence of the number of estimated events of Z+jet events. The ratio to the one with the nominal CR definition is plotted. 131
7.23 Top, middle and bottom plots show P_{T} of the leading and the second leading lepton and the invariant mass of dilepton, respectively, in the Z/γ^* control region. Left (right) shows the one for the ee ($\mu\mu$) channel. The last bin includes the overflow events. The uncertainties indicated here include the uncertainties from the MC statistics and the one related to the normalization of the distribution such as the theoretical uncertainty. The bottom part in each plot shows the ratio between data and the expectation. 136
7.24 Top, middle and bottom plots show the jet multiplicity, the P_{T} of jets and the H_T distribution, respectively, in the Z/γ^* control region. Left (right) shows the one for the ee ($\mu\mu$) channel. The last bin includes the overflow events. The uncertainties indicated here include the uncertainties from the MC statistics and the one related to the normalization of the distribution such as the theoretical uncertainty. The bottom part in each plot shows the ratio between data and the expectation. 137
7.25 The lepton kinematics in the fake lepton control region. Top (Bottom) two figures show the P_T (η) for the leading lepton on the left and the second leading lepton on the right. The last bin for the lepton P_T includes the overflow events. The uncertainties indicated in figures include the uncertainty from the MC statistics, the theoretical cross section uncertainty, and the fake lepton estimate. The bottom part in each plot shows the ratio between data and the expectation. . . . 138
7.26 The top left (right) figure show the $E_{\mathrm{T}}^{\mathrm{miss}}$ (H_T), and the bottom figures show the jet multiplicity and the b-tagged jet multiplicity. The last bin in each plot includes the overflow events. The uncertainties indicated in figures include the uncertainty from the MC statistics, the theoretical cross section uncertainty, and the fake lepton estimate. The bottom part in each plot shows the ratio between data and the expectation. 139
7.27 The electron and muon P_T (top left and right), the invariant mass of the dilepton system, $M_{\ell\ell}$,(bottom left) and the b-tagged jet multiplicity in the $e\mu$ event with one or more jets. The last bin for the lepton P_T includes the overflow events. The uncertainties indicated in figures include the uncertainty from the MC statistics, the theoretical uncertainty, and the fake lepton estimate. The bottom part in each plot shows the ratio between data and the expectation. 141
7.28 Lepton kinematics for ee (top), $\mu\mu$ (middle) and $e\mu$ (bottom) channels. For the ee and $\mu\mu$ channel, the left plots show the P_{T} of the leading lepton, and the right shows the one for second lepton. For the $e\mu$ channel, the P_{T} of electron is on left and the one for muon is on right. The last bin includes the overflow events. The uncertainty band includes the MC statistics and uncertainties related to the MC normalization. 143

7.29 Top, middle and bottom plots are for ee, $\mu\mu$ and $e\mu$ channels. $E_{\mathrm{T}}^{\mathrm{miss}}$ distributions are on the left, and H_{T} on the right. In the $E_{\mathrm{T}}^{\mathrm{miss}}$ plots for the ee and $\mu\mu$ channel, $E_{\mathrm{T}}^{\mathrm{miss}}$ selection is omitted for the illustration purpose. The similar treatment is applied for the H_{T} plot for the $e\mu$ channel. The last bin includes the overflow events. The uncertainty band includes the MC statistics and uncertainties related to the MC normalization. 144
7.30 Top, middle and bottom plots are for ee, $\mu\mu$ and $e\mu$ channels. The left plots shows the number of jets after all selections but the number of jet cut. The right plots show the b-tagged jet multiplicity distribution before requiring the b-tagging selection. The uncertainty band includes the MC statistics and uncertainties related to the MC normalization. 145
7.31 Top, middle and bottom plots are for ee, $\mu\mu$ and $e\mu$ channels. Jet P_{T} distributions for all the selected jets are on the left, and the one for the leading jet on the right. The last bin includes the overflow events. The uncertainty band includes the MC statistics and uncertainties related to the MC normalization. 146
7.32 Top, middle and bottom plots are for ee, $\mu\mu$ and $e\mu$ channels. Jet P_{T} distributions for the second (third) leading jet are on the left (right). The last bin includes the overflow events. The uncertainty band includes the MC statistics and uncertainties related to the MC normalization. 147
7.33 Twice of negative log likelihood ratio as a function of $\sigma_{t\bar{t}}/\sigma_{t\bar{t}}^{\mathrm{Theory}}$. The black solid (dotted) line shows the combined result considering the statistic and the systematic uncertainties (only the statistic uncertainty). The likelihood ratio for the ee, the $\mu\mu$ and the $e\mu$ channels are in blue, red and magenta line, respectively. The green line shows $-2\log\lambda = 1$ which corresponds to the one standard deviation for the combined result. 148
7.34 Measured production cross section of $t\bar{t}$. The yellow band shows a theoretical prediction. 149

8.1 Measured cross sections with various final states performed at ATLAS and CMS. Values are referred from the references of [21, 22, 23, 24, 25, 26]. 152
8.2 Measured cross sections at various center-of-mass energies are indicated with their uncertainties. Our measurement presented in this thesis is shown in the red triangle. The expected production cross section as a function of $\sqrt{s}$ is also shown. The data points at 1.8, 1.96 and 7 TeV are slightly offset horizontally for the illustration purpose. 154
8.3 The dependence of the theoretically calculated and the measured cross sections on the top quark pole mass. Theoretical calculations of [102, 103, 104] are labeled with 'Kidonakis', 'Moch and Uwer' and 'NLO+NNLL' in the legend, respectively. 155
8.4 Probability density function as a function of the top quark mass. The filled or hatched area in each distribution indicates the 68 % interval from the maximum. 155

List of Tables

1.1 Summary of the mass of quarks. . . . 2
1.2 The electric charge (Q), weak isospin (T and its third component T_3) and weak hypercharge (Y) for fermions. . . . 9

2.1 Beam characteristics at extraction from PS [35]. . . . 19
2.2 SPS beam and machine parameters [36]. . . . 19
2.3 Performance goals of LHC and the machine parameters in the 2011 LHC operation [27]. . . . 20

3.1 Main parameters of the solenoid and toroidal magnets in the ATLAS magnets. . 26
3.2 The coverage, granularity and longitudinal segmentation of the EM calorimeter . 36
3.3 The coverage, granularity and longitudinal segmentation of the hadron calorimeters 36
3.4 Overview of the muon detector instrumentation. 'Area covered' refers to the total area of the sensitive region of each subsystem. . . . 39

4.1 The fraction of data flagged as 'good' in each detector subsystem in the 2011 data taking [52]. 'EM' and 'hadron' in the table means the electromagnetic and the hadron calorimeter. . . . 49
4.2 Periods and triggers in the ATLAS 2011 pp collision runs. Period A is not listed since any data in Period A is not used in this analysis. . . . 51
4.3 The mass and the width of W and Z bosons and the top quark used in the MC simulation. . . . 54
4.4 List of MC samples used to estimate the acceptance and the background level. . 54
4.5 List of MC samples used to estimate the systematic uncertainty. . . . 54

5.1 Summary of the electron efficiency. . . . 61

6.1 The ratio between the number of W^+ and W^- bosons $r_{\mathrm{MC}} = N_{W^+}/N_{W^-}$ as a function of jet multiplicity. . . . 84
6.2 Measured numbers of W+jets events in the e+jets and the μ+jets channels after all the selection but the number of jets cut. The uncertainty includes both statistic and systematic. . . . 84
6.3 Predicted and observed numbers of events in the e+jets and the μ+jets channels after all the selections. The sign '(DD)' indicates that the numbers are estimated by the data-driven way. The uncertainty is statistic and systematic combined. . . 91
6.4 The leading $F_{b,c,l}$ fractions for jets with $P_{\mathrm{T}} > 25$ GeV in the e+jets channel, obtained from the simulated events. The category 'Other backgrounds' includes $t\bar{t} \to \ell\nu b\ell\nu b$, Z/γ^*, di-boson and the single top production. Uncertainties are statistical only. . . . 95

6.5 The leading $F_{b,c,l}$ fractions for jets with $P_{\mathrm{T}} > 25$ GeV in the μ+jets channel, obtained from the simulated events. The category 'Other backgrounds' includes $t\bar{t} \to \ell\nu b\ell\nu b$, Z/γ^*, di-boson and the single top production. Uncertainties are statistical only. 95
6.6 Uncertainties on the b-tagging efficiency measurement and the extracted $\sigma_{t\bar{t}}$ in fitting. 100

7.1 Event selections used to measure the top quark pair production cross section for the final states with ee, $\mu\mu$ and $e\mu$. 111
7.2 The number of remaining events for the ee channel at each event selection step for each physics process estimated by MC samples. S/B and $S/\sqrt{S+B}$ are also shown. 112
7.3 The number of remaining events for the $\mu\mu$ channel at each event selection step for each physics process estimated by MC samples. S/B and $S/\sqrt{S+B}$ are also shown. 112
7.4 The number of remaining events for the $e\mu$ channel at each event selection step for each physics process estimated by MC samples. S/B and $S/\sqrt{S+B}$ are also shown. 113
7.5 Systematic uncertainty on the $t\bar{t}$ acceptance. 114
7.6 The number of observed events and the expected events by MC. 'Di-boson' includes $WW/WZ/ZZ$ processes. 'Single top' means the Wt process. 128
7.7 Yields and uncertainties for the $Z/\gamma^* \to ee$ estimate 128
7.8 Yields and uncertainties for the $Z/\gamma^* \to \mu\mu$ estimate 129
7.9 Yields and the systematic uncertainty of the backgrounds in the ee channel which are estimated using MC. 132
7.10 Yields and the systematic uncertainty of the backgrounds in the $\mu\mu$ channel which are estimated using MC. 133
7.11 Yields and the systematic uncertainty of the backgrounds in the $e\mu$ channel which are estimated using MC. 134
7.12 The predicted and the observed numbers of events for each final state. The uncertainties include statistic and systematic uncertainties. The word '(DD)' indicates that the contribution is estimated by the data-driven method. 140
7.13 The measured cross sections in each dilepton channel, and the combination of all three channels. 149
7.14 The summary of the uncertainty for the cross section measurement. 150

Chapter 1

Introduction

The top quark was discovered as the heaviest quark in 1995 at Tevatron at Fermilab. The top quark is thought to be a good probe to test the standard model of the particle physics. Since it has a very short lifetime due to its heavy mass, it decays before forming a top-flavored hadron. This feature allows us to measure the properties of the quark, which is a parton, by studying the decay of the top quark. Currently, this is the only way to access the bare quark information. This fact makes the top quark unique, and therefore, it is important to measure its properties such as charge and spin as precisely as possible. A result of the measurement gives us a clue to understand the standard model. However, the study of the top quark so far has been based on the small statistics. This is because the production rate of the top quark is very low at Tevatron which is the only facility having an ability to produce the top quark before the Large Hadron Collider (LHC) operation. With LHC, the top quark is expected to be produced every few seconds. This is about one hundred times more frequent than the production rate at Tevatron. Because of this, LHC is sometimes called the Top Factory. LHC provides a chance to study the top quark precisely. In this thesis, we present the measurement of the production cross section of the top quark pair $\sigma_{t\bar{t}}$ multiplied by the branching ratio of the particular final state. The result would provide us a clue to understand both production and decay of the top quark, and hence the one to understand the perturbative QCD and the electroweak theory.

1.1 Top quark physics

We have a good chance to study the top quark with the largest statistics ever achieved. In this section, we describe the role that top quark plays to understand the standard model and to probe new physics beyond the standard model.

1.1.1 Importance of the top quark

The top quark plays a very important role in the standard model from various aspects. All things are stemmed from the very large mass of the top quark. Table 1.1 summarizes known mass of quarks. There are six quarks in the standard model. The quarks are categorized into three generations. The top quark is classified as the third generation up-type quark. As shown in Table 1.1, the top quark has an incredibly larger mass than any other quarks. The mass of the top quark is about 172 GeV which is almost the same as the nuclei of the gold atom, approximately 40 times heavier than the second heaviest quark, b-quark, and almost five orders of magnitude heavier than the lightest quark. This fact makes the contribution of the top quark to the radiative correction of the theoretical prediction of mass of the Higgs boson and other unknown particles large because the heavier particle contributes more to the calculation. Below,

Table 1.1: Summary of the mass of quarks.

Generation	Name	Mass
1	up (u)	1.7-3.3 MeV
	down (d)	4.1-5.8 MeV
2	charm (c)	1.18-1.34 GeV
	strange (s)	70-120 MeV
3	top (t)	$172.0 \pm 0.9 \pm 1.3$ GeV
	bottom (b)	$4.19^{+0.18}_{-0.06}$ GeV

we describe the fine tuning problem and the supersymmetric particle characteristics which are thought to be largely affected by the top quark.

Fine tuning problem

The recently discovered Higgs boson has a mass around 125 GeV [1, 2]. This fact points out that there is an unnatural fine tuning to make the mass of the Higgs boson being around the electroweak scale, $\mathcal{O}(100$ GeV). Below, we will explain the fine tuning of the Higgs mass.

The physical (or observed) mass of the Higgs boson receives higher order contributions. When the original mass is written as m, the physical mass, $m_{\rm phys}$, can be written with a higher order correction from fermions ($\delta m_{\rm fermion}$), gauge bosons ($\delta m_{\rm gauge}$) and the Higgs boson ($\delta m_{\rm Higgs}$) as

$$m^2_{\rm phys} = m^2 + \delta m^2_{\rm fermion} + \delta m^2_{\rm gauge} + \delta m^2_{\rm Higgs}. \tag{1.1}$$

The contribution from fermions with one-loop diagram (*e.g.* Figure 1.1) can be written as

$$\delta m^2_{\rm fermion} = - \sum_{\text{all fermions}} \frac{1}{8\pi^2} Y_{\rm f}^2 \Lambda^2, \tag{1.2}$$

where $Y_{\rm f}$ is the Yukawa coupling constant for each fermion, and Λ is the cut-off scale for the

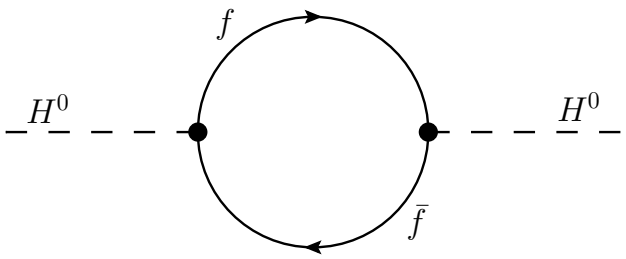


Figure 1.1: The Feynman diagram of fermion one-loop contribution to the Higgs boson.

higher order correction typically set as the Plank scale or the GUT scale, $\mathcal{O}(10^{15\text{-}19}$ GeV). As

seen in the equation, the correction is proportional to the Yukawa coupling constants, and hence to the fermion mass. This means the contribution is dominated by the top quark. The other correction term from the vector bosons can be expressed as

$$\delta m^2_{\text{gauge}} = \frac{1}{16\pi^2}\left(\frac{3}{4}g^2 + \frac{1}{4}g'^2\right)\Lambda^2, \tag{1.3}$$

where g and g' are the gauge coupling constants, and the correction from the Higgs boson loop is

$$\delta m^2_{\text{Higgs}} = \frac{1}{8\pi^2}\lambda\Lambda^2, \tag{1.4}$$

where λ is the Higgs self-coupling constant. The corrections from fermions and the bosons have opposite signs. In the end, one can find that the total size of the correction, $\delta m^2_{\text{total}}$, becomes negative with an order of $\mathcal{O}(\Lambda^2 \approx 10^{30\text{-}38}$ GeV) by the numerical calculation because the Yukawa coupling constant of the top quark, $Y_t \approx 1$, is much larger than g, g' and λ. To force m_{phys} to be around $\mathcal{O}(100$ GeV), the original mass should be fine tuned to be very close to $\delta m^2_{\text{total}}$.

To solve this problem, many new theoretical approaches to cancel this fine tuning are developed. The phenomenon predicted by such new theories are actively searched for in the LHC experiments. In addition to such direct searches, good understandings of the source of the correction, the top quark, is important and might provide a hint to solve this problem from the experimental side (*e.g.* the precise top quark mass measurement).

Supersymmetry model

The supersymmetry (SUSY) is the one of the ideas to extend the standard model. This is actively studied theoretically and experimentally because the predicted particles are expected to be within the reach of the LHC experiments. SUSY introduces a new symmetry that exchanges the bosonic and fermionic fields in the theory as

$$Q|\text{Boson}\rangle = |\text{Fermion}\rangle \quad \text{and} \quad Q|\text{Fermion}\rangle = |\text{Boson}\rangle, \tag{1.5}$$

where the operator Q is the generator of a supersymmetry transformation. The supersymmetry transformation is like the $SU(2)$ doublets that categorize up- and down-type particles. SUSY organizes fermions and bosons in supermultiplets. The standard model particles are paired with so-called superpartners, which are the particles with the same quantum numbers and mass, but have a different spin by 1/2, corresponding to a boson-fermion exchange. The superpartners for fermions are named with the prefix 's-', like squarks, sleptons, stop, selectron. The fermionic superpartners are named with appending '-ino' to the one in the standard model, like gluino, higgsino. Figure 1.2 shows all particles in the standard model and their superpartners.

The minimal supersymmetric standard model (MSSM) is the simple extension of the standard model within the supersymmetry framework. The supersymmetry is interesting symmetry to be considered to solve the open problems in the standard model such as the fine tuning problem and the existence of the dark matter. However, the supersymmetry should be a broken symmetry because we do not discover the light mass superpartner particles, such as the selectron with 511 keV of mass. Therefore, theorists introduce the mechanism to break the supersymmetry in many ways. The model including the mechanism which assumes the gravity works as the mediator to break the supersymmetry is called the gravity mediation symmetry breaking model. There is also a model called the gauge mediated symmetry breaking model (GMSB) which assumes the gauge interaction works as the mediator.

One of the simplest extensions of the standard model with supersymmetry with assuming the gravity mediated model is called mSUGRA. In this model, the superpartner of third generation

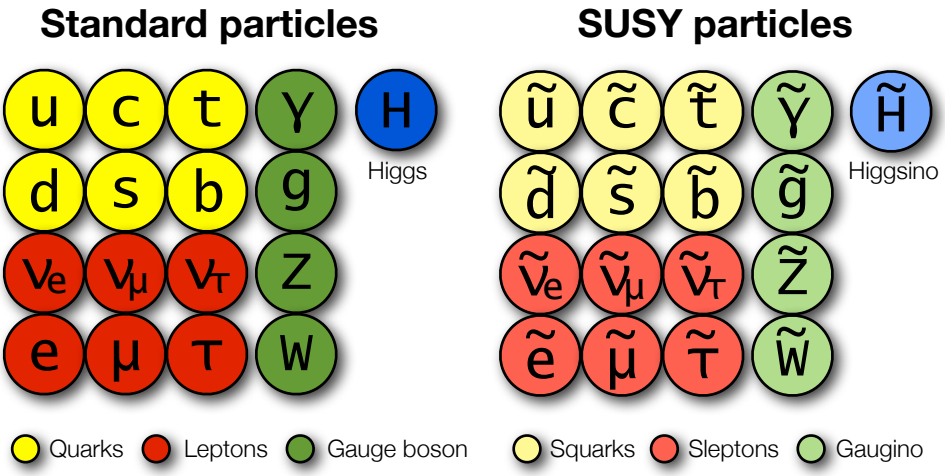


Figure 1.2: All particles in the standard model and their superpartners.

quarks, stop and sbottom, tend to have a relatively light mass with the following mechanism. The mass of the squarks is predicted by evolving down from the reference mass of the bosonic sparticle, so-called m_0, at the reference energy scale, typically set at $\mathcal{O}(10^{15\text{-}16}$ GeV), to the mass at the electroweak scale by using the squared-mass parameter described as $\frac{d}{dt}m^2_{Q_i}$ where $t = \ln(Q/Q_0)$ where Q is the renormalization scale at which the mass is evaluated, and Q_0 is the reference energy scale. The mass parameter of the i-th generation squark is denoted as $m^2_{Q_i}$. The squared mass parameter gets contributions from their superpartner particles. This contribution is positive and proportional to the square of the Yukawa coupling constant. Therefore, the relationship between the squared mass parameters for the first and the second generation squarks and the third generation squarks becomes as

$$\frac{d}{dt}m^2_{Q_3} > \frac{d}{dt}m^2_{Q_{1,2}}. \tag{1.6}$$

This equation means that the third generation squarks have the mass lighter than others at the low energy scale. Not only the mSUGRA model, but also many other models have similar feature about the third generation squarks. Thus, the stop and the sbottom are thought to be the lightest squarks. The details of this discussion and the full description of the mass parameters, Yukawa coupling contributions can be found in the reference [3].

The fact that the stop and the sbottom are lighter than the others implies that top quarks or bottom quarks exist most of the time in the decay products of the supersymmetric particles. Figure 1.3 shows the example of such decays of the supersymmetric particle. The precise measurement of the top quark properties such as cross section and branching ratio might be affected from the contributions of such undiscovered physics processes. In other words, the precise top quark measurement might discover phenomenon of new physics processes.

1.2 Phenomenology of the top quark physics

In this section, the phenomenology of the top quark physics in the hadron colliders is described.

1.2.1 Production of the top quark

The top quark pair production cross section, $\sigma_{t\bar{t}}$, is calculated by QCD. To produce $t\bar{t}$ by pp collisions, the parton should be hard scattered, *i.e.* be scattered with a large momentum transfer

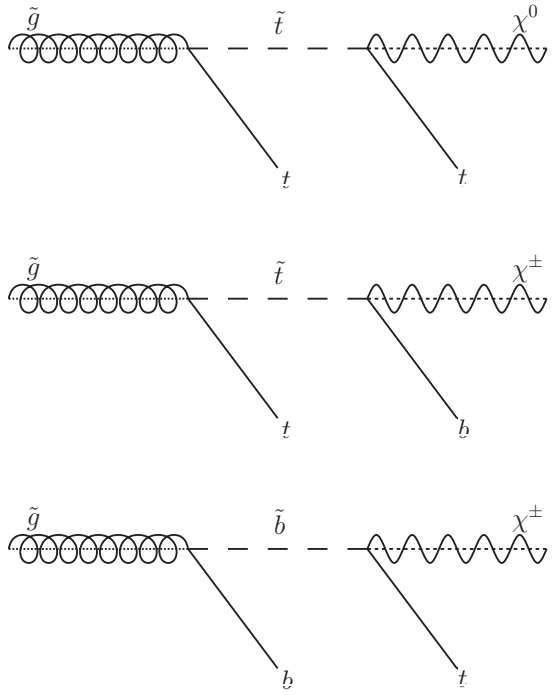


Figure 1.3: Example of the gluino ($\tilde{g}$) decay into the final state with the top quark. The particle χ in the diagrams are chargino or neutralino which are fermionic superpartner predicted in SUSY.

Q^2 as much as the order of the top quark mass. Thanks to the smallness of the strong coupling constant $\alpha_s(\ll 1)$ at such a high energy region, the partonic part of the cross section, $\hat{\sigma}_{ij}$, is calculable in a perturbative way. In the perturbative expansion, infinities such as ultraviolet divergences appear at the higher order calculation. To remove these divergences, the artificial scale called the renormalization scale μ_r is introduced. In the calculation of the cross section, the cross section can be separated into a short-distance part calculable perturbatively and a long-distance part which is not calculable. This separation is called factorization. The border of the long- and short-distance part is defined by an arbitrary factorization scale μ_f. In the long-distance part, one needs to know the probability for a parton inside proton to carry the fractional momentum x to the proton momentum, which is modeled by a parton distribution function (PDF). In general, PDFs are expressed as a function of x and μ_f^2, $f_i(x, \mu_f^2)$ for each parton flavor i (*e.g.* $g, u, \bar{u}$...).

By including two artificial parameters, μ_r and μ_f, the general form of the heavy quark pair production cross section in collisions between proton A and B is expressed as

$$\sigma(s) = \sum_{i,j} \iint dx_A dx_B \hat{\sigma}_{ij}(\hat{s}; \alpha_s(\mu_r^2), \mu_r^2, \mu_f^2) f_i^A(x_A, \mu_f^2) f_i^B(x_B, \mu_f^2), \tag{1.7}$$

where s is the squared center-of-mass energy of the colliding protons, and $\hat{s}$ is the squared effective center-of-mass energy of the colliding partons expressed as $\hat{s} = x_A x_B s$ where x_A and x_B are the fractional momenta carried by the hard scattered partons in the colliding protons A and B, respectively. The PDFs for colliding protons A and B are denoted as $f_i^A(x_A, \mu_f^2)$ and $f_i^B(x_B, \mu_f^2)$. The cross section which is determined by nature is by definition independent on the arbitrary renormalization and factorization scale, although the theoretical calculation has the dependence on such arbitrary scales. This causes an uncertainty in the theoretical prediction.

Below we present how to obtain the partonic cross section and PDFs for the $\sigma_{t\bar{t}}$ calculation.

- The partonic cross section

  The partonic cross sections from parton i and j involved in Equation (1.7) can be expanded into a perturbative series in the strong coupling constant α_s shown as

$$\hat{\sigma}_{ij}(\hat{s}, m_t^2, \mu_r^2) = \frac{\alpha_s^2(\mu_r^2)}{m_t^2}\mathcal{F}_{ij}^{(0)}(\hat{s}, m_t^2) + \frac{\alpha_s^3(\mu_r^2)}{m_t^2}\mathcal{F}_{ij}^{(1)}(\hat{s}, m_t^2) + \dots \,. \tag{1.8}$$

  When the power series is truncated at the order n of α_s, the calculated cross section has a μ_r dependence at $\mathcal{O}(\alpha_s^{n+1})$. The dimensionless parameter $\mathcal{F}_{ij}$ is calculated in order by order by evaluating the appropriate Feynman diagrams. At the leading order (LO), the top quark pair is generated either from quark-antiquark annihilation or gluon-gluon fusion as shown in Figure 1.4. The LO partonic cross sections for each production process,

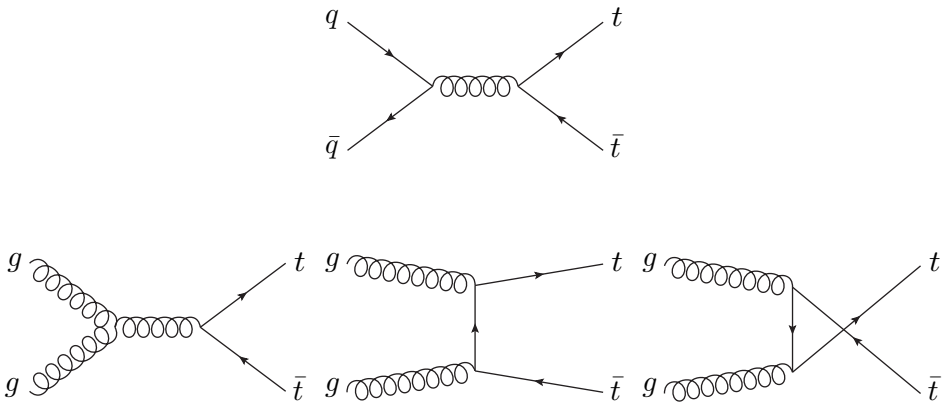


Figure 1.4: The $t\bar{t}$ production process at the lowest order in hadron colliders. The top (bottom) shows quark-antiquark annihilation (the gluon fusion).

  corresponding to $\mathcal{F}_{ij}^{(0)}$ in the expansion, can be obtained as follows. First, the scattering amplitude is derived from each Feynman diagram. Second, the differential cross section is obtained by integrating the squared amplitude over the entire momentum space of the top quark pair. Finally, $\mathcal{F}_{ij}^{(0)}$ is obtained by summing up the contribution from all the possible diagrams. The resulting LO cross sections are shown as

$$\hat{\sigma}(q\bar{q} \to t\bar{t}) = \frac{1}{27}\frac{\pi\alpha_s^2\beta\rho(2+\rho)}{m_t^2} \quad \text{and} \tag{1.9}$$

$$\hat{\sigma}(gg \to t\bar{t}) = \frac{\pi\alpha_s^2\beta\rho}{192m_t^2}\left[\frac{1}{\beta}(\rho^2+16\rho+16)\ln\left(\frac{(1+\beta)}{(1-\beta)}\right) - 28 - 31\rho\right], \tag{1.10}$$

  where $\beta = \sqrt{1-\rho}$ ($\rho = 4m_t^2/\hat{s}$) is the velocity of the top quarks in the partonic center-of-mass frame.

  In general the result of the LO calculation is reliable, *i.e.* describes the nature with reasonable accuracy. However, it is known that the dependence on the renormalization and factorization scale at the LO calculation is larger than the one at the higher order. Therefore, the higher order corrections are essential for the accurate prediction. Even after factoring the collinear divergences into PDF, the higher order differential cross sections still contain collinear terms which are logarithmically divergent at the threshold ($\beta \to 0$).

Physically, these terms correspond to the soft-gluon radiation. To calculate the higher order terms with avoiding such a divergence, the techniques so-called resummation are developed for the next-to-leading order (NLO) corrections and further the next-to-next-leading order (NNLO) corrections. For the LHC experiments, the next-to-next-leading logarithmic (NNLL) corrections are performed. Further details for the resummation can be found in the references [4, 5].

- The parton distribution function

  Because non-perturbative behavior of QCD is modeled by PDF, we have to extract PDFs from the experimental data in some way. While PDF cannot be calculated by the perturbative QCD, the evolution of PDF with a given energy scale μ_f can be theoretically predicted. The evolution is described for all orders by the Dokshitzer-Gribov-Lipatov-Altarelli-Parisi (DGLAP) evolution equation which is derived from the renormalization group equation shown as

$$\mu^2 \frac{d^2}{d\mu^2} f_i(x, \mu^2) = \frac{\alpha_s \mu^2}{2\pi} \sum_{j=q,\bar{q},g} \int_x^1 \frac{d\xi}{\xi} P_{ij}\left(\frac{x}{\xi}, \alpha_s(\mu^2)\right) f_j(\xi, \mu^2), \tag{1.11}$$

  where $i = q, \bar{q}, g$ [6]. The functions P_{ij} are called the Altarelli-Parisi evolution kernels. It is worth noting that P_{ij} which is the core to evolve PDF to other energy scales are calculable by the perturbative expansion shown as

$$P_{ij}(z, \alpha_s) = P_{ij}^{(0)}(z) + \frac{\alpha_s}{2\pi} P_{ij}^{(1)}(z) + \ldots , \tag{1.12}$$

  This DGLAP equation ensures that the measured PDFs at a certain Q^2 is evolved at another energy scale.

  PDFs are obtained from deep-inelastic scattering measurements by fixed target and Tevatron experiments. They are usually measured at a certain energy scale by fitting the experimental data with a model function. Figure 1.5 shows the covered energy range to measure PDFs by some experiments. The PDF sets used by the ATLAS and CMS experiments are obtained from these experiments and the DGLAP evolution. For example, Figure 1.6 shows PDFs for $\mu_f = Q^2 = 10$ and 10^4 GeV^2 using the MSTW 2008 NNLO parametrization.

The top quark pair production cross section at LHC

Assuming two colliding partons i and j have similar momentum, the threshold on the parton's fractional momentum relative to a proton to produce top quark pair can be calculated to be $x_i \sim x_j \sim x_{\rm thr} = 2m_t/\sqrt{s}$. At the center-of-mass energy of 7 TeV, which is the beam energy in 2011, $x_{\rm thr}$ is about 0.025 where the gluon PDF is dominant as shown in Figure 1.6. Therefore, the production of the top quark pair at LHC occurs predominantly through the gluon-gluon fusion. The fraction of the $t\bar{t}$ production via the gluon-gluon fusion is predicted to be about 90 % theoretically.

The calculation of the top quark pair production cross section at $\sqrt{s} = 7$ TeV is performed within the ATLAS top physics working group using the HATHOR program [7] which performs the perturbative QCD at approximate NNLO. The top quark mass m_t is assumed to be 172.5 GeV. MSTW 2008 is used as NNLO PDF. The result is

$$\sigma_{t\bar{t}}^{\rm Approx.NNLO} = 166.78^{+4.68}_{-9.26}({\rm scale})^{+5.12}_{-4.93}(m_t)^{+15.80}_{-15.09}({\rm PDF})\ {\rm pb}. \tag{1.13}$$

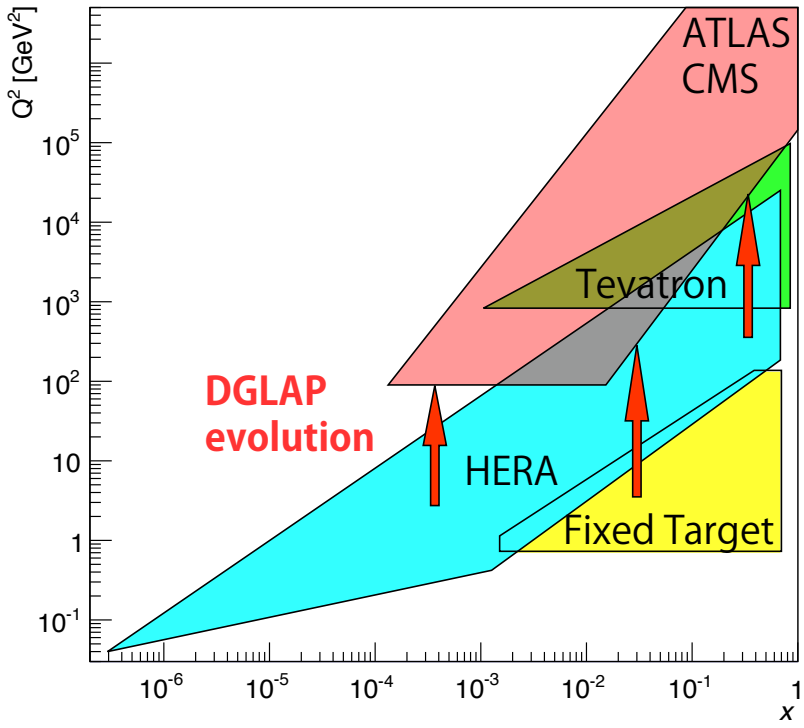


Figure 1.5: The covered fractional energy x and Q^2 range to measure the PDFs by the experiments in HERA, Tevatoron and the fixed target experiments. The ordinal energy range for the physics explored by the ATLAS and the CMS experiments is shown as the red box.

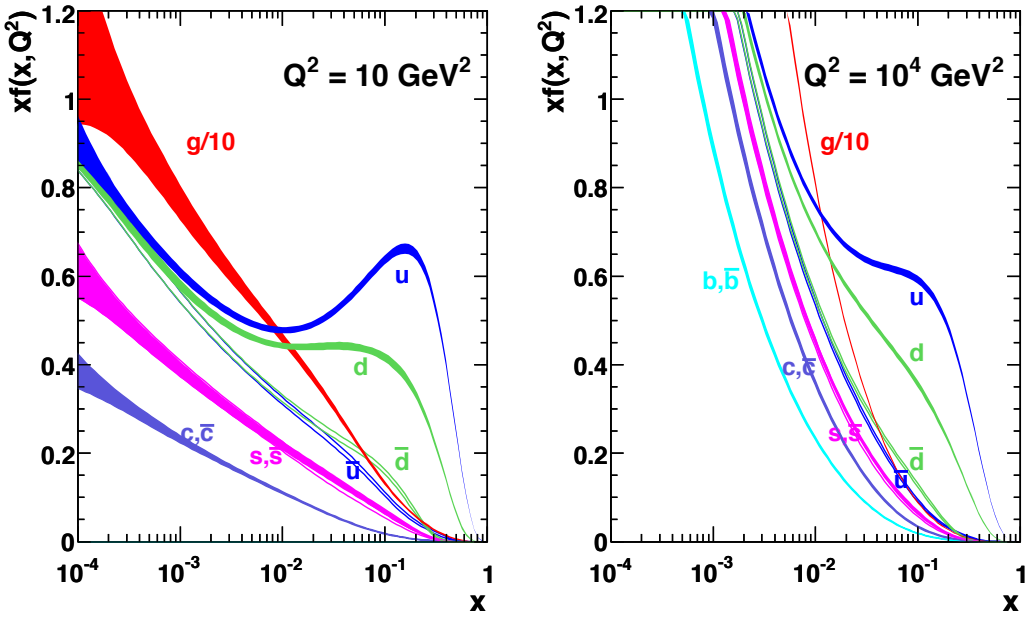


Figure 1.6: The distributions of x times the parton distributions $f(x, Q^2)$ for $Q^2 = 10$ and 10^4 GeV^2 with its uncertainty using the MSTW 2008 NNLO parametrization [8]. The one for gluon is scaled down by factor 10.

The uncertainty labeled as '(scale)' comes from the factorization and the renormalization scale. It is evaluated by varying these scales set at m_t by the factors of 0.5 to 2.0. The uncertainty due to the top quark mass is determined by changing the assumed mass by $\pm$ 1 GeV, and labeled as '(m_t)'. To estimate the uncertainty from PDF, the MSTW 2008 NNLO PDF 90 % C.L. error set [9] is used. The result above is cross checked with the NLO+NNLO calculation [10] implemented in the Top++ program [11] and agrees well within the uncertainty. The value in Equation (1.13) is used as the reference cross section of the $t\bar{t}$ production in this analysis.

1.2.2 Decay of the top quark

In the standard model, a decay of the top quark is described by the electroweak theory based on the $SU(2)_L \times U(1)_Y$ symmetry group. In this framework, there are three generations of left-handed quarks and leptons which transform under the weak interaction as doublets while right-handed quarks and leptons are the weak isospin singlets. Table 1.2 shows the summary of the quantum numbers for each particle. Top quark decays into its weak isospin partner, the

Table 1.2: The electric charge (Q), weak isospin (T and its third component T_3) and weak hypercharge (Y) for fermions.

Fields	Particles			Q	T	T_3	Y
Q_L^i	$\begin{pmatrix} u_L \\ d_L \end{pmatrix}$	$\begin{pmatrix} c_L \\ s_L \end{pmatrix}$	$\begin{pmatrix} t_L \\ b_L \end{pmatrix}$	$+\frac{2}{3}$ $-\frac{1}{3}$	$\frac{1}{2}$	$+\frac{1}{2}$ $-\frac{1}{2}$	$\frac{1}{3}$
L_L^i	$\begin{pmatrix} \nu_L^e \\ e_L \end{pmatrix}$	$\begin{pmatrix} \nu_L^\mu \\ \mu_L \end{pmatrix}$	$\begin{pmatrix} \nu_L^\tau \\ \tau_L \end{pmatrix}$	0 -1	$\frac{1}{2}$	$+\frac{1}{2}$ $-\frac{1}{2}$	$-\frac{1}{2}$
u_R^i	u_R	c_R	t_R	$+\frac{2}{3}$	0	0	$\frac{4}{3}$
d_R^i	d_R	s_R	b_R	$-\frac{1}{3}$	0	0	$-\frac{2}{3}$
e_R^i	e_R	μ_R	τ_R	-1	0	0	-2
ν_R^i	ν_R^e	ν_R^μ	ν_R^τ	0	0	0	0

bottom quark, and the W boson with the large branching ratio. However, the standard model allows that the top quark decays into lower generation quarks, the down and the strange quark, because the weak interaction eigenstates are mixing of the mass eigenstates. The mixing is described by the unitary Cabibbo-Kobayashi-Masukawa (CKM) matrix

$$\begin{pmatrix} d^w \\ s^w \\ b^w \end{pmatrix} = \begin{pmatrix} V_{ud} & V_{us} & V_{ub} \\ V_{cd} & V_{cs} & V_{cb} \\ V_{td} & V_{ts} & V_{tb} \end{pmatrix} \begin{pmatrix} d^m \\ s^m \\ b^m \end{pmatrix}, \tag{1.14}$$

where the superscripted w and m stands for 'weak eigenstate' and 'mass eigenstate'. The CKM matrix has non-zero values for the off-diagonal elements. Decay widths of each final state at the tree level can be described as

$$\Gamma_t^0 = \frac{G_F m_t^3}{8\pi\sqrt{2}} \times |V_{tq}|^2, \tag{1.15}$$

where $q = d, s, b$, m_t is the mass of the top quark, and G_F refers to the Fermi constant defined with the weak coupling constant g as $G_F = \sqrt{2}g^2/8m_W^2$, where m_W is the mass of the W boson.

Using the latest results of the measurement of the CKM matrix element, $V_{td} = 0.00857^{+0.00033}_{-0.00030}$, $V_{ts} = 0.04051^{+0.00060}_{-0.00104}$ and $V_{tb} = 0.999142^{+0.000043}_{-0.000025}$ [12], one can find that the branching ratio of $t \to Wb$ is close to unity,

$$\frac{\mathcal{B}(t \to Wb)}{\mathcal{B}(t \to Wq)} = \frac{|V_{tb}|^2}{|V_{td}|^2 + |V_{ts}|^2 + |V_{tb}|^2} > 0.999, \tag{1.16}$$

where we assume three generations of quarks.

At the next to leading order calculation, the decay width Γ_t^0 is slightly modified. Neglecting terms of order m_b^2/m_t^2, α_s^2 and $(\alpha_S/\pi)m_W^2/m_t^2$, where m_b is the mass of b-quark, the width predicted in the standard model is

$$\Gamma_t = \Gamma_t^0 \left(1 - \frac{m_W^2}{m_t^2}\right)^2 \left(1 + 2\frac{m_W^2}{m_t^2}\right) \left[1 - \frac{2\alpha_s}{3\pi}\left(\frac{2\pi^2}{3} - \frac{5}{2}\right)\right]. \tag{1.17}$$

This implies that Γ_t is about 1.32 GeV, equivalent to the lifetime $\tau_t = 1/\Gamma_t \sim 5 \cdot 10^{-25}$ s. This lifetime is significantly shorter than the time of typical hadronization time via the strong interaction. Therefore, top quarks are expected to decay before forming top-flavored hadrons or $t\bar{t}$ quarkonium bound states.

1.2.3 Top quark signature in the hadron collider

The final state of $t\bar{t}$ has two W bosons and two b-quarks because the top quark decays almost exclusively into a W boson and a b-quark. The b-quark becomes a b-hadron before it decays, and also generates many associated hadrons by a gluon radiation and splitting. In the end, it forms a b-jet. Therefore, the top quark pair final state consists of two b-jets and the decay products of the W bosons.

The probability that a W boson decays into any weak isospin doublets are roughly the same because the phase space is large enough to decay into any doublets, except the top and bottom quark pair. In addition, considering that each quark doublet has three different colors, there are nine possible final states in W boson decay (*e.g.* $W^- \to e^-\bar{\nu}_e$, $\mu^-\bar{\nu}_\mu$, $\tau^-\bar{\nu}_\tau$, $\bar{u}_{\bar{R}}d_R$, $\bar{u}_{\bar{G}}d_G$, $\bar{u}_{\bar{B}}d_B$, $\bar{c}_{\bar{R}}s_R$, $\bar{c}_{\bar{G}}s_G$, $\bar{c}_{\bar{B}}s_B$).

Because there are two W bosons in the final state, the possible combinations of W boson decay products are summarized in Figure 1.7. From an experimental point of view, the final states are categorized into the number of charged leptons from the W boson decays: all-hadronic (no leptons), single lepton, and dilepton channels. The branching ratios are roughly 4/9, 4/9 and 1/9 for the all-hadronic, the single lepton and the dilepton channels, respectively. The characteristics of three types of the final states are summarized below.

All-hadronic channel

The all-hadronic channel has six jets. Both W bosons coming from the top quarks decay hadronically. This channel has the largest branching ratio at roughly 46 % and thus has an advantage in terms of statistics. However, the fact that there are no lepton with large transverse momentum, P_{T}, makes it difficult to suppress large amount of QCD multi-jet backgrounds, resulting in low signal-to-background ratio.

Single lepton channel

In the single lepton channel, also called 'lepton plus jets' channel, only one of the W bosons decays leptonically. This channel has a relatively small background thanks to the presence of the high P_{T} lepton and large momentum imbalance in the plane transverse to the beam due

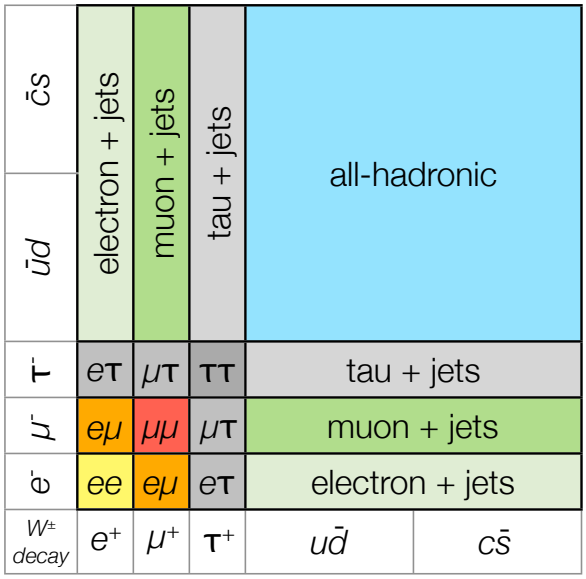


Figure 1.7: The decay channels of top quark pair

to undetected neutrino. This leads well-understood backgrounds with a reasonable amount of statistics.

Dilepton channel

In the dilepton channel which is used in this analysis, both W bosons decay leptonically. The branching ratio of this channel is only about 10 % if tau leptons excluded. However, it is the cleanest final state because few other processes have two high P_{T} leptons and a large momentum imbalance.

1.3 Measurement of the production cross section

In this thesis, the measurement of $\sigma_{t\bar{t}}$ is presented. The production cross section is one of the most basic properties in the top quark physics. The goal is to test the perturbative QCD at the pp collisions with $\sqrt{s} = 7$ TeV. Testing the perturbative QCD is important, because QCD is not understood as precise as the electroweak theory, and also it is not tested at such a high energy region.

The production cross section is related to the top quark mass. As discussed in Section 1.1, the top quark contributes to the radiative correction more than the other quarks due to its heavy mass. This implies that the top quark mass is an important parameter in the theoretical calculation. The direct measurements of the mass by utilizing the invariant mass of the top quark decay products are performed at the Tevatron and LHC experiments and have a good precision [13, 14]. However, the measurements highly rely on the input mass of the top quark for the MC generators which is not in a well-defined renormalization scheme. Therefore, the measured mass has an uncertainty in its definition, and hence the pole mass which is well defined by the renormalization scheme is difficult to be extracted by the direct measurements. On the other hand, the pole mass can be extracted by comparing the $\sigma_{t\bar{t}}$ measurement and the theoretical calculation, because the predicted $\sigma_{t\bar{t}}$ is calculated based on the top quark pole mass as its input. Currently, the measurement of the cross section is believed to be the way to access the top quark pole mass with least theoretical uncertainty.

In addition to the motivations above, there are other several importance in terms of the LHC physics program. First, $t\bar{t}$ is one of the main background processes for most of new physics searches. For example, the SUSY search suffers from large $t\bar{t}$ backgrounds. Understanding of the background process is very important to achieve a high sensitivity to unknown phenomenon. Second, understanding of the top quark production is important because the $t\bar{t}$ events can be used to measure the performance of the b-quark tagging algorithm. Recently, the physics analysis with the b-quark tagging becomes more important at the LHC physics program. Below is an example of such analysis. The ATLAS and the CMS experiments observed the Higgs boson. However, it has not been confirmed that the Higgs boson is the one predicted by the standard model. If it is the case the Higgs boson decays into a b-quark pair with the largest branching ratio. Observing $H \to b\bar{b}$ is one of the most important topic in the future LHC physics program. This is because the Yukawa term which describes the Higgs-fermion coupling is added rather artificially to the standard model Lagrangian to generate the mass of the fermion. Namely, there are no necessities for the theory to exist the Yukawa term. The existence of this term has to be proven by the experiment. Therefore, $H \to b\bar{b}$ should be a key to prove the electroweak theory in the standard model.

1.4 Past measurements

1.4.1 Before the discovery of the top quark

In 1977, the bottom quark was discovered at Fermilab [15]. Because of the discovery of the bottom quark which is the partner of the isospin doublet of the up-type quark, the existence of the top quark was anticipated. The top quark is searched both in the e^+e^- collider like PETRA (DESY), TRISTAN (KEK), SLC (SLAC) and LEP (CERN) and in the $p\bar{p}$ collider like $Sp\bar{p}S$ (CERN). At the beginning of this era, the top quark was searched for as the top-antitop bound state like the $c\bar{c}$ bound state of J/ψ, because the mass of the top quark was thought to be light, $\mathcal{O}(10$ GeV). Because such final states were not found, the experiments set a lower limit for the top quark mass.

In the e^+e^- colliders, the mass reach is limited to a half of the achieved center-of-mass energy because the top quark is expected to be pair-produced. In the experiment with $Sp\bar{p}S$, the center-of-mass energy was large enough to produce top quark pair. However, it was difficult to find the top quark signal because the luminosity and the expected production rate was low. At this stage, the lower limit for the top quark mass was set at 69 GeV by the $Sp\bar{p}S$ collider experiments.

1.4.2 Measurements at Tevatron

In 1995, two Tevatron experiments at Fermilab, CDF and DØ, discovered the top quark in $p\bar{p}$ collisions with $\sqrt{s} = 1.8$ TeV, and measured the mass to be $174 \pm 10^{+13}_{-12}$ GeV and $199 \pm 19^{+21}_{-22}$ GeV, respectively [16,17]. Following the discovery, the production cross section was measured by using their measured mass in their calculations. The CDF experiment yielded $6.8^{+3.6}_{-2.4}$ pb and the DØ experiment yielded 6.4 ± 2.2 pb. The center-of-mass energy was increased to $\sqrt{s} = 1.96$ TeV in Tevatron Run 2 in the 2000's. The cross section was measured in three final states, the dilepton, the single lepton and the all hadronic, with various techniques. The result of the combination of all measurements in CDF and DØ experiments is

$$\sigma_{p\bar{p}\to t\bar{t}} = 7.65 \pm 0.20(\text{stat.}) \pm 0.36(\text{syst.}) \text{ pb}. \tag{1.18}$$

This is consistent with the standard model prediction, $\sigma_{t\bar{t}} = 7.24^{+0.24}_{-0.27}$ pb. The total precision of the measurement is approximately 5 %. Figure 1.8 shows the summary of measurements at Tevatron with $\sqrt{s} = 1.96$ TeV.

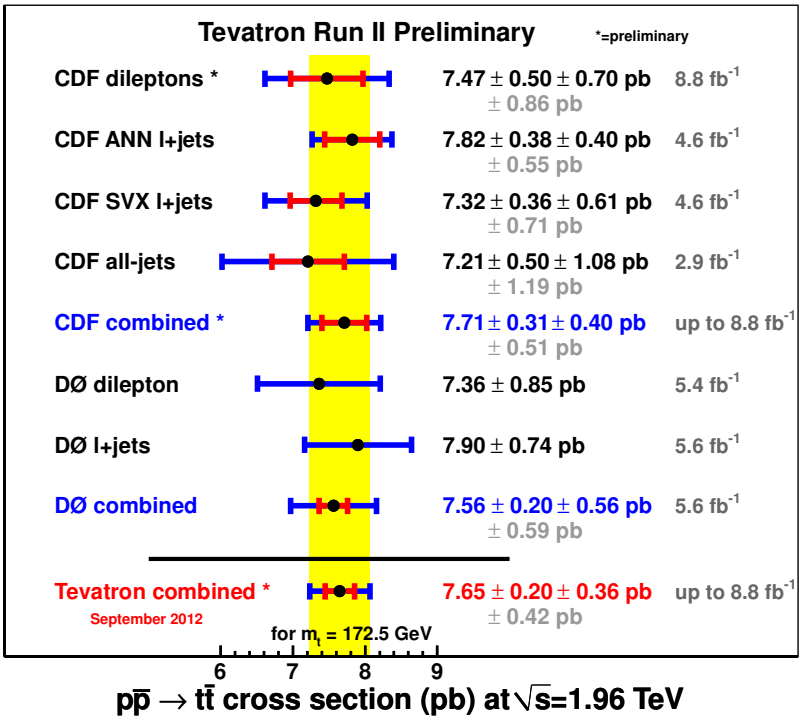


Figure 1.8: Summary of the $\sigma_{t\bar{t}}$ measurement with $p\bar{p}$ collisions at $\sqrt{s} = 1.96$ TeV [18]. The red (blue) bar in each point show the statistical (total) uncertainty.

1.4.3 Measurements at LHC

The pp collisions at LHC started in December 2009 with $\sqrt{s} = 900$ GeV. At the end of March 2010, pp collisions with $\sqrt{s} = 7$ TeV was achieved. Both ATLAS and CMS experiments reported the observation of the top quark pairs in the summer of 2010 [19, 20].

By using more statistics, $\mathcal{O}(1\ \text{fb}^{-1})$ taken in 2011, $\sigma_{t\bar{t}}$ for various final states were measured with an approximately 10 % precision. The most precise result in ATLAS was obtained by combining three major final states to be

$$\sigma_{t\bar{t}} = 177 \pm 20(\text{stat.}) \pm 14(\text{syst.}) \pm 7(\text{lumi.})\ \text{pb}.$$

The one in CMS was from a dilepton channel to be

$$\sigma_{t\bar{t}} = 168 \pm 18(\text{stat.}) \pm 14(\text{syst.}) \pm 7(\text{lumi.})\ \text{pb}.$$

These are consistent with the theoretical prediction, $\sigma_{t\bar{t}} = 166.8^{+16.5}_{-17.8}$ pb. All other results are summarized in Figure 1.9.

The measurements with 8 TeV of center-of-mass energy were also performed in both experiments. The results are

$$\sigma_{t\bar{t}} = 241 \pm 2(\text{stat.}) \pm 31(\text{syst.}) \pm 9(\text{lumi.})\ \text{pb (ATLAS), and}$$
$$\sigma_{t\bar{t}} = 227 \pm 3(\text{stat.}) \pm 11(\text{syst.}) \pm 10(\text{lumi.})\ \text{pb (CMS)}.$$

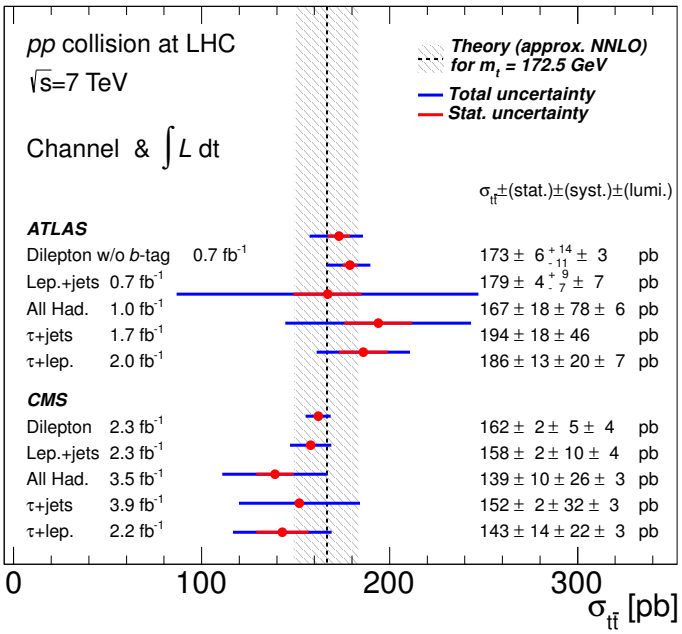


Figure 1.9: Summary of the $\sigma_{t\bar{t}}$ measurements with $\sqrt{s} = 7$ TeV at the ATLAS and the CMS experiments [21, 22, 23, 24, 25, 26].

Both measurements are consistent with the theoretical prediction, $\sigma_{t\bar{t}} = 238^{+22}_{-24}$ pb.

The analysis described in this thesis is the first measurement of $\sigma_{t\bar{t}}$ in the dilepton channel using whole data with $\sqrt{s} = 7$ TeV taken with the ATLAS detector.

1.5 Measurement technique

In this section, the technique of the measurement of $\sigma_{t\bar{t}}$ used in this thesis is presented.

1.5.1 Principle of the measurement

In this analysis, we use the dilepton final state. The number of dilepton events is written as

$$N_{t\bar{t}\to\text{dilepton}} = \sigma_{t\bar{t}} \times \int \mathcal{L}dt \times BR(t\bar{t} \to \text{dilepton}), \tag{1.19}$$

where $\int \mathcal{L}dt$ is an integrated luminosity, and $BR(t\bar{t} \to \text{dilepton})$ is the known branching ratio to the dilepton final state. As seen in Equation (1.19), the cross section can be measured just by counting how many events were produced for a known integrated luminosity. In a real experimental situation, we should consider some other things. First, we cannot detect all the events from the top quark pair due to the imperfect detector coverage, a finite detection efficiency and experimental mis-measurements. Therefore, we must know the acceptance, $\mathcal{A} = N_{\text{accepted}}/N_{t\bar{t}\to\text{dilepton}}$, to select the signal events. Second, we should consider the fact that we cannot get the pure top quark pair samples because there are backgrounds due to experimental mis-measurements, and/or the same final state from other physics processes. The number of observed data, N_{observed}, is thus written as

$$N_{\text{observed}} = N_{\text{accepted}} + N_{\text{BG}}, \tag{1.20}$$

where N_{BG} is the number of background events.

By combining the equations above, the production cross section is written as

$$\sigma_{t\bar{t}} = \frac{N_{\mathrm{observed}} - N_{\mathrm{BG}}}{\mathcal{A} \times \int \mathcal{L}dt \times BR(t\bar{t} \to \mathrm{dilepton})}. \tag{1.21}$$

Selecting top quark pair

We use the ee, $\mu\mu$ and $e\mu$ final states in this analysis. Tau is removed in the nominal analysis because it is more difficult to identify tau than electron and muon.

The electrons and muons from W boson decays in $t\bar{t}$ events tend to have large P_{T} because they come from heavy particle decays. In addition, they are isolated, *i.e.* there are no other particles around them, not like the one in the heavy flavor hadrons such as B and D hadrons. These features help to select the leptons from $t\bar{t}$ events. In addition to the two leptons, there are two neutrinos in the final state. Thus, large momentum imbalance is used as the signature of escaping neutrinos. Because of the existence of two b-quarks decaying from top quarks, identification of b-quark jet, called b-tagging, also helps to isolate the signal from the backgrounds.

In the standard model process, it is very rare to have two isolated high P_{T} leptons, large momentum imbalance, and two b-quark jets. The only process which has such signature is a single top production associated with a W boson. However, this process has a much smaller production cross section than our signal events. Therefore, we expect that we can achieve large signal-to-background ratio just by applying the selections above.

Acceptance and background estimation

To measure the cross section using Equation (1.21), we have to know the acceptance of $t\bar{t}$ events and the amount of the background events. They are estimated by using the Monte Carlo (MC) simulation. In addition, some background processes are also estimated by the data-driven method to avoid bias due to mis-modeling in the MC simulation.

Important point for the measurement

The large signal-to-background ratio implies that the systematic uncertainty for the N_{BG} estimation does not have a large impact on the precision of the cross section measurement. Instead, the precision of this measurement is mostly determined by the understandings of the signal acceptance. Our previous analysis is limited by the systematic uncertainty. To reduce the systematics, we employed new method to measure the b-tagging efficiency more precisely and reliably, since the b-tagging was one of the main systematic sources in the acceptance estimate. In addition, we checked the details of the $t\bar{t}$ event modeling which was also a dominant systematic source.

The remaining of this thesis is organized as follows. The overview of LHC and the ATLAS detector is given in Chapter 2 and 3, respectively. The data and the MC samples used in this analysis are described in Chapter 4. The event reconstruction is presented in Chapter 5. The efficiency measurement of the b-tagging is described in a dedicated chapter 6. We present the measurement of the production cross section in Chapter 7. Finally, we discuss our result in Chapter 8 and conclude in Chapter 9.

Chapter 2

The Large Hadron Collider

The ATLAS experiment is one of the experiments which use proton beams of LHC [27]. LHC is the world's largest and highest energy particle accelerator and collider which was built at the European Organization for Nuclear Research (CERN) at Geneva in Switzerland. In this chapter, a brief overview of LHC and its injector chain is given. The overview of the particle collider is described in Section 2.1. The LHC injector chain and main ring are outlined in Section 2.2 and 2.3, respectively.

2.1 Advantages of the proton-proton collider

The number of events per second generated by particle collisions is

$$N_{\text{event}} = \sigma_{\text{event}} \times \mathcal{L}, \tag{2.1}$$

where σ_{event} is the cross section of the event under study and $\mathcal{L}$ is luminosity. Large N_{event} is preferable to search for events which have not been discovered yet, and also to measure the properties of known particles like the subject of this thesis. Therefore, LHC is designed to have large σ_{event} and $\mathcal{L}$ as we explain below.

Center-of-mass energy

To produce heavy particles, larger center-of-mass energy is required. Especially for LHC which aims to produce the particles which are not studied well or not at all, the higher center-of-mass energy is essential to achieve larger σ_{event}.

The type of colliders can be divided into two groups. One is an electron-positron collider like the Large Electron Positron (LEP) collider [29]. The other is a hadron collider like Tevatron [30] and LHC. The largest difference between these colliders is in energy loss of particle circulating in a ring of the accelerator. Particles lose their energy by a synchrotron radiation by δE per revolution, shown as

$$\delta E \propto \frac{\beta^3}{R}\gamma^4 \simeq \frac{\gamma^4}{R} = \frac{1}{R}\left(\frac{E}{m}\right)^4, \tag{2.2}$$

where the velocity of the particle v is denoted with the symbol β defined as the ratio to the speed of light c, *i.e.* $\beta = v/c$, m is the mass of the rotating particle, the energy of the particle is written as $E = \gamma mc^2$ ($\gamma = 1/\sqrt{1-\beta^2}$), and R is a radius of the circular orbit. Electrons or positrons lose their energy by about 3 % in one turn, when the LEP collider achieved the beam energy of 104.5 GeV. This large energy loss limits the maximum beam energy in LEP. On the other hand, the energy loss by a proton is only a few keV per turn at LHC, because the

energy loss is proportional to m^{-4}, and hence it is not the limiting factor to achieve higher beam energy. Therefore, a hadron collider is a good choice for the energy frontier accelerator. But the beam energy at the hadron collider is limited by the bending magnetic field. The strength of the magnetic field to keep beams in the same orbit is proportional to the beam energy shown as

$$B = \frac{mv}{qR} = \frac{p}{qR} \propto p. \tag{2.3}$$

At LHC, one needs approximately seventy (7 TeV(LHC)/104.5 GeV(LEP)) times larger magnetic field compared to LEP. Compared to an another energy frontier hadron collider, Tevatron, LHC uses the twice stronger magnetic field for bending with a 4.5 times larger radius of the accelerator to reach seven times more energy.

Luminosity

The luminosity of a collider is given by

$$\mathcal{L} = f\frac{n_1 n_2}{4\pi\sigma_x\sigma_y}, \tag{2.4}$$

where $n_{1,2}$ are the numbers of particles in colliding beams, $\sigma_{x,y}$ are the Gaussian transverse beam profiles in the horizontal and the vertical directions. This equation shows that high frequent collisions with intense beams help to achieve higher luminosity. The previous highest energy hadron collider Tevatron was a proton-anti-proton collider. The anti-proton needs to be produced artificially by striking the primary beam on a target because the anti-proton does not exist in the nature. The production rate of anti-proton is about five orders of magnitude lower than the one for proton [31]. Even if the production rate is improved by increasing energy and intensity of the primary beam, it is difficult to cool down the secondary anti-proton so that it can be used as beam. This limits the luminosity of Tevatron. Therefore, a proton-proton collider is the good choice to increase the luminosity to search for rarer events like the Higgs boson or other particles from physics beyond the standard model, and also to collect the large amount of heavy particles like the top quark.

2.2 The LHC injector chain

Protons are supplied to LHC from the injector chain, Linac2 - Proton Synchrotron Booster (PSB) - Proton Synchrotron (PS) - Super Proton Synchrotron (SPS), as shown in Figure 2.1. Linac2, PSB and PS are described in 2.2.1, and SPS in 2.2.2, respectively.

2.2.1 The proton pre-injectors

Protons for the LHC beams are produced in a Duoplasmatron Proton Ion Source [33]. The principle of the proton source is an electrical discharge in hydrogen gas between a hot thermionic oxide cathode and anode. A process of the duoplasmatron can be written as

$$\begin{aligned} H_2 + e^- &\rightarrow H_2^+ + 2e^- \\ H_2^+ + e^- &\rightarrow H^+ + H + e^- \\ H + e^- &\rightarrow H^+ + 2e^-. \end{aligned}$$

With this process, two protons from one hydrogen molecule ($H_2 \rightarrow 2H^+ + 2e^-$) are extracted with 91 kV extraction voltage. The proton beam current at this stage is more than 200 mA. Next, protons from the duoplasmatron source go through a RF quadrupole and are accelerated

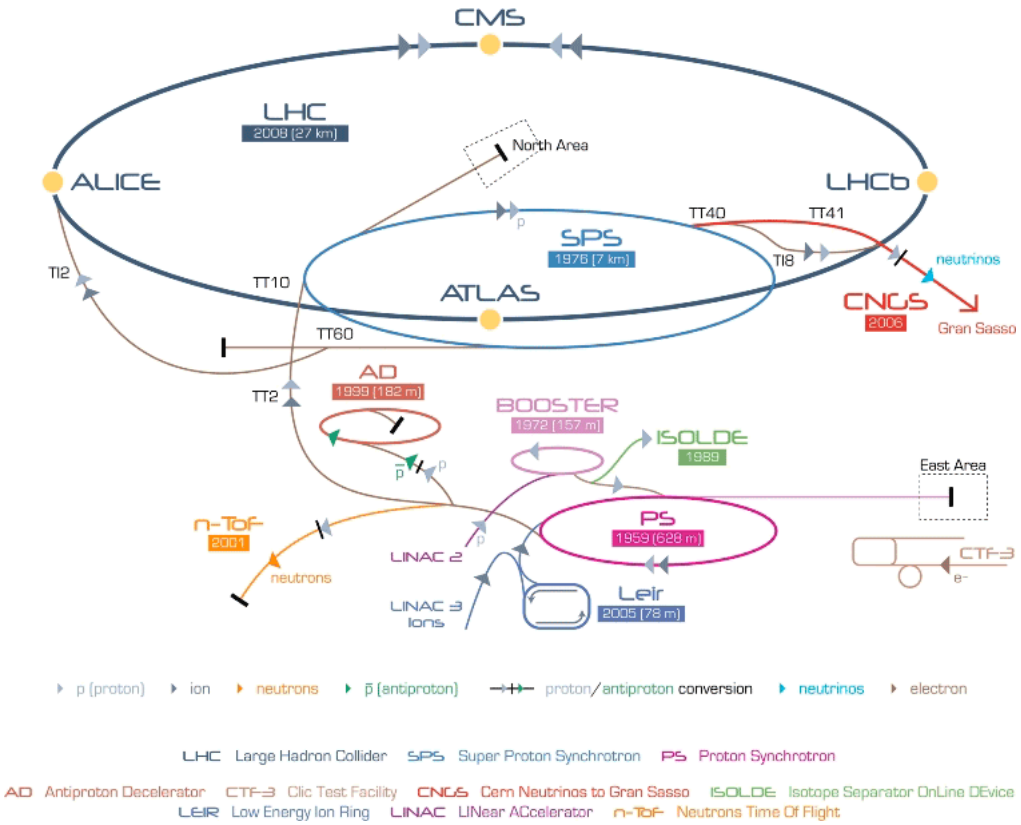


Figure 2.1: CERN accelerator complex [32]. PSB is indicated as 'BOOSTER'.

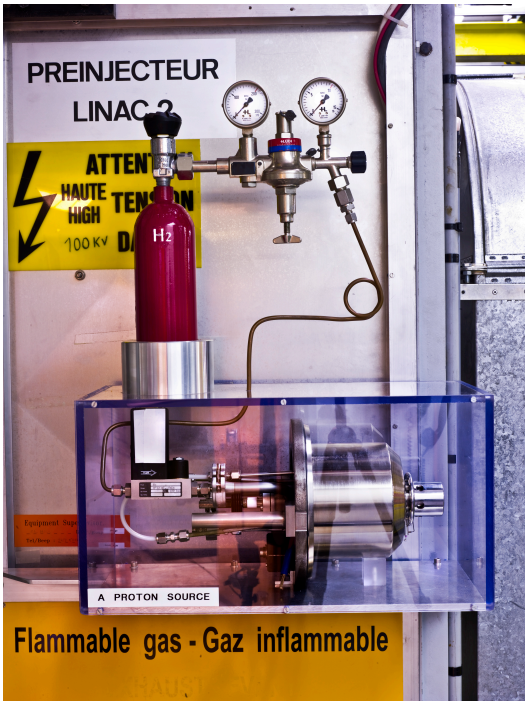


Figure 2.2: Duoplasmatron proton ion source [34].

to 750 keV. These protons are injected to a 30 m long linac called Linac2. The linac accelerates the proton beam with the beam current 180 mA up to 50 MeV. After protons are transferred from Linac2 to PSB, they are accelerated to 1.4 GeV, then injected to PS. PS is designed to accommodate 84 bunches with 1.15×10^{11} protons per bunch for a LHC-filling with 25 ns bunch spacing to make a bunch train in LHC. The circumference of PS is 628.3 m. Protons are accelerated to 26 GeV, and then transferred to SPS. Table 2.1 summarizes the beam characteristics at the extraction from PS.

Table 2.1: Beam characteristics at extraction from PS [35].

	Unit	Value
Proton momentum	[GeV/c]	26
Number of PS batches to fill SPS		3
PS repetition time	[s]	3.6
Number of bunches		84 (81 to SPS)
Bunch spacing	[ns]	25
Number of protons per bunch		1.15×10^{11}
Transverse normalized RMS emittance	[μm]	3.0
Longitudinal emittance	[eVs]	0.35
Bunch length	[ns]	4
Relative momentum spread $\delta p/p$ (4σ)		0.004

2.2.2 SPS as the LHC injector

SPS is a proton synchrotron which provides a 450 GeV proton beam as the last component of the LHC injector[1)]. The beam and machine parameters of SPS are summarized in Table 2.2.

Table 2.2: SPS beam and machine parameters [36].

	Unit	Value
Proton momentum	[GeV/c]	450
Machine radius	[m]	1100
Min. Vacuum pipe radius	[mm]	25
Revolution time / frequency	[μs/kHz]	23/43.3
Number of bunches		243
Protons / bunch		1.15
Total intensity	[A]	0.177
Bunch spacing	[ns]	25
Bunch frequency	[MHz]	40
Bunch length	[ns]	4
Average beam size	[mm]	2.3
Transverse normalized emittance	[μm]	3.0
Longitudinal emittance	[eVs]	0.35
Main RF frequency	[MHz]	200

In SPS, 26 GeV protons from PS are injected. PS can accommodate 81 bunches of protons

[1)] Also it is used for fixed target experiments

for SPS and all bunches are injected to SPS. This injection procedure is repeated three times. Each injection is separated by 3.6 seconds corresponding to the PS injection cycle. In the end, there are 243 bunches are filled in SPS. Just after the last injection from PS, SPS is ramped up to 450 GeV. The ramp takes 8.25 seconds to complete. Once ramping up is finished, about one second flat top is required to take some actions to extract bunches to LHC. These actions include switching RF system frequency to 400 MHz to compress the bunch length longitudinally, adjusting a phase of SPS with respect to LHC to inject into the correct place in LHC, and ramping up the extraction magnet system. At the end of the flat top, the beam is extracted to one of the LHC rings, either via the west extraction line TI2, or the east extraction line TI8, as shown in Figure 2.1. This repetitive cycle is called a supercycle. A total of 24 such supercycles is required to fill LHC with beam. Each supercycle takes typically 21.6 seconds. In total, the LHC filling time is about 8 minutes.

2.3 The LHC main ring

LHC is designed to provide collisions with the center-of-mass energy of 14 TeV and with the luminosity of 10^{34} cm^{-2}s^{-1}. It consists of two ring superconducting accelerators installed in the 26.7 km-long LEP tunnel. LHC can store up to 2808 proton bunches with 25 ns interval corresponding to the 40 MHz RF frequency. In 2011, LHC was operated with the center-of-mass energy of 7 TeV. The luminosity was improved gradually by tuning machine parameters and by increasing the number of bunches up to 1317. At the end of 2011, LHC achieved the peak instantaneous luminosity of 3.3×10^{33} cm^{-2}s^{-1}. The performance goals of LHC and parameters in the 2011 LHC operation are summarized in Table 2.3.

Table 2.3: Performance goals of LHC and the machine parameters in the 2011 LHC operation [27].

	Unit	**Injection**	**Collision (Design)**	**Collision (2011)**
Peak luminosity	[cm^{-2}s^{-1}]	-	10^{34}	3.3×10^{33}
Proton energy	[GeV]	450	7000	3500
Number of bunches		2808		138 $\sim$ 1317
Protons / bunch		1.15×10^{11}		$(1.12 \sim 1.79)\times10^{11}$
Total intensity	[A]	0.58		-
Stored energy per beam	[MJ]	23.3	362	-
Bunch spacing	[ns]	25		50 $\sim$ 75
Transverse normalized emittance	[μm]	3.5	3.75	-
Longitudinal emittance	[eVs]	1.0	2.5	-
RMS beam size	[μm]	375.2	16.7	-
RMS bunch length	[cm]	11.24	7.55	-
Energy spread (4σ)	[10^{-3}]	1.9	0.45	-
β^* at the IP1	[m]	18	0.55	-

2.3.1 Magnets

LHC uses many types of magnets which use leading-edge technologies.

One of the main components of the magnet system is a superconducting dipole, called a cryodipole, used to bend and to store two proton beams in LHC. LHC accommodates 1232 main dipoles. They all have the same basic design. The cryodipole plays a critical role in the machine. Figure 2.3 shows the cross-section of the cryodipole. Two proton beams are bended in

one cryodipole to satisfy the requirement of a space limitation in the tunnel and the cost. This dipole generates 8.33 T magnetic field as the design value corresponding to a bending radius of 2804 m for protons with energy of 7 TeV.

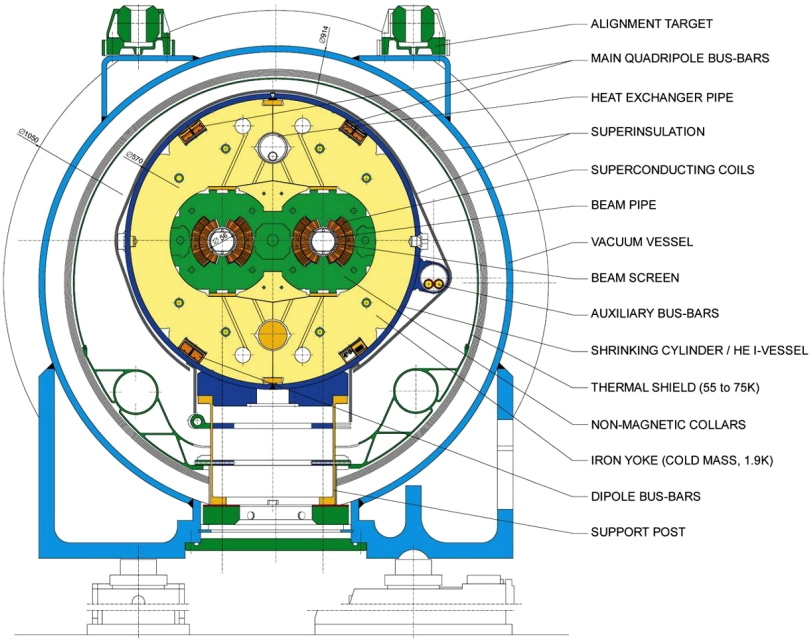


Figure 2.3: The cross-section of cryodipole (lengths in mm) [27].

Magnet system for the final focusing to provide the high luminosity collision at the ATLAS experiment is shown in Figure 2.4. Two rings of LHC must be connected around the collision

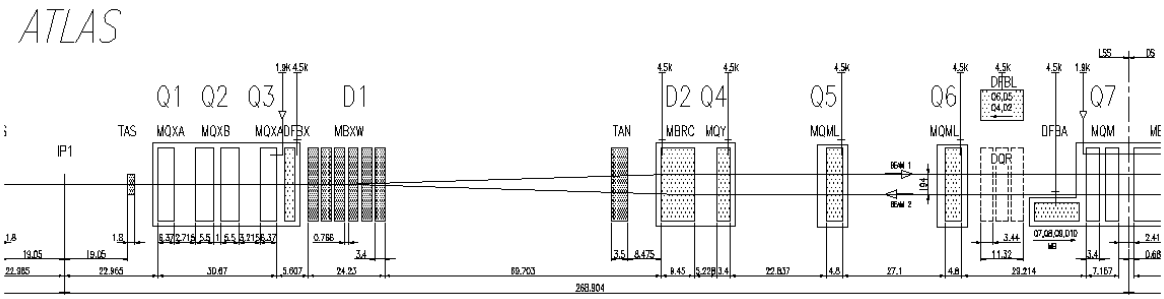


Figure 2.4: Magnet system near the interaction point for the ATLAS experiment, IP1, shown on the left side of the figure. The length in the figure is given in meters. Q1, Q2 and Q3 are the final focusing quadrupole magnet triplets to provide high luminosity collisions at the interaction point [27].

point. As shown in Figure 2.4, the two beams share an approximately 140 m long common beam pipe around the interaction point for the ATLAS experiment so-called IP1. Two dipole magnets, shown in Figure 2.4 as D1 and D2, bring two beams onto the collision orbit and then separate the beams again beyond the interaction point. The twin-bore superconducting magnets with the magnetic fields of 3.8 T are used for D2 shown in Figure 2.5, while robust normal conducting magnets with the magnetic field of 1.28 T are used for D1 because a higher radiation level is expected. The final focusing for the high-luminosity collision is performed by

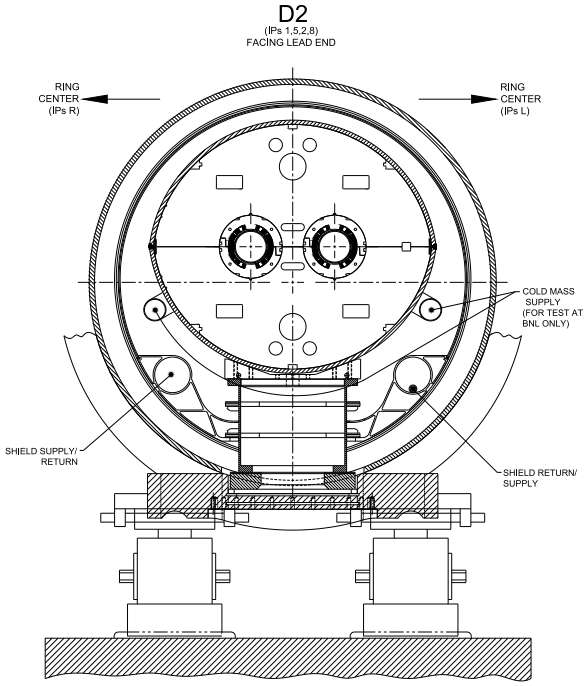


Figure 2.5: Cross section of the D2 cryodipole [27].

the superconducting quadrupole triplets Q1, Q2 and Q3 shown in Figure 2.4. Within Q1, Q2 and Q3, two types of magnets, called MQXA made by KEK and MQXB made by FNAL, are used. Both magnets are single bore quadrupole magnet as shown in Figure 2.6 and can provide a high gradient of magnetic field of 215 T/m. The peak strength of the magnetic fields of each magnet is 8.6 T for MQXA and 7.7 T for MQXB. In IP1, two beams are crossing in the vertical plane with the angle of 142.5 μrad.

In the 2011 LHC operation, all the magnets were operated with approximately half of the magnetic field strength against the design value due to the lower beam energy of 3.5 TeV.

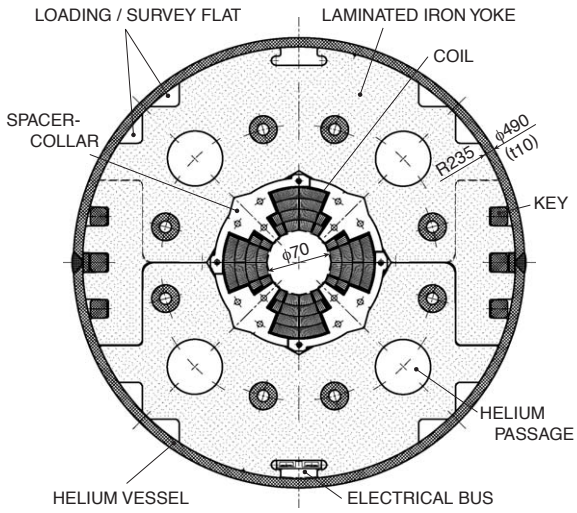


Figure 2.6: Cross section of the MXQA insertion quadrupole [28].

Chapter 3

The ATLAS experiment

The ATLAS[1)] detector is one of the general purpose detectors at LHC. The detector surrounds the interaction point and the beam pipe hermetically. It consists of cylindrical layers and two end-caps. The detector is 44 m in length and 25 m in height, and has a weight of approximately 7000 tons. Figure 3.1 shows the full ATLAS detector. The detector components, called as subsystems, are categorized into the inner tracker, the electromagnetic and hadron calorimeter, and the muon spectrometer, from inside to outside. Besides, the ATLAS detector is equipped with the magnets and the forward detectors.

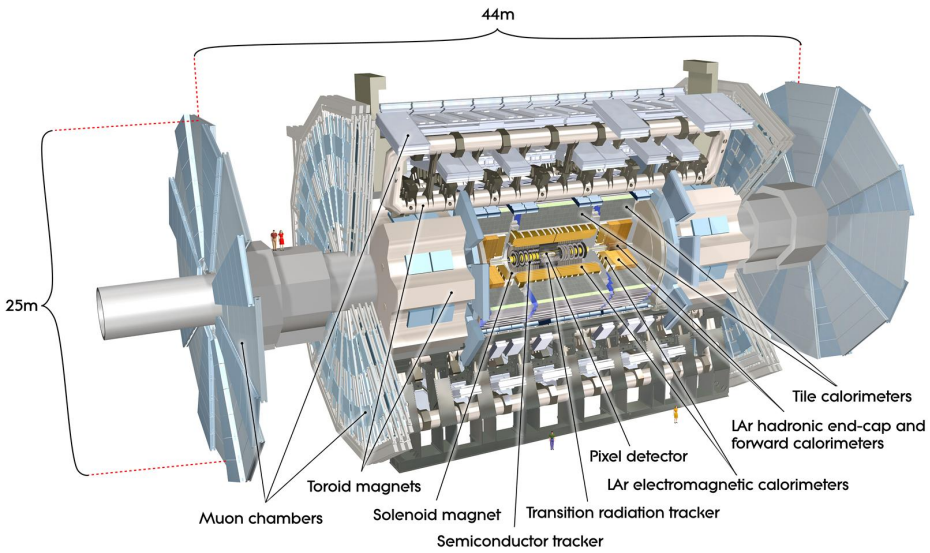


Figure 3.1: The full ATLAS detector [37].

In this chapter, sections are organized as follows. The ATLAS coordinate system is explained in Section 3.1. The details of each subsystem are described in Section 3.2 to 3.6. After describing the ATLAS detector, the trigger system and the data acquisition (DAQ) system is outlined in Section 3.7. The ATLAS computing system is explained in Section 3.8.

[1)] The ATLAS stands for 'A Toroidal LHC ApparatuS'

3.1 ATLAS coordinate system

The position within the detector is described by a right-handed Cartesian coordinate system with the origin at the interaction point. The z-axis follows the beam direction. The positive x points to the center of the LHC ring and the positive y points up. A cylindrical coordinate system is also used since the detector is symmetric with respect to the z-axis. As shown in Figure 3.2, a radial distance $r = \sqrt{x^2 + y^2}$, the azimuthal angle ϕ are defined. The range of the azimuthal angle is defined within $[-\pi, +\pi)$[2)]. A direction which is perpendicular to the z-axis is called the transverse direction. The pseudorapidity η is often used instead of the polar angle, because the number of particles produced in rapidity intervals of the same size is roughly constant. The pseudorapidity is defined as $\eta = -\ln[\tan(\theta/2)]$ where θ is the polar angle defined as shown in Figure 3.2. The range of the pseudorapidity is $(-\infty, +\infty)$. To denote the distance in the η-ϕ plane, ΔR is defined as $\Delta R = \sqrt{\Delta\eta^2 + \Delta\phi^2}$.

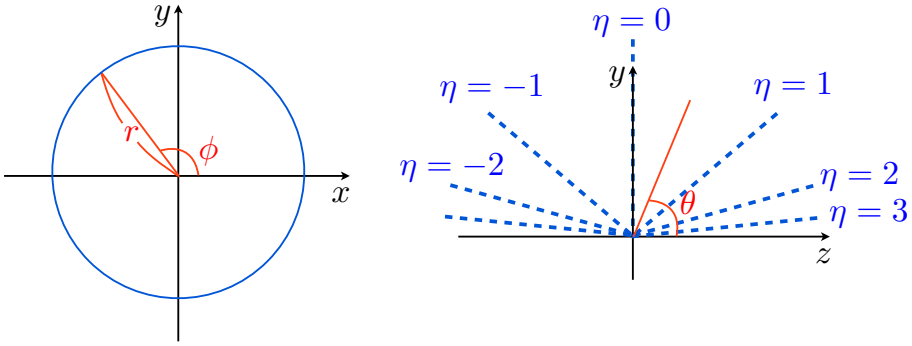


Figure 3.2: The ATLAS coordinate system. The azimuthal angle ϕ is measured from the positive x-axis. The polar angle θ is measured from the positive z-axis. The pseudorapidity $\eta = \pm 1, \pm 2$ and ± 3 are indicated in blue lines on the right plots.

3.2 Magnets

Magnets are important components in the ATLAS detector to provide a bending power required to precisely measure the momentum of the charged tracks. Figure 3.3 shows the geometry of the ATLAS magnets. There is a central solenoid to measure the momentum at the inner tracker, surrounded by three large air-core toroidal magnets for the muon spectrometers. Main parameters for each magnet are summarized in Table 3.1. The details of each magnet are described in the following.

Solenoid magnet

The central solenoid is the super-conducting magnet providing approximately 2 Tesla magnetic field at the center of the inner tracker volume. The solenoid magnet is placed just inside the barrel electromagnetic calorimeter. To minimize a degradation of the calorimeter performance, the solenoid magnet was designed to have minimum amount of material. As a result, the solenoid is housed inside the same cryostat as the electromagnetic calorimeter. The iron absorber of the hadron calorimeter described in Section 3.4.2 is used as the return yoke for this magnet. The field strength is shown in Figure 3.4. The magnetic field is not completely uniform because the location of the iron yoke is far from the inner tracker volume.

[2)] The vector pointing upwards has $\phi = \pi/2$, the one pointing to downward has $\phi = -\pi/2$.

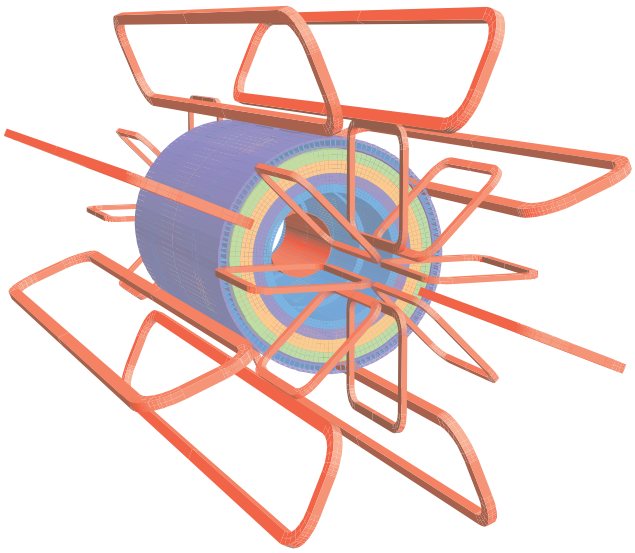


Figure 3.3: Geometry of the ATLAS magnets. The eight barrel toroid coils and two eight end-cap toroid coils (red rectangles) are around the solenoid winding (blue cylinder) [38].

Table 3.1: Main parameters of the solenoid and toroidal magnets in the ATLAS magnets.

	unit	**Central solenoid**	**Barrel toroid**	**End-cap toroid**
Overall dimensions:				
Inner diameter	m	2.44	9.4	1.65
Outer diameter	m	2.63	20.1	10.7
Length in z-direction	m	5.3	25.3	5
Number of coils	m	1	8	8
Weight:				
Conductor	tones	3.8	118	20.5
Cold mass	tones	5.4	370	160
Total assembly	tones	5.7	830	239
Coils:				
Number of turns per coil	-	1173	120	116
Operating current	kA	7.6	20.5	20
Stored energy	MJ	38	1080	206
Peak field	T	2.6	3.9	4.1

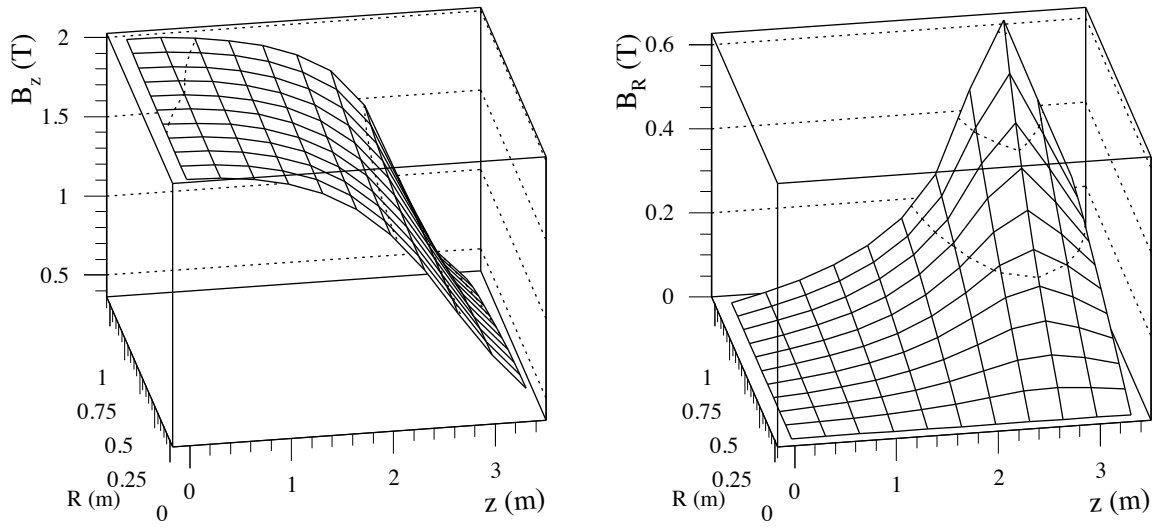


Figure 3.4: The magnetic field strength along the beam direction (left) and the radial component of the magnetic field (right) as a function of r and z [39].

Toroid magnet

The toroid magnets consist of three components, the barrel toroid and two end-cap toroids. All magnets are super-conducting air-core magnets. The toroidal magnet field gives the advantage of having its direction almost perpendicular to particle tracks even at the forward, large $|\eta|$, region. Each magnet is composed of eight coils and housed in its own cryostat. The generated field strength is shown in Figure 3.5. Due to its eight-fold design, the strength of the magnetic field depends on ϕ.

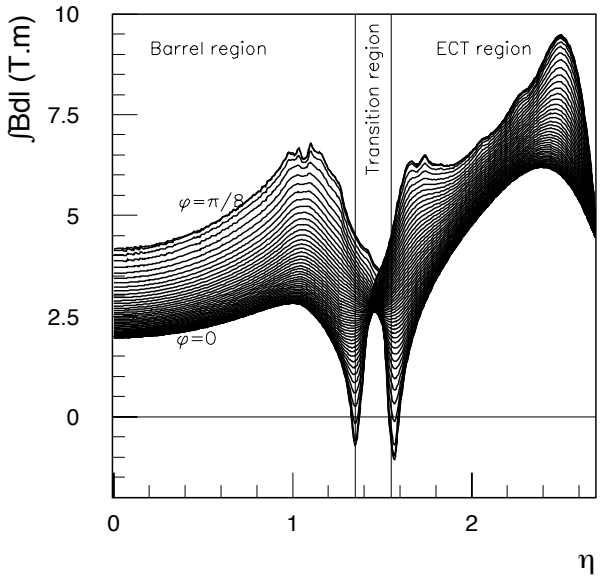


Figure 3.5: Integrated field strength by the toroidal magnets as a function of pseudorapidity [38].

3.3 Inner tracker

The inner tracker is placed at the center of the ATLAS detector, thus inside the magnetic field by the solenoid magnet. The inner tracker is 6.2 m long in the z-direction and 2.1 m in diameter. The primary purpose of the inner tracker is to detect the position where the charged particles go through. This information is essential to reconstruct charged particle tracks and to determine pp interaction points and secondary vertices. The inner tracker consists of three detectors, Pixel detector, SemiConductor Tracker (SCT) and Transition Radiation Tracker (TRT). The layout of these three detectors is shown in Figure 3.6.

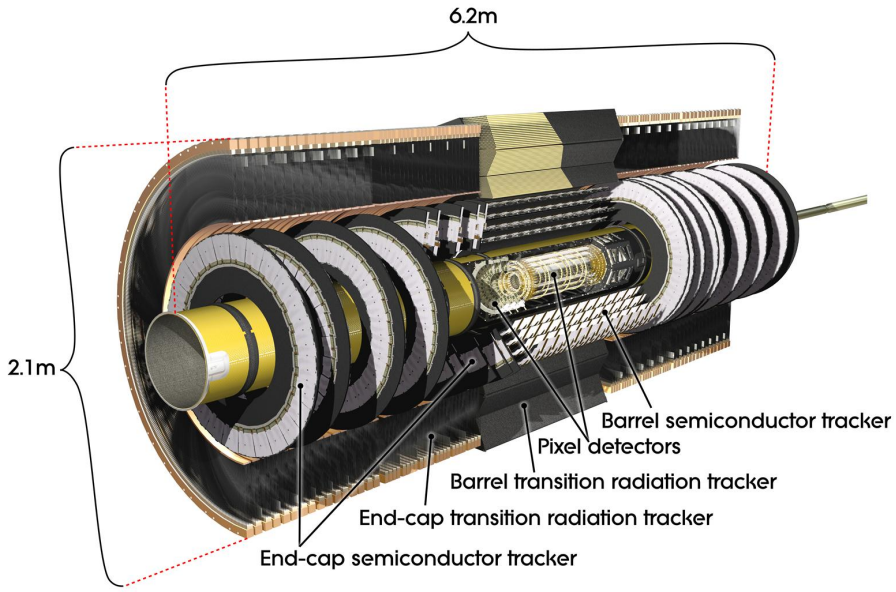


Figure 3.6: The cut-away image of the inner tracker [40].

3.3.1 Pixel detector

The pixel detector is located just outside of the beam pipe. It is equipped with a very small detection unit of 50×400 μm^2 sensitive area to detect particles from pp collisions without overlaps, where typically 500-1000 charged particles hit the pixel detector per bunch crossing. It is made from silicon sensors to achieve such a high granularity. The smallest units of the pixel detector are modules as shown in Figure 3.7. One pixel module consists of the silicon sensor sandwiched with a front-end chip (FE in the figure) to read out the signal, and a flex circuit to send the signal to the outside of the ATLAS detector. One pixel module covers 16×57.6 mm^2 area with 320×144 pixels. Pixel support structure in Figure 3.8 contains 1456 modules on three barrel layers, and 288 modules on three disk layers (end-cap) on each side, resulting in 1744 modules in total. The distance between the beam pipe center and each barrel layer is 50.5, 88.5 and 122.5 mm, respectively. The innermost layer is attached to the beam pipe, called the B-layer. The three layers on each side are placed at $z = \pm 495, \pm 580$ and ± 650 mm, respectively. This layout provides three hits per track up to $|\eta| = 2.5$.

The pixel detector can measure the time that the electric signal exceeds a given threshold, called time-over-threshold, which represents the size of energy deposit in the sensor. Using this charge information, when there are two or more neighboring hit pixels, the hit position is

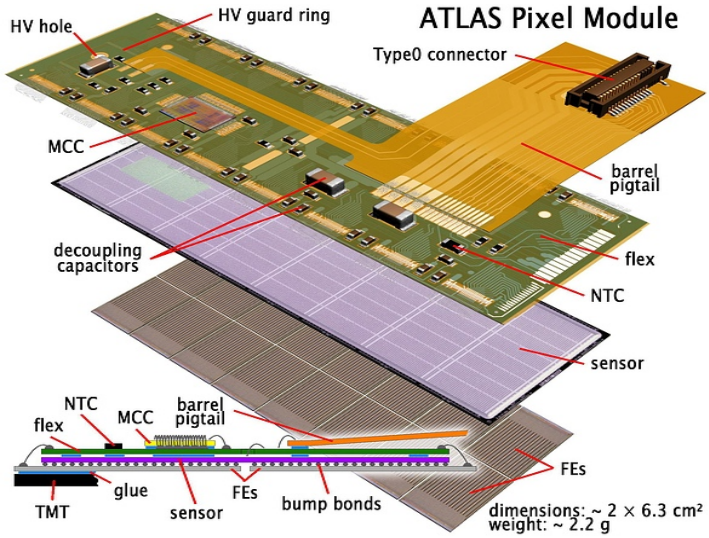


Figure 3.7: The ATLAS pixel detector module [41].

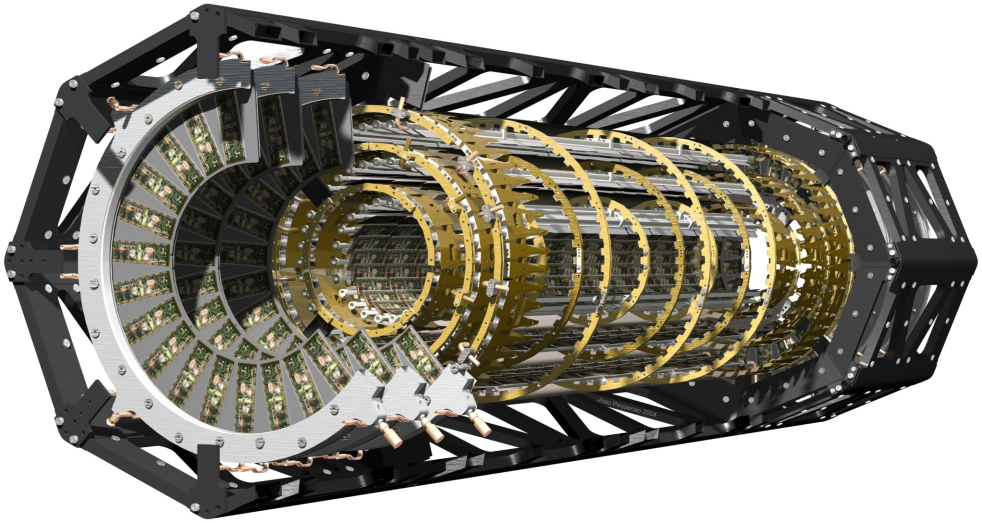


Figure 3.8: The pixel support structure [42].

estimated by interpolating the collected charges. Note that, for tracks from the pp collisions, the average number of pixel hits is about 1.5 for the typical incident angle of 0.2 radians.

To see the position resolution, the residual of the hit position is checked using the pp collision data. The residual is defined as the distance between the hit position on the detector and the estimated hit position by using the track which is reconstructed without the pixel module under study not to bias the estimate. Figure 3.9 shows the root mean square (RMS) of the residual distribution as a function of the track incident angle against the module. The residual is measured in two directions, the ϕ and the z direction on each module denoted as the local x and y residual in the figure, respectively. RMS of the residual distribution is affected by the intrinsic pixel position resolution, the hit position clustering algorithm, the expected position uncertainty, the detector alignment effect, etc.. There are two clustering algorithms, one defines the hit position as the center of the cluster, and the other calculates the hit position by using the deposit charge information. As shown in Figure 3.9, the two algorithms have different RMSes. The latter method is used to determine the hit position in this analysis. The RMS of the residual of 15-20 (70-220) μm for the ϕ (z) direction is achieved by this method.

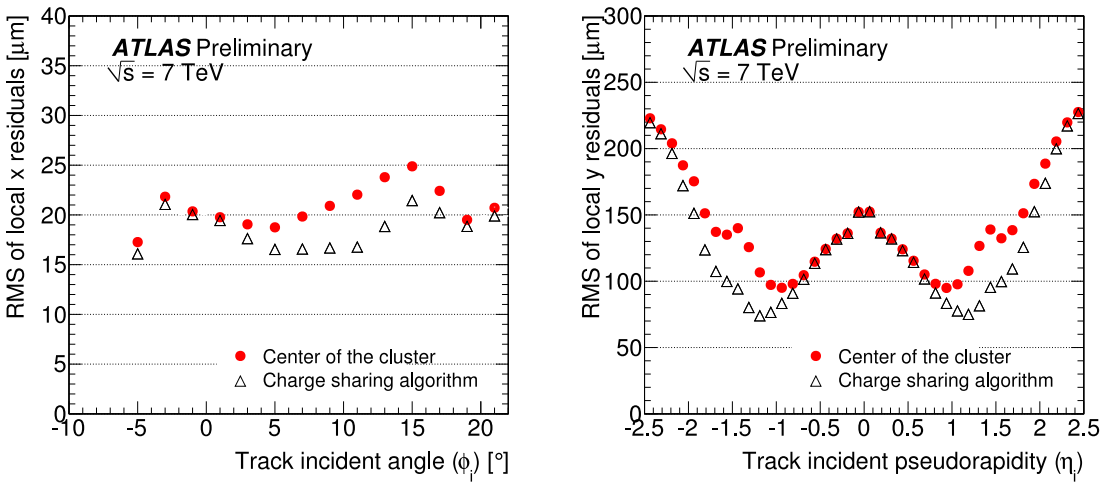


Figure 3.9: RMS of residuals in the ϕ direction (left) and the z direction (right) as a function of the track incident angle [43]. The residual is measured by taking the difference between the estimated hit position using the reconstructed track and the actual hit position on the module. The hit position is estimated by using two algorithms, one taking the center of the cluster of hit pixels (red circle) and the other considering the amount of deposit charges (triangle).

3.3.2 SemiConductor Tracker

SCT is also the silicon detector covering an acceptance of $|\eta| < 2.5$ as a part of the inner tracker. It consists of traditional strip type silicon detectors with a 80 μm pitch. As shown in Figure 3.10, a module consists of two sensors which are glued back-to-back with the crossing angle of 40 mrad between strips on each side. The crossing angle and hits on both sides provide a passing point of a charged track in local x and y direction. The dimension of each SCT module is approximately 6 cm $\times$ 12 cm with 768 strips where the different types of modules are used at barrel layers and end-cap disks. SCT consists of four barrel layers with 2112 modules and nine end-cap disks at each side resulting in 988 modules for each side. The geometrical layout of the barrel layers and the end-cap disks are shown in Figure 3.11. This layout is chosen so that tracks within the SCT acceptance have at least four passing points in SCT.

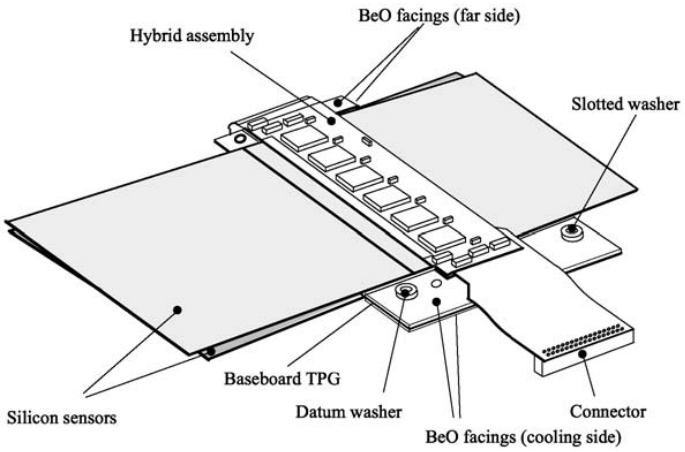


Figure 3.10: The ATLAS SCT module [44]

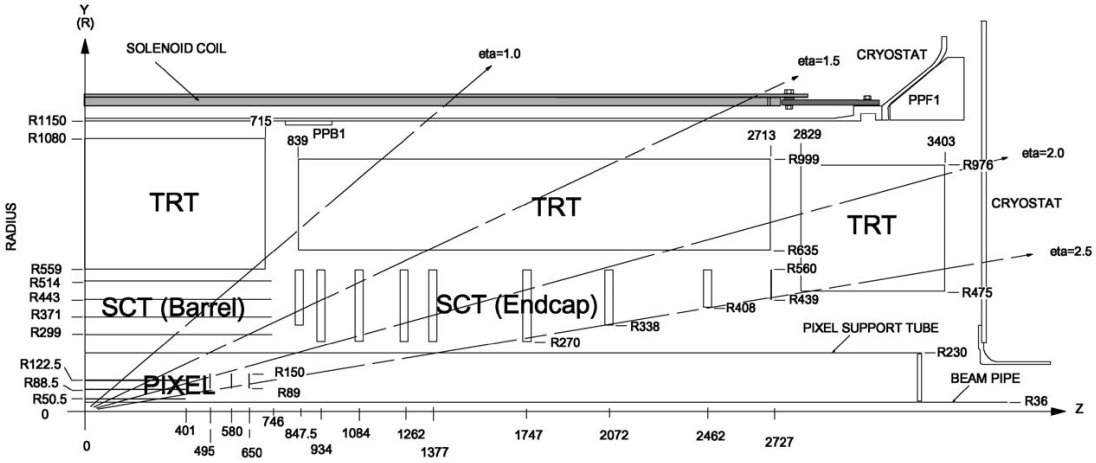


Figure 3.11: The layout of the ATLAS inner tracker [44]. The distances are given in mm.

The hit information from the SCT strips is binary, *i.e.* only 'hit' or 'not hit' is provided. In the same way as the pixel detector, the residual between the actual and the expected hit positions is measured with collision data to check the position resolution of SCT. Figure 3.12 shows the result of the measurement. The residuals of 42 μm and 45 μm in the ϕ direction are achieved for the barrel and the end-cap module, respectively. The hit efficiency for the

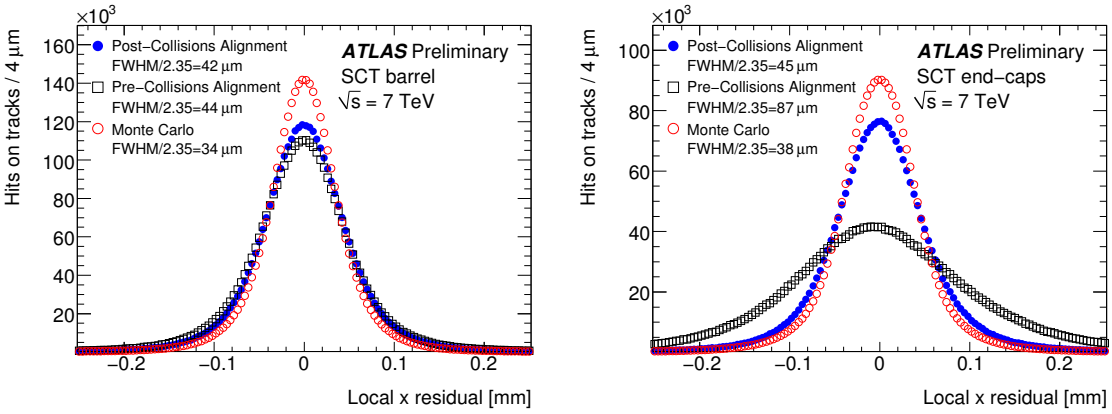


Figure 3.12: The residual in the ϕ direction for the barrel region (left) and the end-cap region (right). The data reconstructed with different detector alignment setting are plotted in blue circles and black boxes. The distribution of MC is also shown in red circles.

charged particles is also measured with the collision data. The method to measure the hit efficiency is similar to the residual measurement. We calculate the fraction of the number of hits at the expected hit position which is determined by the track reconstructed without the SCT module under study. Typically, 99.8 % efficiency is achieved for all detector regions as shown in Figure 3.13.

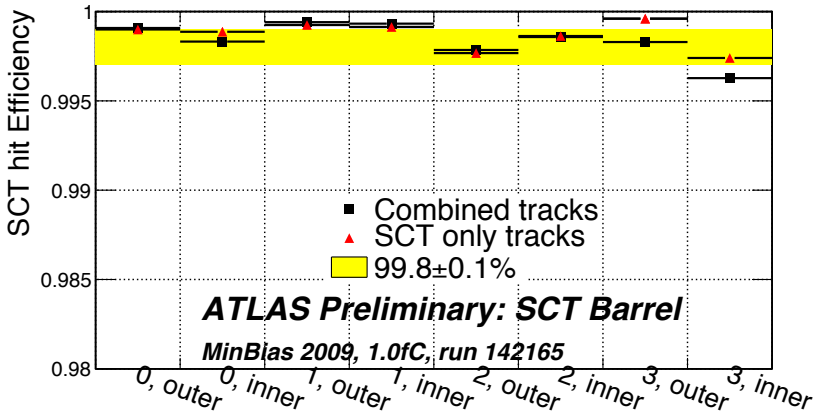


Figure 3.13: The hit efficiency for the SCT barrel module [46]. Each bin corresponds to the sensors for inside or outside of each module on each detector layer. The efficiency is shown for two different types of tracks, SCT stand-alone tracks which are the tracks reconstructed with only the hit information in SCT and inner tracker combined tracks.

3.3.3 Transition Radiation Tracker

TRT consists of a barrel and two end-caps. The barrel is comprised of 52544 144 cm-long drift tubes oriented parallel to the beams. Each end-cap contains 122880 37 cm-long and 36864 50 cm-long straws. Each straw is 4 mm in diameter equipped with a gold-plated tungsten sense wire. The non-flammable gas mixture, Xe (70 %), CO_2 (27 %) and O_2(3 %), is used. The geometrical layout is shown in Figure 3.11. The detector covers up to $|\eta| = 2.5$, and the geometry guarantees that particles cross 35-40 straws in $|\eta|$ up to 2.0. The TRT supplies continuous tracking at larger radii of the inner tracker while enhancing its pattern recognition ability. This gives an advantage for the software-based trigger to reconstruct tracks quickly. The spatial resolution of TRT is 120-130 μm as shown in Figure 3.14.

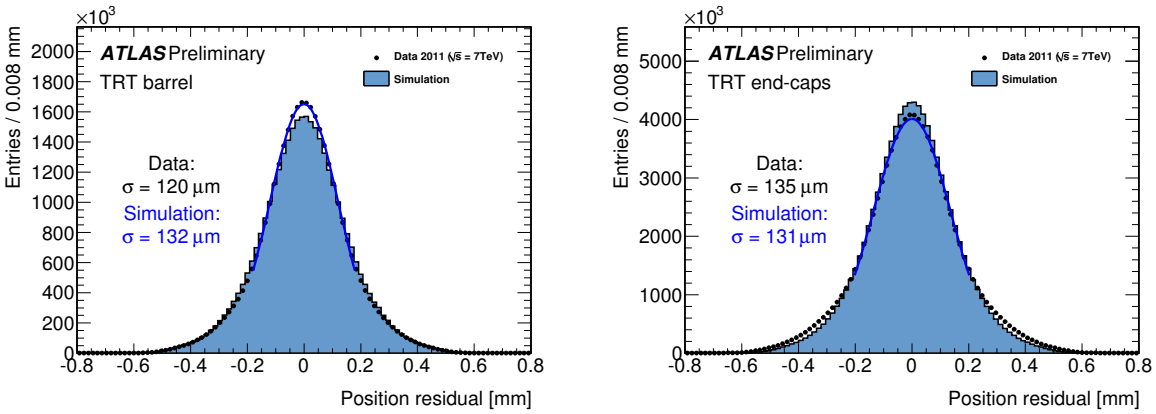


Figure 3.14: The residual distribution in the ϕ direction for the TRT barrel (left) and end-cap (right) detecter. The single gaussian fitting is performed to extract the width [47].

In addition to the particle tracking, TRT provides a standalone electron identification capability between electrons and pions by detecting transition radiation photons created in a radiator between the straws. The pion mis-identification probability ranges between 1 and 10 %, with the electron selection efficiency of 90 %, as shown in Figure 3.15.

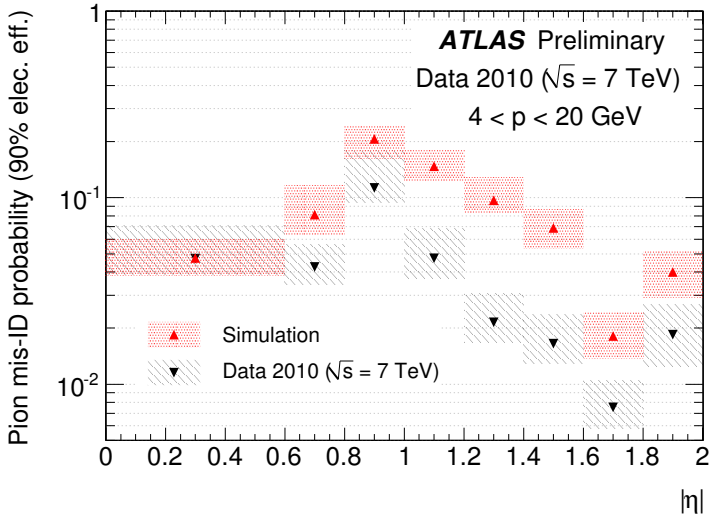


Figure 3.15: The pion mis-identification probability by TRT with the requirement of the electron selection efficiency of 90 % [47].

3.4 Calorimeters

The ATLAS calorimeter consists of two components, the electromagnetic (EM) and the hadron calorimeter. The EM calorimeters are located inside the hadron calorimeters as shown in Figure 3.16, because the EM showers are usually dense and well localized while the hadronic showers are more widely spread, due to the fact that the radiation length is much shorter than the nuclear interaction length in heavy materials used in calorimeters. The two calorimeters play significant roles in a precise energy measurement and an identification of electrons, photons and jets, and also the measurement of the transverse missing energy. It is also important used to provide a trigger. In the following, the EM calorimeters are described in Section 3.4.1, and the hadron calorimeters in Section 3.4.2.

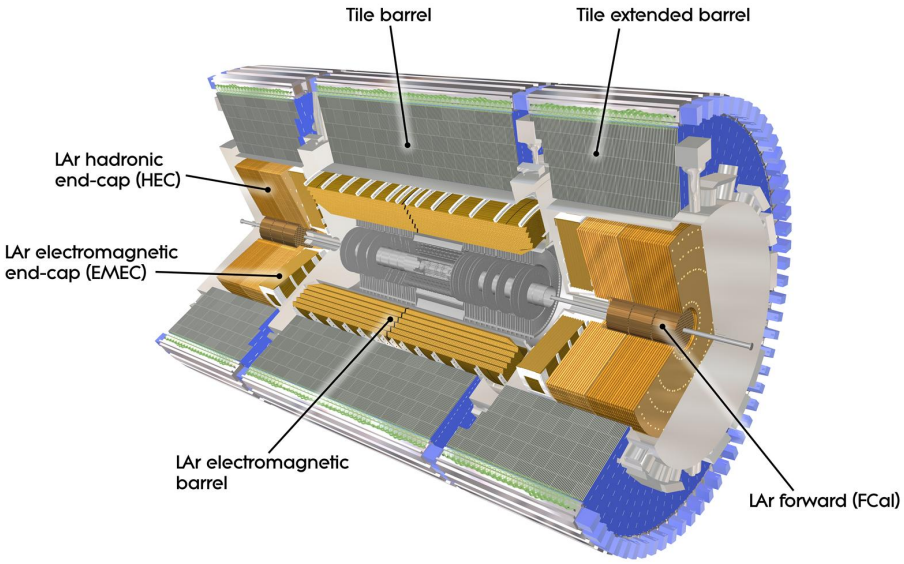


Figure 3.16: The layout of the ATLAS calorimeters [48]

3.4.1 Electromagnetic calorimeter

The EM calorimeter consists of a lead-liquid Argon (LAr) sampling calorimeter with accordion-shaped absorbers and electrodes as shown in Figure 3.17. This structure ensures an azimuthal uniformity for an electromagnetic interaction. The LAr was chosen as a sensitive material for its radiation hardness and its response speed. This calorimeter provides at least 24 radiation lengths. The barrel LAr calorimeter is housed with the solenoid magnet in the same central cryostat. The end-cap LAr calorimeter is in the other cryostat dedicated for the end-cap calorimeters. Both calorimeters are cooled nominally at 87 K. The coverage of the EM calorimeter is matched to that of the inner tracker, $|\eta| < 2.5$. There are three sampling layers in depth and a fine granularity strip sampler at the innermost layer, called the Sampling 1, to measure the direction of electrons and photons precisely. The readout granularity of the EM calorimeters is shown in Figure 3.18 and Table 3.2. The energy resolution is evaluated with the test beam before installing the detector into the ATLAS detector. The calorimeter was exposed to electron, muon and hadron beams to test the response. This test proved that the energy resolution is $\delta E/E = 10/\sqrt{E(\mathrm{GeV})} \oplus 0.245/E(\mathrm{GeV}) \oplus 0.7$ %, which is approximately equivalent to the requirement, $\delta E/E = 10/\sqrt{E(\mathrm{GeV})} \oplus 0.7$ %.

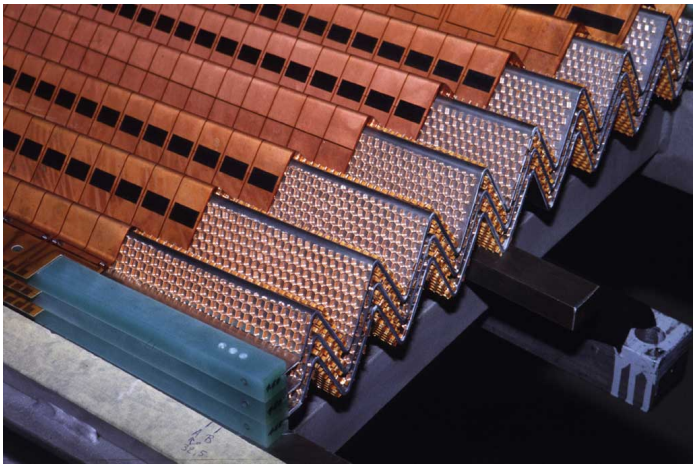


Figure 3.17: The accordion-shaped lead-LAr sampling calorimeter [49]. The honeycomb spacers position the electrodes between the lead absorber plates.

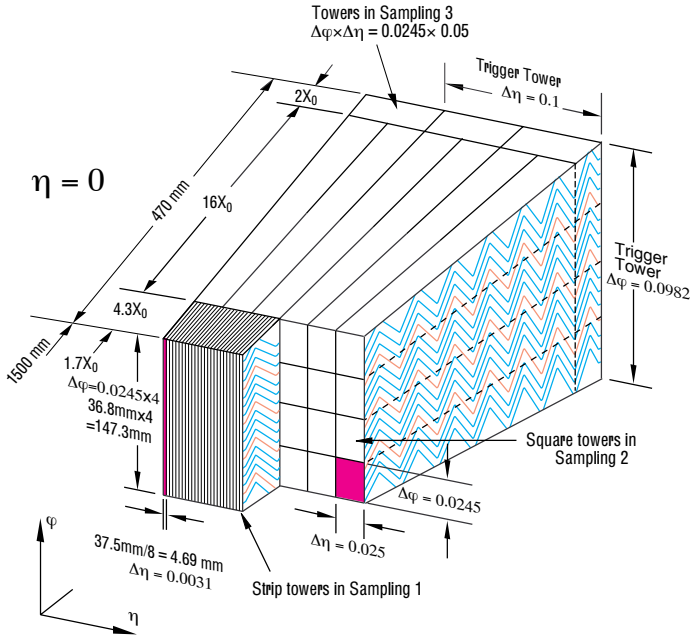


Figure 3.18: The readout granularity of the EM calorimeter [50]

Table 3.2: The coverage, granularity and longitudinal segmentation of the EM calorimeter

	barrel	**end-cap**	
Coverage	$\|\eta\| < 1.475$	$1.375 < \|\eta\| < 3.2$	
Longitudinal segmentation	3 samplings	3 samplings	$1.5 < \|\eta\| < 2.5$
		2 samplings	$1.375 < \|\eta\| < 1.5$
			$2.5 < \|\eta\| < 3.2$
Granularity ($\Delta\eta \times \Delta\phi$)			
Sampling 1	0.003×0.1	0.025×0.1	$1.375 < \|\eta\| < 1.5$
		0.003×0.1	$1.5 < \|\eta\| < 1.8$
		0.004×0.1	$1.8 < \|\eta\| < 2.0$
		0.006×0.1	$2.0 < \|\eta\| < 2.5$
		0.1×0.1	$2.5 < \|\eta\| < 3.2$
Sampling 2	0.025×0.025	0.025×0.025	$1.375 < \|\eta\| < 2.5$
		0.1×0.1	$2.5 < \|\eta\| < 3.2$
Sampling 3	0.05×0.025	0.05×0.025	$1.5 < \|\eta\| < 2.5$

3.4.2 Hadron calorimeter

Outside the LAr barrel calorimeter, there is an iron-scintillator sampling calorimeter, called the Tile calorimeter (TileCal), used as a hadron calorimeter. The iron-scintillator was chosen to cover a large area within affordable costs. The detector design of TileCal is shown in Figure 3.19. TileCal is categorized into two, the Tile barrels and the extended Tile barrels. The acceptance of TileCal is $|\eta| < 1.7$. The signal from the sampling scintillator is transferred through the wave length shifting fiber and read out by photo multiplier tubes located on the back of the iron-scintillator sampling layers. For the end-cap hadron calorimeter, a Cu-LAr sampling calorimeter, called HEC, is used. The detector has alternating layers of 8.3 mm LAr gaps sampling energies and 2.5 cm-thick copper absorber plates. It is located in the common end-cap cryostat with the end-cap LAr EM calorimeter. HEC covers the region of $1.5 < |\eta| < 3.2$. The illustration of the detector location for each type of calorimeters is shown in Figure 3.16. The hadron calorimeter has a total thickness of about 10 interaction lengths. Other specifications of the hadron calorimeters are summarized in Table 3.3.

Table 3.3: The coverage, granularity and longitudinal segmentation of the hadron calorimeters

	Tile barrel	**Extended Tile barrel**	**HEC**	
Coverage	$\|\eta\| < 1.0$	$0.8 < \|\eta\| < 1.7$	$1.5 < \|\eta\| < 3.2$	
Longitudinal segmentation	3 samplings	3 samplings	3 samplings	
Granularity ($\Delta\eta \times \Delta\phi$)				
	0.1×0.1 (Sampling 1 and 2)		0.1×0.1	$1.5 < \|\eta\| < 2.5$
	0.2×0.1 (Sampling 3)		0.2×0.2	$2.5 < \|\eta\| < 3.2$

The energy resolution was evaluated by the test beam before the installation. This test proves that the energy resolution is $\delta E/E = 50\ \%/\sqrt{E(\mathrm{GeV})} \oplus 3\ \%$ which satisfies the requirement.

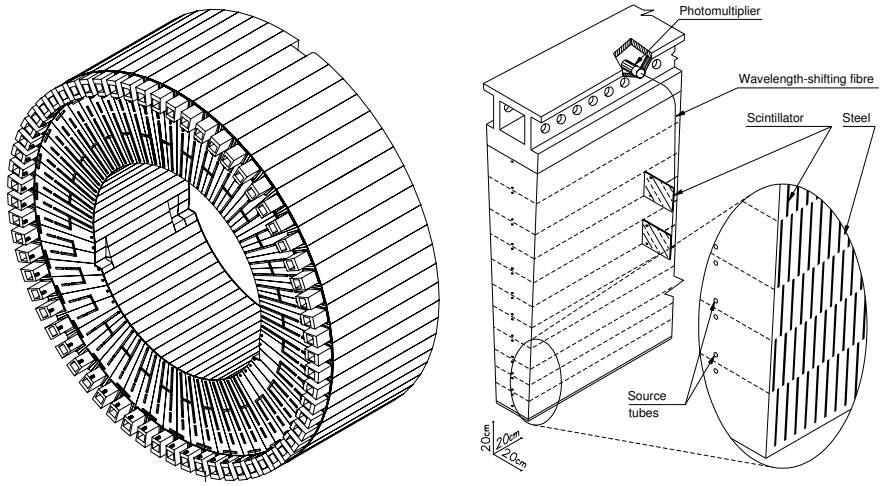


Figure 3.19: Detector design of TileCal. The signal from the sampling scintillator is read out by the photo multiplier tubes through the wave length shifting fiber.

3.5 Muon spectrometer

The ATLAS muon spectrometer is located at the outside of the calorimeter *i.e.* the outermost subsystem of the ATLAS detector. The energy of muon at the pp collisions with LHC can be very high, typically 50-100 GeV. The sagitta of the muon track becomes too small to precisely measure the momentum of the muon by the relatively small inner tracker at such a high energy. Accordingly, this makes the large muon spectrometer with the precise particle tracking ability extremely important for detecting high energy muons. The muon spectrometer is composed of four types of detectors. Two of them, Monitored Drift Tube (MDT) and Cathode Strip Chamber (CSC), are for the precise measurement of muon tracks, and the others, Resistive Plate Chamber (RPC) and Thin Gap Chamber (TGC), are dedicated for the fast muon trigger and providing a second coordinate which is orthogonal to the bending direction of muons. The overview of the ATLAS muon spectrometer are shown in Figure 3.20. All detectors are designed in a 16-fold segmentation in azimuth to follow the eightfold azimuthal symmetry of the magnet structure. The barrel detectors are composed of three cylindrical layers at radii of 5, 7.5 and 10 m. They cover the pseudorapidity range $|\eta| < 1.0$. The end-cap detectors form four disks at $z = 7$, 10, 14 and 21-24 m, and cover the range $1 < |\eta| < 2.7$. Each barrel and end-cap layer is referred to as the station in the following. The positions of these detectors are optimized to be low cost, well hermetic[2)] and to have the optimum momentum resolution by considering the precision of the sagitta measurement. Table 3.4 summarizes the instrumentation of each sub-detector. The details of each detector are described in the following sections.

3.5.1 Monitored Drift Tube

MDT is a drift tube tracking detector used for both barrel and end-cap regions. They cover the range $|\eta| < 2.0$ with three stations and the range $2.0 < |\eta| < 2.7$ with two stations. The basic

[2)] At $\eta = 0$, there is a hole for cables and services of the inner tracker, the solenoid magnet and the calorimeters.

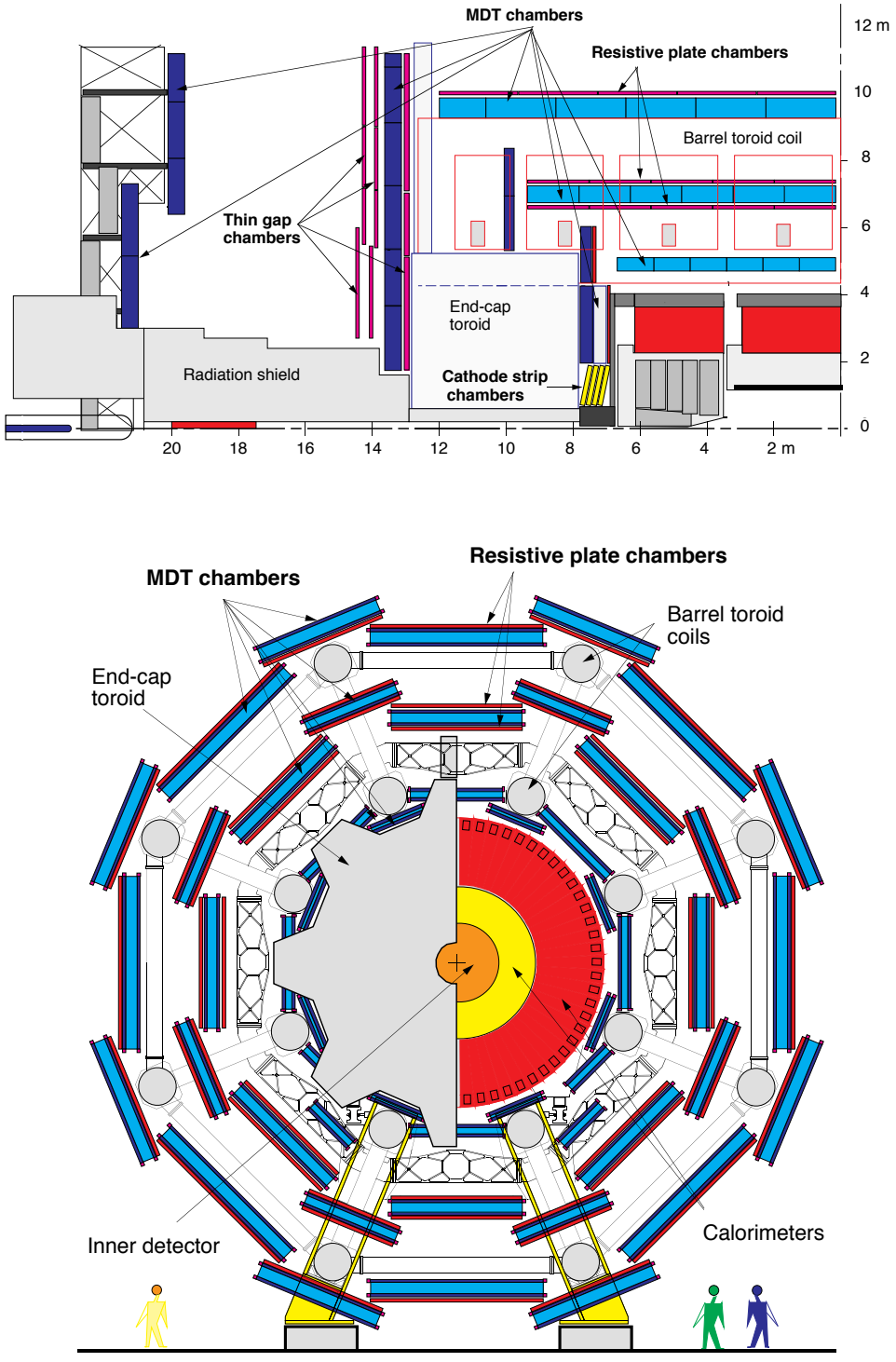


Figure 3.20: Side view of one quadrant of the muon spectrometer (Top) and Transverse view of the spectrometer (bottom) [38].

Table 3.4: Overview of the muon detector instrumentation. 'Area covered' refers to the total area of the sensitive region of each subsystem.

	Precision chambers		**Trigger chambers**	
	CSC	**MDT**	**RPC**	**TGC**
Number of chambers	32	1194	596	192
Number of readout channels	67 000	370 000	355 000	440 000
Area covered (m^2)	27	5500	3650	2900

detection element is a cylindrical aluminum drift tube of 30 mm diameter with a W-Re sense wire with the diameter of 50 μm. Tubes are aligned with the orthogonal direction to the beam axis, *i.e.* orthogonal to the bending direction. MDT is operated with a non-flammable gas composed of Ar (91 %), N_2 (4 %) and CH_4 (5 %) at 3 bar absolute pressure to reduce diffusion and ionization fluctuation. At the nominal operation gas mixture, the position resolution of 80 μm is achieved. The individual chamber is assembled of six parallel layers of drift tubes on a support frame as shown in Figure 3.21. Integrating the information from all the layers, 40 μm precision for one coordinate and 0.4 mrad angular resolution are achieved.

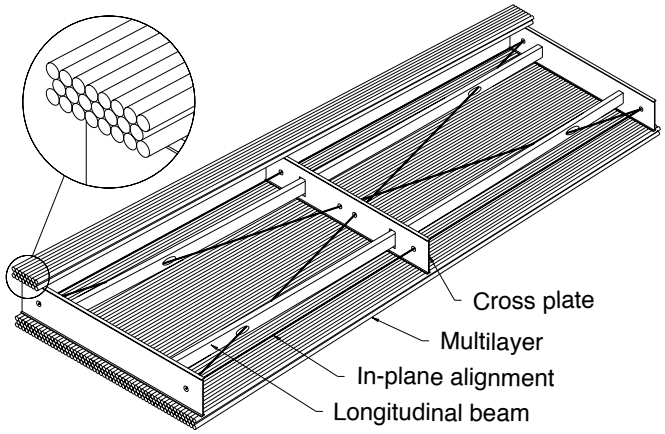


Figure 3.21: Schematic drawing of an MDT chamber [38]. There are eight layers rather than six layers for the innermost station to improve a pattern recognition capability.

3.5.2 Cathode Strip Chamber

CSC is a multi-wire proportional chamber with a cathode strip readout. It locates just outside of HEC, covering the region $2 < |\eta| < 2.7$. A cutaway view of the one layer of CSC is shown in Figure 3.22. CSC consists of 2×4 layers. There are two cathode strips on CSC to provide the hit position in the bending direction and the second coordinate which is orthogonal to the bending direction. The cathode strips for the bending direction are oriented orthogonal to the z-axis. The second cathode strips and the anode wires are parallel to the z-axis. The hit position is measured based on the charge induced on the cathode strips by the avalanche produced around W-Re anode wires. The pitch of the anode wires is 2.54 mm, and pitch of cathode strips is 5.08 mm. The position resolution of 60 μm in the bending direction is achieved with this configuration. The spatial resolution of CSC is sensitive to the incident angle of tracks and the Lorentz angle. To decrease deteriorations of the resolution, CSC is tilted such that the detector

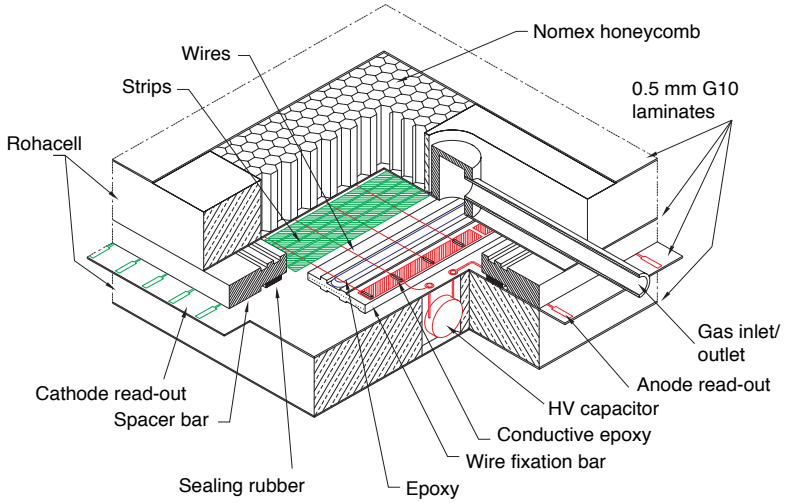


Figure 3.22: Cutaway view of a single CSC layer [38]

surface is perpendicular to straight tracks originating from the interaction point as shown in Figure 3.20. CSC gas is a non-flammable mixture of Ar (30 %), CO_2 (50 %) and CF_4 (20 %). Due to the absence of the hydrogen in the gas, CSC is not sensitive to neutron background and fully operational even if it is located at the relatively large pseudorapidity region and near the interaction point.

3.5.3 Resistive Plate Chamber

RPC is used to provide muon triggers in the region of $|\eta| < 1.0$. It is a gaseous detector with a narrow gas gap formed by two parallel resistive bakelite plates, separated by insulating spacers. Graphite is coated to the resistive plates to apply a high and uniform electric field of typically 4.5 kV/mm. If a charged particle passes through the gas gap, primary ionization electrons induce electron avalanche. Amplification in avalanche mode produces pulses of typically 0.5 pC on read out strips via the capacitive coupling. The signal is read out by the strips on both sides of the resistive plates. A chamber is arranged with two detector layers glued back-to-back to each other interfacing with 6 mm polystyrene support structure and sandwiched with 50 mm and 10 mm support structure as shown in Figure 3.23. Each detector layer is equipped with two

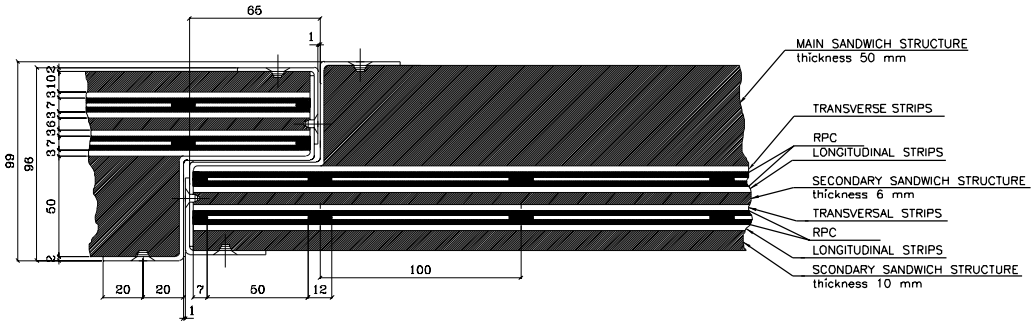


Figure 3.23: Mechanical structure of an RPC chamber [38]

orthogonal readout strip panels. One set of strips is oriented in the same direction as the MDT wires and supplies a bending view of the trigger detector. The other set, orthogonal to the

MDT wire, provides a second coordinate measurement which is required in the offline pattern recognition. The pitches of the strips vary from 30.0 to 39.5 mm depending on the detector position. RPC is operated with the non-flammable and environmental-safe gas mixture of 97 % tetrafluoroethane ($C_2H_2F_4$) and 3 % isobutane (C_4H_{10}) with a total volume of 18 m^3. The time resolution of RPC is important because RPC has to issue the trigger. By optimizing many detector components such as the readout strips, the printed circuit for readout and the readout ICs, 1.5 ns timing resolution which is fast enough to distinguish 25 ns bunch spacing of LHC is achieved.

3.5.4 Thin Gap Chamber

TGC consists of a multi-wire proportional chambers used to provide trigger signal in the end-cap regions. The gas gap of the chamber is 2.8 mm, and in the gap, anode wires with the diameter of 50 μm are strung with a 1.8 mm pitch. Unlike the normal proportional chamber, TGC has a larger anode wire pitch than the cathode-anode distance. This design is adopted to achieve a good timing resolution by the short drift time. TGC is constructed in doublets and in triplets as shown in Figure 3.24. The anode plane is sandwiched with two cathode planes made of 1.6 mm G-10 plates coated with graphite cathode. On the back side of the cathode plates facing the center of the chamber, there are etched copper strips to provide the readout of the azimuthal coordinate[3)]. The seven layers, consisting of one triplet and two doublets, are installed at the middle station, and one doublet is placed at the inner station, which only provides a measurement of the second coordinate that is orthogonal to the bending direction for the muon track reconstruction. The pitch of the strips is between 14.6 and 49.1 mm depending on the detector position. To generate a trigger signal, several anode wires are grouped and read out at once. The number of wires in one ganged group varies from 4 to 20 depending on the required granularity as a function of pseudorapidity.

TGC is operated with a highly quenching gas mixture of CO_2 (55 %) and n-C_5H_{12} (45 %). This type of gas mixture allows operation in the saturated mode and gives a short pulse tail well within 25 ns. Due to this characteristic, TGC can issue a trigger with a correct bunch crossing identification index. Unlike other muon detectors, the gas mixture needs special treatments in some respects, because the gas mixture for TGC is extremely flammable, and also the n-C_5H_{12} is liquid at room temperature and the atmospheric pressure.

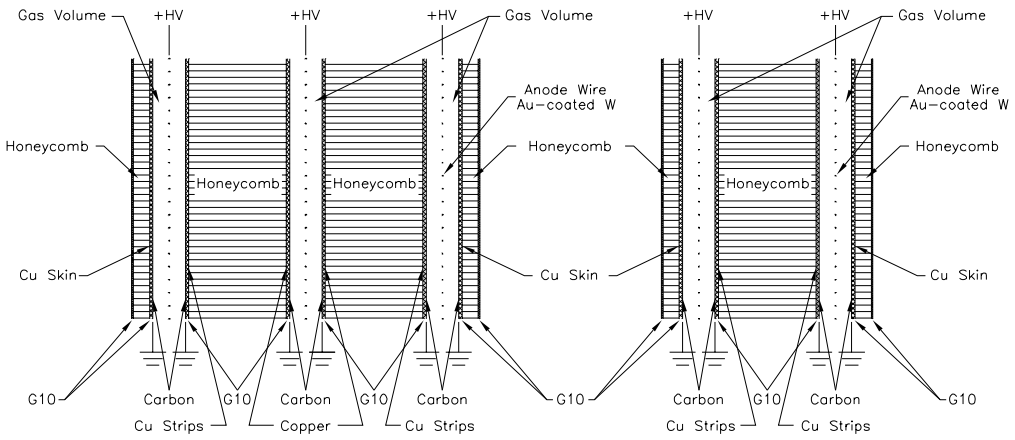


Figure 3.24: Schematic cross-section of a triplet (left) and of a doublet of TGC. The width of the gas gap is shown enlarged [38].

[3)] No readout strips at the central layer of a triplet.

3.6 Forward detectors

In this section, the forward detectors which are mainly used for the luminosity determination in the ATLAS experiment are described.

3.6.1 LUCID

The detector called LUCID, LUminosity measurement using a Cherenkov Integrating Detector, is primarily used to monitor the number of inelastic pp interactions per bunch crossing by counting the number of particles detected in one bunch crossing. The front of LUCID is located at the $z = \pm 16.98$ m. LUCID covers the region of $5.4 < |\eta| < 6.1$. Each side of the detecter contains 200 thin, 1.5 m long, cylindrical gas Cherenkov counters. The counters are arranged to surround the beam pipe with five concentric layers, and to point to the ATLAS detector center. The cross section and overview of the detector are shown in Figures 3.25 and 3.26.

The Cherenkov light from each counter is transferred through quartz fibers and is readout

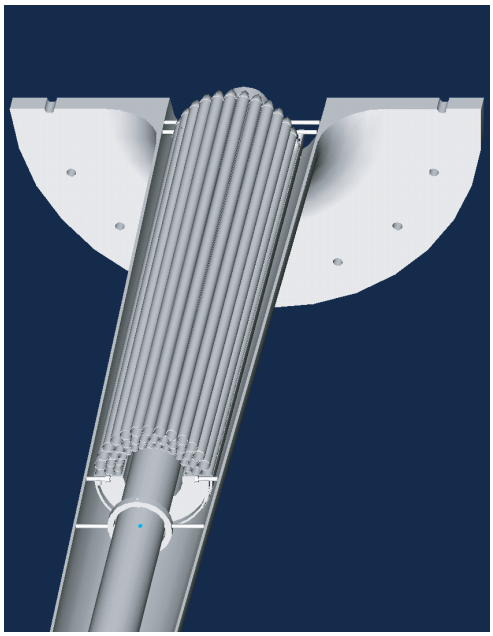


Figure 3.25: The LUCID detector is installed between the beam pipe and the conical support tube of the beam pipe [51].

by photo-multiplier tubes. C_4F_{10} is used as the gas radiator since it has one of the largest refraction index, which is 1.00137, at atmospheric pressure and good transparency. The larger refraction index is favored for LUCID to increase the number of tracks which can be detected in the detector to reduce an uncertainty. The particle coming from the interaction point normally passes through the full length of the detector. However, the particles from other interactions like beam gas scattering and cosmic showers tend to pass shorter length in the radiator volume, resulting in smaller pulse. In addition, the Cherenkov light yield is proportional to the number of incoming particles. This allows to count the number of interactions.

3.6.2 Beam Condition Monitor

Beam Condition Monitor (BCM) is installed to monitor the beam condition of LHC to avoid the potential detector damage resulting from the anomalies of the LHC beam. BCM is also

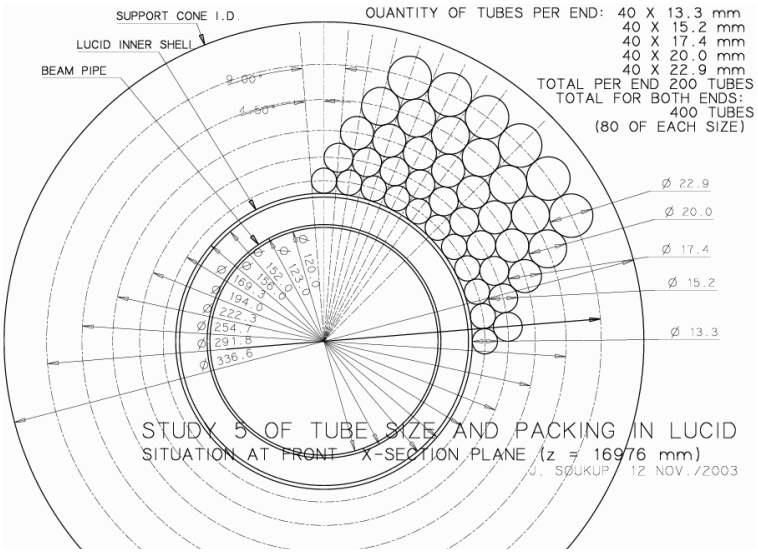


Figure 3.26: The cross section of LUCID at the front of the detector ($z = \pm 16.98$ m) [51].

useful to make complementary measurements of the luminosity by LUCID. BCM is located at the radius of 55 mm, which is 20 mm outside the beam pipe, and at $z = \pm$ 183.8 cm. This corresponds to a pseudorapidity of approximately ± 4.2. To make the detector radiation hard, the diamond is chosen as the sensor material. Charged tracks passing through the detector deposit energy, and generates a minimum ionizing particle (MIP) signal. BCM detects this signal and records pulse height, and the time-of-flight from the interaction point to the BCM sensor. MIP signals from the diamond sensors follows a Landau distribution. When multiple particles traverse the sensor simultaneously, we can still measure the total energy deposit from the pulse height information because the pulse shape is identical to the one generated by the single particle. This invariance of the pulse shape allows us to count the number of particles and hence the number of interactions just by measuring the pulse hight.

3.7 Trigger and the data acquisition system

The Trigger and Data Acquisition system (TDAQ) in the ATLAS experiment is described in this section. The trigger system has three levels, Level-1 (L1), Level-2 (L2) and the Event Filter (EF). The L2 trigger and EF are called the High-Level Trigger (HLT). The L1 trigger makes a hardware-based trigger decision, while HLT makes a trigger decision based on software with commonly used computers and networking. Each trigger level refines the decisions made by the previous level. At the end, 40 MHz frequency pp collision data at LHC are reduced to 400 Hz with the event size of approximately 1.3 Mbyte. The block diagram of the TDAQ system is shown in Figure 3.27. The details of each level of triggers are described in the following.

3.7.1 Level-1 trigger

The L1 trigger searches for the signatures from high P_{T} muons, electrons/photons, jets, and tau leptons decaying into hadrons. Not only the single physics objects (*i.e.* leptons, jets, photons) but also the combination of them are also used to make decisions. For example, missing transverse energy which is defined as the negative signed vector sum of the transverse momentum of the physics objects is used to select the events containing the undetected particles

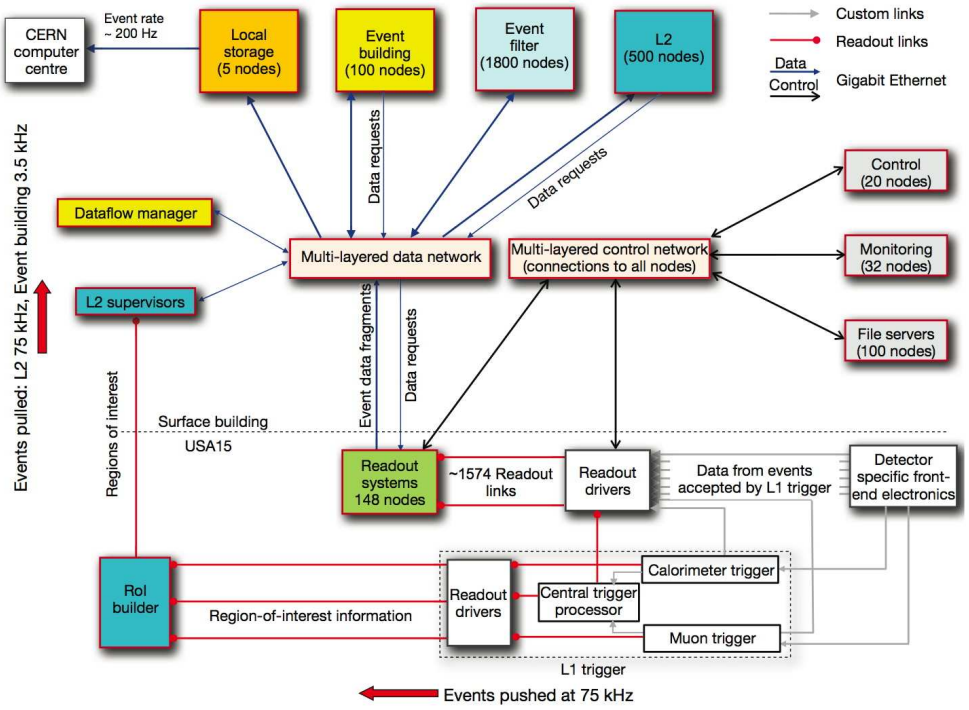


Figure 3.27: Block diagram of the ATLAS trigger and data acquisition systems. In this figure, the event rate is written as 200 Hz, which is the design value. However, data were taken with 400 Hz in the 2011 operation [41].

like neutrinos. The L1 trigger uses the information from RPC and TGC, and from all the calorimeter subsystems with reduced granularity for the electromagnetic or hadronic clusters. The maximum L1 accept rate is 75 kHz. The trigger decision has to be made within 2.5 μs after the bunch crossing. In this thesis, because only high P_{T} electron and muon triggers are used, the details of them are described below.

Electron trigger

To make the electron trigger decision, trigger towers are defined as shown in Figure 3.28. The trigger is made by identifying 2×2 clusters of trigger tower in the electromagnetic calorimeter, which includes at least one of four possible two-tower pair of neighbor electromagnetic towers exceeding a pre-defined deposit energy threshold. To remove the fake trigger due to hadrons, it is required that 4×4 hadronic trigger towers, which is behind the electromagnetic tower shown in red and magenta in Figure 3.28, does not have a significant energy deposit.

Muon trigger

The source of muon trigger is provided by the dedicated trigger detectors, RPC for the barrel region and TGC for the end-cap region, as described in Section 3.5.3 and 3.5.4. The trigger algorithm is operated in the following way. The RPC and TGC chambers, defined as RPC1 - RPC3 and TCG1 - TGC3, are arranged as shown in Figure 3.29. The muon trigger decision is basically made by requiring a coincidence of these layers. For the decision in the barrel, if a hit is generated at RPC2, a hit is searched for in RPC1 within the corresponding windows whose center is defined by the line from the hit at RPC2 to the interaction point. Because the curvature of the particle gets smaller when the momentum gets larger, the width of the

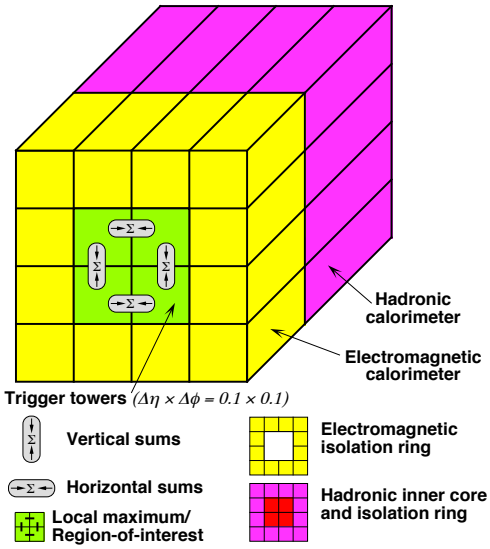


Figure 3.28: Calorimeter clusters used in the L1 calorimeter trigger system. One trigger tower is defined as the size in η-ϕ plane of $\Delta\eta \times \Delta\phi = 0.1 \times 0.1$ in most parts. It is larger at the forward region [41].

coincidence window corresponds to the threshold of the muon P_{T}. Since there are four detection layers inside the two RPC layers, three out of four coincidences is required. This algorithm gives a very good rejection of fake tracks from noise hits. The coincidence between RPC1 and RPC2 is used for the low-P_{T} trigger decision. The high-P_{T} trigger decision makes use of the additional information generated in RPC3. The decision algorithm at the end-cap is almost the same as the one at the barrel. First a coincident hit is searched for in TCG2 seeded by the hit at TGC3. This coincidence between TGC2 and TGC3 decides low-P_{T} triggers. Another hit is searched for in TGC1 for the high-P_{T} trigger decision.

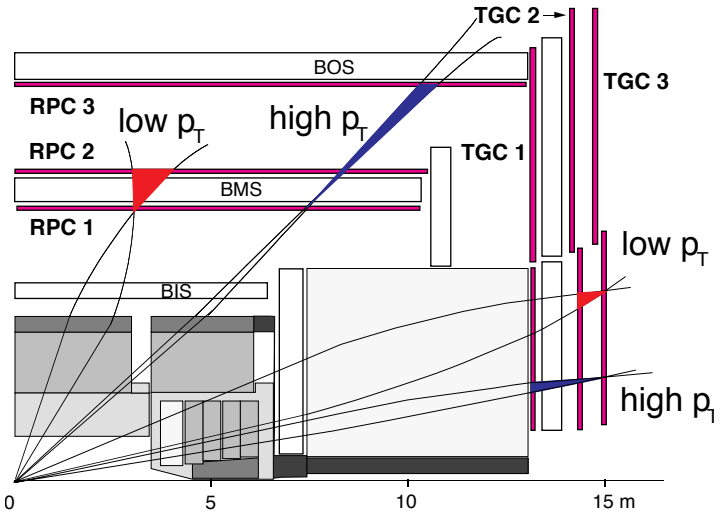


Figure 3.29: Level-1 muon trigger scheme [38].

Region of interest

The information from the L1 trigger includes the selected trigger type and the location of trigger objects in η and ϕ. The Region of Interest (RoI) is defined based on the η and ϕ in the L1 trigger information so that the software-based HLT can quickly reconstruct events by processing data only around RoIs. The size of RoI is $\Delta\eta \times \Delta\phi = 0.2 \times 0.2$, corresponding to 2×2 trigger towers for electrons, and $\Delta\eta \times \Delta\phi = 0.1 \times 0.1$ for muons. The amount of data in RoI is typically 1-2 % of full data.

3.7.2 High-Level Trigger

HLT is based on the computing farm with 1116 nodes dedicated for processing data to reduce the recording rate to below 400 Hz which is the maximum writing speed on the disk storage. There are two stages, the L2 trigger and EF. The difference between these stages is how to reconstruct the event. At the L2 trigger, the event is reconstructed by looking at only the region specified by RoI. On the other hand, the event is reconstructed for the whole region of the detector in the EF level. The L2 processing farm consists of approximately 800 nodes. The L2 trigger reduces the event rate from 75 kHz of the L1 output to 6 kHz. The EF additionally reduces the event rate from 6 kHz to 400 Hz.

In terms of the event selection for the electron and muon triggers at the HLT, the information of the inner tracker is also used at this stage. For the electron trigger, the location of the electromagnetic cluster is required to match the track reconstructed from the inner tracker hits. This selection reduces the fake electron trigger caused by the high P_{T} photon interaction at the EM calorimeter. For the muon trigger, the reconstructed track in the muon spectrometer is required to match the track identified in the inner tracker. In addition, it is required that the energy deposit in the calorimeters corresponds to the MIP particle. This selection ensures that the muon does not emerge from the decay of the hadrons in a jet.

3.8 ATLAS computing system

The operation and analysis at the ATLAS experiment highly rely on the advanced computing system based on the GRID technology. A complex set of tools and distributed services, enabling the automatic distribution and processing of the large amounts of data, has been developed and deployed by ATLAS in cooperation with the LHC Computing Grid (LCG) project.

The ATLAS software is based mainly on the `C++` language. The software is built on a common framework called Athena. All processing of the data in the ATLAS experiment, including a software-based HLT, detector simulation, event reconstruction, and data analysis is taken place within the Athena framework.

The *pp* collision events passing the trigger selection are transferred as the byte stream to the CERN computing center. This byte stream is stored as Raw Data Objects (RDO) there. After the event data are handed over to the reconstruction algorithm, the results are stored as Analysis Object Data (AOD). AOD is further processed to reduce the event size, and filtered out as the Derived Physics Data (DPD). DPD is a n-tuple style representation of event data for the end-user analyses and histogramming. Consequently, the data size at the DPD stage for each bunch crossing event becomes a few kByte from 1.3 Mbyte at the RDO stage.

In this analysis, DPDs which are produced with the Athena release 17 are used.

Chapter 4

Data samples

In this chapter, the dataset used for the $\sigma_{t\bar{t}}$ measurement is described. This analysis makes use of pp collisions produced by LHC and recorded by the ATLAS detector during the year of 2011. A description of the pp collision data is presented in Section 4.1. To understand the data and our detector behavior, we prepared simulated pp collision data and describe it in Section 4.2.

4.1 Collision data

Figure 4.1 shows the data taking efficiency per day. Average efficiency of 93.5 % is achieved in the 2011 operation. Figure 4.2 shows the integrated luminosity, for both delivered by LHC, and

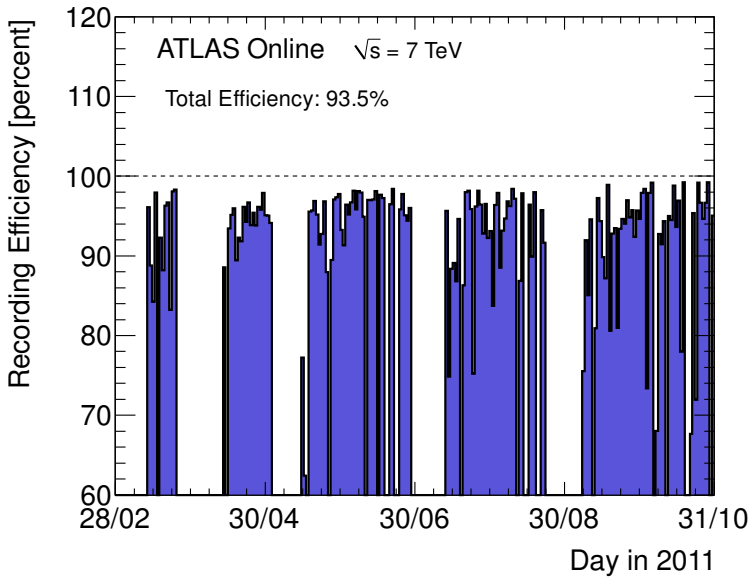


Figure 4.1: The luminosity weighted data taking efficiency per day [52].

recorded by the ATLAS experiment. In total, 5.61 fb^{-1} of data was provided with $\sqrt{s}$ =7 TeV by LHC in 2011. The ATLAS detector successfully recorded 5.25 fb^{-1}. The ATLAS experiment monitors the data quality (DQ) in various ways. The details of the ATLAS DQ monitoring system can be found in the reference [53]. The collision data is tagged and recoded with the 'Run Number' and the 'Luminosity Block (LB)' where one LB corresponds to one minute. The online and offline ATLAS DQ monitoring system assigns the data quality flag classified as

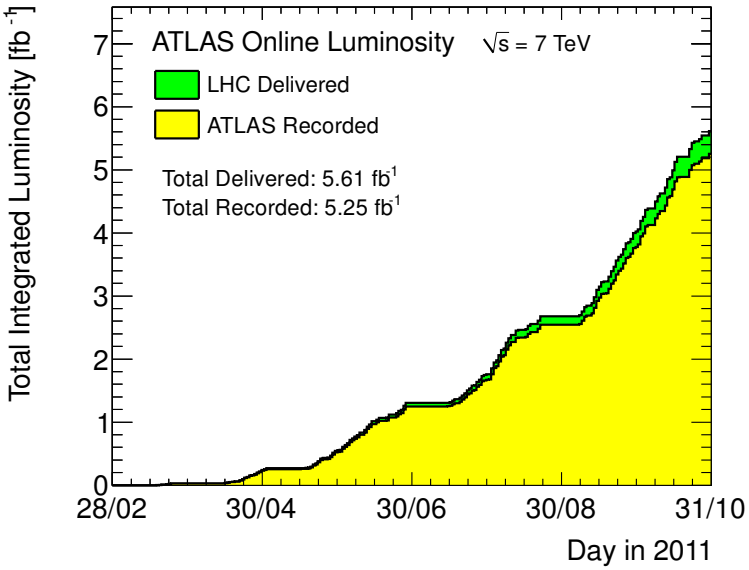


Figure 4.2: The integrated delivered luminosity from LHC and the recorded luminosity with the ATLAS detector in 2011 [52].

'`good/warning/bad`' to each LB. The quality flag is set by the condition of each subsystem. This data quality status is stored in a database. The flag of the analyzed data is required to be all '`good`'. This guarantees that the data is taken by the fully operated ATLAS detector subsystems and trigger systems. The fraction of the good quality data determined by each subsystem is summarized in Table 4.1. The efficiency of all detectors except LAr electromagnetic calorimeter ranges approximately 99-100 %. Inefficiency of the LAr EM calorimeter is mostly caused by high voltage trips and noise bursts [1)]. After requiring the data to be flagged as all `good`, the integrated luminosity is 4.71 fb^{-1}.

4.1.1 Luminosity determination

In this section, we describe how the luminosity is measured in the ATLAS experiment. The luminosity is one of the most important parameters to measure $\sigma_{t\bar{t}}$. The uncertainty of the luminosity measurement directly affects the precision of the measurement.

Principle of the measurement

The luminosity, $\mathcal{L}$, can be expressed as

$$\mathcal{L} = \frac{\mu n_b f_r}{\sigma_{\text{inel}}}, \tag{4.1}$$

where μ is the average number of inelastic interactions per bunch crossing, n_b is the number of colliding bunch pairs, f_r is the machine revolution frequency, and σ_{inel} is the pp inelastic cross section. Using the observed interaction rate per bunch crossing, μ_{vis}, the luminosity is

$$\mathcal{L} = \frac{\mu_{\text{vis}} n_b f_r}{\sigma_{\text{vis}}}, \tag{4.2}$$

[1)] Cluster of the noisy calorimeter cells by the hardware problems.

Table 4.1: The fraction of data flagged as 'good' in each detector subsystem in the 2011 data taking [52]. 'EM' and 'hadron' in the table means the electromagnetic and the hadron calorimeter.

	Subsystem	Efficiency [%]
Inner Tracker	Pixel	99.8
	SCT	99.6
	TRT	99.2
Calorimeters	LAr EM (barrel)	97.5
	LAr EM (end-cap)	99.5
	LAr hadron	99.2
	TileCal	99.2
Muon Detectors	MDT	99.4
	CSC	99.4
	RPC	98.8
	TGC	99.1
Magnets	Solenoid	99.8
	Toroid	99.3

where σ_{vis} is the total inelastic cross section multiplied by the detection efficiency of a particular detector and an algorithm. At present, the ATLAS experiment monitors μ_{vis} for the luminosity calculation.

According to Equation (4.2), the luminosity calibration is equivalent to determining the visible cross section σ_{vis}. However, the inelastic pp cross section at $\sqrt{s} = 7$ TeV has not been measured yet precisely. In addition, the uncertainty of the detection efficiency may be significant. To determine σ_{vis} without any *a priori* knowledge of the detection efficiency and σ_{inel}, an alternative equation of the absolute luminosity inferred from the direct measurements of the machine parameters is used;

$$\mathcal{L} = \frac{n_b f_r n_1 n_2}{2\pi \Sigma_x \Sigma_y}, \tag{4.3}$$

where $n_{1,2}$ are the numbers of protons per bunch in the beam 1 and the beam 2, respectively, and $\Sigma_{x,y}$ is the size of the colliding beams in the x and the y direction. For the Gaussian shaped beams, $\Sigma_{x,y}$ is defined as

$$\Sigma_u = \sqrt{\sigma_{1u}^2 + \sigma_{2u}^2}, \tag{4.4}$$

where $u = x, y$ and σ_{iu} is the beam width modeled as Gaussian in the u direction for the beam i. This is more general form of Equation (2.4) without assuming that the beam 1 and the beam 2 have the same width.

By combining Equation (4.2) and Equation (4.3), we obtain the desired σ_{vis} as

$$\sigma_{\text{vis}} = \mu'_{\text{vis}} \frac{2\pi \Sigma_x \Sigma_y}{n_1 n_2}, \tag{4.5}$$

where μ'_{vis} is the number of interactions when $n_{1,2}$ and Σ_u are determined. By assuming that the acceptance and the efficiency do not change during the whole data taking period, we can measure the luminosity by using σ_{vis} determined from $n_{1,2}$, μ'_{vis} and $\Sigma_{x,y}$ as the input to Equation (4.2).

- The determination of the number of protons

The number of protons per bunch is determined by the following process. The total beam current for each beam is monitored by the DC current transformers (DCCT) with high accuracy.

The DCCT, however, does not have an ability to separate individual bunch populations. The other detector called the fast bunch current transformer (FBCT) is used to measure the relative fraction of the individual bunch population to the total current. Using these two measurements, the number of protons per bunches are determined.

- The determination of $\mu'_{\rm vis}$ and $\Sigma_{x,y}$

We determined $\mu'_{\rm vis}$ and $\Sigma_{x,y}$ simultaneously by the dedicated *Van de Meer* (VdM) scans [54]. During the VdM scan, $\mu_{\rm vis}$ is measured by changing the separation between the two beams in both x and y directions. The luminosity as a function of the distance between the beams in the u direction, d_u, is expressed as

$$\mathcal{L}'(d_u) = \mathcal{L}\exp\left[\frac{-d_u^2}{2\Sigma_u^2}\right]. \tag{4.6}$$

Σ_u can be extracted from the distribution of the observed event rate as a function of d_u because the event rate should be proportional to the luminosity. Besides, $\mu'_{\rm vis}$ is determined as the observed maximum number of interactions during the VdM scan where $\Sigma_{x,y}$ are determined.

Now, one can obtain the instantaneous luminosity by just counting $\mu_{\rm vis}$, since n_b, f_r and $\sigma_{\rm vis}$ in Equation (4.2) are known.

Measurement

Two sets of the VdM scan were performed in May 2011. The data taken with these scans is used to obtain $\sigma_{\rm vis}$. The obtained $\sigma_{\rm vis}$ is used to measure the integrated luminosity for the whole 2011 data. LUCID and BCM are used to measure $\mu_{\rm vis}$. The result of the measurements by the two detector systems are consistent each other. Many sources of the systematic uncertainty is evaluated. The biggest contributions come from the long-term stability, the emittance growth and the bunch population measurement. Short descriptions for these uncertainties are presented below.

- The long-term stability

The assumption that the measured $\sigma_{\rm vis}$ is stable during the 2011 runs would be a source of the systematic uncertainty, since $\sigma_{\rm vis}$ might vary due to the change of the detector response and the LHC condition, particularly the number of colliding bunches. To estimate this uncertainty, the mean number of interactions measured by various algorithms are compared with each LHC fill. All measurements are consistent with each other across the algorithms with different detectors. The maximum difference of 0.7 % is assigned as the systematic uncertainty from this source.

- The emittance growth

The $\sigma_{\rm vis}$ measurement assumes that the beam sizes $\Sigma_{x,y}$ are constant. However, a slight increase of the beam size due to the blow-up of the transverse beam emittance is observed during the two set of scans. This emittance growth would decrease the measured luminosity. The relative difference of $\sigma_{\rm vis}$ between the two scans is considered as the systematic uncertainty, which is 0.67 %.

- The bunch population measurement

The bunch population measurement to determine $\sigma_{\rm vis}$ has an uncertainty due to the finite resolution of the beam current measurement by DCCT and FBCT. In addition, the fact that DCCT can measure only the total beam current becomes the potential bias. The measured beam current by DCCT includes the contribution from the protons at the out-of-time position where the proton do not participate in the collision. Therefore, $\sigma_{\rm vis}$ might be biased to be small

when we include such protons. By considering these effects, the systematic uncertainty from the bunch population is evaluated to be about 0.54 %.

We estimate the uncertainty from other fourteen possible sources, such as the beam-beam interaction effect, background subtraction etc. It is found that each source contributes by 0.2-0.5 %. By combining all the sources, the total uncertainty of the absolute luminosity measurement in the whole 2011 data is estimated to be 1.8 %. The full descriptions of this measurement can be found in the reference [55].

4.1.2 Data taking period, trigger setup and data stream

The 2011 *pp* collision runs are divided into thirteen periods named 'Period A' to 'Period M'. A period is renewed when the trigger setting is changed significantly or LHC stops running for the machine development and/or the technical shutdown.

Trigger setup

The ATLAS experiment records data with a given set of triggers in each data taking period. The definition of the set of the triggers is varied time to time to maintain the total trigger rate below the acceptable level since the instantaneous luminosity gradually increased during 2011. The data used in this analysis is collected by the single electron or muon trigger with the lowest threshold without pre-scaling, where 'pre-scale' is an artificial random data drop at the trigger decision level to reduce the total trigger rate. The correspondence between each period and the trigger setting used for this analysis is summarized in Table 4.2. The details of the trigger setting is described in the following.

Table 4.2: Periods and triggers in the ATLAS 2011 *pp* collision runs. Period A is not listed since any data in Period A is not used in this analysis.

<table>
<tr><th rowspan="2">Period</th><th rowspan="2">$\int \mathcal{L}dt$ [pb]</th><th>Electron trigger</th><th>Muon trigger</th></tr>
<tr><th>L1 → L2 → Event Filter</th><th>L1 → L2 → Event Filter</th></tr>
<tr><td>Period B</td><td rowspan="3">178</td><td rowspan="8">L1_EM14 → L2_e20_medium → EF_e20_medium</td><td rowspan="6">L1_MU10 → L2_mu18 → EF_mu18</td></tr>
<tr><td>Period C</td></tr>
<tr><td>Period D</td></tr>
<tr><td>Period E</td><td rowspan="4">949</td></tr>
<tr><td>Period F</td></tr>
<tr><td>Period G</td></tr>
<tr><td>Period H</td></tr>
<tr><td>Period I</td><td>338</td></tr>
<tr><td>Period J</td><td>226</td><td rowspan="3">L1_MU11 → L2_mu18_medium → EF_mu18_medium</td></tr>
<tr><td>Period K</td><td>590</td><td>L1_EM16 → L2_e20_medium → EF_e22_medium</td></tr>
<tr><td>Period L</td><td rowspan="2">2432</td><td>L1_EM16VH → L2_e22vh_medium1 → EF_e22vh_medium1</td></tr>
<tr><td>Period M</td><td>OR L1_EM30 → L2_e45_medium → EF_e45_medium</td></tr>
</table>

Electron trigger

Four types of the single electron trigger are used to collect the events with electrons as shown in Table 4.2. For Period B to J (K), threshold of 20 GeV (22 GeV) on the electron transverse energy[2)] at EF is used. These triggers are named `EF_e20_medium` and `EF_e22_medium` and seeded

[2)] The transverse energy E_{T} is defined as $E_{\mathrm{T}} = E \sin\theta$

by the L1 trigger with the threshold of 14 GeV (`L1_EM14`) and 16 GeV (`L1_EM16`), respectively. For Period L and M, the same trigger as Period K with threshold of 22 GeV but with the hadronic core veto at the L1 trigger level is used. This trigger is named `EF_e22vh_medium1`. This trigger has a small inefficiency at a very high electron E_{T} region ($\gg$ 100 GeV). To achieve higher efficiency for such electrons, a logical OR of `EF_e22vh_medium1` and `EF_e45_medium1`, which has the threshold of 45 GeV without the hadronic core veto, is used.

Muon trigger

The triggers with the threshold of 18 GeV on muon P_{T} at EF are used for the whole period. These triggers are named `EF_mu18` and `EF_mu18_medium`. The difference between them is their seed trigger. The seed trigger of `EF_mu18` is `L1_MU10` while the one of `EF_mu18_medium` is `L1_MU11`. Both L1 triggers require at least 10 GeV for a muon measured by the muon trigger chamber, not as the name implies for `L1_MU11`. `L1_MU11` requires a coincidence of hits across three stations in TGC and RPC whereas `L1_MU10` requires three in TGC and only two in RPC.

Data stream

The triggered data is sent to the pre-defined streams that collect only some specific data sets categorized by the trigger. For instance, the `physics_Egamma` (`physics_Muons`) stream contains the events that pass the electron triggers or the photon triggers (the muon triggers). Both the `physics_Egamma` stream and the `physics_Muons` stream are used. There are some overlapped events between the streams, which causes a problem of double counting for the analysis in the $e\mu$ channel. The overlap is solved by requiring the trigger condition as follows at the offline analysis. We require that the electron trigger is fired, and do not require anything for the muon trigger when we analyze the data in the `physics_Egamma` stream, while we require that the electron trigger is 'not' fired, and require that the muon trigger is fired when we analyze the data in the `physics_Muon` stream.

4.2 Monte Carlo samples

In this section, the details of Monte Carlo (MC) simulation samples are described. MC simulations are used to calculate the acceptance of the $t\bar{t}$ events and also to evaluate the contributions from some background processes. All MC samples are simulated with GEANT4 [56] for the ATLAS detector. Two types of the detector simulation called the full simulation and the fast simulation are used. The only difference between the full and the fast simulation is how to simulate the calorimeter activity. The fast simulation uses the pre-defined parametrized calorimeter response, implemented by FastCaloSim [57], instead of the full simulation to reduce CPU time from a several minutes to a few seconds per event. The samples generated with the full simulation are used for the nominal analysis, while the one with the fast simulation are used to estimate the systematic uncertainties.

4.2.1 Common setting for all Monte Carlo samples

Simulation of multiple pp interactions

The average number of interactions per one bunch crossing is shown in Figure 4.3. Up to twenty four interactions are observed. To take into account the multiple pp interactions in one bunch crossing, MC events are overlaid with some low Q^2 pp collision events generated by

PYTHIA6 [58]. The number of overlaid events in the MC samples is adjusted to reproduce the observed distribution in data.

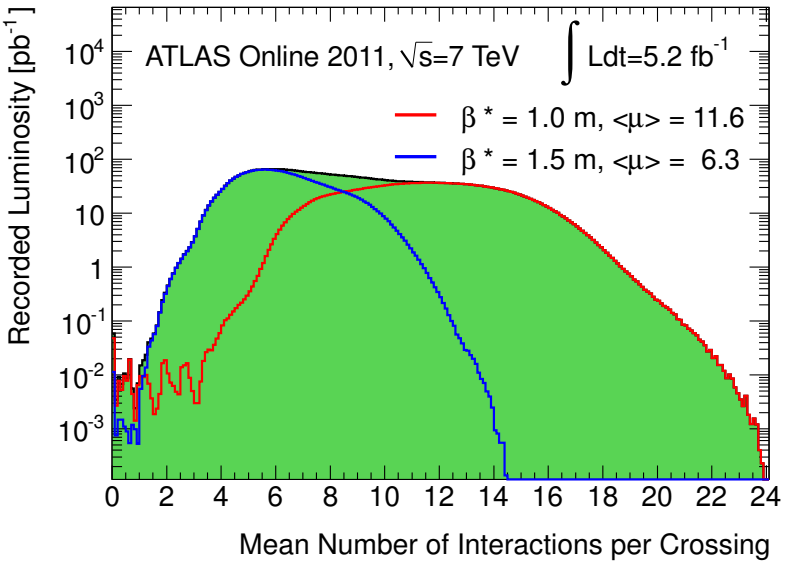


Figure 4.3: The distribution of the mean number of interactions per bunch crossing in 2011 [52]. The red (blue) shows for data taken before (after) the september technical shutdown where β^* was reduced from 1.5 m to 1.0 m.

Underlying event simulation

There are two partons which participate in a hard scattering of the pp collisions. Beside that, there are some other interactions so called an underlying event. The underlying event includes Initial State Radiation (ISR) and Final State Radiation (FSR) and also beam-beam remnants interactions. ISR and FSR are the QCD counterpart of the electromagnetic radiation from an accelerated charge. Beam-beam remnants refer to the hadrons generated from the partons that do not participate in the hard scattering processes. Some of the MC samples described below use HERWIG [59] for the underlying event modeling[3)]. PYTHIA6 is used for this purpose as well for the rest of samples. The underlying event is difficult to model theoretically, since there are many contributions which cannot be calculated from the first principle. Therefore, the parameters of the model are tuned to reproduce the observed distributions in data. Two different tunes examined in the references [60, 61] are used for HERWIG and PYTHIA, respectively.

Mass and width of gauge bosons and the top quark

The mass and the width of W and Z bosons are set to the PDG values [62]. The mass of the top quark is set to 172.5 GeV. This value is artificially chosen still within the uncertainty of PDG value which is $172.9 \pm 0.6 \pm 0.9$ GeV. The top quark decay width is set to 1.320 GeV based on the NLO theoretical calculation. All the values are listed in Table 4.3.

[3)] HERWIG is always interfaced with JIMMY when it is used to model the underlying event for the ATLAS MC production.

Table 4.3: The mass and the width of W and Z bosons and the top quark used in the MC simulation.

	W boson	Z boson	top quark
Mass [GeV]	80.399	91.1876	172.5
Width [GeV]	2.085	2.4952	1.320

4.2.2 List of the MC samples

Table 4.4 summarizes the MC samples used to measure $\sigma_{t\bar{t}}$. For each sample, the type of the generator and the parton shower modeling, the PDF set, and the cross section which is used to normalize the MC events are given there. The cross section of $t\bar{t}$ and the single top is calculated with the NNLO accuracy. The one for the other samples are obtained with the NLO accuracy.

Table 4.4: List of MC samples used to estimate the acceptance and the background level.

Process	Generator	Parton shower	PDF	Cross section [pb]
$t\bar{t}$	MC@NLO	HERWIG	CT10	$166.8^{+16.5}_{-17.8}$ (NNLO)
W	ALPGEN	HERWIG	CTEC6L1	31376 ± 1017 (NLO)
Z/γ^*	ALPGEN	HERWIG	CTEC6L1	15188 ± 352 (NLO)
Single top (s-channel)	MC@NLO	PYTHIA	CT10	1.50 ± 0.06 (NNLO)
Single top (t-channel)	ACERMC	PYTHIA	LO**	$20.9^{+0.9}_{-0.6}$ (NNLO)
Single top (Wt)	MC@NLO	PYTHIA	CT10	15.7 ± 1.2 (NNLO)
WW, ZZ, WZ (Dilepton)	ALPGEN	HERWIG	CTEC6L1	7.61 ± 0.82 (NLO)
WW, ZZ, WZ (Inclusive)	HERWIG	HERWIG	LO**	23.07 ± 2.49 (NLO)

Table 4.5 summarizes the MC samples used to estimate the uncertainty of the acceptance of $t\bar{t}$ events. All the samples in this table are simulated with the fast simulation.

Table 4.5: List of MC samples used to estimate the systematic uncertainty.

Process	Generator	Parton shower	Description
$t\bar{t}$	MC@NLO	HERWIG	Reference sample
$t\bar{t}$	POWHEG	HERWIG	For the uncertainty by the generator
$t\bar{t}$	POWHEG	PYTHIA	For the uncertainty by the parton shower
$t\bar{t}$	ACERMC	PYTHIA	For the uncertainty by ISR/FSR

The number of events for each MC sample is generated as much as the one expected in the integrated luminosity of approximately 10 to 100 fb^{-1}. All the events are used in the analysis, but scaled to match the number of events expected in 4.7 fb^{-1} by assuming the cross sections given in Table 4.4.

The details of each MC sample are described in the following sections.

4.2.3 Signal Monte Carlo sample

Simulated $t\bar{t}$ events are generated using the NLO MC generator called MC@NLO [63, 64] with the NLO PDF set by CT10 [65]. The renormalization and the factorization scales are fixed to the top quark mass. The parton showering and the hadronization for this sample are modeled by HERWIG [59] with NLO accuracy. The branching ratio of the W boson leptonic decay is set to 10.8 % for each lepton flavor, but at least one of the W bosons from top quarks decay is specified to decay leptonically. The partons which are generated by HERWIG with more than 10 GeV of transverse momentum are considered as the final state partons and used as the input of the hadronization. To reduce the systematic uncertainty from the MC statistics, approximately 15 million events are produced, which corresponds to the number of top quark pairs in 130 fb^{-1}.

4.2.4 Background Monte Carlo samples

We use four types of the simulated background, Z/γ^*, W boson, single top and di-boson events.

Z/γ^* and W boson samples

The Z/γ^* and the W boson events associated with jets are modeled with the ALPGEN generator [66] interfaced by HERWIG with the LO PDF set CTEC6L1 [67]. This generator implements the exact LO matrix element calculations for the final state with up to five partons. During the underlying event simulation and the hadronization process by HERWIG, an additional hard parton on top of the one already generated in the matrix element calculation might appear. This alters the number of partons in final state, although the cross section is calculated by ALPGEN. To avoid such inconsistency, so-called the MLM matching scheme [68] is used. It rejects the events which have the additional hard scattered partons generated by HERWIG that are apart from the partons generated by the matrix element calculation by $\Delta R = 0.7$.

To improve the generation efficiency, some additional settings described below are applied.

- The Z/γ^* and W bosons are forced to decay $Z/\gamma^* \to \ell^+\ell^-$ and $W \to \ell\nu$, respectively.
- The minimum parton transverse momentum is specified to be 15 GeV within the pseudo-rapidity range of $|\eta| < 6.0$.
- The events with heavy flavor quarks are generated separately by specifying the associated parton to be b-quarks or c-quarks.
- The Z/γ^* events are generated with the limited range of the dilepton mass, 10 GeV $< M_{\ell\ell} <$ 2000 GeV.

Single top samples

The single top events can be categorized into three groups by its generation diagram, t-channel, s-channel production, and the top quark production associated with W boson (Wt). The single top production in s-channel and with the W boson are generated by the MC@NLO generator [69] with the same setting as the signal $t\bar{t}$ MC generation, *e.g.* for the parton shower and PDF etc. The diagram-removal scheme [70] is used to remove the overlap with the $t\bar{t}$ production. The single top production via t-channel is modeled with the ACERMC [71] MC generator instead of the MC@NLO generator. For the ACERMC generator, LO PDF set LO** in the LHAPDF [72] package is used.

The W boson in s- and t-channel is specified to decay into leptonically, while the events of the Wt production are simulated inclusively.

The production cross section is obtained by the NNLO calculation performed in the references [73,74,75], which are 1.50 ± 0.06 pb, $20.9^{+0.9}_{-0.6}$ pb and 15.7 ± 1.2 pb for s-channel, t-channel, and the Wt production, respectively.

Di-boson samples

In this analysis, WW, WZ and ZZ events are called as the di-boson background. Two types of the di-boson samples are produced. One is produced with the ALPGEN generator, and the other with the HERWIG generator.

- ALPGEN samples
The exactly the same setting for PDF, the MLM matching scheme and so on as Z/γ^* and W boson simulations are used. For all the samples, the events with up to three partons are generated. The decay of the W/Z boson is specified to contain the charged lepton to enhance the production efficiency. Two W bosons in WW events are forced to decay into $\ell\nu\ell\nu$ where ℓ denotes the three types of charged leptons. In the WZ events, Z boson is required to decay into $\ell\ell$ and W boson inclusively. Similarly, one of the Z bosons in the ZZ events is forced to decay into $\ell\ell$, and the other inclusively.

- HERWIG samples
The samples generated with the HERWIG standalone mode are required to have at least one lepton with the transverse momentum greater than 10 GeV and the absolute value of pseudo rapidity less than 2.8. The LO PDF set LO** from the LHAPDF package is used.

The number of events are normalized to match the total cross section by the NLO QCD predictions based on the MCFM program [76].

4.2.5 Top quark pair samples for systematics

Several MC samples are produced to evaluate the systematic uncertainties due to the acceptance of the $t\bar{t}$ production. As mentioned at the beginning of this section, all the samples for the systematic study are simulated with the fast simulation.

Generator uncertainty

To estimate the uncertainty by the MC generator, we prepared the MC samples generated with the POWHEG generator [77] which is the NLO generator like MC@NLO. This sample is ideal to check the difference of generators because we can prepare the MC sample which is generated with the same setting other than the generator. For this comparison, we use the MC@NLO sample processed with the fast simulation to remove the difference between the full and the fast simulation. We compare the acceptance between MC@NLO+HERWIG and POWHEG+HERWIG, and take the difference as the systematic uncertainty from the generator.

Parton shower modeling uncertainty

To estimate the uncertainty by the underlying event modeling, we used the $t\bar{t}$ MC sample generated with POWHEG. POWHEG can be interfaced not only by HERWIG but also by PYTHIA for the underlying event modeling. We compare the acceptance obtained by POWHEG+PYTHIA with the one by POWHEG+HERWIG, and take the difference as the systematic uncertainty from the parton shower and hadronization modeling.

ISR and FSR uncertainty

To estimate the uncertainty by ISR and FSR modeling, the MC samples generated with AcerMC is used. The QCD parameters in this generator are varied to increase or decrease the final state partons. The half of the difference of the acceptance in the samples with increased or decreased ISR and FSR is taken as the systematic uncertainty due to ISR and FSR.

Chapter 5

Event reconstruction

In this chapter, the event reconstruction and the particle identification are described. The reconstruction of charged tracks and pp interaction vertex are described in Section 5.1 and 5.2. Electrons, muons, and jets are expected to exist in the final state. For each particle, their reconstruction method, the selection criteria, and their measured performance are described in Section 5.3 to 5.5. In addition to the particles above, missing transverse energy, $E_{\mathrm{T}}^{\mathrm{miss}}$, as the signature of invisible neutrinos is reconstructed. The $E_{\mathrm{T}}^{\mathrm{miss}}$ reconstruction and a measured performance are described in Section 5.6. The algorithm and performance of b-tagging are described in Section 5.7.

5.1 Charged track

The charged track information is one of the most essential information. Charged tracks are used in the reconstruction of all the physics objects described in the following sections.

In the ATLAS track reconstruction scheme, there are two algorithms, the inside-out and the outside-in tracking. The inside-out tracking is used as the baseline to reconstruct primary charged particles which are directly produced in pp interaction or from the subsequent decay. The inside-out tracking algorithm begins with searching for a track seed in the silicon detector volume. However, the track seed search may fail because of a mis-measurement such as inefficiency of the silicon detector. To compensate this shortage, or to save the non-reconstructed particle with the inside-out algorithm, the outside-in algorithm is implemented. The outside-in algorithm is important especially for the reconstruction of long-lived particle decays and photon conversions where secondary particles emerge from a non-pp collision point.

In the both algorithms, the input to the track reconstruction are space points of charged tracks hitting the inner tracker. Each hit on the pixel detector directly provides a three-dimensional space point. The space point from SCT is formed by hit strips on each side of the sensor in a module. In TRT, drift circles are the input to the algorithms.

The inside-out algorithm searches seed tracks by finding a straight line by combining hits on the pixel detector and the innermost layer of SCT. Candidate tracks are formed by picking up hits based on the extrapolated seed tracks at the outer layer of SCT by using Kalman fitter smoother [78]. At this stage, candidate tracks are selected by their scores which are decided by the so-called *track scoring* strategy [79] to reject fake tracks. In general, the hits associated with a track gives a better score to favor fully reconstructed tracks rather than short track segments. This scoring process also takes into account the precision of the hit position, the inactive materials on tracks and hits shared with other candidate tracks etc.. Selected tracks are extended further through TRT and associated with its drift circles. Using all associated

silicon hits and drift circles, a re-fitting is performed to obtain a charged track.

In the outside-in algorithm, the seed track search is performed in TRT. The seed track is formed in the r-ϕ plane in the barrel region and the z-θ plane in the end-cap region by finding continuous hits because TRT does not provide any information of hit positions along the TRT straw direction. Commonly used Hough transformation [80] is utilized with the center of hit straws as the input to find a compatible set of hits in TRT. Using the set of drift circles found by the Hough transformation, the track segment is reconstructed with the Kalman filter-smoothing within the TRT volume. When track segments overlapped with the track already reconstructed with the inside-out algorithm, such track segment is removed to save CPU time. The remaining TRT track segments are followed back into the silicon tracker volume, which allows to find short track segments in the silicon detector that are not reconstructed with the first inside-out reconstruction stage.

Within this charged track reconstruction, tracks with transverse momentum greater than 400 MeV are stored as a reconstructed track and used as an input for the other physics object reconstruction.

5.2 Interaction vertex

In this analysis two types of vertex are considered, the vertices from pp interaction and secondary vertices. Secondary vertices are made by decays of long-lived hadrons, such as K_S, Λ and b-hadron, and particle interactions in materials like photon conversions inside the inner tracker volume.

The reconstruction of the vertex from pp interactions begins with searching for a position in z direction on the beam axis where the closest approaches of tracks to the center of the beam spot are most densely populated. The vertex is formed by the adaptive vertex fitting [81] which takes the position determined above and tracks around that position as the input. The association of the track to the reconstructed vertex is computed by checking if the closest approach of each track is compatible within 7 σ which is the error of the vertex position. This procedure is repeated until no non-associated tracks to the vertices are left in the event or no additional vertex can be found. All reconstructed vertices are stored as vertex candidates in an event. Vertices by pp interactions are further categorized into two groups, the primary vertex (PV) and so-called pileup vertices. Both are similarly reconstructed, but the vertex that has the largest sum of squared P_{T} of the associated tracks is chosen as PV to select hard scattered pp interaction.

The secondary vertex finding begins with selecting tracks based on impact parameter significance which is the impact parameter divided by its error. All pairs of tracks whose impact parameter significance is larger than 3 are selected as two-track vertex when they intersect with each other within the uncertainty. The secondary vertex is reconstructed by fitting with all the tracks which are associated to two-track vertices. The successfully fitted vertex is stored as a secondary vertex and is used as input to some b-tagging algorithms.

5.3 Electron

Reconstruction

Electron reconstruction starts from searching for a seed cluster, 3×5 calorimeter cells in the η-ϕ plane in the middle layer of the EM calorimeter, with an transverse energy more than 2.5 GeV. The seed cluster is checked whether it matches to the track with the criteria below.

- $|\eta_{\text{track}} - \eta_{\text{cluster}}| < 0.05$
- $|\phi_{\text{track}} - \phi_{\text{cluster}}| < 0.1$ (0.05) for the case where track hits at the side which is located in the track bending direction (for the other side).

The seed cluster is considered as an electron candidate if there is at least one track matching to the cluster. In case there are two or more tracks matched to the cluster, the one with the smallest $\Delta R_{\text{track-cluster}}$ is chosen as the matched track.

The electron energy is determined by taking into account the four different contributions, the measured energy deposit in the cluster, the estimated energy loss in the materials in front of the EM calorimeter, the estimated external energy deposit outside the cluster (lateral leakage) and behind the EM calorimeter (longitudinal leakage). The four terms are parametrized as functions of the energy deposit in the pre-sampler detector and the one in each sampling layer of the EM calorimeter. The four momentum of the electron is determined by taking the final EM cluster energy as its energy and the matched track direction at the vertex as its direction.

Selection

The reconstructed electron is further selected based on more than twenty discriminant variables categorized as follows.

- Energy leakage to the hadron calorimeter
- Energy deposit in the middle layer of the EM calorimeter
- Shower width in the strip layer of the EM calorimeter
- The associated track quality and the tighter track matching
- Information of particle identification from TRT
- Photon conversion veto

All the discriminants are intended to reject hadrons by requiring dense energy deposit in the EM calorimeter, and photons from photon conversion by selecting the associated track with good quality. We required electrons to pass the pre-defined criteria so-called `tight++` [82] which consists of the selections by the variables mentioned above. According to the study using the MC simulation, 78 % of the real electron passes the `tight++` criteria. The expected mis-identification probability to select hadrons as electron is about 1/50000.

For electrons,

- $E_{\text{T}} > 25$ GeV and
- $|\eta| < 2.47$ excluding $1.37 < |\eta| < 1.52$

are required to ensure that we use electrons which are triggered at the fully efficient region in terms of E_{T}, and to guarantee electrons to be within the tracker acceptance and remove electrons in the barrel-end-cap transition region.

Because the electrons coming from W/Z boson decays are well separated from other particles, the isolation requirements are applied. The isolation discriminants are computed from the scalar sum of the momenta of tracks within $\Delta R = 0.3$, and the sum of the energy deposit in the calorimeter cells within $\Delta R = 0.2$. The cut value is adjusted based on electron energy, pseudorapidity, and the number of pileup vertices so that the selection efficiency against electrons from the W/Z boson is 90 % for each requirement.

In addition to the requirements above, electrons hitting the EM calorimeter with readout problems are removed from the analysis.

Performance

- Trigger/Reconstruction/Identification/Isolation efficiency

Efficiency of the electron selection is measured with a 'tag and probe' method. The key point of the method is to collect pure unbiased electron sample, so-called 'probe', by requiring so-called 'tag' selections. For example, let us think about measuring the electron reconstruction efficiency with $Z \to ee$ events, as shown in Figure 5.1. We select one electron with rather

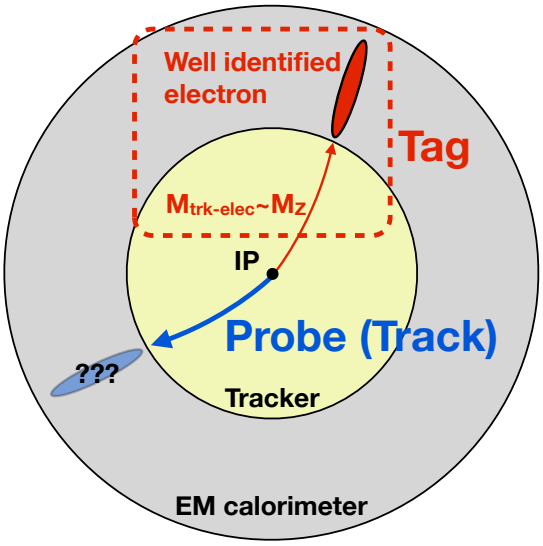


Figure 5.1: The idea of the tag and probe method using Z bosons

tight requirement, called tag electron, and another isolated track as the probe. After requiring the invariant mass reconstructed from the tag electron and the probe track to be typically 80 GeV $< M_{ee} <$ 100 GeV, the probability of the track to be real electron becomes more than 95 %. In this way, it is possible to have pure unbiased electron sample. Any efficiency can be measured by checking if the probe track satisfies the requirement. The similar idea is used for W boson events by taking the neutrino signature as the tag selection.

The electron efficiency is divided into four categories, the trigger, the reconstruction, the identification and the isolation efficiency, where the identification efficiency refers to the selection efficiency by the `tight++` criteria. Each efficiency has some dependences on the electron kinematics and the number of pileup vertices. Therefore, we measured the efficiency as functions of E_{T}, η, or the number of vertex candidates. Table 5.1 summarizes the tag and probe sample, the used parametrization, the mean efficiency and the size of the uncertainty for each measurement.

Table 5.1: Summary of the electron efficiency.

	Calib. Sample	Parametrization	Mean efficiency	Typical uncertainty
Trigger	$Z \to ee$	η, E_{T}	97 %	0.1 %
Reconstruction	$Z \to ee$	η	98 %	1 %
Identification	$Z \to ee$, $W \to e\nu$	η, E_{T}	78 %	2 %
Isolation	$Z \to ee$	#vertices	90 %	3 %

Figures 5.2 and 5.3 show the examples of the measured trigger efficiency and the electron

selection efficiency which is the combined efficiency of the reconstruction, identification and isolation. In addition, we derive the scale factor between data and MC defined as $\mathrm{SF} = \varepsilon_{\mathrm{data}}/\varepsilon_{\mathrm{MC}}$ where the efficiency in data (MC) is denoted as $\varepsilon_{\mathrm{data}}$ ($\varepsilon_{\mathrm{MC}}$). The trigger efficiency in the barrel region, $|\eta| < 1.47$, is modeled well in MC, while the one in the forward region is not. The selection efficiency is systematically higher in data. This mis-modeling is investigated and known to be the effect of the shower shape and the soft-scattered particle mis-modelings, especially in the forward region.

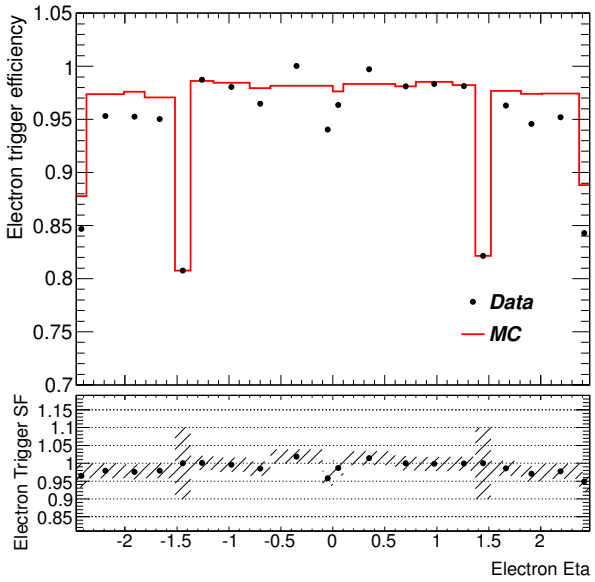


Figure 5.2: Example of the electron trigger efficiency and its scale factor as a function of the electron η. The shaded band in the bottom plot indicates the uncertainty. This efficiency is evaluated at the electron transverse energy of 50 GeV.

The systematic uncertainty for each measurement is evaluated for various sources. In total, the typical size of the uncertainty ranges 0.1-3 % as shown in Table 5.1. Here, the details of the possible largest uncertainty source, the identification and isolation efficiency, are presented below. Full description of the electron efficiency measurement can be found in the reference [83].

The uncertainty of the identification efficiency is dominated by the bias of the tag selection. We performed the MC closure test to check the size of the bias by varying the tag selection criteria. The estimated efficiency in each pseudorapidity bin is compared with the true efficiency. The largest difference found in any pseudorapidity bins is taken as the systematic uncertainty. The background contamination estimated by the template fitting is subtracted for the efficiency calculation. This is also considered as the possible uncertainty source. The background is re-estimated by a different model, and the difference from the nominal result is considered as the systematic uncertainty. Including these uncertainties, the size of the uncertainty is estimated to be about 2 %.

The uncertainty of the isolation efficiency mainly comes from the dependence on the pileup effect. The spread of measured efficiency as a function of the reconstructed vertices are about 2 %, therefore the half of the spread, 1 %, is assigned as the systematic uncertainty by the pileup effect. The possible difference between Z and $t\bar{t}$ samples is also investigated. The difference of the isolation efficiency between the two samples is estimated by using MC true information, and is found to be 2 %. The other possible systematics sources are estimated with the similar

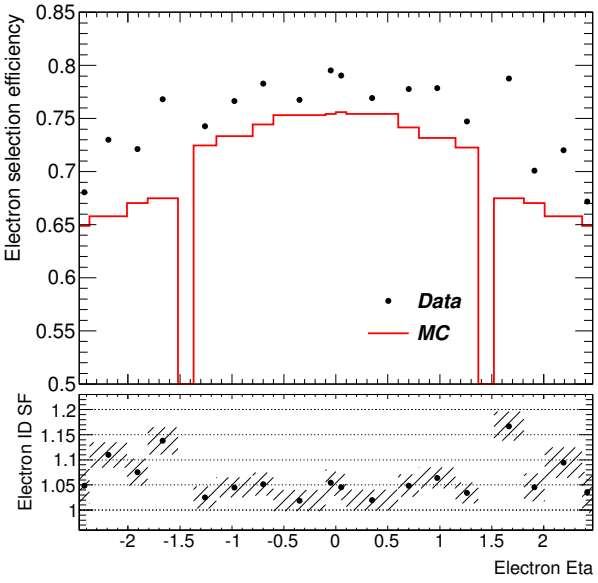


Figure 5.3: Example of the electron selection efficiency and its scale factor. Selection efficiency includes the reconstruction, the `tight++` selection and the isolation requirement. The shaded band in the bottom plot indicates the uncertainty. This efficiency is evaluated at the electron transverse energy of 50 GeV.

method as the identification efficiency. The estimated uncertainties are added in quadrature, which is about 3 % in total.

- Energy scale and resolution

Electron energy scales are calibrated with the events of $Z \to ee$, $J/\psi \to ee$ and $W \to e\nu$. Electron energy scale in data is corrected as a function of η, ϕ and E_T to reproduce the well-known mass of Z, W and J/ψ. The systematic uncertainty of these corrections are about $\pm$1-1.5 %. This is dominated by the uncertainty to the knowledge of the detector material. The size of the effect is evaluated by the MC simulation with modified amount of materials by approximately 1 %. The other possible uncertainty coming from the bias from the Z, W and J/ψ event selection, the pileup modeling etc., is evaluated and is found to be almost negligible, about 0.1 % level.

The energy resolution is evaluated by using $Z \to ee$ events. The electron energy in MC is smeared by $\sim$1 % to match the di-electron mass distribution obtained in data. We think that the source of this resolution mis-modeling comes from the inner detector mis-alignment, and the shower shape mis-modeling in the EM calorimeter.

5.4 Muon

Reconstruction

Muons are first reconstructed with information of hits in the muon spectrometers. A global pattern recognition based on two independent Hough transformations [80] in the bending and the non-bending planes is performed to find muon track candidates. Track segments defined as

the coincidence of hits at both the precision and the trigger chambers in each muon station are used as the inputs for this pattern recognition. The segment on the outermost station is used as a seed for the track fitting. If more than one track candidates are found for one seed segment, the one with the highest number of hits is chosen. In the case more than one track candidates have the same number of hits, the one with the smallest chi-square of the track fitting is treated as a muon candidate. The muon candidates are re-fitted with taking the full material effects into account. The candidates reconstructed at the muon spectrometers are required to match to the track reconstructed inside the inner tracker. Finally, a track fitting to all hits associated to the muon candidate including the matched track reconstructed at the inner tracker is performed. This final muon candidate is stored as the reconstructed muon.

Selection

To select muons, the following selection criteria are imposed.

- The track is within the detector acceptance $|\eta| < 2.5$.
- $P_{\mathrm{T}} > 20$ GeV to guarantee to be in the plateau for the muon trigger efficiency.
- Passing the hit requirements for the associated inner detector track.
- $E_{\mathrm{T}}^{\mathrm{cone20}} < 4.0$ GeV, where $E_{\mathrm{T}}^{\mathrm{cone20}}$ is defined as the energy sum in the calorimeter cell around the extrapolated track within the cone with the radius of $\Delta R = 0.2$.
- $P_{\mathrm{T}}^{\mathrm{cone30}} < 2.5$ GeV, where $P_{\mathrm{T}}^{\mathrm{cone30}}$ is defined as the scalar sum of momentum of tracks around the muon candidate track within the cone with the radius of $\Delta R = 0.3$.
- Overlap removal between a jet and a muon: $\Delta R_{\mu\text{-jet}} > 0.4$, where only jets which come from PV with $P_{\mathrm{T}} > 25$ GeV are considered. The exact requirement for a jet to originate from PV will be described in Section 5.5.

Performance

- Reconstruction/Isolation/Trigger efficiency

The muon selection efficiency is measured with the 'tag and probe' method using $Z \to \mu\mu$ events as for the electron efficiency measurement with $Z \to ee$. The reconstruction efficiency is measured for each data taking period shown in Table 4.2 to take into account the period dependence due to the change of the instantaneous luminosity. The measured efficiency is parametrized as functions of the muon P_{T}, η and ϕ. The isolation efficiency, which is the selection efficiency against the $E_{\mathrm{T}}^{\mathrm{cone20}}$ and $P_{\mathrm{T}}^{\mathrm{cone30}}$ cut, is also measured for each data taking period, but without any parameterizations to the kinematics of muons. The combined efficiency of the reconstruction and isolation is shown in Figure 5.4 together with the scale factor between data and MC.

The systematic uncertainty is evaluated and also shown in the bottom part of the figure. The main uncertainty comes from the mis-understandings of the kinematics of probe muons and the background contamination in the probe sample. To estimate the size of the effect from them, the measurement is repeated by changing the probe selection criteria. The difference from the nominal result is taken as the systematic uncertainty, which is typically below 0.5 %.

The muon trigger efficiency on the η-ϕ plane is measured as shown in Figure 5.5. The efficiency in the barrel region, $|\eta| < 1.05$, is lower than the one in the end-cap region because of the absence of trigger chambers to put the support structure of the ATLAS detector. The

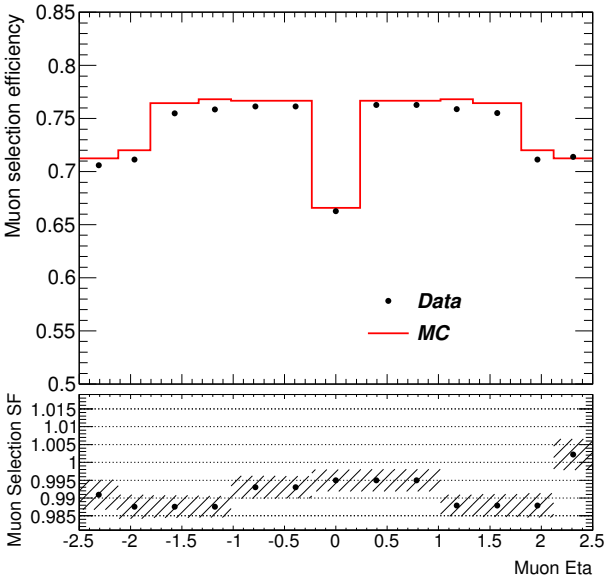


Figure 5.4: The efficiency and the scale factor of the muon selection. The selection efficiency contains reconstruction and isolation efficiency. The shaded band indicates the uncertainty. This efficiency is evaluated at the muon transverse energy of 50 GeV.

trigger efficiency and its scale factor between data and MC are shown in Figure 5.6. The scale factors for the barrel region are lower than unity in most of the bins. This is due to the timing issue of the trigger chambers or other hardware problems. This efficiency difference is corrected in MC by using the derived scale factors. The main source of the uncertainty is the tag and probe muon selection criteria as well as the one for the reconstruction, isolation efficiency measurement. The same approach with the measurement of muon reconstruction and isolation efficiency is adopted to estimate the uncertainty. In the end, the typical size of the uncertainty of the trigger efficiency measurement is found to be 1 %.

- Momentum scale and resolution

The muon momentum scale and the resolution are checked in data by using the Z boson decays. Figure 5.7 shows the di-muon mass distribution before correcting the muon momentum. The muon momentum in MC is scaled and smeared to reproduce the well known mass of the Z boson. The size of the correction for the momentum scale corresponds to below 0.1 % level. For the momentum resolution, the muon momentum is smeared by ∼10 % to match the distribution in data.

5.5 Jet

Partons produced in pp collisions become many hadrons after fragmentation and hadronization. A bunch of hadrons produced in this process is called a hadronic jet. Such hadrons make a hadronic shower in the calorimeter and deposit their energy in the calorimeter cells. Using the cluster of energy deposit in the calorimeter, we reconstruct a jet as the signal of the hard scattered quarks or gluons.

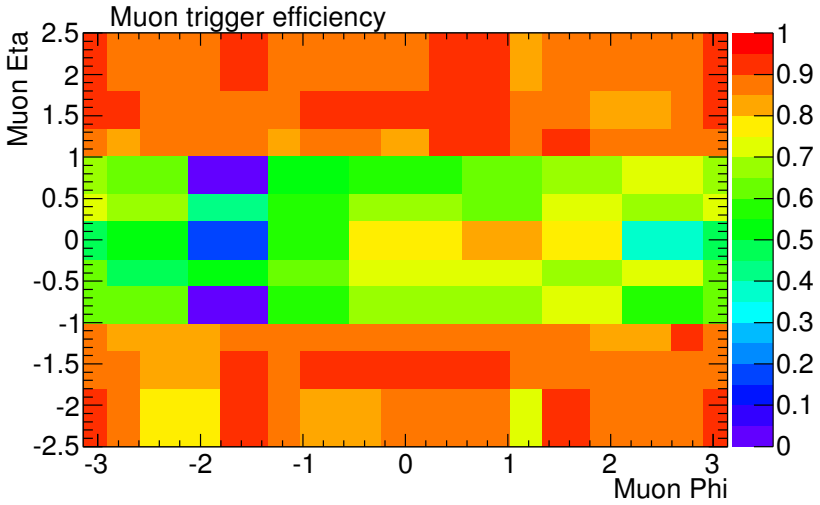


Figure 5.5: The muon trigger efficiency measured in data in the η-ϕ plane. The low efficiency region at $\phi \sim -1.8$ is due to the ATLAS support structure.

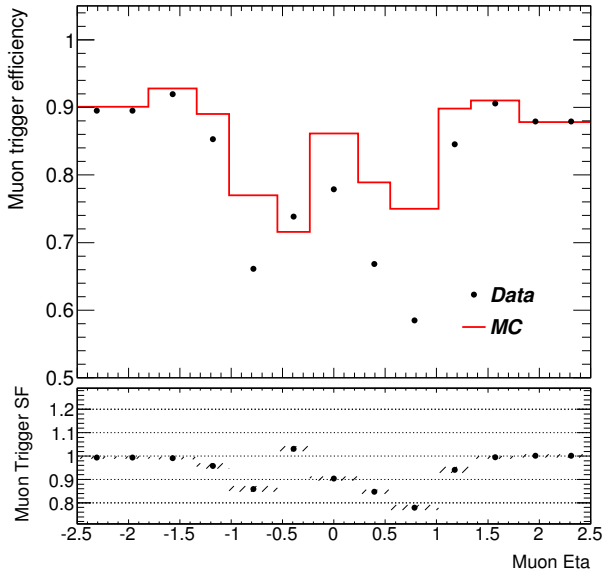


Figure 5.6: The muon trigger efficiency and the scale factors between data and MC. This efficiency is evaluated at the muon transverse energy of 50 GeV. The discrepancy between data and MC in the barrel region, $|\eta| < 1.05$, is caused by hardware problems in RPC.

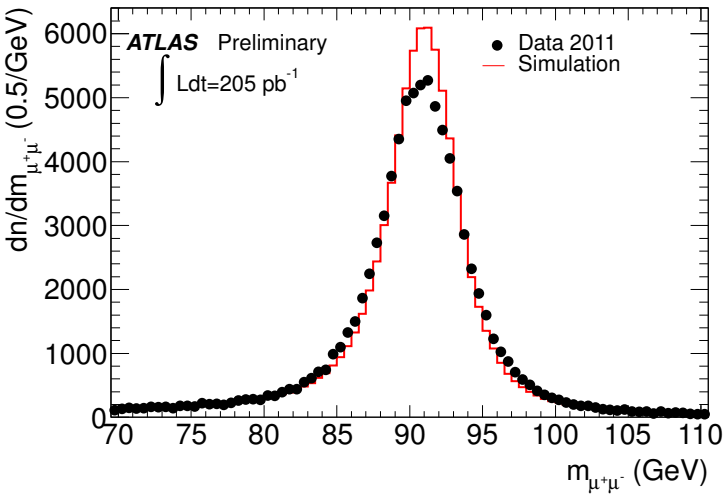


Figure 5.7: Invariant mass reconstructed from di-muon. For MC, the distribution is made before applying the muon momentum smearing.

Reconstruction

A cluster of the calorimeter cells with significant energy deposit is formed by 'three dimensional TopoCluster' algorithm [84]. In this algorithm, a seed cell is required to have more than 4 $\sigma_{\rm noise}$ of energy deposit where $\sigma_{\rm noise}$ is the width of the pedestal for each calorimeter cell. Typical size of $\sigma_{\rm noise}$ is about 40 MeV. The neighbor cell is the one surrounding the seed cells in the all directions, r, η, and ϕ, with more than 2 $\sigma_{\rm noise}$ of the energy deposit. The cells adjacent to the neighbor cell are defined as the other cell. The group of cells consisting of the seed associated with the neighbor and other cells is counted as a cluster. The cluster can be split or merged depending on the local maxima or minima within the clusters. Four momenta of each cell within the cluster are summed up with their energy weight, which is treated as the four momentum of the cluster. These clusters are used as the input to the jet reconstruction algorithm.

In general, the jet reconstruction algorithm is required to be infrared safe and collinear safe to compare experimental data with theoretical predictions. In other words, the algorithm should be insensitive to soft gluon radiation and splitting. Unlike most of cone-type algorithms, the algorithm called 'anti-k_t' is infrared and collinear safe [85]. On top of that, jets reconstructed by the anti-k_t algorithm have circular shapes as shown in Figure 5.8, in contrast to the SIScone algorithm. This makes the experimental treatment such as the jet energy calibration easy. With these reasons, we chose the anti-k_t algorithm for jet reconstruction.

The principle of the anti-k_t algorithm is merging clusters around the cluster which have largest energy in the events. The cluster which locates within a certain distance from the most energetic cluster is considered to be merged. This is the mechanism which gives more circular shape to energetic jets. The concrete procedure used in the anti-k_t algorithm is following. The anti-k_t algorithm first computes d_{ij} for all the combinations of i-th and j-th clusters. The d_{ij} is defined as

$$d_{ij} = \min(k_{t_i}^{-2}, k_{t_j}^{-2}) \frac{\Delta R_{ij}}{R}, \tag{5.1}$$

where k_t is the transverse momentum of the cluster. R is called distance parameter, and $R = 0.4$ is used in this analysis. ΔR_{ij} is the distance between the cluster i and j in the η-ϕ plane. The algorithm merges the clusters i' and j' where $d_{i'j'}$ is a minimum value among all d_{ij} and treated

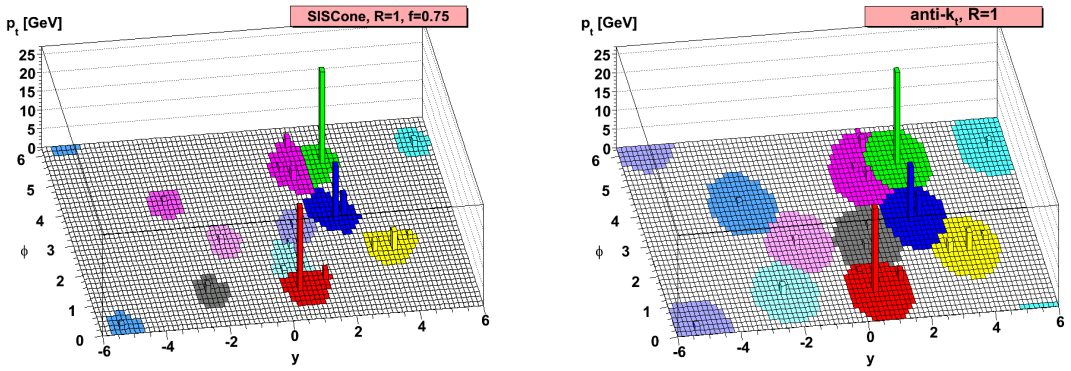


Figure 5.8: The jet shape in the y (rapidity)-ϕ plane for the SISCone (left) and the anti-k_t (right) algorithm [85]. SISCone is one of the cone-type algorithms and is shown to see the shape difference between the algorithms.

as a new cluster. The algorithm repeats this procedure until no cluster left. In parallel, d_{iB} which is defined as

$$d_{iB} = k_{t_i}^{-2} \tag{5.2}$$

is computed for each repetitive process. Once d_{iB} is smaller than all the d_{ij}, the cluster i is regarded as a jet and removed from the list of clusters. The algorithm performes this procedure until no cluster left.

Jet energy calibration

After jets are reconstructed, the energy of each jet is calibrated with a robust electromagnetic (EM) scale which is designed to measure the energy deposited by EM showers. The EM scale has been obtained by the electron test-beam before installing the calorimeter into the ATLAS experimental cavern. It provides a good estimate on the energy for electrons and photons, but does not correct for the effects from

- difference of the detector response between EM and hadron showers,
- energy loss at the inactive materials in the calorimeters, and
- energy deposit by particle from pileup pp interactions.

To account for these effects, the jet energy is further calibrated to the hadronic energy scale (JES). The baseline JES is derived as a simple correction relating the calorimeter's response to the true jet energy using MC simulations.

We checked the validity of JES for data in 2011 by using the *in situ* method. Two types of precise measurements have been performed in the ATLAS experiment, the γ+jet and the Z+jet analysis. The idea is to utilize momentum conservation in the r-ϕ plane as shown in Figure 5.9. The precision of the momentum measurement of electron, muon and photon is much better than that of jets. Therefore we can use the momentum of photons and Z bosons reconstructed from decayed leptons as the reference to measure the momentum of jets. Measurements in both samples complement each other in terms of the covered jet P_{T} range.

Figures 5.10 and 5.11 show the result of the jet energy calibration obtained by the Z+jets and the γ+jets analysis, respectively. The energy scale is typically 2 % lower than the one expected in MC. To compensate for this difference, the jet energy in MC is corrected to match

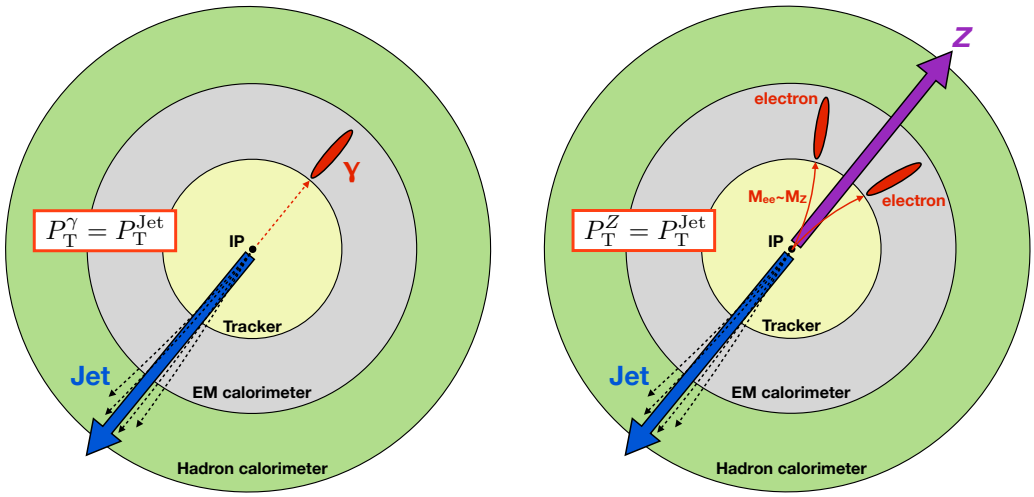


Figure 5.9: Images of the principle of the JES measurement in the γ+jets and the Z+jets analysis. Momentum in the transverse direction must be conserved.

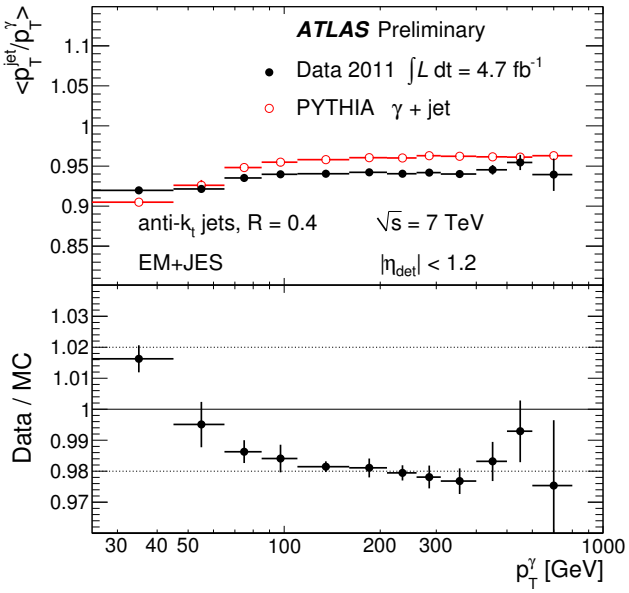


Figure 5.10: The mean P_T balance, P_T^{jet}/P_T^γ, as a function of the P_T of the reference photon measured in the γ+jets analysis. The bottom plot shows the data-to-MC ratio [86].

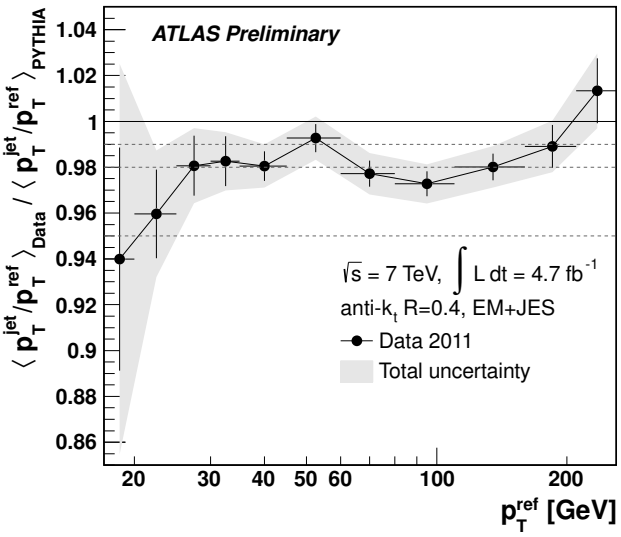


Figure 5.11: Data-to-MC ratio of the mean P_{T} balance as a function of the P_{T} of the Z boson measured in the Z+jets analysis. Dashed lines show the $-1\%, -2\%$ and -5% shifts [87].

the energy observed in data. Systematic uncertainties for JES are summarized in Figure 5.12 and 5.13. The main source of the systematic uncertainties in the low energy region, below $P_{\mathrm{T}} \sim 30$ GeV, is limited by the statistics of the Z events. Including this, the uncertainty is estimated to be approximately 2 % in total. For the high jet energy region, the main source of the systematic uncertainty comes from the photon and electron energy scale which would change the reference momentum. The uncertainty is estimated by repeating the analysis by varying photon or electron energy by $\pm 1\sigma$. The difference from the nominal energy scale is taken as the systematic uncertainty, which is about 1 %.

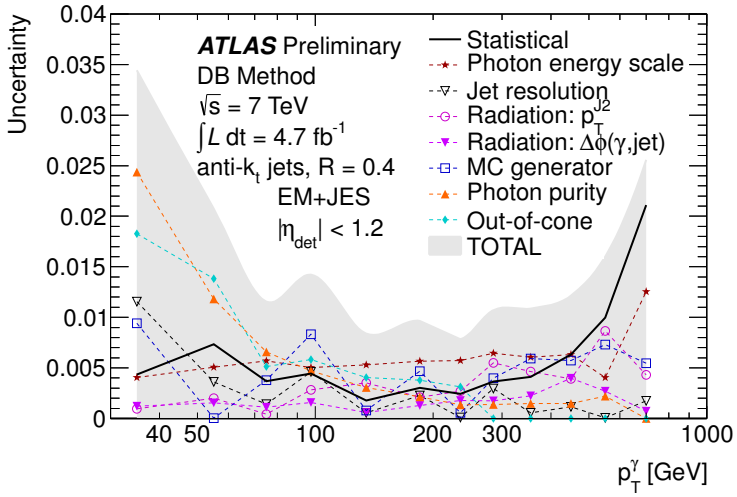


Figure 5.12: Summary of the uncertainty for JES measured in the γ+jets analysis [86]

The energy resolution in data is also measured with the similar method to measure JES. The width of the $P_{\mathrm{T}}^{jet}/P_{\mathrm{T}}^{\gamma,Z}$ distribution can be considered as the jet energy resolution. The resolution obtained with data is found to be consistent with the one in MC. No energy smearing against the jet energy in MC is applied.

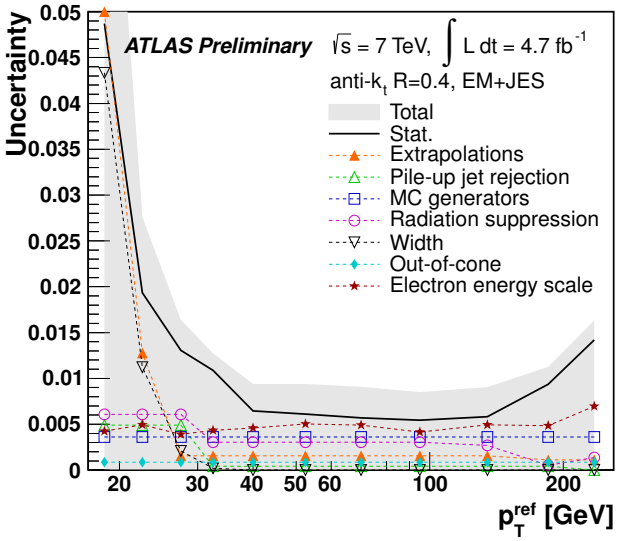


Figure 5.13: Summary of the uncertainty for JES measured in the Z+jets analysis [87]

Selection

The definition of selected jets used in this analysis is described in this section. From reconstructed jets, a jet which is matched to the selected electron within the radius $\Delta R = 0.4$ is removed. P_{T} of jets is required to be greater than 25 GeV. The absolute value of the pseudo-rapidity should be less than 2.5. For each jet, the jet vertex fraction (JVF) is computed as the parameter to judge if the jet is associated to PV. The JVF for a given $\mathrm{Jet_i}$ is defined as

$$\mathrm{JVF(Jet_i)} = \frac{\Sigma_k P_{\mathrm{T}}(\mathrm{Trk}_k^{\mathrm{Jet}_i}, \mathrm{PV})}{\Sigma_n \Sigma_l P_{\mathrm{T}}(\mathrm{Trk}_l^{\mathrm{Jet}_i}, \mathrm{Vtx_n})}, \tag{5.3}$$

where $P_{\mathrm{T}}(\mathrm{Trk}^{\mathrm{Jet_i}}, \mathrm{Vtx_n})$ is the momentum of the track which is matched to the Jet_i within the radius $\Delta R = 0.4$ and is associated to the n-th vertex. For a jet which falls outside of the fiducial region of the inner detector and a jet with no associated tracks, JVF $= -1$ is assigned. Figure 5.14 illustrates the event topology of interest described by Equation (5.3) for example. |JVF| is required to be greater than 0.75.

Reconstruction/JVF selection efficiency

The jet reconstruction efficiency is measured by using track-jets which are jets reconstructed from charged tracks [88]. The reconstruction efficiency is defined as the ratio of the number of the reconstructed calorimeter-based jets to the track-jets. The observed reconstruction efficiency in data for a jet with high P_{T} is almost consistent with MC. But a small inefficiency, by $\sim$1 %, for jets below 30 GeV is observed in data. This is considered as a systematic uncertainty source.

The selection efficiency based on the $|\mathrm{JVF}| > 0.75$ requirement is measured using the $Z \to ee/\mu\mu$ samples. To obtain the efficiency for both hard-scattered jets and jets from the pile-up vertices called 'pile-up jets', the Z boson samples are divided into two categories based on P_{T} of the Z boson which is measured by the ee or $\mu\mu$ system. When the Z boson is boosted in the transverse direction, there should be a hard scattered jet in the opposite direction of the Z boson to conserve the transverse momentum, and *vice versa*. Therefore, to collect the hard-scattered jets, the Z boson is required to have P_{T} greater than 30 GeV. In addition, the

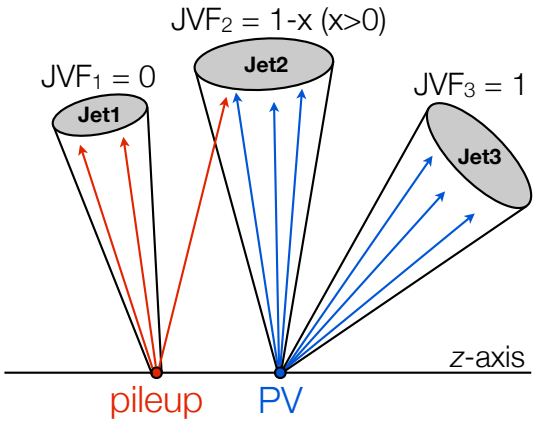


Figure 5.14: The schematic image of JVF. Jet1 is a jet originating from a pileup vertex. Jet2 and Jet3 come from PV. Tracks from PV (the pileup vertex) are indicated in the blue (red) lines. JVF of Jet1 (JVF_1) is zero because there is no matched tracks associated to PV. For Jet3, JVF equals to unity because all the associated tracks comes from PV. On the other hand, Jet2 originally coming from PV have an associated track from the pileup vertex. Therefore, JVF_2 should be smaller than unity.

jet in this Z boson event is required to be back-to-back against the Z boson. This selection gives the sample of the hard-scattered jet with 2 % contamination of pile-up jets. On the other hand, to collect the pile-up jet sample, the Z boson is required to have P_{T} less than 10 GeV. The pile-up jet sample with 20 % contamination of hard-scattered jets can be obtained by this selection. Using these two samples, the JVF selection efficiency is measured and parametrized as a function of jet P_{T} as shown in Figure 5.15. A few percent higher efficiency than MC expectation is observed. To reproduce the efficiency observed in data, MC events are scaled with this scale factor. The uncertainty is evaluated by changing the reference jet selection for both hard-scattered and pile-up jets. The typical size of the uncertainty is around 0.5 %.

5.6 Missing transverse energy

Missing transverse energy ($E_{\mathrm{T}}^{\mathrm{miss}}$) is defined as the momentum imbalance on the plane transverse to the beam direction. Such an imbalance implies a presence of the undetected particles such as neutrinos or other unknown stable and weakly-interacting particles. The momentum imbalance is obtained from the negative vectorial sum of the momenta of all particles detected in the ATLAS detector. The procedure of the $E_{\mathrm{T}}^{\mathrm{miss}}$ reconstruction is summarized below and details can be found in [89].

$E_{\mathrm{T}}^{\mathrm{miss}}$ is calculated from the reconstructed electrons, jets, soft-jets, and muons. Here, the jets with the transverse momentum greater (less) than 20 GeV is categorized as 'jets' ('soft-jets'). The lower energy jets are treated separately to use the robust EM scale energy calibration instead of the EM+JES energy calibration as for the higher energy jets. The x (y) components of the vector sum for each component are denoted as $\Sigma E_{x(y)}^{e}$, $\Sigma E_{x(y)}^{\mathrm{jet}}$, $\Sigma E_{x(y)}^{\mathrm{softjet}}$, and $\Sigma E_{x(y)}^{\mu}$, respectively. To obtain $\Sigma E_{x(y)}^{e}$ and $\Sigma E_{x(y)}^{\mu}$, electrons and muons which are reconstructed as explained in Section 5.3 and 5.4 are used. Energy deposit in the calorimeter cells associated to electrons and muons is removed from the calculation for other terms. For $\Sigma E_{x(y)}^{\mathrm{jet}}$ and $\Sigma E_{x(y)}^{\mathrm{softjet}}$, the reconstructed jets as explained in Section 5.5 are used. In addition to these terms, the energy deposits which are not associated to any components above at the calorimeter is computed as

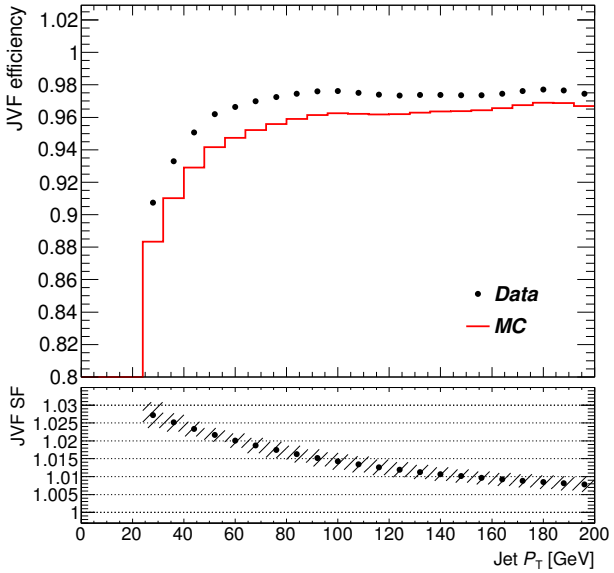


Figure 5.15: The efficiency of the selection based on the JVF requirement for the hard scattered jet as a function of jet P_{T} together with its scale factor $\varepsilon_{\mathrm{data}}/\varepsilon_{\mathrm{MC}}$. The shaded band in the bottom plot indicates the uncertainty.

the cellout term, $\Sigma E^{\mathrm{cellout}}_{x(y)}$, and used in the $E^{\mathrm{miss}}_{\mathrm{T}}$ calculation. The total missing momentum in the x (y) direction, $E^{\mathrm{miss}}_{x(y)}$, is computed as

$$E^{\mathrm{miss}}_{x(y)} = \Sigma E^{e}_{x(y)} + \Sigma E^{\mathrm{jet}}_{x(y)} + \Sigma E^{\mathrm{softjet}}_{x(y)} + \Sigma E^{\mu}_{x(y)} + \Sigma E^{\mathrm{cellout}}_{x(y)}. \tag{5.4}$$

In the end, $E^{\mathrm{miss}}_{\mathrm{T}}$ and its azimuthal coordinate (ϕ^{miss}) are calculated as the following.

$$E^{\mathrm{miss}}_{\mathrm{T}} = \sqrt{(E^{\mathrm{miss}}_{x})^2 + (E^{\mathrm{miss}}_{y})^2} \tag{5.5}$$

$$\phi^{\mathrm{miss}} = \arctan(E^{\mathrm{miss}}_{y}/E^{\mathrm{miss}}_{x}) \tag{5.6}$$

Performance

The resolution and scale of $E^{\mathrm{miss}}_{\mathrm{T}}$ are investigated. In principle, there is no real $E^{\mathrm{miss}}_{\mathrm{T}}$ in $Z \to \ell^+\ell^-$ events except the case where there are additional heavy flavor jets decaying semileptonically. Therefore, the measured $E^{\mathrm{miss}}_{\mathrm{T}}$ in such events is due to the mis-measurement and provides the clue of the $E^{\mathrm{miss}}_{\mathrm{T}}$ resolution. Figure 5.16 shows the width of $E^{\mathrm{miss}}_{\mathrm{T}}$ distribution in each bin for both x and y directions as a function of the scaler sum of the transverse energy of the reconstructed objects used in the $E^{\mathrm{miss}}_{\mathrm{T}}$ reconstruction, ΣE_{T}. The $E^{\mathrm{miss}}_{\mathrm{T}}$ resolution is affected much from the amount of the energy in the event because the $E^{\mathrm{miss}}_{\mathrm{T}}$ calculation depends basically on the deposit energy in calorimeters. Therefore, the resolution gets worse due to the fluctuation of the energy measurement when ΣE_{T} gets large. For the $t\bar{t}$ events with the typical ΣE_{T} of 100-200 GeV, the resolution of 5-10 GeV is achieved.

$E^{\mathrm{miss}}_{\mathrm{T}}$ is affected by the energy scale and resolution of the particles which are used to calculate $E^{\mathrm{miss}}_{\mathrm{T}}$. In order to estimate the systematic uncertainty by the energy scale of electron, muon

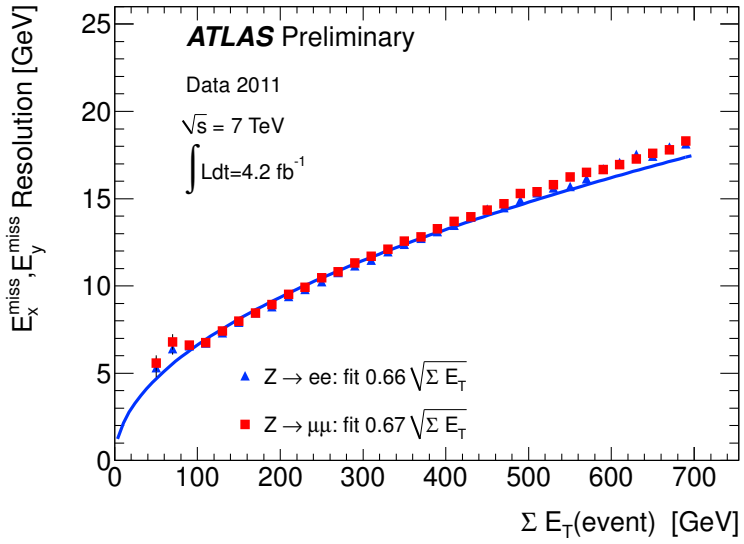


Figure 5.16: $E_{\mathrm{T}}^{\mathrm{miss}}$ resolution as a function of the total energy sum in the event [89].

and jet, $E_{\mathrm{T}}^{\mathrm{miss}}$ is recalculated with modifying the energy scale of each particle. The change of $E_{\mathrm{T}}^{\mathrm{miss}}$ by this recalculation is embedded in the energy scale uncertainties for each particles.

To estimate the other uncertainties which relate only to $E_{\mathrm{T}}^{\mathrm{miss}}$, the soft-jet and the cell-out term is investigated. The main uncertainty comes from the knowledge of the amount of dead materials and the hadron shower modeling used in MC. To estimate the effect of the dead materials, each term is recalculated by changing the amount of materials inside the inner tracker volume by 5 %. The difference from the nominal modeling is taken as the systematic uncertainty. To estimate the effect of the hadron shower modeling, the MC simulation with two different shower models, QGSP and FTFP_BERT, are used. The maximum difference from the nominal value is considered as the systematic uncertainty. Including these uncertainties, the size of the uncertainty for the soft-jet and cell-out term is estimated as approximately 13 % and 10 %, respectively.

In addition to the energy scale uncertainties for each term, the effect of the number of interactions per pp bunch crossing is investigated as the source of the change of $E_{\mathrm{T}}^{\mathrm{miss}}$. By using clean $Z \to \mu\mu$ events, the dependence of $E_{\mathrm{T}}^{\mathrm{miss}}$ to the number of interactions is checked. The maximum difference from the average value of 6.6 % is taken as the systematic uncertainty for the $E_{\mathrm{T}}^{\mathrm{miss}}$ energy scale by the pileup interaction effect.

5.7 Identification of the b-quark jet

To distinguish b-quark jets (b-jets) from light flavor jets which originate from u, d, s-quarks and gluons (l-jets or light-jets) and c-quark jets (c-jets), the characteristics that the b-hadron tends to decay after flying a few millimeters from the original pp interaction point are used. Decay products of the b-hadron are observed as displaced tracks from the interaction point. Existence of the secondary vertex inside a jet is also a signature of b-jets.

Various b-tagging algorithms have been exploited in the ATLAS experiment. We use the algorithm based on the neural network with three inputs that are the outputs from the impact parameter based algorithm, the secondary vertex based algorithm and the algorithm named JetFitter. JetFitter makes use of the topology of '$b \to c \to$ something' cascade decay. Each sub-algorithm is explained in the following.

Common track selection

The b-tagging starts with selecting well-measured tracks to reject fake tracks and tracks from long-lived particles other than b-hadron, K_S and Λ, and the interactions at materials such as photon conversions or hadronic interactions. To remove the effect of long-lived particles, tracks which form the secondary vertex whose mass, m_{vertex}, satisfies either $|m_{\text{vertex}} - m_{K_S}| < 15$ MeV or $|m_{\text{vertex}} - m_{\Lambda}| < 8$ MeV are removed. To remove tracks by the interaction with material, the tracks forming secondary vertex reconstructed at materials are removed. For the remaining tracks, further quality selections, P_{T} greater than 1 GeV and at least seven hits in the silicone detector including at least two hits in the pixel detector and a hit at the B-layer are required. For the selected tracks, the association to each jet is performed based on a cut on ΔR between the tracks and a given jet. The threshold of ΔR is varied depending on the P_{T} of the jet in order to take into account of the fact that jets with higher P_{T} are more collimated. The ΔR threshold is 0.45 at 20 GeV, while it is 0.25 for jets with P_{T} around 150 GeV.

Impact parameter based algorithm

The impact parameter based algorithm called the IP3D algorithm uses the impact parameters of the tracks associated to the jet of interest. The transverse impact parameter, d_0, is the distance of the closest approach of the track to PV in the r-ϕ plane. The longitudinal impact parameter, z_0, is defined as the distance in the z direction between PV and the closest approach on the z-θ plane. To increase the discriminating power, these impact parameters are transformed into so-called signed impact parameters based on the direction of the associated jet. Figure 5.17 shows the example of the determination of the sign of the impact parameters. Decay products of b-hadron should appear on the path of the jet direction. The positive sign is assigned if the track crosses the jet direction at the side which the considered jet exists, and negative otherwise. Figure 5.18 shows the signed d_0 for the b-, c- and light-jets obtained with MC. We can clearly

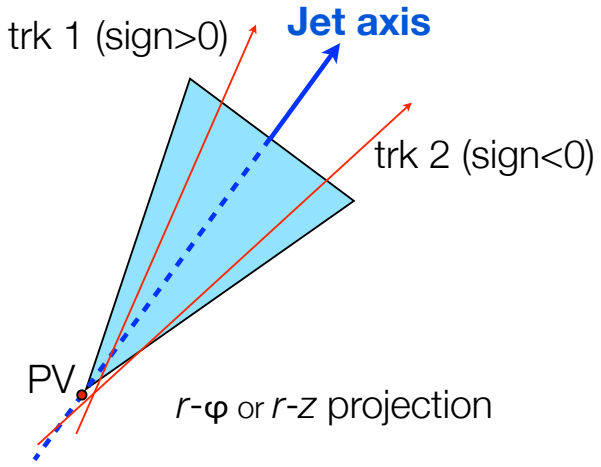


Figure 5.17: Schematics of the signed impact parameters (d_0 for the r-ϕ plane, z_0 for the r-z plane). The track labeled with 'trk 1' crosses the jet axis at the side which the jet is toward. In this case, the sign of the impact parameter is defined as positive. The track indicated as 'trk 2' traverses the jet axis at the opposite side. The sign of the impact parameter is negative in this case.

see the longer positive tail for b-jets. The signed d_0 and z_0 are used as the input to the likelihood with the b- and light-jet hypothesis based on MC to make the discriminant variable.

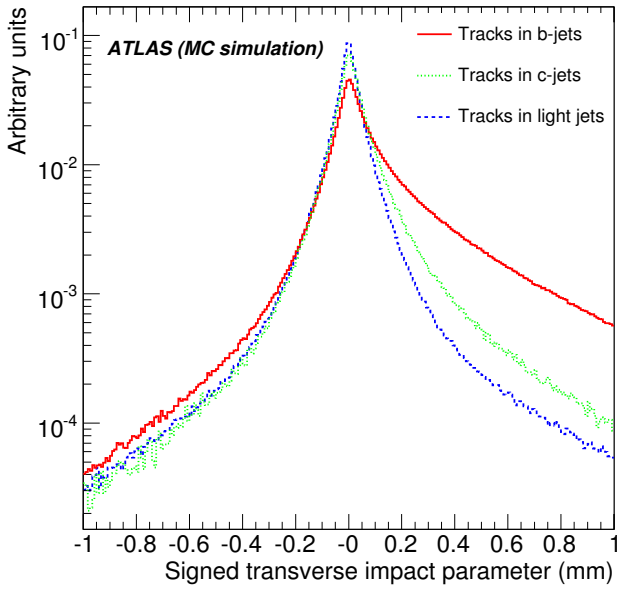


Figure 5.18: The normalized signed transverse impact parameter for b-, c- and light-jets obtained with MC [90]

Secondary vertex based algorithm

The secondary vertex based algorithm called SV1 is a very powerful method to discriminate between b-jets and light-jets because this explicitly requires a vertex formed by the decay product of the b-hadron or the subsequent c-hadron decay. The method of the secondary vertex reconstruction is already presented in Section 5.2. Once the secondary vertex is found in a jet, the likelihood value for each b-jet and light-jet hypothesis based on the following four input variables are computed:

- The three dimensional decay length significance, L/σ_L, where L and σ_L are defined as the distance between the primary vertex and the secondary vertex and its uncertainty,
- The invariant mass reconstructed from all tracks associated to the secondary vertex,
- The ratio of the sum of energy of the associated tracks to the one of all tracks inside the jet, and
- The number of two-track vertices.

The probability distribution functions for the likelihood calculation for each variable and for both hypotheses are obtained from MC. The likelihood ratio between the b-jet and the light-jet hypothesis is the final discriminant variable of SV1.

JetFitter algorithm

JetFitter is a newly developed algorithm in the ATLAS collaboration [91] based on the studies of the *ghost track algorithm* developed by the SLD Collaboration [92]. This is complementary to the secondary vertex based algorithm which cannot reconstruct the vertex in case only one track is generated by b- or c-hadron decays. JetFitter assumes that all tracks from the b-

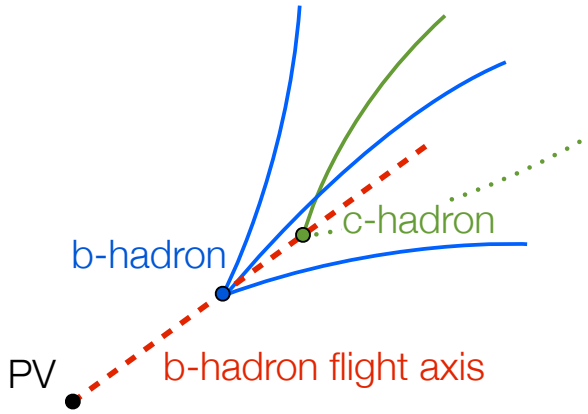


Figure 5.19: The image of the b- and c-hadron cascade decay

and c-hadron decays are produced on the b-hadron flight axis as shown in Figure 5.19. This assumption is confirmed to be valid because the average deviation of the c-hadron decay vertex from the b-hadron flight axis is small enough compared to the resolution of the vertex position measurement. The Kalman filter is used to find the flight axis. The discriminant variable of JetFitter is computed based on the likelihood ratio technique whose inputs are the topology information of the vertices found on the b-hadron flight axis such as the number of vertices with at least two tracks, the number of tracks at vertices, and the number of additional single tracks crossing on the b-hadron flight axis. The probability distribution functions for each variables are obtained by MC.

Combined algorithm

We combine the three discriminant variables of the IP3D, SV1 and JetFitter algorithms based on the neural network to compute a final discriminant variable called MV1. For this analysis, the threshold of MV1 to tag a jet as a b-jet is set so that the efficiency is 85 % for true b-jets in the top quark pair MC sample. The rejection factor against light-jets, inverse of the mis-tagging rate for light-jets, is around ten with this threshold.

Performance

The performance of the b-tagging algorithm can be separated into two, the b-tagging efficiency for real b-quark jets and the b-tagging fake rate for non-b-quark jets. Because of the low background environment in the dilepton final state, the cross section measurement is not so sensitive to the b-tagging fake rate. However, the b-tagging efficiency measurement becomes one of the main systematic sources. Therefore, the dedicated b-tagging efficiency measurement will be presented in Chapter 6. In this section, only the b-tagging fake rate measurement is presented.

- Fake rate for light-jets

To measure the fake rate against light-jets, we have to know the number of light-jets before and after requiring the b-tagging. In principle, it is difficult to collect the light-jet sample. Therefore, the ATLAS experiment employs two independent methods, the secondary vertex mass method and the negative tag method, to obtain the number of light-jets in a given jet sample. The details for both methods are described below.

The secondary vertex mass method uses the shape difference of the secondary vertex mass distribution among b-, c- and light-jets shown in Figure 5.20 to extract the number of light-jets in a given jet sample. The difference comes from the mass difference of the b-, c- and other

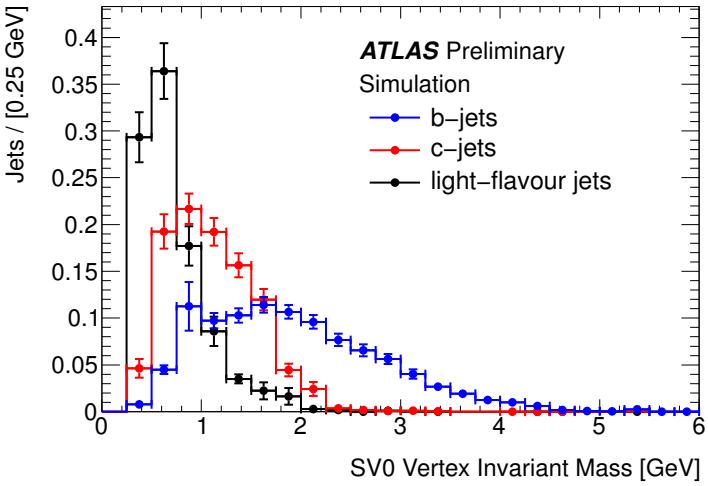


Figure 5.20: The normalized secondary vertex mass distribution for b-, c- and light-jets obtained with MC [93]

light quark hadrons, which are typically 5 GeV, 2 GeV and a few hundred MeV, respectively. The template fitting to the mass distribution for a given jet sample performed before and after applying the b-tagging to determine the number of light-jets (and b- and c-jets). The fake rate is derived from the ratio of the number of light-jets before and after the b-tagging.

The principle of the negative tag method is based on the fact that the mis-tagging of the light-jet is primarily caused by the displaced tracks due to the finite detector resolution. For example, the signed impact parameter distribution for light-jets has a certain width due to resolution as shown in Figure 5.17 even though the tracks in the light-jet come from PV. If we assume that the width comes from resolution, the signed impact parameter distribution of light-jets are expected to be symmetric. In general, the fake rate, the fraction of the number of jets satisfying $W < w$ where w is the discriminant variable for each jet and W is the threshold of b-tagging, is equivalent to the negative tagging rate defined as the fraction of the number of jets satisfying $-w < -W$. This method has a big advantage to avoid the difficulty to make pure light-jet sample. The negative tagging rates of b- and c-jets are the same as the one of the light-jet because the negative tails for b- and c-jets are also caused by the resolution effect. Therefore, one does not need to care about the contamination of heavy flavor jets. In reality, however, the shape of the discriminant variable is not perfectly symmetric, which introduces small correction.

Both measurements are performed by dividing a data sample into jet P_{T} and η bins. The measured fake rates are consistent between the two methods and with the one in MC. The main source of the systematic uncertainty is due to the trigger bias and the long-lived particle modeling. In these measurements, the single jet trigger is used to select the event. To estimate the trigger bias, the measurement is repeated for the jets with second leading P_{T}, because it is expected to have less bias from the trigger. The long-lived particle in the light-jet produces the real displaced tracks or secondary vertex, and causes the fake rate mis-modeling. To put the conservative uncertainty for this source, the light-jets containing long-lived particles are removed from MC and then the fake rate measurement is repeated. For both uncertainty sources, the difference from the nominal analysis is taken as the systematic uncertainty. Including these

uncertainties, the size of the uncertainty ranges 10-14 %.

- Fake rate for c-jets

As same as light-jets, it is difficult to collect pure c-jets sample. Therefore, we have to estimate the number of c-jets before and after applying b-tagging in a given jet sample in some ways. To increase the purity of c-jets, we utilize the events with the D^{*+} meson decaying into $D^0(\rightarrow K^-\pi^+)\pi^+$. Using the jet containing D^{*+} which represents the c-quark jets, the fake rate against c-jets is measured by taking the ratio between the number of jets before and after applying b-tagging.

To select D^{*+}, the D^0 candidate is selected first by reconstructing its mass from the oppositely charged tracks with assigning the kaon mass to the negative charged track and the pion mass to the positive one. We consider the two tracks as the D^0 candidate when $|m_{\text{tracks}} - m_{D^0}| < 40$ MeV is satisfied where m_{D^0} is the mass of D^0. Following this, the additional π^+ which emerges from the point compatible to the D^{*+} decay vertex is searched for. The event with such π^+ is used for the measurement. Figure 5.21 shows the difference of the mass reconstructed with $K^-\pi^+\pi^+$ and the one with $K^-\pi^+$. When D^{*+} is successfully reconstructed

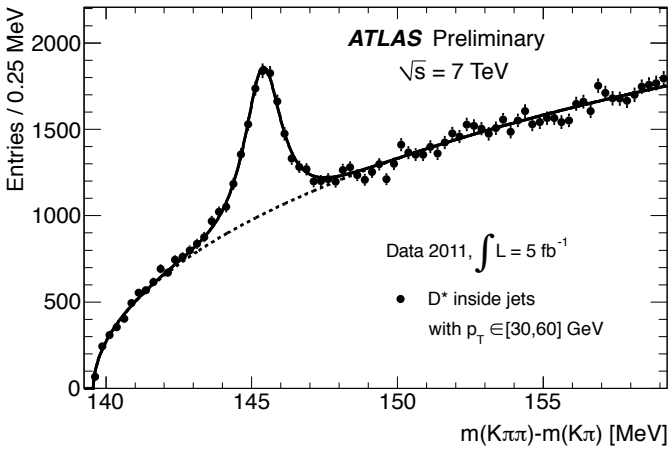


Figure 5.21: The distribution of the difference of the mass reconstructed by $K^-\pi^+\pi^+$ and by $K^-\pi^+$ [94]

by $K^-\pi^+\pi^+$, the mass difference becomes about 145.4 MeV ($= m_{D^{*+}} - m_{D^0}$). The clear mass peak by D^{*+} can be seen in the figure. Subtracting the background by the side-band fitting, we can obtain the number of c-jets in a given jet sample before and after applying b-tagging. The fake rate for the c-jet is derived from these numbers.

The measured c-tag efficiency is consistent with the one in MC. The main systematic source is the method to extrapolate the efficiency measured with D^{*+} to the inclusive c-jets. It is found that the track multiplicity and the mis-modeling of the charm-baryon fraction in the fragmentation process affects the result. The size of the uncertainty is evaluated by taking the difference from the nominal analysis and the one obtained with MC with the modified charm-baryon fraction. Including these uncertainties, the uncertainty is estimated approximately to be 10-20 %.

Chapter 6

b-tagging efficiency

It is very important to understand the signal acceptance since the uncertainty of the acceptance directly affects the precision of the $\sigma_{t\bar{t}}$ measurement in this analysis, and is the dominant uncertainty source. In our previous analysis which has been performed with the data collected in 2010 and the beginning of 2011 with the ATLAS experiment [95, 96], it is found that one of the main systematic uncertainty sources is related to the b-tagging efficiency measurement. The ATLAS experiment performs the b-tagging efficiency measurement by using the jet sample containing a muon [97]. We perform the b-tagging efficiency measurement with completely different method to achieve higher precision of the $\sigma_{t\bar{t}}$ measurement. In this chapter, the details of the estimate of b-tagging efficiency is described.

6.1 Control sample of the b-quark jets

The b-tagging efficiency, ε_b, is defined as

$$\varepsilon_b = \frac{(\text{the number of } b\text{-tagged jets})}{(\text{the number of } b\text{-jets})}. \tag{6.1}$$

Getting the numerator is obvious, just counting the number of jets which pass the b-tagging criteria in a given jet sample. However getting the denominator is not trivial because it is difficult to define a high purity b-jet control sample. The $t\bar{t}$ events can be the good candidates to collect b-jets with high purity because the top quark decays into a b-quark and a W boson with almost 100 % of the branching ratio. We use the $t\bar{t}$ events with the single lepton channel for the ε_b measurement instead of the dilepton channel which is used to measure $\sigma_{t\bar{t}}$ in the main analysis. This has the advantage that one does not need to consider the event overlap with the signal for the $\sigma_{t\bar{t}}$ measurement, and to correct the kinematic dependences of the b-tagging because the topology of b-jets does not depend on the decay mode of W bosons from the top quark. This is another advantage of this method over the ATLAS measurement of ε_b with the samples of jets with associated muon where the kinematic dependence meeds to be explicitly corrected.

Due to the difficulty of the precise tau identification, two final states, the electron + jets (e+jets) and the muon + jets (μ+jets) are considered. Electrons and muons which come from tau decays are implicitly included.

6.2 Tag counting method

There are several options to measure ε_b using the single lepton final state of the $t\bar{t}$ events. The technique called the tag counting method is used here.

To explain the idea to measure ε_b with the tag counting method, let's assume an extremely simple case in the dilepton final state, instead of the lepton+jets, of the $t\bar{t}$ events where there are only two b-jets and no other jets. Let's also assume that there are no background processes, the detector acceptance and the efficiency of the trigger, the object and the event reconstruction are 100 %. In this condition, the number of events with n b-tagged jets, $\langle N_n \rangle$, is written as

$$\langle N_n \rangle \quad = \quad \sigma_{t\bar{t}} \cdot \mathcal{L} \cdot BR(t\bar{t} \to bl\nu bl\nu) \times {}_2C_n \varepsilon_b^n (1-\varepsilon_b)^{2-n}, \tag{6.2}$$

where $\mathcal{L}$ is the integrated luminosity used in the analysis, $BR(t\bar{t} \to bl\nu bl\nu)$ is the branching ratio of which both W bosons decay leptonically, ${}_nC_m = n!/m!(n-m)!$ is the number of combination to choose m out of n samples. In this condition, we can solve Equation (6.2) for two unknowns, $\sigma_{t\bar{t}}$ and ε_b, because we can obtain two equations by $\langle N_0 \rangle$ to $\langle N_2 \rangle$ observed in data and the relation of $\langle N_0 \rangle + \langle N_1 \rangle + \langle N_2 \rangle = \sigma_{t\bar{t}} \cdot \mathcal{L} \cdot BR$.

Now, let's go back to the realistic situation. There are four jets in the final state typically, plus additional jets arisen from ISR/FSR. There are some contributions from background. There are also some effects of the detector acceptance, the reconstruction efficiency and b-tagging fake contributions from c- and light-jets. Taking all of them into account, $\langle N_n \rangle$ can be denoted as

$$\langle N_n \rangle = \sum_{b,c,l} \left\{ \left[\sigma_{t\bar{t}} \cdot \mathcal{L} \cdot BR \cdot A_{t\bar{t}} \cdot F_{b,c,l}^{t\bar{t}} + N_{W+\text{jets}} \cdot F_{b,c,l}^{W+\text{jets}} + N_{\text{OtherBG}} \cdot F_{b,c,l}^{\text{OtherBG}} \right] \times \right.$$
$$\left. \sum_{b'+c'+l'=n} {}_bC_{b'} \varepsilon_b^{b'} (1-\varepsilon_b)^{b-b'} \cdot {}_cC_{c'} \varepsilon_c^{c'} (1-\varepsilon_c)^{c-c'} \cdot {}_lC_{l'} \varepsilon_l^{l'} (1-\varepsilon_l)^{l-l'} \right\} \tag{6.3}$$

where BR is the branching ratio to the e+jets or μ+jets final state, $A_{t\bar{t}}$ is the acceptance of $t\bar{t}$ events, $N_{W+\text{jets}}$ is the number of W+jets events, N_{OtherBG} is the number of backgrounds except W+jets, ε_c and ε_l are the b-tagging efficiency to c-jets and light-jets. $F_{b,c,l}^{t\bar{t}}$, $F_{b,c,l}^{W+\text{jets}}$ and $F_{b,c,l}^{\text{OtherBG}}$ are the flavor fraction to get how many b-, c- and light-jets exist in the final state of $t\bar{t}$, W+jets and other background processes, respectively, where b, c and l denote the numbers of b-, c- and light-jets, respectively. For instance, '$F_{202}^{t\bar{t}} = 0.25$' means that 25 % of the selected $t\bar{t}$ events have two b-jets, zero c-jet and two light-jets. The equation becomes much complicated, but it is still just the number of jets multiplied by the b-tagging efficiency. The W+jets events are treated separately since it is the dominant background. Including e+jets and μ+jets, there are more equations than unknowns by observing $\langle N_n \rangle$ in data, which leads that the equations are overconstrained. Due to the error of the measurement, the unique solution cannot be obtained. Therefore, Equation (6.3) is fitted by floating $\sigma_{t\bar{t}}$ and ε_b to extract them from data with the following likelihood function,

$$L = \prod \left(\text{Poisson} \left(N_n^{\text{obs}}, \langle N_n \rangle \right) \right), \tag{6.4}$$

where N_n^{obs} is the number of the observed events with n b-tagged jets, and Poisson(m',m) is the probability that m' events are observed while m events are expected to observe. In this analysis, the events with zero b-tagged jets are omitted from the calculation because such events are dominated by the W+jets events. The variables in Equation (6.3) other than $\sigma_{t\bar{t}}$ and ε_b are treated as the input values for the fitting. $\mathcal{L}$ is obtained by the luminosity measurement described in Section 4.1.1. BR is obtained from the PDG value. The $\varepsilon_{c,l}$ measured with collision data, which is described in Section 5.7, are used. The details of the determination of $A_{t\bar{t}}$, $N_{W+\text{jets}}$, N_{OtherBG}, $F_{b,c,l}^{t\bar{t}}$, $F_{b,c,l}^{W+\text{jets}}$ and $F_{b,c,l}^{\text{OtherBG}}$ will be described in Section 6.4 through 6.8 after presenting the event selection for this measurement in Section 6.3.

6.3 Event selection

In this section, the event selection to enhance the single lepton final state of $t\bar{t}$ is described. First of all, for both data and MC events the electron trigger is required for the e+jets channel, and the muon trigger for the μ+jets channel. After the trigger selection, the following event quality selections are applied.

- To guarantee a well reconstructed primary vertex, the PV candidate must have at least five associated tracks with P_{T} greater than 400 MeV.
- The events with noise bursts in the LAr EM calorimeter are removed.
- We define the `LooseBad` quality jets which does not have an in-time real energy deposit. Such jets arise from the hardware problems such as the noise from the readout electronics, the bad LHC beam conditions and the cosmic-ray showers. The events with `LooseBad` jets with $P_{\mathrm{T}} > 20$ GeV are removed. This removal process does not consider jets which are treated as the electron candidates.

After the event quality cuts above, the event is required to have exactly one reconstructed electron (muon) in the e+jets (μ+jets) channel. This lepton has to point to the same direction to the EF trigger object within $\Delta R < 0.15$ to guarantee that the event of interest is triggered by the selected lepton. The W+jets and the QCD multi-jets production are the dominant background. To suppress them, we require the events to satisfy the following requirement.

- In the e+jets channel, $E_{\mathrm{T}}^{\mathrm{miss}} > 30$ GeV and $m_{\mathrm{T}}(W) > 30$ GeV,
- In the μ+jets channel, $E_{\mathrm{T}}^{\mathrm{miss}} > 20$ GeV and $E_{\mathrm{T}}^{\mathrm{miss}} + m_{\mathrm{T}}(W) > 60$ GeV,
- To suppress W+jets, at least four selected jets exist.

Here, $m_{\mathrm{T}}(W)$, so-called W transverse mass, is defined as $\sqrt{2p_{\mathrm{T}}^{\ell}E_{\mathrm{T}}^{\mathrm{miss}}(1-\cos\Delta\Phi)}$, where $\Delta\Phi$ is the opening angle between $E_{\mathrm{T}}^{\mathrm{miss}}$ and the lepton in the r-ϕ plane, and p_{T}^{ℓ} is the transverse momentum of the lepton.

6.4 Estimate of the top quark pair acceptance

The acceptance is estimated using the MC sample described in Section 4.2.3. Some corrections are applied to the MC sample to reproduce the conditions of real data. In specific, the trigger efficiency for both electron and muon triggers, the energy scale, the energy resolution and the reconstruction efficiency of leptons, JES, the jet selection efficiency and the b-tagging fake rate for c- and light-jets are corrected. In addition, the number of superimposed pp interactions generated by Pythia in the MC samples is re-weighted to reproduce the observed one in data. The size of these correction for each source is typically below a few per cent. After all the corrections, the acceptance for the e+jets (μ+jets) channel is found to be 0.1262 (0.1997). The acceptance at each event selection step can be seen in Figure 6.1.

6.5 Estimate of backgrounds

To perform the tag counting method, one must determine the amount of backgrounds. Some backgrounds are estimated by using MC samples, and some by real data to reduce the uncertainty.

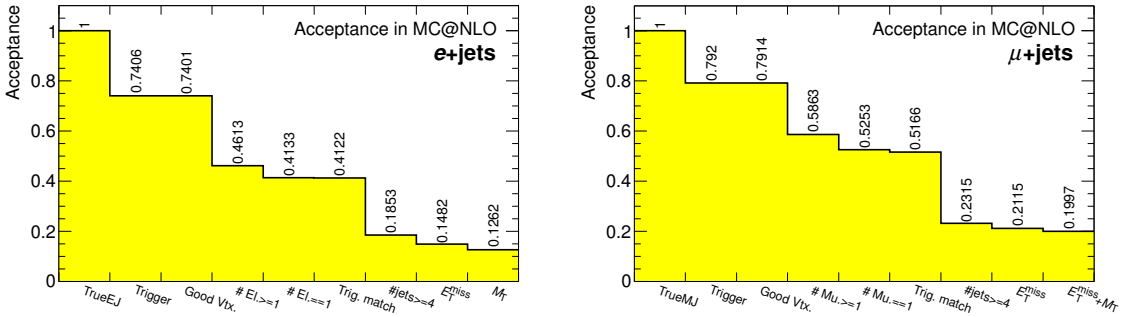


Figure 6.1: The acceptance of the e+jets channel (left) and the μ+jets channel (right) to the true e+jets and μ+jets events in the MC@NLO MC sample.

6.5.1 W+jets backgrounds

In principle, the amount of the W+jets events can be estimated from the predicted cross section, the measured integrated luminosity and the acceptance including the efficiency estimated by MC. However, the uncertainty of the cross section is very large, especially for the events with additional partons. For example, $\delta\sigma_W/\sigma_W$ is approximately 50 % for the events with more than four partons. In order to reduce the uncertainty, we exploit the fact that the theoretical uncertainty of the cross section ratio between W^+ and W^- is much smaller than the inclusive cross section.

In the proton-proton collider like LHC, the production cross sections of W^+ and W^- are not the same. For the W^+ production, the dominant parton level process is $u\bar{d} \to W^+$. The rate of this process depends on the PDFs of the u-quark and the $\bar{d}$-quark. On the other hand, for the W^- production, the dominant process is $d\bar{u} \to W^-$. This rate depends on the PDFs of the d-quark and the $\bar{u}$-quark. In the end, the W^+ production exceeds the W^- production at LHC because there are more valence u-quarks than the valence d-quarks in proton, while the $\bar{u}$- and the $\bar{d}$-quarks have the similar existence probability. The ratio between the production cross sections of $W^\pm$ boson, $r = \sigma_{W^+}/\sigma_{W^-}$, is precisely calculated in theory because the systematic uncertainties common to the $W^\pm$ production are cancelled out [98]. The main systematic uncertainty of r comes from PDFs. In total, r is calculated to $\sim$1 % precision.

By using r instead of the inclusive cross section, the amount of the W+jets events, $N_{W+\text{jets}}$, can be estimated as

$$N_{W+\text{jets}} = (N_{W^+} + N_{W^-}) = \left(\frac{r+1}{r-1}\right)\left(N_{W^+}^{\text{data}} - N_{W^-}^{\text{data}}\right), \tag{6.5}$$

where the variables with the superscript 'data' are observed values in data. Table 6.1 lists r_{MC} for each jet multiplicity. These numbers are obtained from the W+jets MC samples after applying all the event selections except the number of jets selection.

To obtain the term $(N_{W^+}^{\text{data}} - N_{W^-}^{\text{data}})$, we use the difference between the number of events with the positively charged and the negatively charged lepton, denoted as $(D^+ - D^-)$. The approximation of $(D^+ - D^-) \approx (N_{W^+} - N_{W^-})$ is valid even with the contamination of $t\bar{t}$, QCD multi-jets, Z+jets, because they are charge symmetric. The contributions of the small charge asymmetry from the single top production are subtracted by using the MC simulation.

The estimated yields of the W+jets events for the different jet multiplicity after all the event selections are summarized in Table 6.2. The uncertainties in this table includes the statistical and systematic uncertainties. The systematic uncertainties on r_{MC} due to the MC generator

Table 6.1: The ratio between the number of W^+ and W^- bosons $r_{\mathrm{MC}} = N_{W^+}/N_{W^-}$ as a function of jet multiplicity.

	r_{MC} (e+jets)	r_{MC} (μ+jets)
1 jet	1.415	1.484
2 jets	1.448	1.521
3 jets	1.513	1.569
$\geq$ 4 jets	1.646	1.661

choice, the charge mis-identification, JES and the PDF variations have been evaluated. When

Table 6.2: Measured numbers of W+jets events in the e+jets and the μ+jets channels after all the selection but the number of jets cut. The uncertainty includes both statistic and systematic.

	$N_{W+\mathrm{jets}}$ (e+jets)	$N_{W+\mathrm{jets}}$ (μ+jets)
1 jet	$(8.30 \pm 7.00) \times 10^6$	$(1.57 \pm 0.54) \times 10^7$
2 jets	$(1.00 \pm 0.64) \times 10^6$	$(2.08 \pm 1.67) \times 10^6$
3 jets	$(2.23 \pm 3.12) \times 10^5$	$(4.44 \pm 0.49) \times 10^5$
$\geq$ 4 jets	$(6.21 \pm 1.11) \times 10^4$	$(1.10 \pm 0.16) \times 10^5$

we show the distributions which includes the contribution from the W+jets in the following, the MC samples of the W+jets events are scaled to match these measured yields.

6.5.2 Fake lepton backgrounds

Even after all the event selection, there are events with mis-identified leptons that arise from several sources such as photon conversions, pion/kaon punch through, a lepton from heavy flavor quark decay. Here we call even true leptons as mis-identified leptons or fake leptons if they do not directly come from the W/Z boson decay, including the electron or the muon from the decay of tau which is the daughter particle of the W boson. Due to the extraordinary large cross section, QCD multi-jets events is the main source of the fake lepton for the single lepton final state. Fake lepton backgrounds must be estimated by the data-driven method because it is difficult to model the mechanism of the fake. The fake lepton contribution is estimated with so-called the matrix method explained in the following.

The matrix method is based on selecting the events with lepton which is selected by two criteria so-called 'loose' and 'tight'. The number of events which contains one loose lepton N^{loose} is written as

$$N^{\mathrm{loose}} = N^{\mathrm{loose}}_{\mathrm{real}} + N^{\mathrm{loose}}_{\mathrm{fake}}, \tag{6.6}$$

where $N^{\mathrm{loose}}_{\mathrm{real}}$ and $N^{\mathrm{loose}}_{\mathrm{fake}}$ are the numbers of events which have exactly one loose lepton originating from W/Z, called as a real lepton, and a fake lepton, respectively. Similarly, the number of events containing one tight lepton N^{tight} is written as

$$N^{\mathrm{tight}} = \varepsilon_{\mathrm{real}} N^{\mathrm{loose}}_{\mathrm{real}} + \varepsilon_{\mathrm{fake}} N^{\mathrm{loose}}_{\mathrm{fake}}, \tag{6.7}$$

where $\varepsilon_{\mathrm{real}}$ and $\varepsilon_{\mathrm{fake}}$ are the efficiency defined as

$$\varepsilon_{\mathrm{real}} = N^{\mathrm{tight}}_{\mathrm{real}}/N^{\mathrm{loose}}_{\mathrm{real}}, \quad \varepsilon_{\mathrm{fake}} = N^{\mathrm{tight}}_{\mathrm{fake}}/N^{\mathrm{loose}}_{\mathrm{fake}}, \tag{6.8}$$

where $N^{\text{tight}}_{\text{real}}$ and $N^{\text{tight}}_{\text{fake}}$ are the number of events with one real and fake lepton passing the tight lepton criteria. By combining Equation (6.6) to (6.8), the number of fake lepton events passing the tight selection requirement can be expressed as

$$N^{\text{tight}}_{\text{fake}} = \frac{\varepsilon_{\text{fake}}}{\varepsilon_{\text{real}} - \varepsilon_{\text{fake}}}(\varepsilon_{\text{real}} N^{\text{loose}} - N^{\text{tight}}). \tag{6.9}$$

The tight lepton selection criteria are the same as the one described in Section 5.3 and 5.4. There are some points to consider the definition of the loose lepton to achieve a reasonable precision of the fake background estimate.

- There should be a numerically sufficient difference between $\varepsilon_{\text{real}}$ and $\varepsilon_{\text{fake}}$ to avoid the divergence in Equation (6.9).
- The efficiency must be as independent on the event topology as possible, because efficiency determined in a particular control region is applied to the signal regions.
- Any significant dependence of efficiency on kinematics and topologies must be parametrized.

Considering the above, the selection criteria of the loose muon are defined as the same requirement as the one for tight muon, but omitting the isolation requirement. For the loose electron, the same requirement as the tight electron but

- requiring loose isolation selection which have 98 % efficiency for the real electron instead of 90 % in the tight electron,
- removing the hit requirement on B-layer for the electron track to enhance the photon conversion,

are used.

Having $\varepsilon_{\text{real}}$ and $\varepsilon_{\text{fake}}$, we can measure the amount of fake leptons through Equation (6.9) just by counting N^{loose} and N^{tight}. Below, we discuss the determination of $\varepsilon_{\text{real}}$ and $\varepsilon_{\text{fake}}$ in data.

Estimate of $\varepsilon_{\text{real}}$

To estimate $\varepsilon_{\text{real}}$, $Z \to \ell\ell$ event is used to collect a pure real lepton sample, where the following selection criteria are applied.

- Exactly two loose same flavor leptons exist.
- Two loose leptons have an opposite signed charge.
- The invariant mass of two loose lepton system $M_{\ell\ell}$ satisfies $|M_{\ell\ell} - M_Z| < 10$ GeV where M_Z is 91 GeV.
- $E^{\text{miss}}_{\text{T}}$ is required to be less than 40 GeV to increase purity.

This selection gives the purity more than 99 %. For the events passing the above criteria, the tag lepton is defined to be the tight lepton whose direction is consistent with the corresponding trigger object, while another lepton plays a role of the probe, as discussed in Section 5.3. Figure 6.2 shows the real lepton efficiency measured with full 2011 data as a function of the loose lepton P_{T}, η and the number of jets. No strong dependences on the kinematics of the lepton have been found. Therefore, the inclusive efficiency is used as $\varepsilon_{\text{real}}$ for both electron and muon. The values used in the fake estimate are $\varepsilon_{\text{real}} = 0.795$ and $\varepsilon_{\text{real}} = 0.976$ for electron and muon, respectively. The possible bias from the small kinematic dependence is considered as the systematic uncertainty source and discussed later.

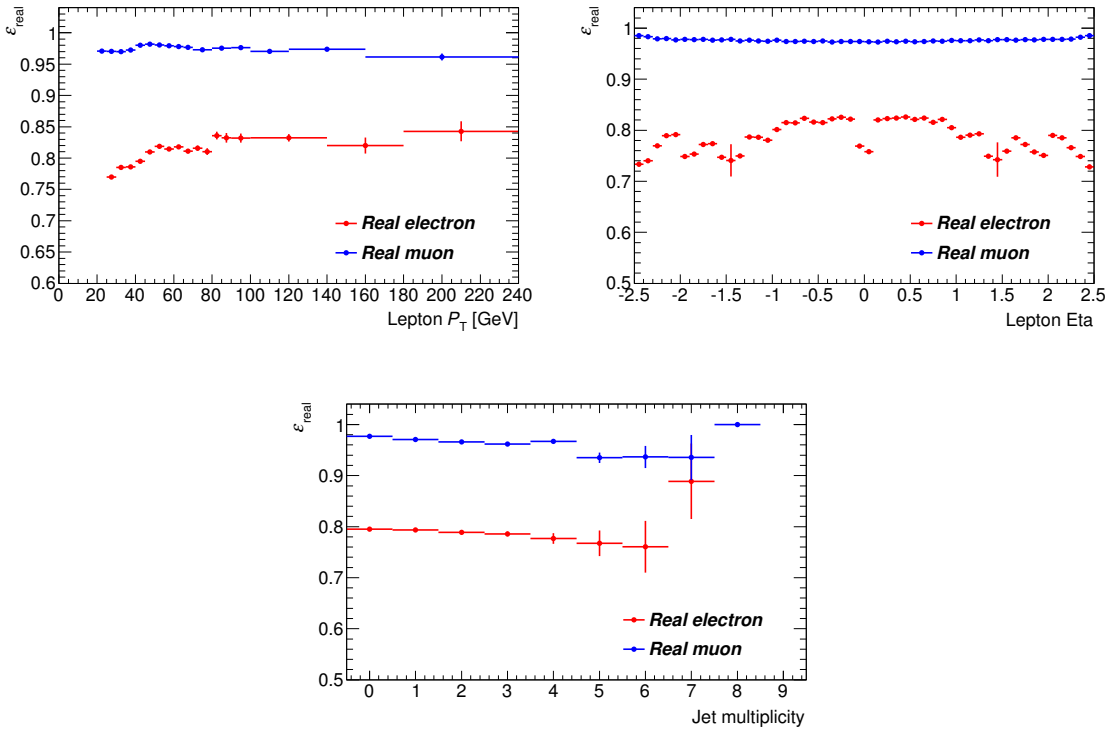


Figure 6.2: The measured efficiency for real loose leptons to pass the tight lepton requirements as a function of the lepton P_{T}, η and the number of jets in the event.

Estimate of $\varepsilon_{\mathrm{fake}}$

To estimate $\varepsilon_{\mathrm{fake}}$, the QCD multi-jet event is used with the following selection requirement.

- Exactly one loose lepton exists.
- At least one jet exists.
- The distance ΔR between the loose lepton and the leading jet must be greater than 0.7.
- $E_{\mathrm{T}}^{\mathrm{miss}}$ must be less than 20 GeV to suppress W+jets process.

Figure 6.3 shows $E_{\mathrm{T}}^{\mathrm{miss}}$ and the jet multiplicity distributions for the events passing the above requirements for the e+jets and the μ+jets channel. Because there is no MC expectation for the QCD multi-jet event, the difference between data and the MC expectation accumulating the contributions from W+jets, Z/γ^*+jets, $t\bar{t}$, di-boson and the single top production is attributed to the QCD multi-jet events with the fake electron and muon. One can see $10 \sim 20$ % of the real lepton contamination from the decay of W/Z bosons. To obtain $\varepsilon_{\mathrm{fake}}$, the real lepton contribution estimated from MC is subtracted from the observed number of events in data. Taking the ratio of the numbers of fake lepton events before and after the tight selection, $\varepsilon_{\mathrm{fake}}$ is obtained as shown in Figure 6.4. More than 10 % of the dependence has been found in some variables. However, it is difficult to model such dependences in the multi-dimensional variable space with the current statistics. Therefore, the simpler parametrization below is adopted. For the fake electron efficiency, $\varepsilon_{\mathrm{fake}}^{\mathrm{elec}}$, the pseudorapidity of electrons is divided into two regions, $|\eta| < 2.0$ and $2.0 \leq |\eta|$. The values obtained by fitting each region with a constant, $\varepsilon_{\mathrm{fake}}^{\mathrm{elec}} =$

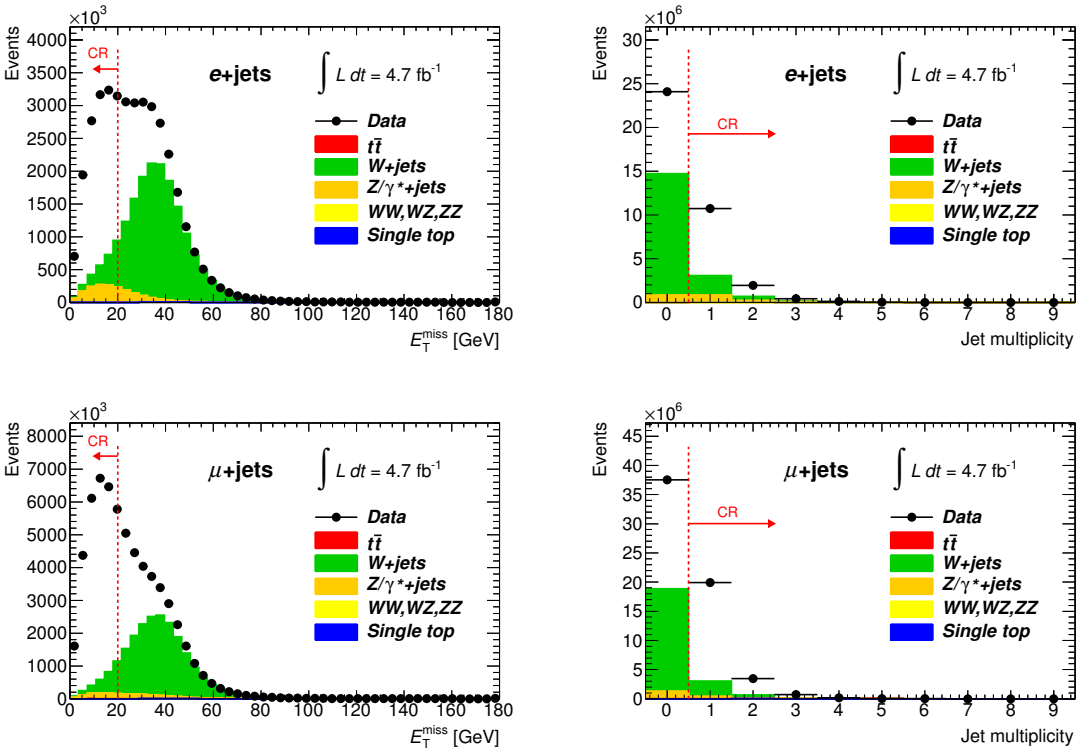


Figure 6.3: $E_{\mathrm{T}}^{\mathrm{miss}}$ (left) and the jet multiplicity (right) distributions after requiring the selection to enhance QCD multi-jet events for the e+jets (top) and the μ+jets (bottom). $E_{\mathrm{T}}^{\mathrm{miss}}$ (the jet multiplicity) cut is not applied for the illustration purpose. The required cut positions are indicated in the red doted lines.

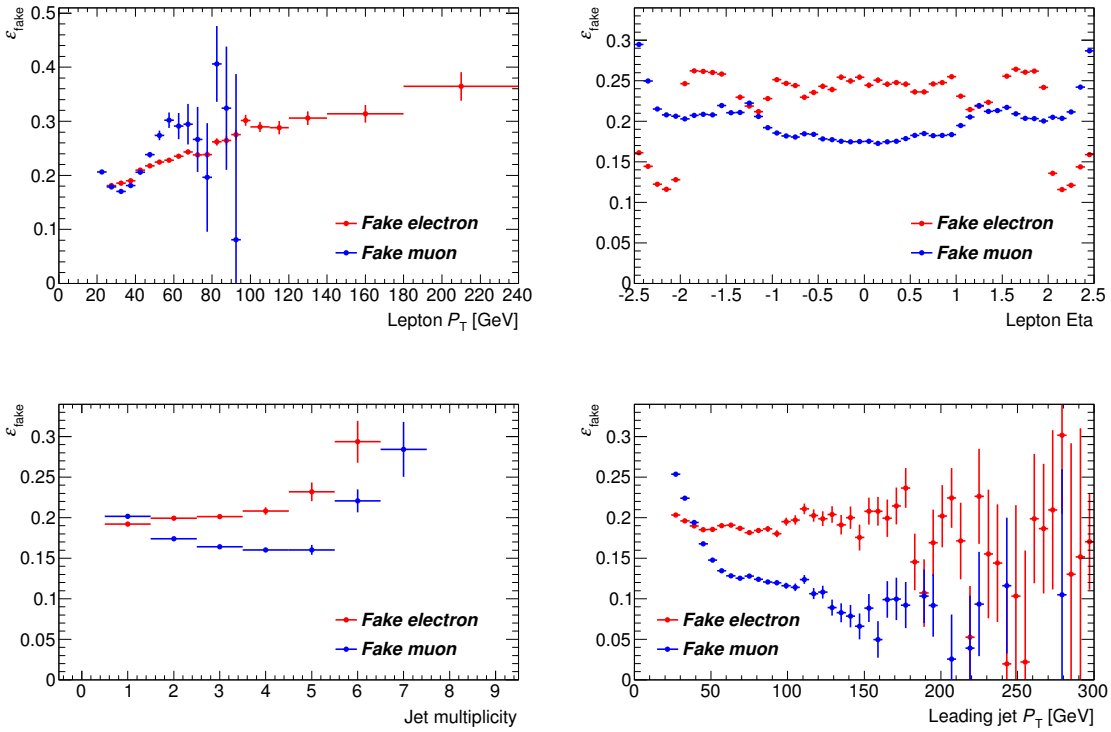


Figure 6.4: $\varepsilon_{\text{fake}}$ as a function of lepton P_{T} (top left), lepton eta (top right), the jet multiplicity in the event (bottom left) and the leading jet P_{T} (bottom right).

0.2428 for the $|\eta| < 2.0$ region and $\varepsilon^{\text{elec}}_{\text{fake}} = 0.1303$ for $2.0 \leq |\eta|$ are used. On the other hand, the inclusive efficiency, 0.1969, is used for $\varepsilon^{\text{mu}}_{\text{fake}}$ without any categorization. This $\varepsilon_{\text{fake}}$ modeling is considered as the systematic uncertainty source for the ε_b measurement, which will be discussed in Section 6.11.

Yields of the events with the fake lepton

The ingredients for the matrix method have been measured above. The number of events with the fake lepton in the signal region is calculated to be 3047.5 for the e+jets, 7249.9 for the μ+jets. To estimate the possible uncertainty from the parametrization of the real and fake lepton efficiency, we compare the yields with the one obtained by using the other parametrization which is adopted for the $\sigma_{t\bar{t}}$ measurement in the single lepton final state at the ATLAS experiment [99]. The yield is obtained to be 3351 for the e+jets channel and 5508 for the μ+jets channel. The difference from our result is about 10 % to 25 %. To cover the possible further bias due to the difficulty of the fake lepton efficiency modeling, the uncertainty of 30 % is assigned for both channels as the systematic uncertainty.

In the analysis later on, to check the distribution of the event kinematics such as $E^{\text{miss}}_{\text{T}}$, one needs to obtain the distribution by the fake lepton. Not only the total amount but also the shape of any given variables for the fake lepton events can be estimated by the matrix method. By using Equation (6.9) with $\varepsilon_{\text{real}}$ and $\varepsilon_{\text{fake}}$, one can obtain the expectation value that the event of interest contains the fake lepton event by event basis. Accumulating these expectation values

for a given variables, one can get the shape from the events with fake leptons. This technique is used for all the plots through this thesis when it contains fake lepton contributions.

6.5.3 Other backgrounds

MC samples are used to estimate the contribution from the other background processes which contain a real lepton originating from the W/Z boson decay. We consider the physics process listed below as the background which includes one or more real leptons.

- $t\bar{t} \to \ell\ell\nu\nu bb$ ($\ell : e, \mu, \tau$)
- $Z \to \ell\ell$ ($\ell : e, \mu, \tau$)
- WW, WZ and ZZ productions
- Single top productions (production via the s- and t-channel, Wt production)

All the same corrections mentioned in Section 6.4 are applied for the background MC samples as well.

6.6 Distributions in background enhanced regions

We checked some distributions in the control regions, where the W+jets events or the fake lepton events are enhanced, to see the validity of the background modeling.

The W+jets enhanced region is defined to be the events passing all the selections as the signal candidates except that the event must have one, two, or three jets. The events with no jets are removed because the amount of fake lepton events cannot be estimated by the matrix method.

The fake lepton enhanced region is defined to be the events passing all the selections as the signal candidates except for $E_{\mathrm{T}}^{\mathrm{miss}}$ and $M_{\mathrm{T}}(W)$ requirements. $E_{\mathrm{T}}^{\mathrm{miss}}$ is required to be less than 30 (20) GeV for the e+jets (μ+jets) channel, and $M_{\mathrm{T}}(W)$ to be less than 30 GeV for the e+jets channel and $E_{\mathrm{T}}^{\mathrm{miss}} + M_{\mathrm{T}}(W) < 60$ GeV for the μ+jets channel.

W+jets enhanced region

Figure 6.5 shows some kinematic distributions in the W+jets enhanced region. A distinctive shape of the W+jets events appears in the $M_T(W)$ distribution. The Jacobian peak around 80 GeV is clearly seen and well modeled by the data-driven method. One can also see that not only the overall W+jets amounts but also the shape of the kinematic distribution in the W+jets is well modeled.

There are some interesting points found in these plots. In the muon P_{T} plot, one can see the data deficit at the high P_{T} region. One of the possible reasons to explain this is the mis-measurement of the muon momentum due to the alignment of the muon system, where the muon momentum becomes low at the very high momentum region with the imperfect alignment. Besides, as seen in the jet multiplicity plots, the uncertainty seems to be overestimated, *i.e.* all the data points exist almost the center of the uncertainty band.

Fake lepton enhanced region

Figure 6.6 shows the lepton P_{T}, η and b-tagged jet multiplicity distributions in the fake lepton enhanced region. There are some contributions from other physics processes, since it is difficult to enhance only the fake lepton because of the tight requirements of the lepton identification.

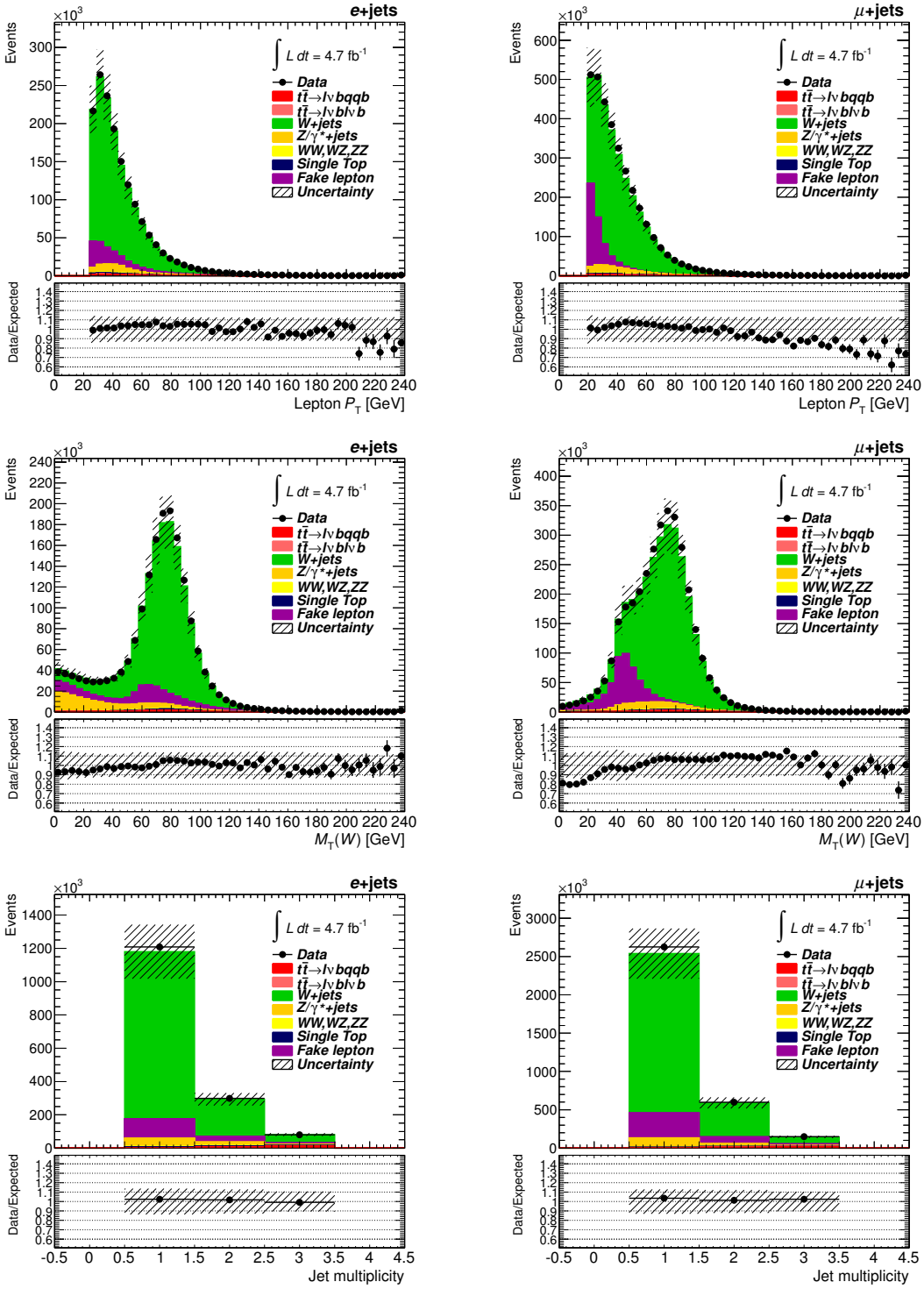


Figure 6.5: The lepton P_{T}, $M_{\mathrm{T}}(W)$ and the jet multiplicity distributions in the W+jets enhanced region for e+jets (left) and μ+jets (right) channels. The last bin contains overflowing events. The uncertainties considered here are the estimated numbers of fake leptons and W+jets events, the theoretical cross section uncertainties for $t\bar{t}$, Z/γ^*, di-boson and the single top production and MC statistics.

The difference of the fraction of the fake lepton events between the channels is due to the different lepton P_{T} threshold. As seen in the lepton P_{T} distributions, the larger contributions from the fake lepton can be seen in the μ+jets channel at the low P_{T} region. This implies that we could achieve more fake lepton suppression by selecting the higher P_{T} leptons. Some kinematic dependences can be seen in the lepton η distribution for both channels, which mainly comes from the modeling of $\varepsilon_{\mathrm{fake}}$. On top of that, we have seen some systematic deficit in data for the μ+jets channel. However, the observed and the expected distributions are still in agreement within the uncertainty.

6.7 Yields and distributions in the signal region

Table 6.3 compares the event yields observed in data with the expectation after applying all the event selections. Uncertainties in the table are both statistic and systematic combined. The expected yields agree very well with data.

Table 6.3: Predicted and observed numbers of events in the e+jets and the μ+jets channels after all the selections. The sign '(DD)' indicates that the numbers are estimated by the data-driven way. The uncertainty is statistic and systematic combined.

	Yields(e+jets)	Yields(μ+jets)
$t\bar{t} \to \ell\nu b\ell\nu b$	$(1.30^{+0.28}_{-0.20}) \times 10^3$	$(1.91^{+0.39}_{-0.29}) \times 10^3$
W+jets (DD)	$(1.37 \pm 0.18) \times 10^4$	$(2.28 \pm 0.31) \times 10^4$
Z/γ^*+jets	$(2.75 \pm 1.55) \times 10^3$	$(2.71 \pm 1.48) \times 10^3$
Di-boson	$(2.13^{+0.58}_{-0.47}) \times 10^2$	$(3.43^{+0.89}_{-0.76}) \times 10^2$
Single top	$(9.33^{+1.67}_{-2.24}) \times 10^2$	$(1.53^{+0.26}_{-0.36}) \times 10^3$
Fake lepton (DD)	$(3.05 \pm 0.91) \times 10^3$	$(7.25 \pm 2.17) \times 10^3$
Total background	$(2.20 \pm 0.26) \times 10^4$	$(3.66 \pm 0.41) \times 10^4$
$t\bar{t} \to \ell\nu bqqb$ (signal)	$(1.68^{+0.21}_{-0.27}) \times 10^4$	$(2.73^{+0.33}_{-0.40}) \times 10^4$
Total expected	$(3.88^{+0.33}_{-0.37}) \times 10^4$	$(6.38^{+0.53}_{-0.57}) \times 10^4$
Observed data	38857	67015

Figure 6.7 and 6.8 show the kinematic distributions in the signal region. One can see there are significant contributions from the $t\bar{t}$ production, which is used as the b-jet sample for the ε_b measurement. Even though the b-tagging efficiency correction is not applied to the MC samples, a good agreement between data and the expectation is observed. It implies that ε_b in MC must be close to the one in data which will be measured.

In the jet related plots, there are some points to be noted. In the jet multiplicity distributions, the data excess is observed at the high multiplicity bins starting from the six jets bin. In these events, there should be additional jets produced by ISR and/or FSR. In the MC simulation, those jets are simulated by the fragmentation and the parton shower modeling. The excess would be explained by the mis-modeling of these processes. However, the effect is expected to be negligible because the fraction of such events is very small.

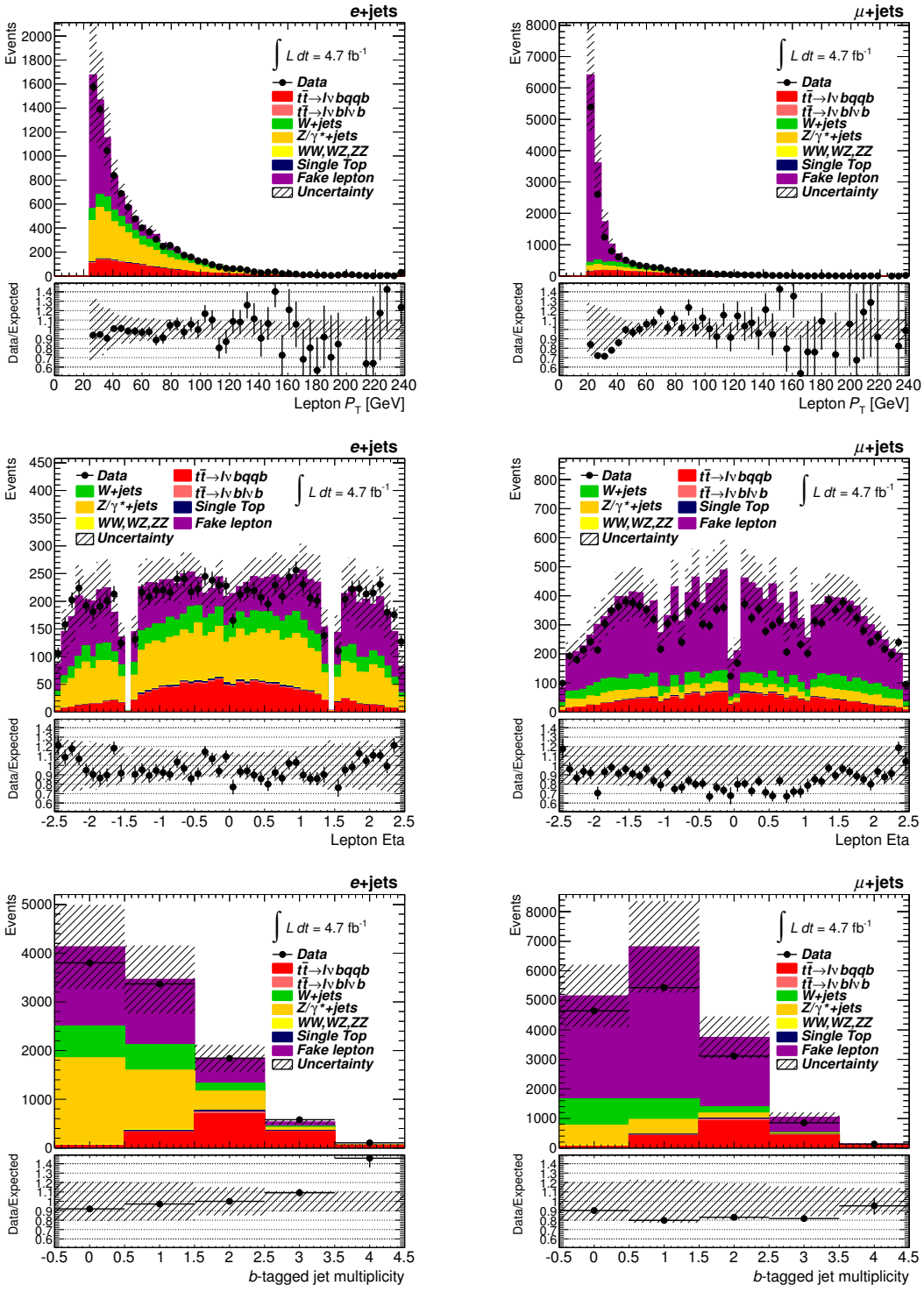


Figure 6.6: The lepton P_{T}, η, and the b-tagged jet multiplicity distributions in the fake lepton enhanced region for e+jets (left) and μ+jets (right) channels. The last bin in the top and bottom plots contains overflowing events. The uncertainties considered here are the estimated numbers of fake leptons and W+jets events, the theoretical cross section uncertainties for $t\bar{t}$, Z/γ^*, di-boson and the single top production and MC statistics.

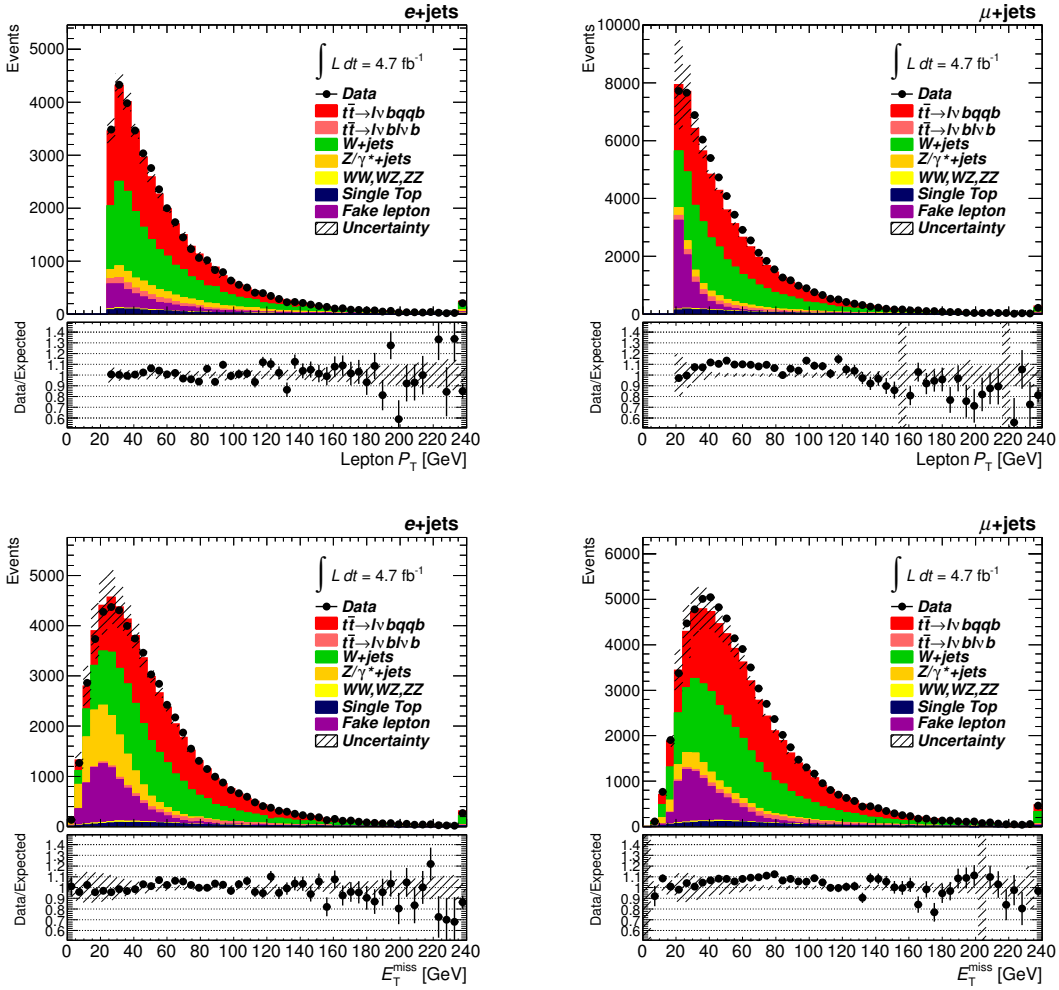


Figure 6.7: The lepton P_{T} and $E_{\mathrm{T}}^{\mathrm{miss}}$ distributions in the signal region for e+jets (left) and μ+jets (right) channels. The last bin contains overflowing events. The uncertainties considered here are the estimated numbers of fake leptons and W+jets events, the theoretical cross section uncertainties for $t\bar{t}$, Z/γ^*, di-boson and the single top production and MC statistics.

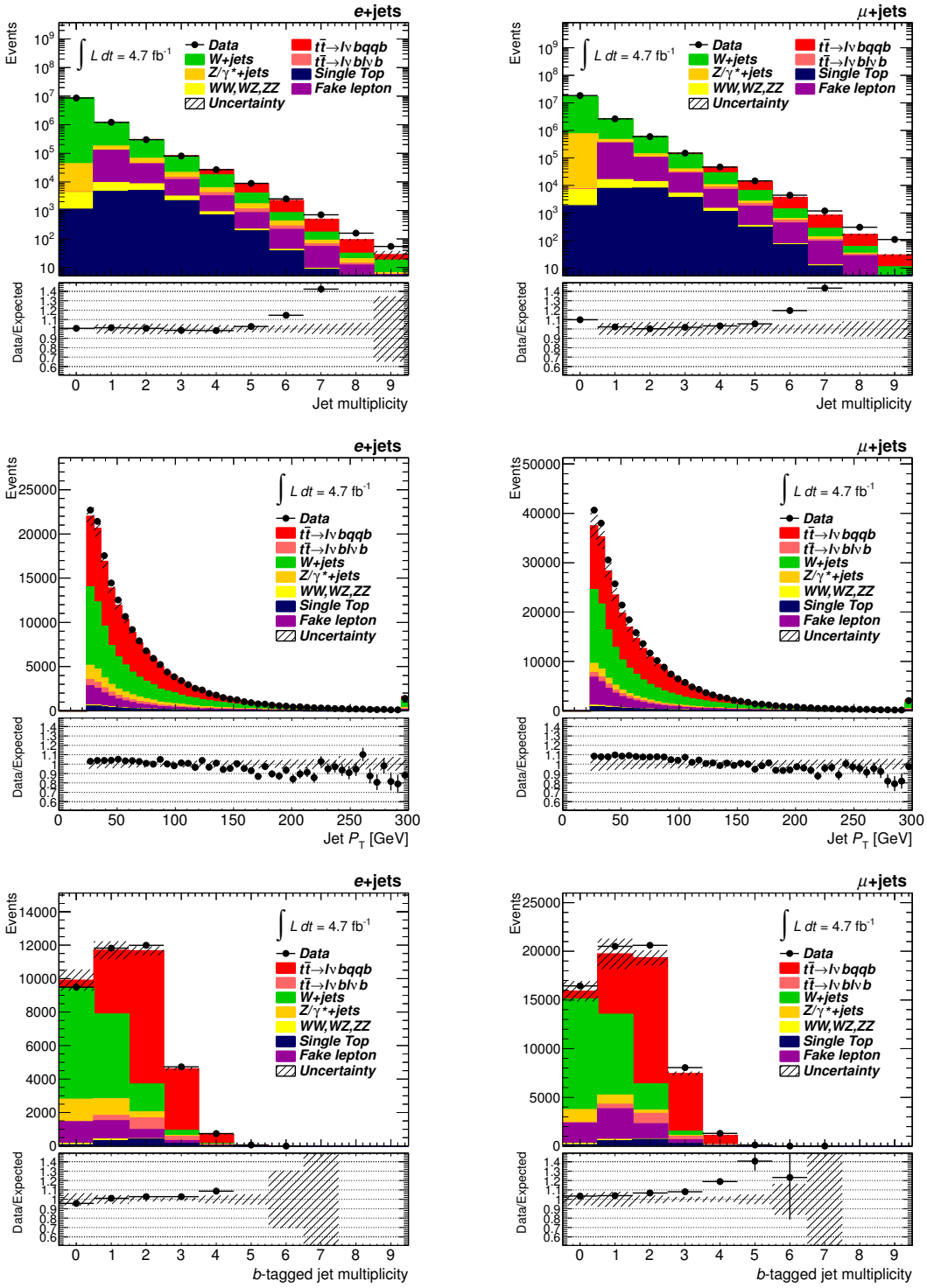


Figure 6.8: The jet multiplicity, P_{T} and b-tagged jet multiplicity in the signal region for e+jets (left) and μ+jets (right) channels. The last bin contains overflowing events. The uncertainties considered here are the estimated numbers of fake leptons and W+jets events, the theoretical cross section uncertainties for $t\bar{t}$, Z/γ^*, di-boson and the single top production and MC statistics.

6.8 Determination of the flavor fraction

The last ingredients of the likelihood fitting is the flavor fraction, $F_{b,c,l}$, for each process. After applying all the event selections and corrections to the MC samples, we extracted the fraction of the jet flavor composition, $F_{b,c,l}$, by using true information in MC samples. Events with up to eight jets are used to compute $F_{b,c,l}$. This selection covers more than 99 % of remaining events after the selections. Table 6.4 and 6.5 list $F_{b,c,l}$ for $t\bar{t}$, W+jets and other backgrounds by descending order down to ninth largest values. The uncertainties include the statistical uncertainty by the MC sample size.

Table 6.4: The leading $F_{b,c,l}$ fractions for jets with $P_{\mathrm{T}} > 25$ GeV in the e+jets channel, obtained from the simulated events. The category 'Other backgrounds' includes $t\bar{t} \to \ell\nu b\ell\nu b$, Z/γ^*, diboson and the single top production. Uncertainties are statistical only.

$t\bar{t}$		W+jets		Other backgrounds	
$F_{b,c,l}$	Fraction [%]	$F_{b,c,l}$	Fraction [%]	$F_{b,c,l}$	Fraction [%]
F_{202}	26.29 ± 0.09	F_{004}	57.39 ± 0.68	F_{004}	37.60 ± 0.40
F_{211}	15.18 ± 0.07	F_{013}	14.20 ± 0.22	F_{202}	15.04 ± 0.14
F_{203}	13.20 ± 0.06	F_{005}	12.14 ± 0.24	F_{005}	10.13 ± 0.20
F_{212}	9.21 ± 0.05	F_{014}	3.27 ± 0.10	F_{103}	8.26 ± 0.13
F_{103}	8.63 ± 0.05	F_{006}	2.51 ± 0.15	F_{013}	5.50 ± 0.14
F_{112}	6.13 ± 0.04	F_{103}	2.43 ± 0.10	F_{203}	5.09 ± 0.08
F_{204}	4.28 ± 0.04	F_{022}	2.19 ± 0.08	F_{006}	2.59 ± 0.10
F_{213}	3.39 ± 0.03	F_{202}	0.87 ± 0.05	F_{104}	2.23 ± 0.07
F_{104}	3.13 ± 0.03	F_{015}	0.67 ± 0.04	F_{112}	2.22 ± 0.06

Table 6.5: The leading $F_{b,c,l}$ fractions for jets with $P_{\mathrm{T}} > 25$ GeV in the μ+jets channel, obtained from the simulated events. The category 'Other backgrounds' includes $t\bar{t} \to \ell\nu b\ell\nu b$, Z/γ^*, diboson and the single top production. Uncertainties are statistical only.

$t\bar{t}$		W+jets		Other backgrounds	
$F_{b,c,l}$	Fraction [%]	$F_{b,c,l}$	Fraction [%]	$F_{b,c,l}$	Fraction [%]
F_{202}	25.99 ± 0.07	F_{004}	57.66 ± 0.50	F_{004}	32.25 ± 0.38
F_{211}	15.08 ± 0.05	F_{013}	13.65 ± 0.16	F_{202}	18.68 ± 0.13
F_{203}	13.21 ± 0.05	F_{005}	12.56 ± 0.20	F_{103}	9.90 ± 0.12
F_{212}	9.19 ± 0.04	F_{014}	3.16 ± 0.07	F_{005}	7.70 ± 0.18
F_{103}	8.59 ± 0.03	F_{006}	2.71 ± 0.11	F_{203}	6.32 ± 0.08
F_{112}	6.11 ± 0.03	F_{103}	2.33 ± 0.07	F_{013}	5.49 ± 0.13
F_{204}	4.41 ± 0.03	F_{022}	2.05 ± 0.06	F_{112}	2.96 ± 0.06
F_{213}	3.43 ± 0.02	F_{202}	0.85 ± 0.03	F_{104}	2.43 ± 0.06
F_{104}	3.09 ± 0.02	F_{015}	0.66 ± 0.03	F_{211}	1.97 ± 0.05

6.9 Simultaneous fitting for data

After the event selections discussed in Section 6.3, the maximum likelihood fitting described in Section 6.2 is applied to the observed distribution of the number of the b-tagged jets shown in Figure 6.8. For this fitting, the entries in the bin of five or more b-tagged jets are combined. The e+jets and the μ+jets channels are fitted simultaneously. The log-likelihood as a function of the b-tagging efficiency and the $t\bar{t}$ cross section is shown in Figure 6.9.

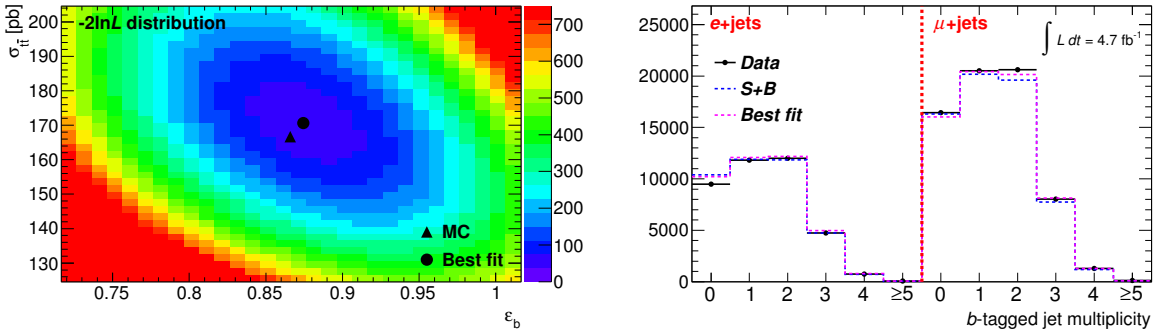


Figure 6.9: Left : The log-likelihood distribution in the $\sigma_{t\bar{t}}$ and ε_b plane. For the later use to estimate the error from the likelihood by using Wilks theorem, $-2\ln L$ is shown. Expected value in MC is indicated in the triangle and the best fit point, the minimum of $-2\ln L$, in the circle. Right : the number of b-tagged jets distribution for e+jets and μ+jets channels. Blue histogram shows the estimated shape obtained with using the predicted $\sigma_{t\bar{t}}$ and ε_b in MC. The magenta shows the shape for the best fit result. The points shows the distribution obtained from data.

The fitting yields

$$\varepsilon_b \quad = \quad 0.8744 \pm 0.0070.$$

The error here is only data statistics. Since we fitted ε_b and $\sigma_{t\bar{t}}$ simultaneously, we obtained $\sigma_{t\bar{t}}$ which is 170.6 ± 2.3 pb. As shown in Section 6.11, $\sigma_{t\bar{t}}$ suffers the large systematic uncertainty, and hence is treated as just a byproduct of the fitting here.

6.10 Validation of the tag counting method

Pseudo experiments are performed to check if there is a bias, and if the size of the error of the fitting is reasonable. The pseudo data is prepared by the following procedure. The distribution of interest is the b-tagged jet multiplicity which is used in the fitting. A base distribution is prepared using MC with the arbitrary values of $\sigma_{t\bar{t}}$ and ε_b. The content of each bin in the base distribution is forced to fluctuate following the Poisson statistics. To obtain enough amount of the pseudo data, this procedure is repeated ten thousand times for each combination of $\sigma_{t\bar{t}}$ and ε_b. The range of $\sigma_{t\bar{t}}$ is $0.5 \times \sigma_{t\bar{t}}^{\mathrm{Theory}} \sim 1.5 \times \sigma_{t\bar{t}}^{\mathrm{Theory}}$ with $0.05 \times \sigma_{t\bar{t}}^{\mathrm{Theory}}$ step, and the one for ε_b is $0 \sim 100$ % with 5 % step.

Figure 6.10 shows the result of the pseudo experiments with $\sigma_{t\bar{t}}$ to be 164 pb and ε_b to be 85 %. The top two plots show $\sigma_{t\bar{t}}$ and ε_b obtained from the fitting. The mean values of these distribution are consistent with the input value within a few per mill precision. The bottom two plots show the pull distribution defined as $(Output - Input)/(\delta Output)$, where $Output$ and

$\delta Output$ are the output value and its error in the fitting, and $Input$ is the true input value. The sigmas are found to be consistent with unity implying the validity of the error size. Repeating the same procedure for other input combinations, it is found that no fitting bias exists, and the size of the error is reasonable for all the input combinations. The results are summarized in Figures 6.11, 6.12 and 6.13.

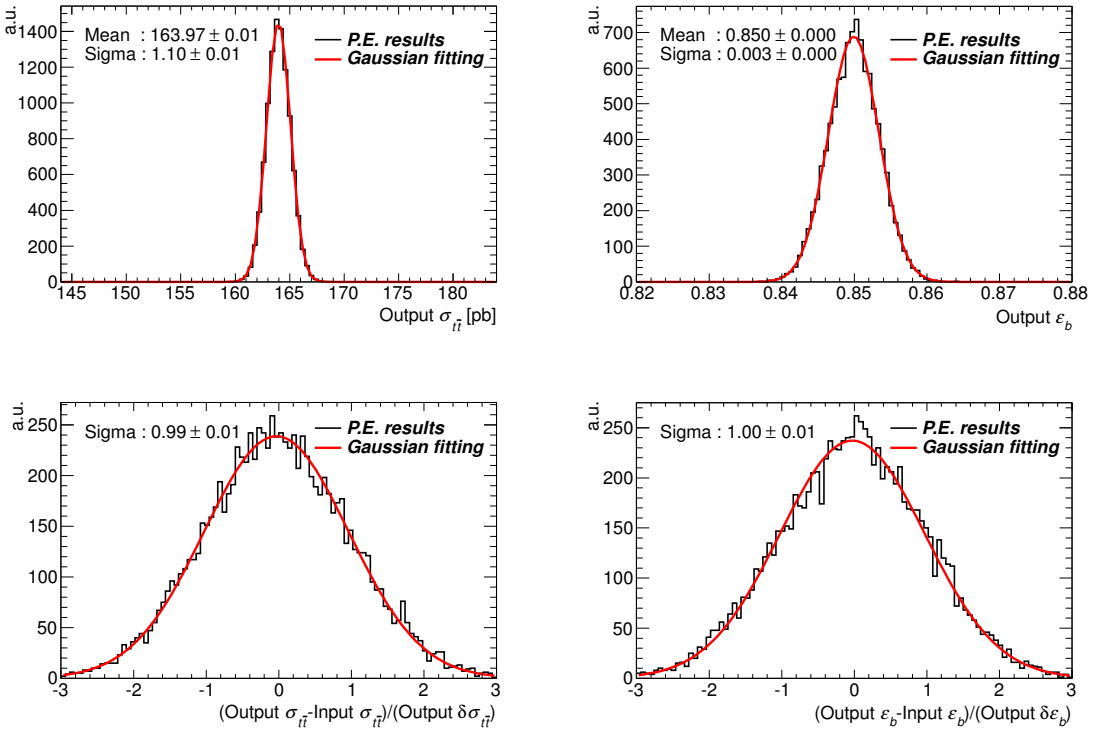


Figure 6.10: The result of the pseudo experiments with the input $\sigma_{t\bar{t}} = 164$ pb and $\varepsilon_b = 85$ %. The black histograms are the Pseudo Experiment results. The red line shows the result of the Gaussian fitting. The outputs of the Gaussian fitting are shown as 'Mean' and 'Sigma' inside the plots.

6.11 Systematic uncertainties

In our likelihood fitting, the extracted ε_b is sensitive to the shape of the b-tagged jet multiplicity but amount of the expected number of events. The extracted $\sigma_{t\bar{t}}$ has the opposite tendency of the ε_b measurement. In this section, the effects of the systematic uncertainty for both measurements are investigated and discussed.

To estimate the systematic uncertainty, we repeat the measurement with MC varied by ± 1 sigma for the given uncertainty source, *e.g.* with more W+jets contribution by $+1$ sigma. The size of the uncertainty is basically evaluated by taking a difference between the nominal result presented in Section 6.9 and the one obtained with the modified MC as the systematic uncertainty. The obtained uncertainty for the ε_b measurement and the extracted $\sigma_{t\bar{t}}$ is summarized in Table 6.6. Total systematic uncertainty is obtained by the quadratic sum of all the contributions, which is $+9.2/-8.7$ % for ε_b. The dominant uncertainty source is the W+jets background estimate and JES. The details of the effect of each uncertainty source are described in the following.

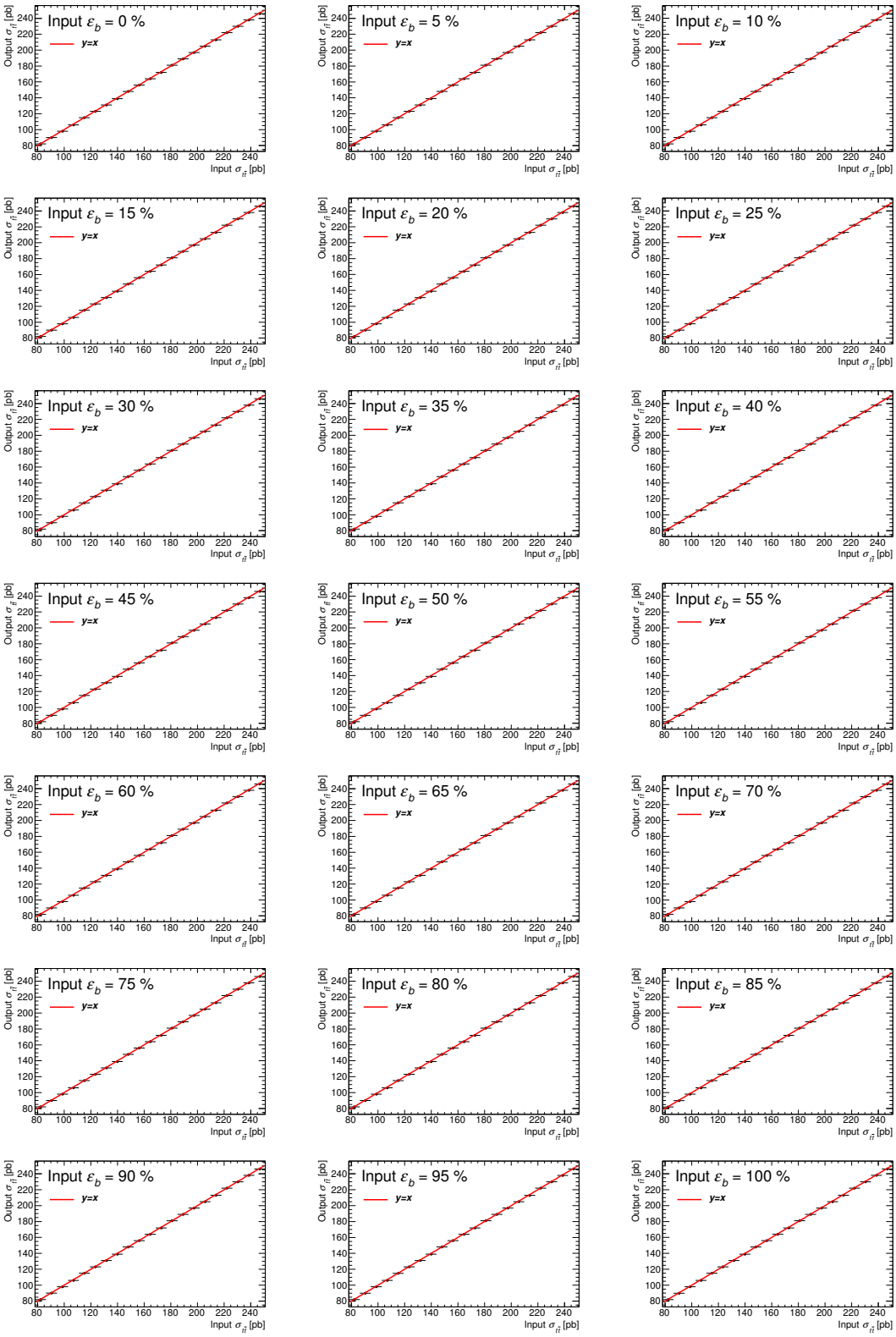


Figure 6.11: The linearity of the $\sigma_{t\bar{t}}$ measurement for all the input combinations. Horizontal bars indicate the extracted $\sigma_{t\bar{t}}$ by the pseudo experiments against each input value. The red line shows the line of (Output $\sigma_{t\bar{t}}$) = (Input $\sigma_{t\bar{t}}$).

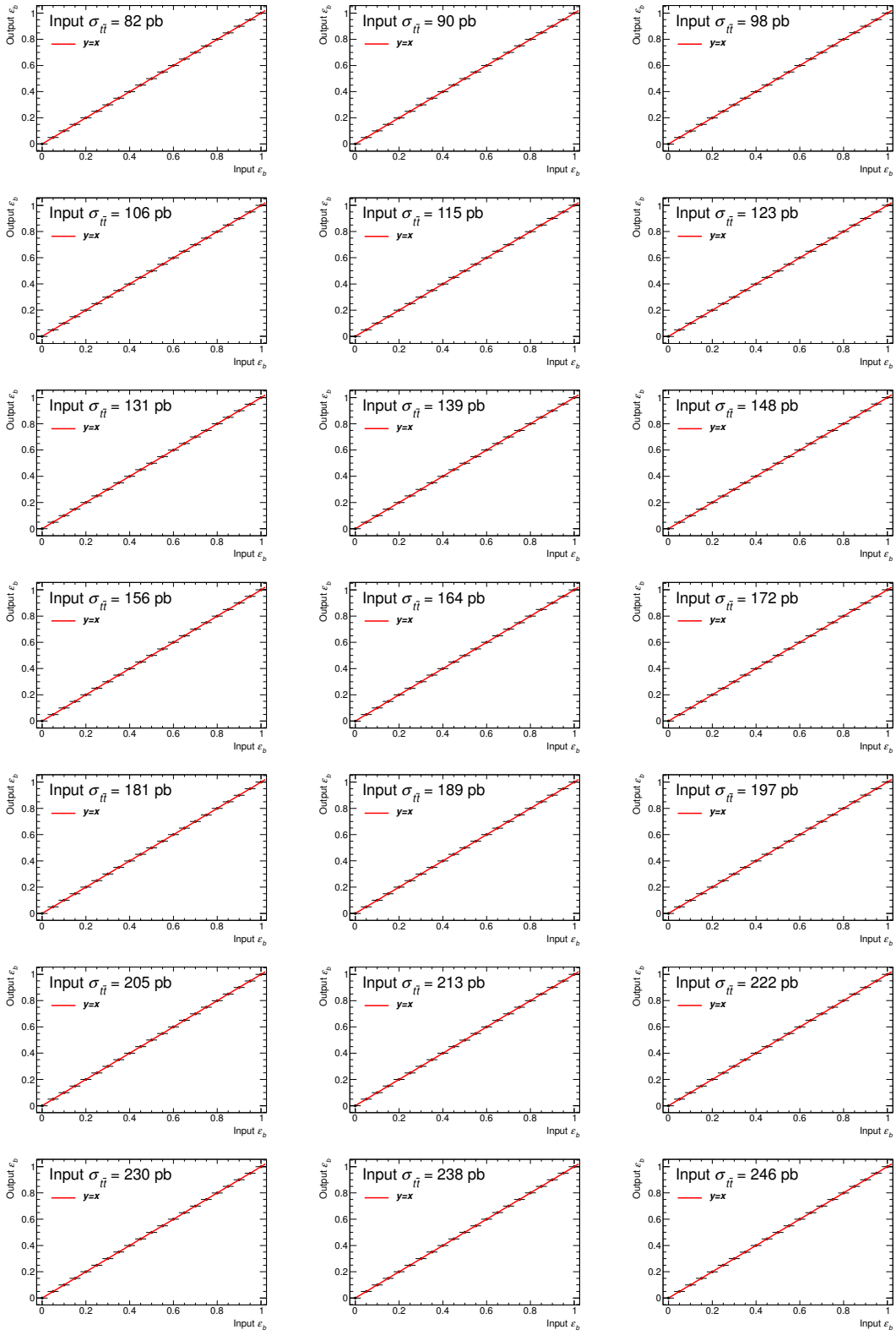


Figure 6.12: The linearity of the ε_b measurement for all the input combinations. Horizontal bar indicate the extracted ε_b by the pseudo experiments against each input value. The red line shows the line of (Output ε_b) = (Input ε_b).

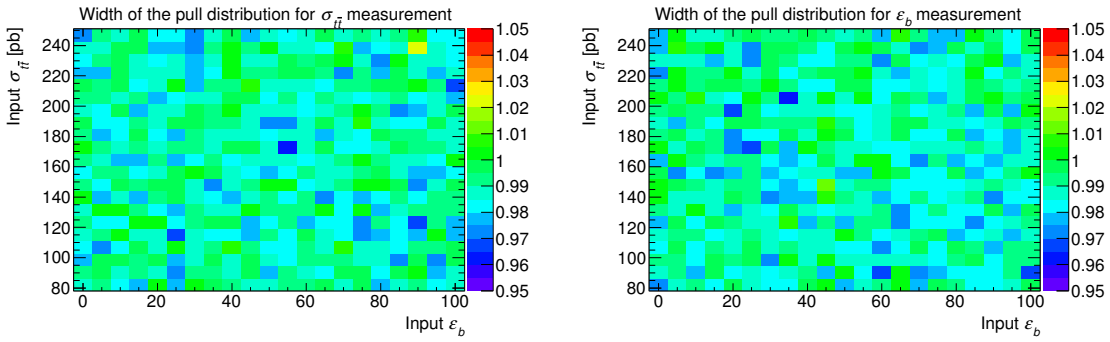


Figure 6.13: The width of the pull distributions for each combination of the inputs. The left plot shows the one for the $\sigma_{t\bar{t}}$ measurement, and the right one for the ε_b measurement.

Table 6.6: Uncertainties on the b-tagging efficiency measurement and the extracted $\sigma_{t\bar{t}}$ in fitting.

	$\delta\varepsilon_b/\varepsilon_b$ [%]	$\delta\sigma_{t\bar{t}}/\sigma_{t\bar{t}}$ [%]
Data stat.	+ 0.80 / − 0.80	+ 1.37 / − 1.37
Luminosity	+ 0.13 / − 0.13	+ 2.19 / − 2.11
#W+jets	+ 5.46 / − 5.64	+ 9.17 / − 8.56
Heavy flavor fraction	+ 0.40 / − 2.14	+ 2.84 / − 5.34
#Fake Electron	+ 1.23 / − 1.19	+ 2.39 / − 2.55
#Fake Muon	+ 1.29 / − 1.18	+ 2.54 / − 2.78
Fake lep. dist. shape	+ 1.58 / − 1.58	+ 2.30 / − 2.30
Jet energy scale	+ 5.56 / − 3.99	+ 23.69 / − 22.11
Jet energy resolution	+ 2.87 / − 2.87	+ 4.94 / − 4.94
Jet reco. efficiency	+ 0.02 / − 0.02	+ 0.08 / − 0.08
Jet vertex fraction	+ 0.77 / − 1.15	+ 5.10 / − 3.37
$E_{\mathrm{T}}^{\mathrm{miss}}$ soft terms	+ 0.12 / − 0.12	+ 0.30 / − 0.30
El. energy scale	+ 0.06 / − 0.06	+ 0.15 / − 0.15
El. energy resolution	+ 0.07 / − 0.00	+ 0.00 / − 0.14
El. reco. efficiency	+ 0.62 / − 0.49	+ 1.93 / − 2.21
El. trigger	+ 0.43 / − 0.32	+ 1.29 / − 1.57
Mu. energy scale	+ 0.11 / − 0.11	+ 0.34 / − 0.34
Mu. energy resolution	+ 0.00 / − 0.00	+ 0.08 / − 0.08
Mu. reco. efficiency	+ 0.28 / − 0.13	+ 0.67 / − 1.06
Mu. Trigger	+ 0.36 / − 0.25	+ 1.20 / − 1.49
c-tagging efficiency	+ 0.13 / − 0.01	+ 0.00 / − 0.23
t-tagging efficiency	+ 0.16 / − 0.00	+ 0.00 / − 0.30
Generator	+ 1.98 / − 1.98	+ 4.78 / − 4.78
Parton shower	+ 1.95 / − 1.95	+ 3.98 / − 3.98
ISR/FSR	+ 0.76 / − 0.76	+ 0.50 / − 0.50
Total systematics	+ 9.20 / − 8.71	+ 27.80 / − 26.46
Total uncertainty	+ 9.23 / − 8.75	+ 27.83 / − 26.50

6.11.1 Integrated luminosity

As mentioned in Section 4.1.1, the measurement of the total integrated luminosity of the whole 2011 pp collision samples has an 1.8 % uncertainty. The uncertainty affects the expected numbers of $t\bar{t}$ signal and the background processes except for the W+jets and the fake lepton events which are estimated from data. When the luminosity value is shifted, each bin content of any distributions is increased or decreased equally, *i.e.* the varying the integrated luminosity does not change the shape of distributions so much. Therefore, the uncertainty of the luminosity have a small effect on the ε_b measurement and larger on $\sigma_{t\bar{t}}$. The size of the uncertainty is estimated to be $\pm$ 0.1 % for the ε_b and $+2.2/-2.1$ % for the $\sigma_{t\bar{t}}$ measurement.

6.11.2 W+jets background estimate

The uncertainty for the number of W+jets events with four or more jets is about 15 % as seen in Table 6.2. The mis-understandings of the amount of W+jets changes both shape and amount in the b-tagged jet multiplicity distribution, which means that it affects both measurements. The size of the uncertainty is estimated to be $+5.5/-5.6$ % for the ε_b and $+9.2/-8.6$ % for the $\sigma_{t\bar{t}}$ measurement.

6.11.3 Fake lepton background

The expected yields for the e+jets and the μ+jets final state are 3047.5 ± 914.3 and 7249.9 ± 2175.0, respectively. The size of the error due to the estimate of fake lepton events is obtained by the common procedure described at the beginning of this section. The fake electron and the fake muon contributions are varied independently. The estimated error due to the fake lepton is about $\pm$1.2 % for the ε_b and about $\pm$2.5 % for the $\sigma_{t\bar{t}}$ measurement for each source.

6.11.4 Fake lepton background distribution shape

The mis-modeling of the distribution of the fake leptons may bias the fitting results. To estimate this effect, the maximum likelihood fitting with the different shape for the fake lepton distribution is performed 10,000 times. For each trial, the entry of each bin in the b-tagged jet multiplicity by the fake lepton events is fluctuated by 30 % assuming Gaussian. This 30 % is based on the overall scale uncertainty for the fake lepton contribution. Figure 6.14 shows the shift from the nominal results in each trial. The widths of these distributions are adopted as the systematic uncertainty from the mis-modeling of the fake lepton distribution, which is $\pm$1.6 % for the ε_b and $\pm$2.3 % for the $\sigma_{t\bar{t}}$ measurement.

6.11.5 Jet related uncertainties

Both the amount of the events and the shape of the distribution would be biased by the mis-modeling of JES, the jet energy resolution and the jet efficiency. We expect to see a large effect even if each jet have a small uncertainty since we require at least four jets in the final state. In addition, the mis-understandings of jets causes the acceptance mis-modeling not only by the jet selection efficiency but also by the $E_{\mathrm{T}}^{\mathrm{miss}}$ selection efficiency. This is the another reason why the jet related uncertainty affects much.

Jet energy scale and resolution

JES has the uncertainty of 1-3 % as shown in Figures 5.12 and 5.13. To estimate the size of the error due to JES, the analysis is repeated as already mentioned above. The systematic

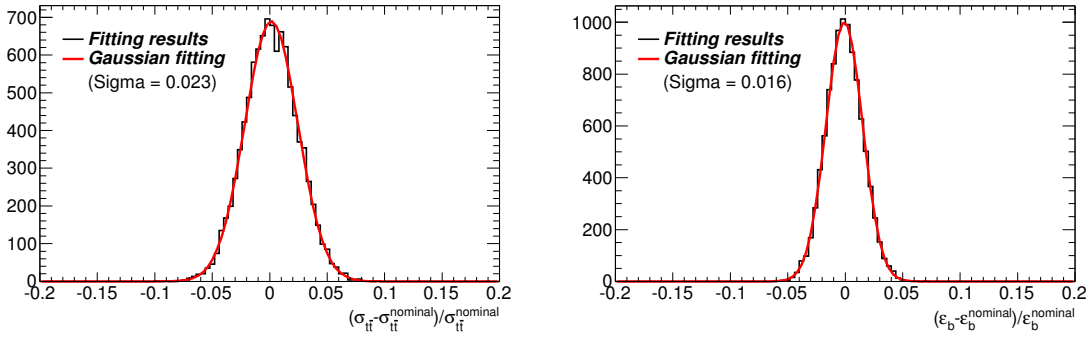


Figure 6.14: The result of 10000 trials of the likelihood fitting with varying the fake lepton distribution shape. The relative difference of the fitting results from the nominal fitting result are plotted. The plot on the left is for the cross section measurement and the right one for the b-tagging efficiency measurement. The widths of distribution are extracted by the gaussian fitting.

uncertainty from JES is evaluated to be $+5.6/-4.0$ % for the ε_b and $+23.6/-22.1$ % for the $\sigma_{t\bar{t}}$ measurement.

The observed jet energy resolution in data is slightly larger than the one in MC, but still within the uncertainty. However, we estimated the possible systematic uncertainty due to the mis-understanding of the resolution. To estimate the size of the error due to the jet energy resolution, the analysis is repeated with smearing the jet energy to match the observed resolution in data. The difference from the nominal result described at Section 6.9 is taken as the systematic uncertainty, which is 2.9 % for the ε_b and 4.9 % for the $\sigma_{t\bar{t}}$ measurement. We put the same size of the uncertainty for the negative direction to cover the systematic uncertainty for the opposite direction with assuming that the similar variation could be observed.

Jet reconstruction and JVF selection efficiency

Small inefficiency, $\sim$1 %, for a jet below 30 GeV is observed in data as described in Section 5.5. To estimate the size of the error due to the inefficiency, the analysis is repeated by randomly rejecting the reconstructed jets based on the measured jet reconstruction efficiency. The difference from the nominal result described at Section 6.9 is taken as the systematic uncertainty, which is 0.02 % for the ε_b and 0.08 % for the $\sigma_{t\bar{t}}$ measurement. The obtained uncertainties are by definition single sided. We put the same size of the uncertainty for the opposite direction assuming that a similar variation could observed there.

The correction of the JVF selection efficiency is applied to MC to cover the discrepancy of the efficiency between data and MC. The measured efficiency with data has an uncertainty of 0.5 %. The size of the error due to the JVF selection efficiency is estimated by the common procedure described at the beginning of this section, which is $+0.8/-1.2$ % for the ε_b and $+5.1/-3.4$ % for the $\sigma_{t\bar{t}}$ measurement.

6.11.6 Lepton related uncertainties

We require exact one selected lepton in the final state as described in Section 6.3. Therefore, the uncertainties related to the leptons needs to be propagated into the result of ε_b and $\sigma_{t\bar{t}}$ measurements. The possible bias mainly varies the amount of the expected events but the shape of the b-tagged jet multiplicity distribution. This means that they basically biases $\sigma_{t\bar{t}}$

and have a small effect to ε_b. Below, we describe the details of the effects from each source of the systematic uncertainty.

Lepton energy scale

Reconstructed electrons have the energy scale uncertainty of 1-1.5 %, while muons have the uncertainty below 1 %. The size of the error due to the lepton energy scale is estimated by repeating the analysis by the common procedure described at the beginning of this section for electrons and without applying the energy correction for muons. The uncertainties due to the electron (muon) energy scale is assigned as 0.06 (0.11) % for the ε_b and 0.15 (0.34) % for the $\sigma_{t\bar{t}}$ measurement.

The original size of the energy uncertainty for the electron is larger than the one for muon, however the electron has less impact to the resultant uncertainty in the ε_b and $\sigma_{t\bar{t}}$ measurement than the muon with the mechanism below. If the energy scale of electron is increased (decreased), we observe less (more) jets because of the overlap removal between an electron and a jet, specifically the jet would be removed while the electron left. In this way, the event selection efficiency is less sensitive to the electron energy scale. Therefore, the acceptance gain (loss) due to the number of selected electrons would be cancelled by the loss (gain) due to the requirement of the number of jets for the electron case.

Lepton energy resolution

The electron (muon) energy in MC is smeared by 1 (10) %. The size of the error due to the electron energy resolution is estimated by the common procedure described at the beginning of this section. On the other hand, we adopt the different procedure for muon since we measure the muon energy resolution due to the inner tracker and the muon spectrometer separately. The analysis is repeated by changing the smearing parameter for the inner tracker and the muon spectrometer by $\pm$ 1 sigma individually. The largest difference from the nominal result is taken as the systematic uncertainty. In the end, the uncertainties due to the electron (muon) energy resolution is assigned as 0.07 (0.00) % for the ε_b measurement and 0.14 (0.08) % for the $\sigma_{t\bar{t}}$ measurement.

Reconstruction and trigger efficiencies

The reconstruction and identification efficiency for electron has the uncertainty of about 3 %, while below 1 % for muon as described in Section 5.3 and 5.4. The trigger efficiency has the uncertainty of typically 1 % for both electron and muon. The size of the error due to the efficiency is evaluated by the common procedure described at the beginning of this section, which is comma a few % for the ε_b and 1-2 % for the $\sigma_{t\bar{t}}$ measurement.

6.11.7 Mis-tagging efficiency for the b-tagging

The b-tagging efficiency for c-jets and light-jets, ε_c and ε_l, are the direct input to the expected number of b-tagged jets. The typical size of uncertainty for ε_c and ε_l is 12 % and 50 %, respectively. The size of the error due to the mis-tag efficiency for the b-tagging is estimated by the common procedure described at the beginning of this section. The size of the uncertainty is estimated to be almost negligible, comma a few per cent, for both ε_b and $\sigma_{t\bar{t}}$ measurement.

6.11.8 Missing transverse energy uncertainty

$E_{\mathrm{T}}^{\mathrm{miss}}$ is calculated with considering the soft interactions in the calorimeters as the soft-jet term and the cell-out term discussed in Section 5.6. The uncertainties for these terms are estimated to be approximately 10 %. In addition to these terms, $E_{\mathrm{T}}^{\mathrm{miss}}$ is sensitive to the multiple pp interactions which mostly affect the soft-term. The size of the error due to the $E_{\mathrm{T}}^{\mathrm{miss}}$ reconstruction is estimated by the common procedure described at the beginning of this section, which is ± 0.1 % for the ε_b and ± 0.3 % for the $\sigma_{t\bar{t}}$ measurement.

6.11.9 Heavy flavor fraction

The ATLAS experiment has performed the measurement of the W+b-jets cross section [100]. The measured cross section is approximately twice the theoretical prediction, although it is still consistent with the prediction within the uncertainty. The mis-modeling of the heavy flavor fraction varies the shape of the b-tagged jet multiplicity distribution. To estimate the size of uncertainty due to the mis-modeling of the heavy flavor fraction, the analysis is repeated by varying the fraction of b- and c-jets to twice and a half of the one in MC. The difference from the nominal result described at Section 6.9 is taken as the systematic uncertainty, which is $+0.4/-2.1$ % for the ε_b and $+2.8/-5.3$ % for the $\sigma_{t\bar{t}}$ measurement.

6.11.10 Generator, parton shower modeling

The imperfect modeling of the various kinematics in MC may result in the bias of the acceptance. To estimate the uncertainty due to the MC generator, the POWHEG sample is used instead of MC@NLO which is used as the baseline generator. The size of the error due to the MC generator is estimated by repeating the analysis with the acceptance calculated with the POWHEG sample. The difference from the nominal result is taken as the systematic uncertainty, which is ±2.0 % for the ε_b and ±4.8 % for the $\sigma_{t\bar{t}}$ measurement.

In order to study the effect of the parton shower modeling and the hadronization, both HERWIG and PYTHIA are used to hadronize the POWHEG samples. The difference between the POWHEG+HERWIG and the POWHEG+PYTHIA samples is used to estimate the systematic uncertainty. The relative difference of the acceptance between the two results is taken as the systematic uncertainty, which is ±2.0 % for the ε_b and ±4.0 % for the $\sigma_{t\bar{t}}$ measurement.

6.11.11 Initial and final state radiation

The amount of ISR and FSR varies the number of jets and the transverse momentum of particles in the event. Selection cuts for top quark events are sensitive to the number and kinematics of the jets. This means that ISR and FSR have some effect on the selection efficiency. In order to evaluate the uncertainties arising from ISR and FSR, the ACERMC generator interfaced with PYTHIA is used. The PYTHIA parameters related to ISR and FSR are varied in a range consistent with experimental data. The size of the error due to the mis-modeling of ISR and FSR is estimated by taking the difference between the ISR/FSR varied samples. The half of the difference is taken as the systematic uncertainty which is ± 0.8 % for the ε_b and ± 0.5 % for the $\sigma_{t\bar{t}}$ measurement.

6.11.12 MC statistics

The uncertainty introduced by the MC statistics is estimated from the uncertainties given in Table 6.4 and 6.5. This is found to be negligible.

6.12 Result

The measurement of the b-tagging efficiency with 4.7 fb^{-1} of pp collision data has been performed. The result is;

$$\varepsilon_b \quad = \quad 0.8744 \pm 0.0070(\text{stat.})^{+0.0807}_{-0.0765}(\text{syst.}).$$

This is consistent with the result obtained by using jets containing muon [97]. The precision of $+9.2/-8.8$ % is achieved. The data-MC scale factor of the b-tagging efficiency ($SF = \varepsilon_b^{\text{Data}}/\varepsilon_b^{\text{MC}}$) is obtained as

$$SF_{\text{Data-MC}} \quad = \quad 1.0098 \pm 0.0080(\text{stat.})^{+0.0932}_{-0.0883}(\text{syst.}).$$

This value is used in the analysis of the $\sigma_{t\bar{t}}$ measurement in dilepton final states.

The simultaneously extracted $\sigma_{t\bar{t}}$ is 170.6 $\pm$ 2.3 (stat.) $\pm$ 46.4 (syst.) pb which is consistent with the theoretical prediction of 166.78 pb, but has a huge uncertainty. The precise measurement of $\sigma_{t\bar{t}}$ in the dilepton final state will be described in the next chapter.

Chapter 7

Measurement of the production cross section

In this analysis, the measurement of the $t\bar{t}$ production cross section is based on the cut-based counting method using the dilepton final state as described in Section 1.5. The dilepton final state considered here is categorized into three groups, the ee, the $\mu\mu$ and the $e\mu$ channel. Each channel has a different acceptance and background contribution. Therefore, the analysis for each channel is treated separately. The final state with tau leptons is not considered. On the other hand, electrons and muons coming from tau decay is included as the signal event because they are isolated and cannot be distinguished from the lepton directly decayed from W bosons.

In the following, the event selection is described in Section 7.1. The estimate of the signal event acceptance is described in Section 7.2. In Section 7.3, the estimate of the background contribution is discussed. The distributions in the background control region and the signal region are shown in Section 7.4 and 7.5, respectively. Finally, the result of the measurement is summarized in Section 7.6.

7.1 Event selection

The event selection begins with the quality cuts below. Events are required to fire the single electron or muon trigger as discussed in Section 4.1.2. At least one of the selected leptons should match the trigger object at the EF level within $\Delta R < 0.15$. To guarantee the existence of the well reconstructed PV of the pp collision, at least five tracks are required to be associated to PV. The event with a `LooseBad` flagged jet described in Section 6.3 is discarded from the analysis to use the events with well reconstructed jets and $E_{\mathrm{T}}^{\mathrm{miss}}$. In order to remove the contamination of the cosmic muons in the $\mu\mu$ and $e\mu$ channel, the events are removed when there is a pair of muons which satisfies the criteria below;

- muons have opposite charge,
- $\Delta\phi$ between the muons is greater than 3.1 radian,
- both muons have the transverse impact parameter greater than 0.5 mm with respect to the beam spot, and
- both muons pass through the same side of x' where the coordinate x' is defined as same as the x axis but with its origin on the beam spot,

where the muons passing the muon selection criteria but the overlap removal with jets are considered here. The events are removed when an electron and a muon are reconstructed with

using a same track reconstructed by the inner detector, where the electron and the muon passing the selection criteria except the overlap removal with jets are considered. Only in MC samples, the selected lepton is required to match the true lepton from W or Z. This selection ensures that acceptance obtained from MC does not include a mis-identified lepton which is difficult to model in the simulation.

After these event quality cuts, we apply the following event selections to enhance the dilepton final state of $t\bar{t}$.

Two isolated leptons

We require the events to have exactly two isolated leptons with opposite charge. For the electron (muon) candidate, P_{T} is required to be greater than 25 (20) GeV, and pseudorapidity to satisfy $|\eta| < 2.47$ except $1.37 < |\eta| < 1.52$ ($|\eta| < 2.5$). The requirement of two isolated leptons gives a significant reduction of the QCD multi-jet and W+jets events.

$Z \to ee/\mu\mu$ veto

There are many remaining background events from Z/γ^* after requiring two isolated leptons in the ee and $\mu\mu$ channels. One can see a distinct shape difference between signal and Z/γ^* events in the distribution of the invariant mass of the dilepton system, $M_{\ell\ell}$, as shown in Figure 7.1. Events with $M_{\ell\ell}$ close to the Z boson mass, $M_Z = 91$ GeV, are vetoed to reject Z/γ^* events.

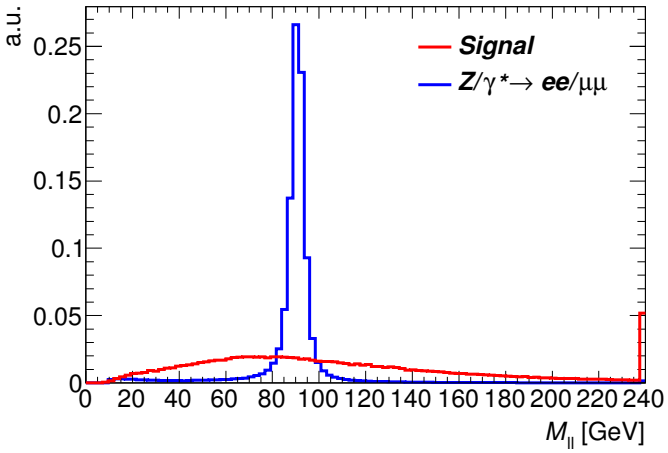


Figure 7.1: Invariant mass of dilepton system in $t\bar{t}$ and $Z/\gamma^* \to ee/\mu\mu$ events.

This selection is referred to as 'Z-veto' or 'Z-window cut'. The selection threshold will be optimized and discussed in Section 7.1.1.

Low-mass resonance suppression

In order to suppress the low-mass resonances of ee and $\mu\mu$ such as J/ψ production, we require the events to satisfy $M_{\ell\ell} > 15$ GeV.

Large missing transverse energy and sum of transverse energy

To suppress the dominant background from Z/γ^* events, large $E_{\mathrm{T}}^{\mathrm{miss}}$ is required for the ee and $\mu\mu$ channels since there is large $E_{\mathrm{T}}^{\mathrm{miss}}$ in the signal events due to the neutrinos as shown in Figure 7.2. The high $E_{\mathrm{T}}^{\mathrm{miss}}$ requirement also suppresses a QCD multi-jet contamination.

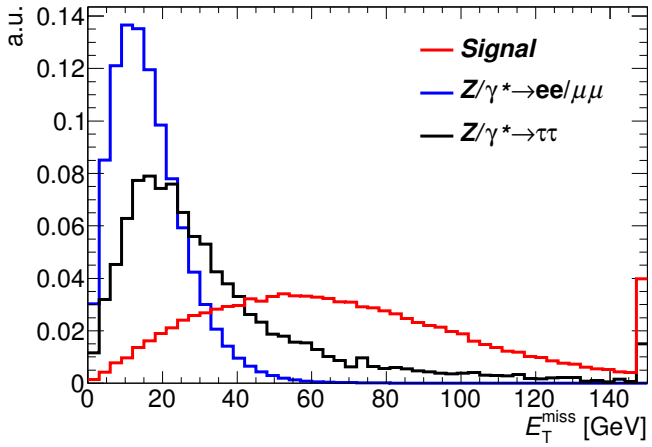


Figure 7.2: $E_{\mathrm{T}}^{\mathrm{miss}}$ distribution in $t\bar{t}$, $Z/\gamma^* \to ee/\mu\mu$ and $Z/\gamma^* \to \tau\tau$ events.

In the $e\mu$ channel, $Z/\gamma^* \to \tau\tau$ is a large background not like the ee and $\mu\mu$ channel. Due to the finite $E_{\mathrm{T}}^{\mathrm{miss}}$ from $Z/\gamma^* \to \tau\tau \to e\mu + \text{neutrinos}$, $E_{\mathrm{T}}^{\mathrm{miss}}$ is not a good variable to suppress $Z/\gamma^* \to \tau\tau$ as shown in Figure 7.2. Instead, the scalar sum of E_{T} of the selected leptons and jets, called H_{T}, shown in Figure 7.3, is used to reject $Z/\gamma^* \to \tau\tau$.

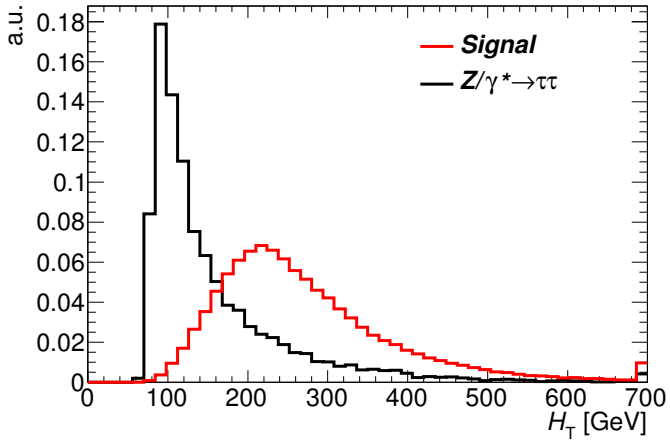


Figure 7.3: H_{T} distribution in $t\bar{t}$ and $Z/\gamma^* \to \tau\tau$ events.

The selection thresholds for $E_{\mathrm{T}}^{\mathrm{miss}}$ and H_{T} will be optimized and discussed in Section 7.1.1.

At least two jets

Selecting the events with high jet multiplicity enhances $t\bar{t}$ events as shown in Figure 7.4. This is because the production cross section of Z/γ^* events, which are the dominant background with two isolated leptons, with two additional partons is about sixteen times less than the inclusive cross section. The requirement of high jet multiplicity also suppresses the di-boson contamination. We require the events to have at least two selected jets with P_{T} greater than 25 GeV.

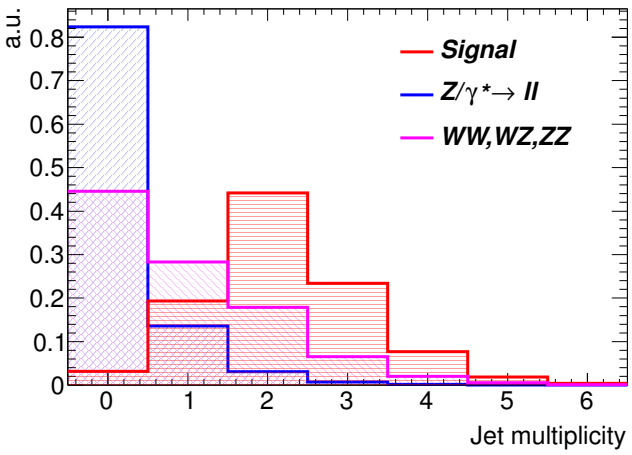


Figure 7.4: The jet multiplicity distribution in $t\bar{t}$, $Z/\gamma^* \to \ell\ell$ and di-boson events.

Identification of jets originating from b-quarks

Top quark pair events contain two b-quarks. On the other hand, jets generated by the strong interaction tend to originate from light quarks or gluons. Typically, the fraction of the events with c-quark is 8% and the one with b-quark is 3 %. Hereby, the requirement of the existence of the b-quark jet can reject many types of background without top quarks as shown in Figure 7.5. We require the events to have at least one b-tagged jet. The operating point with 85 % efficiency for true b-jets in the MC sample of $t\bar{t}$ is used as mentioned in Section 5.7.

7.1.1 Cut values

The cut values are determined so that the uncertainty for the $\sigma_{t\bar{t}}$ measurement, $\delta\sigma_{t\bar{t}}$, is minimized. The uncertainties considered here are the statistical error in data and the systematical errors from JES and the b-tagging which are expected to be the dominant source of the systematic uncertainty. Here, the integrated luminosity is assumed to be 500 pb^{-1}. We repeat the full analysis with various combinations of the cut values, and compare each uncertainty.

Figure 7.6 shows the expected uncertainty for the ee and the $\mu\mu$ channels with some combinations of $E_{\mathrm{T}}^{\mathrm{miss}}$ and Z-window cuts. The minimum is found at the requirement of $E_{\mathrm{T}}^{\mathrm{miss}} >$ 40 GeV and $M_{\ell\ell} < 81$ GeV or 101 GeV $< M_{\ell\ell}$, which we adopt as the event selection. As seen in Figure 7.6, the expected precision are almost the same if the cut value on $E_{\mathrm{T}}^{\mathrm{miss}}$ is greater than 35 GeV and Z mass window is wider than 10 GeV. This means that the precision of our

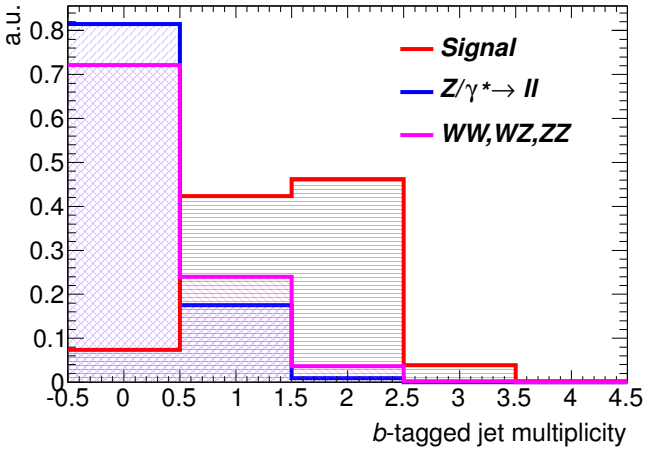


Figure 7.5: The b-tagged jet multiplicity distribution in $t\bar{t}$, $Z/\gamma^* \to \ell\ell$ and di-boson events.

measurement is insensitive to the possible difference between data and simulation in terms of $E_{\mathrm{T}}^{\mathrm{miss}}$ modeling.

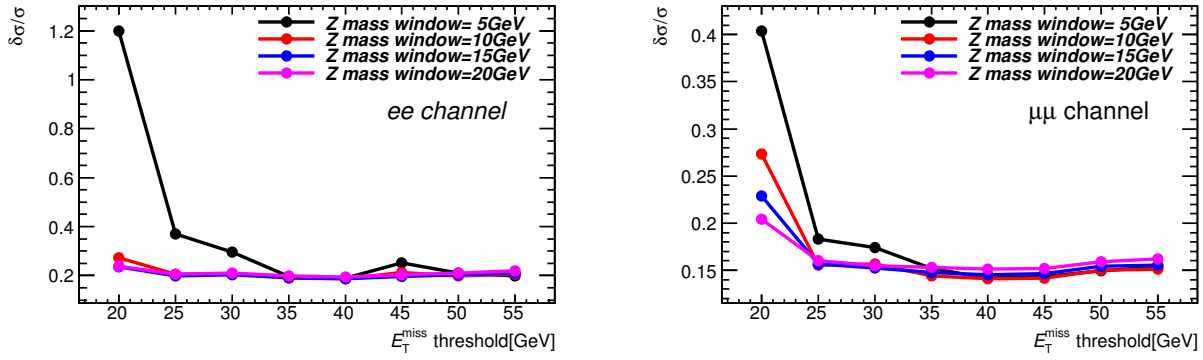


Figure 7.6: The expected uncertainties of the cross section measurement in the ee and $\mu\mu$ channels with different combinations of the selection threshold.

For the $e\mu$ channel, we compare the expected precision with the different cut value on H_{T}. As shown in Figure 7.7, the precision does not change for H_{T} below around 150 GeV. So far, we consider $\delta\sigma_{t\bar{t}}$ only, but the higher signal-to-noise ratio is preferable if $\delta\sigma_{t\bar{t}}$ is the same. Therefore, we require the events to satisfy $H_{\mathrm{T}} > 130$ GeV.

Now all the cut values are determined. Table 7.1 summarizes all the event selections used in this analysis.

7.1.2 Remaining events expected by the MC samples

We check the expected number of events by using the MC samples to see how each selection works. The considered processes are the signal and the background events including single lepton final state of $t\bar{t}$ events, W/Z boson, di-boson and single top productions by s-, t-channel and Wt process. We also check the expected signal-to-background ratio denoted as S/B and

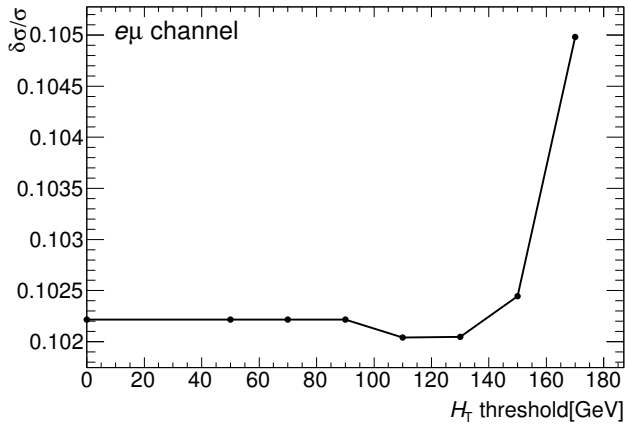


Figure 7.7: The expected uncertainties of the cross section measurement in the $e\mu$ channel with a different H_{T} threshold.

Table 7.1: Event selections used to measure the top quark pair production cross section for the final states with ee, $\mu\mu$ and $e\mu$.

	ee	$\mu\mu$	$e\mu$
Trigger requirement	Electron trigger	Muon trigger	Electron or muon trigger
Trigger match	at least one lepton matching trigger $\Delta R < 0.15$		
Non collision BG rejection	requiring a primary vertex with at least 5 tracks		
Jet cleaning	remove events with a `LooseBad` jet		
Cosmic rejection	-	does not have a cosmic muon candidate	
e/μ overlap rejection	reject events if an electron and a muon share a track		
Lepton requirement	$N_e = 2$	$N_\mu = 2$	$N_e = 1$ and $N_\mu = 1$
Lepton charges	Leptons have an opposite charge		
Z-veto selection	$\lvert M_{\ell\ell} - M_Z \rvert$ >10 GeV		-
Low-mass resonance veto	$M_{\ell\ell}$ >15 GeV		-
$E_{\mathrm{T}}^{\mathrm{miss}}$/ H_{T}	$E_{\mathrm{T}}^{\mathrm{miss}} > 40$ GeV		$H_{\mathrm{T}} > 130$ GeV
Jet requirement	$N_{\mathrm{jet}} \geq 2$ with $P_{\mathrm{T}} > 25$ GeV		
b-tagging	at least one b-tagged jet		
Truth match (MC only)	The selected lepton matches the true lepton		

the signal significance defined as $S/(\sqrt{S+B})$, where S is the number of signal events and B the number of background events. All the necessary corrections for MC are applied. The results are listed in Table 7.2, 7.3, 7.4 for the ee, the $\mu\mu$ and the $e\mu$ channel, respectively, at each step of the selection.

Table 7.2: The number of remaining events for the ee channel at each event selection step for each physics process estimated by MC samples. S/B and $S/\sqrt{S+B}$ are also shown.

Selection	$t\bar{t}$ dilepton	$t\bar{t}$ background	Z+jets	W+jets	Single top	WW, WZ ZZ	Background (Total)	$\frac{S}{B}$	$\frac{S}{\sqrt{S+B}}$
Trigger requirement	10312.6	101625.1	3699863.6	21454316.0	32445.4	12889.7	25301139.8	0.0	2.0
Non colliding BG rejection	10305.2	101559.0	3569077.2	20443848.0	32411.1	12645.6	24159540.9	0.0	2.1
Cosmic rejection	10305.2	101559.0	3569077.2	20443848.0	32411.1	12645.6	24159540.9	0.0	2.1
#Lepton ≥ 2	1779.6	4.1	691417.6	55.4	183.3	1356.4	693016.8	0.0	2.1
Trigger matching	1769.0	4.1	684857.6	54.6	182.2	1344.8	686443.3	0.0	2.1
e/μ overlap rejection	1769.0	4.1	684857.6	54.6	182.2	1344.8	686443.3	0.0	2.1
No bad jet	1750.0	4.1	677740.6	54.6	180.1	1330.4	679309.7	0.0	2.1
$E_{\mathrm{T}}^{\mathrm{miss}}/H_{\mathrm{T}}$	1309.1	2.9	6938.3	21.3	128.5	437.0	7528.0	0.2	13.9
#Jet$\geq$2	1028.6	2.5	1227.7	2.5	49.4	96.0	1378.1	0.7	21.0
#Lepton==2	1028.4	2.4	1227.6	2.5	49.4	89.8	1371.7	0.7	21.0
Opposite sign leptons	1021.6	1.5	1213.2	1.8	49.3	80.1	1346.0	0.8	21.0
$M_{\ell\ell} \geq 15$GeV	1016.9	1.5	1205.6	1.8	48.9	79.8	1337.6	0.8	21.0
Z-veto selection	855.7	1.5	199.8	1.2	41.3	34.7	278.5	3.1	25.4
Truth match	849.2	0.0	199.8	1.2	41.3	34.7	277.0	3.1	25.3
b-tagging	820.2	0.0	65.8	0.6	37.1	10.9	114.4	7.1	26.7

Table 7.3: The number of remaining events for the $\mu\mu$ channel at each event selection step for each physics process estimated by MC samples. S/B and $S/\sqrt{S+B}$ are also shown.

Selection	$t\bar{t}$ dilepton	$t\bar{t}$ background	Z+jets	W+jets	Single top	WW, WZ ZZ	Background (Total)	$\frac{S}{B}$	$\frac{S}{\sqrt{S+B}}$
Trigger requirement	10204.2	110513.1	4232618.1	23557996.0	35517.1	12863.4	27949507.7	0.0	1.9
Non colliding BG rejection	10198.9	110439.2	4068932.2	22328522.0	35482.2	12609.0	26555984.6	0.0	2.0
Cosmic rejection	10198.9	110439.2	4068932.2	22328522.0	35482.2	12609.0	26555984.6	0.0	2.0
#Lepton ≥ 2	4581.6	28.8	1724388.6	70.5	448.3	3357.2	1728293.4	0.0	3.5
Trigger matching	4293.5	27.3	1639028.1	71.5	419.9	3179.0	1642726.0	0.0	3.3
e/μ overlap rejection	4293.5	27.3	1639028.1	71.5	419.9	3179.0	1642726.0	0.0	3.3
No bad jet	4241.0	27.0	1620075.3	71.0	414.4	3139.2	1623726.9	0.0	3.3
$E_{\mathrm{T}}^{\mathrm{miss}}/H_{\mathrm{T}}$	3258.6	18.4	19048.2	33.0	305.2	1092.4	20497.2	0.2	21.1
#Jet$\geq$2	2495.2	15.4	3059.0	1.2	112.0	211.7	3399.2	0.7	32.5
#Lepton==2	2494.8	14.9	3059.0	1.2	112.0	196.6	3383.7	0.7	32.5
Opposite sign leptons	2494.7	8.5	3058.9	1.2	111.5	185.3	3365.3	0.7	32.6
$M_{\ell\ell} \geq 15$GeV	2474.8	8.4	3031.7	1.2	111.1	184.4	3336.7	0.7	32.5
Z-veto selection	2098.8	6.7	610.5	1.2	96.6	78.9	794.0	2.6	39.0
Truth match	2098.8	6.1	610.5	1.2	96.6	78.9	793.3	2.6	39.0
b-tagging	2070.2	5.3	198.2	0.0	87.4	23.8	314.6	6.4	41.7

The efficiency of selecting two leptons for events with two real leptons such as the signal and Z events are 18 % for the ee channel, 43 % for the $\mu\mu$ channel and 28 % for the $e\mu$ channel. This corresponds to the selection efficiency of 42 % for electron and 66 % for muon. The difference between the electron and muon comes from the detector acceptance and the particle identification efficiency.

One can see that the events without two real leptons such as W+jets is well suppressed by the requirement of two leptons. For the W/Z+jets and the di-boson events, the requirement of the two additional jets and the b-tagging requirement gives a good background suppression as we expected. Approximately 5 % of the single top events contain two real leptons through the

Table 7.4: The number of remaining events for the $e\mu$ channel at each event selection step for each physics process estimated by MC samples. S/B and $S/\sqrt{S+B}$ are also shown.

Selection	$t\bar{t}$ dilepton	$t\bar{t}$ background	Z+jets	W+jets	Single top	WW, WZ ZZ	Background (Total)	$\frac{S}{B}$	$\frac{S}{\sqrt{S+B}}$
Trigger requirement	20709.6	198572.8	7919665.2	45003524.0	66206.2	23299.5	53211267.7	0.0	2.8
Non colliding BG rejection	20695.6	198445.2	7625546.1	42763648.0	66139.4	22857.9	50676636.5	0.0	2.9
Cosmic rejection	20695.6	198445.2	7625546.1	42763648.0	66139.4	22857.9	50676636.5	0.0	2.9
#Lepton ≥ 2	5773.9	23.7	3954.4	137.0	581.2	1759.6	6455.8	0.9	52.2
Trigger matching	5753.6	23.6	3931.8	135.5	579.1	1750.2	6420.3	0.9	52.1
e/μ overlap rejection	5753.6	23.6	3931.8	135.5	579.1	1750.2	6420.3	0.9	52.1
No `LooseBad` jet	5684.2	23.3	3888.0	134.9	573.0	1728.4	6347.6	0.9	51.8
$E_{\mathrm{T}}^{\mathrm{miss}}$ /H_{T}	5348.2	21.7	424.1	26.7	470.4	779.8	1722.7	3.1	63.6
#Jet$\geq$2	4319.8	19.4	207.0	16.2	208.9	228.1	679.6	6.4	61.1
#Lepton==2	4318.9	19.1	204.1	16.2	208.9	206.1	654.4	6.6	61.2
Opposite sign leptons	4303.6	10.8	195.7	4.6	207.1	172.2	590.4	7.3	61.5
$M_{\ell\ell} \geq 15$GeV	4295.2	10.8	195.2	4.6	206.7	172.0	589.3	7.3	61.5
Z-veto selection	4295.2	10.8	195.2	4.6	206.7	172.0	589.3	7.3	61.5
Truth match	4279.9	7.6	195.2	4.6	206.7	172.0	586.1	7.3	61.4
b-tagging	4245.8	6.9	61.5	1.4	186.2	53.0	308.9	13.3	61.7

Wt production. In fact, the dilepton final state via the Wt production is the only irreducible background because the process of $Wt \to \ell\nu\ell\nu b$ contains the two leptons, large $E_{\mathrm{T}}^{\mathrm{miss}}$ and the b-quark jet.

The expected S/B is 7.4, 6.4 and 13.3 for the ee, the $\mu\mu$ and the $e\mu$ channels, respectively. This estimate includes the events with leptons which do not come from W/Z bosons which are not reliable in MC. In addition, there are no estimate for the QCD multi-jet events. However, we can still expect to achieve a high S/B since the contribution from them is small.

7.2 Signal acceptance

Acceptance and the branching ratios of the $t\bar{t}$ events are evaluated using the MC sample generated by the MC@NLO generator. The estimated acceptance is 6.74 %, 16.72 % and 16.99 % for the ee, the $\mu\mu$ and the $e\mu$ channel, respectively. The branching ratios of the $t\bar{t}$ events decaying into the ee, the $\mu\mu$ and the $e\mu$ final state are also extracted from the same sample to be 1.63 %, 1.61 % and 3.23 %, respectively.

As shown in Table 7.2, 7.3 and 7.4, the signal-to-background ratio is high. Therefore, the uncertainty related to background estimation is not numerically important. The systematic uncertainty of the acceptance limits the precision of the $\sigma_{t\bar{t}}$ measurement. Table 7.5 summarizes the systematic uncertainty for each channel. The total uncertainty is obtained by adding all contributions in quadrature. The size of the uncertainty is determined to be $+12.1/-12.6$ %, $+7.0/-7.9$ % and $+8.2/-8.5$ % for the ee, the $\mu\mu$ and the $e\mu$ channels, respectively. The main contributions come from JES, the lepton efficiency, the b-tagging efficiency and the signal modeling. Some of the uncertainties are cancelled in the channel containing a muon. This is why the estimated acceptance for the $\mu\mu$ channel is the most precise. The details of the systematic uncertainty including the mechanism of the cancelation of the uncertainty in the $\mu\mu$ and $e\mu$ channel are described below.

To estimate the systematic uncertainty, we take a difference between the nominal acceptance shown in Table 7.5 and the one estimated by MC with the parameter of interest varied by ± 1 sigma. This is the same procedure used in the ε_b measurement presented in Section 6.11 unless otherwise stated.

Table 7.5: Systematic uncertainty on the $t\bar{t}$ acceptance.

Process	ee	$\mu\mu$	$e\mu$
Acceptance [%]	6.74	16.72	16.99
Acceptance× BR[%]	0.11	0.27	0.55
	$\delta\mathcal{A}/\mathcal{A}$ [%]	$\delta\mathcal{A}/\mathcal{A}$ [%]	$\delta\mathcal{A}/\mathcal{A}$ [%]
MC statistics	+1.2 / −1.2	+0.8 / −0.8	+0.6 / −0.6
Jet energy scale	+4.4 / −4.2	+2.7 / −3.5	+2.0 / −2.5
Jet energy resolution	+0.2 / −0.2	+0.5 / −0.5	+0.7 / −0.7
Jet reco. efficiency	+0.0 / −0.0	+0.0 / −0.0	+0.1 / −0.1
Jet vertex fraction	+0.7 / −1.3	+0.9 / −1.2	+1.1 / −0.7
Missing Et uncertainty	+0.0 / −0.0	+0.1 / −0.1	+0.0 / −0.0
El. energy scale	+0.3 / −0.3	+0.0 / −0.0	+0.2 / −0.2
El. energy resolution	+0.1 / −0.1	+0.0 / −0.0	+0.1 / −0.1
El. reco. efficiency	+5.8 / −5.7	+0.0 / −0.0	+2.9 / −2.9
El. trig. efficiency	+3.9 / −4.2	+0.0 / −0.0	+2.2 / −1.8
Mu. energy scale	+0.0 / −0.0	+0.2 / −0.2	+0.2 / −0.2
Mu. energy resolution	+0.0 / −0.0	+0.0 / −0.0	+0.1 / −0.1
Mu. reco. efficiency	+0.0 / −0.0	+1.6 / −1.7	+1.1 / −0.7
Mu. trig. efficiency	+0.0 / −0.0	+2.9 / −3.0	+0.1 / −0.0
b-tagging efficiency	+3.1 / −4.5	+3.4 / −4.3	+3.7 / −4.4
c-tagging efficiency	+0.0 / −0.2	+0.0 / −0.1	+0.1 / −0.0
l-tagging efficiency	+0.0 / −0.3	+0.0 / −0.2	+0.1 / −0.0
Generator	+2.7 / −2.7	+2.1 / −2.1	+3.5 / −3.5
Parton shower modeling	+4.4 / −4.4	+2.2 / −2.2	+2.6 / −2.6
ISR/FSR	+5.7 / −5.7	+1.3 / −1.3	+3.0 / −3.0
PDF	+2.8 / −2.8	+2.5 / −2.5	+2.2 / −2.2
Total uncertainty	+12.1 / −12.6	+7.0 / −7.9	+8.2 / −8.5

MC statistics

Using the whole sample, corresponding to approximately 15 million events, the size of the statistical uncertainty becomes 1.2 % for the ee, 0.8 % for the $\mu\mu$ and 0.6 % for the $e\mu$ channel.

JES uncertainty

A shift in JES causes the bias of the selection efficiency of at least two jets requirement, because the shape of the jet multiplicity distribution is varied as shown in Figure 7.8. On top of that, the mis-understandings of JES changes the shape of the $E_{\mathrm{T}}^{\mathrm{miss}}$ distribution as shown in Figure 7.9. The size of the uncertainty due to JES is determined to be $+4.4/-4.2$ %, $+2.7/-3.5$ % and $+2.0/-2.5$ % for the ee, the $\mu\mu$ and the $e\mu$ channel, respectively.

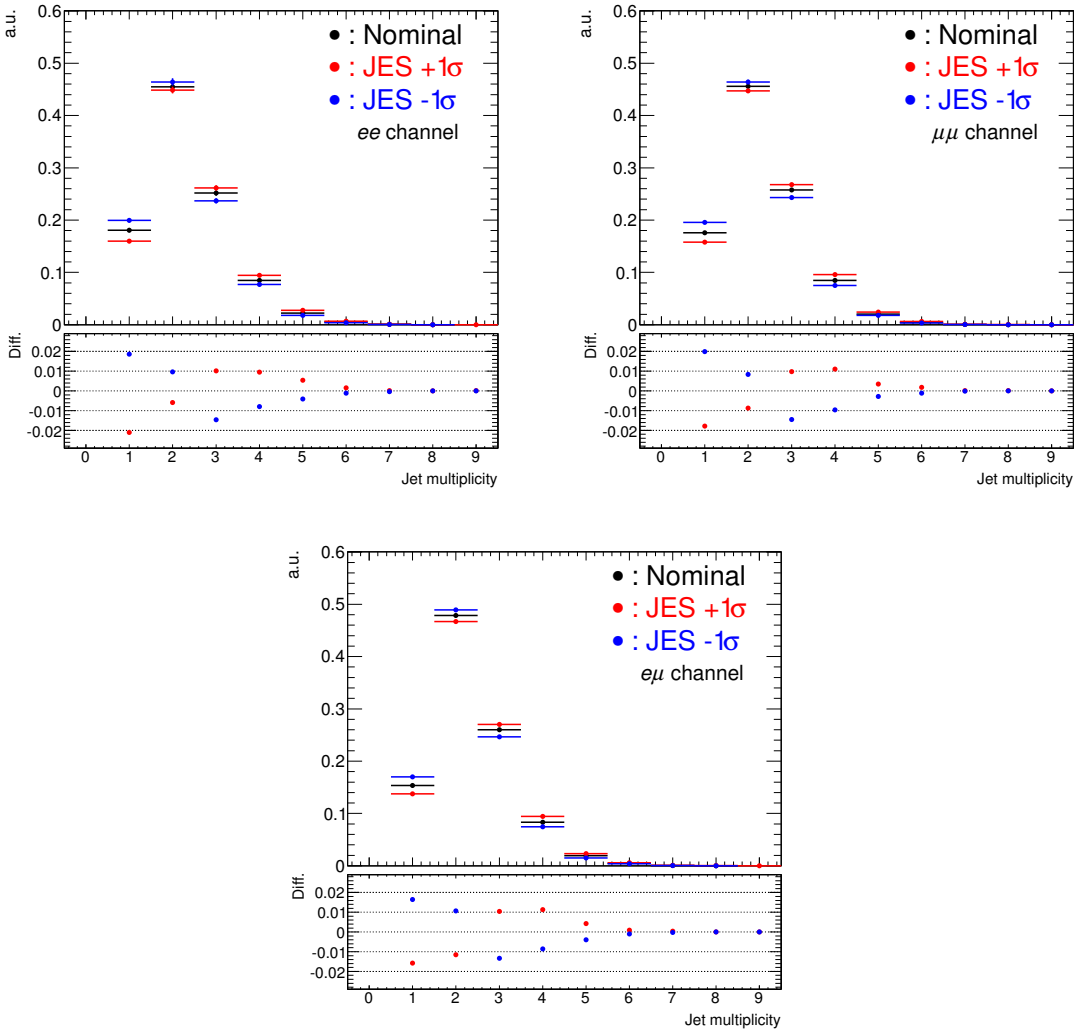


Figure 7.8: The comparison of the number of jets distribution among the samples with different JES. The bottom plot in each figure shows the difference from the nominal sample for JES $+1\sigma$ (red) and for JES -1σ (blue) cases.

The ee channel has a larger uncertainty even though the shift of jet multiplicity and $E_{\mathrm{T}}^{\mathrm{miss}}$ due to JES variation is almost the same for the three channels. This is explained by the

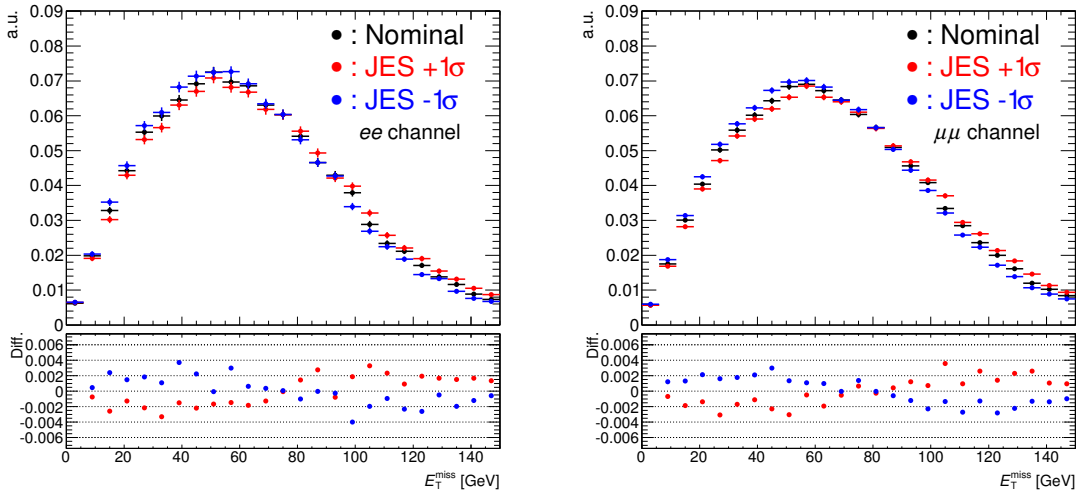


Figure 7.9: The comparison of the $E_{\mathrm{T}}^{\mathrm{miss}}$ distribution among the samples with different JES. The bottom plot in each figure shows the difference from the nominal sample for JES $+1\sigma$ (red) and for JES -1σ (blue) cases.

different order of selecting jets and leptons. In the reconstructed particle selection, jets around the selected electron are removed, while muons around the jet are killed. This means that the acceptance gain due to the increased number of jets for example is partly canceled in the $\mu\mu$ channel by the acceptance loss of muons, and *vice versa*. This effect can be seen in Figure 7.10 which shows the acceptance at each selection step. In the final state containing muon, the acceptance is decreased when we require the existence of two leptons in the sample with increased JES, which is not the case in the ee channel.

Jet energy resolution uncertainty

Mis-understanding of the jet energy resolution makes a similar effect to the acceptance as seen in the case of the JES mis-understanding. It basically changes the number of selected jets and the $E_{\mathrm{T}}^{\mathrm{miss}}$ distribution. The uncertainty on the acceptance from the resolution uncertainty is estimated to be ± 0.2 %, ± 0.5 % and ± 0.7 % for the ee, the $\mu\mu$ and the $e\mu$ channel, respectively.

Jet reconstruction and selection efficiency

The acceptance can be mis-modeled by the mis-understanding of the jet reconstruction and the JVF selection efficiency. As discussed in Section 5.5, the reconstruction efficiency is lower by one percent in real data for the jets with P_{T} below 30 GeV. In addition, the JVF selection efficiency in real data is lower by a few percent. The size of the uncertainty from the jet reconstruction is estimated to be negligible for all the channels, while the uncertainty from the JVF selection efficiency is $+0.7/-1.3$ %, $+0.9/-1.2$ % and $+1.1/-0.7$ % for the ee, the $\mu\mu$ and $e\mu$ channel, respectively.

Lepton energy uncertainty

The size of the uncertainty from the lepton energy scale and resolution for electron and muon is estimated to be $\mathcal{O}(0.1)$ % for all the channels. This relatively small uncertainty is achieved by a high precision calibration made with high statistics Z samples.

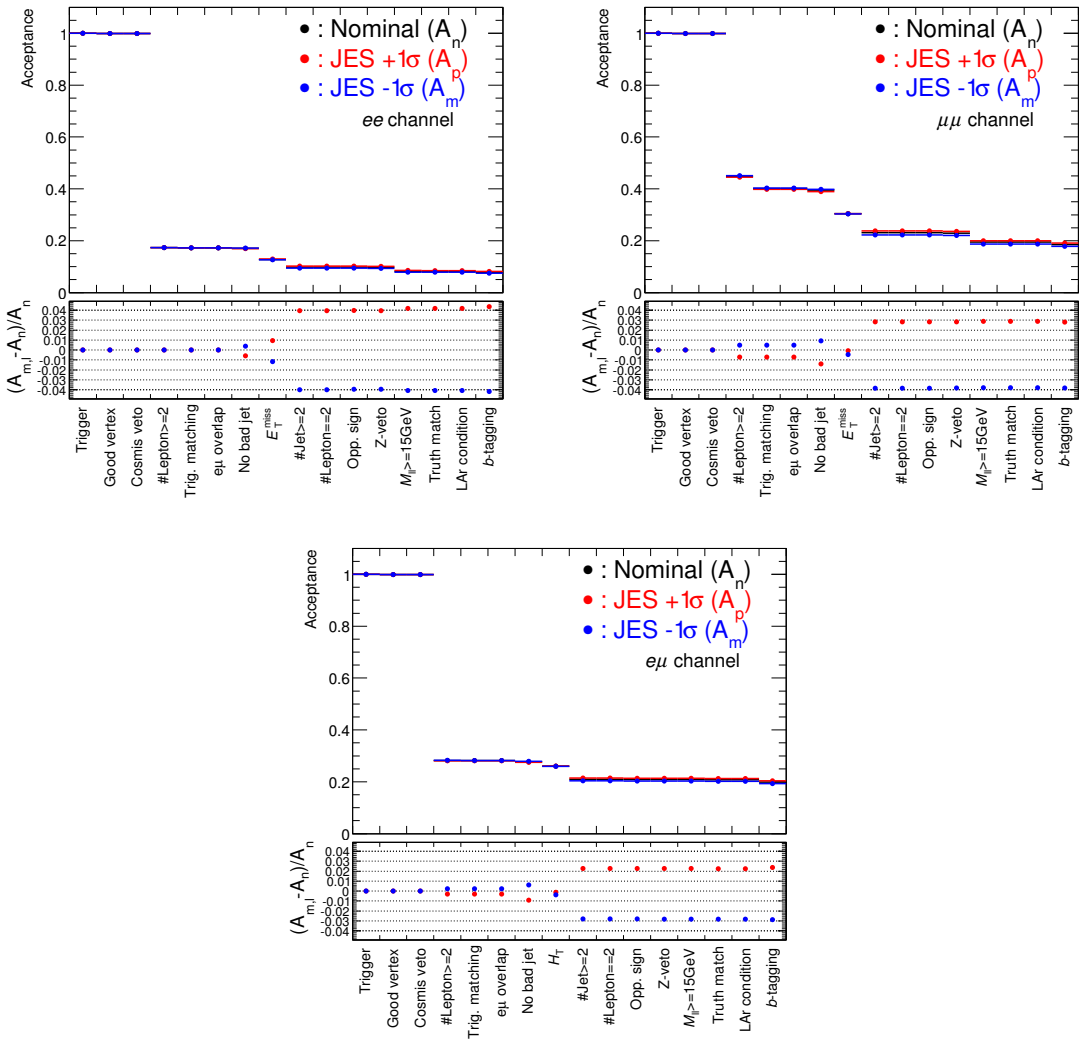


Figure 7.10: The acceptance at each selection step of the sample with various JES for the ee (top left), the $\mu\mu$ (top right) and the $e\mu$ (bottom) channel. The bottom plot in each figure shows the relative difference from the nominal JES sample. The red (blue) points show the sample with shifted JES by $+1$ (-1) sigma.

Lepton efficiency uncertainty

The total uncertainty from the lepton trigger, reconstruction and selection efficiency turns out to be approximately 7 %, 3 % and 4 % for the ee, the $\mu\mu$ and the $e\mu$ channel, respectively. This is rather large uncertainty because the lepton related efficiency directly affects the acceptance.

$E_{\mathrm{T}}^{\mathrm{miss}}$ related uncertainty

The effect of mis-modeling of $E_{\mathrm{T}}^{\mathrm{miss}}$ due to the energy scale of jets and leptons is implicitly included in the uncertainty from JES and lepton energy scales presented above. Here, the uncertainty sources which relate only to the $E_{\mathrm{T}}^{\mathrm{miss}}$ calculation, the soft-jet and cell-out terms, are discussed. The soft-jet and cell-out terms are sensitive to the number of associated pp interactions and have a 6-13 % uncertainty, as described in Section 5.6. But the size of the uncertainty on the acceptance is estimated to be negligible.

b-tagging related uncertainty

The measurement of the b-tagging performance is described in Section 5.7 and Chapter 6. The typical uncertainty for the b-tagging efficiency for b-, c- and light-jets are 9 %, 30 % and 50 %, respectively.

Although the estimated fake rate has a large uncertainty, the size of the uncertainty on the acceptance from the fake rate is almost negligible, less than one percent, because signal events do not have many c-jets or light-jets.

The uncertainty of the b-tagging efficiency is the main source of the systematic uncertainty on acceptance, because it is much larger than the ones for other particles such as leptons or jets. Therefore, we try to measure the b-tagging efficiency as precisely as possible as described in Chapter 6. On top of that, the loose operation point with the requirement of at least one b-tagged jet is adopted to reduce the uncertainty. The mechanism is described as the following. Assuming N_{BG} is negligible since the signal-to-background ratio is expected to be high, the acceptance $\mathcal{A}$ is the only variable affected by the b-tagging uncertainty. Let us also assume that the signal events have two b-jets in the final state. The acceptance with the requirement of at least one b-tagged jet can be written as

$$\mathcal{A} \propto \varepsilon_b^2 + 2\varepsilon_b(1-\varepsilon_b). \tag{7.1}$$

Defining the uncertainty of $\sigma_{t\bar{t}}$, $\mathcal{A}$ and ε_b, as $\delta\sigma_{t\bar{t}}$, $\delta\mathcal{A}$ and $\delta\varepsilon_b$, respectively, one can immediately see the following relation,

$$\begin{aligned} \delta\sigma_{t\bar{t}} &\propto \delta\mathcal{A} \left(= \frac{d\mathcal{A}}{d\varepsilon_b}\delta\varepsilon_b\right) \\ &\propto 2\,(1-\varepsilon_b)\,\delta\varepsilon_b. \end{aligned} \tag{7.2}$$

This indicates that it is important to choose an operation point giving the higher efficiency to suppress the systematic uncertainty, while keeping the background suppression high enough.

The uncertainty caused by $\delta\varepsilon_b$ is $+3.1/-4.5$ %, $+3.4/-4.3$ % and $+3.7/-4.4$ % for the ee, the $\mu\mu$ and the $e\mu$ channels, respectively. This is smaller than $\delta\varepsilon_b$ itself, 9 %, as we expected.

$t\bar{t}$ modeling uncertainty

We chose the MC@NLO generator interfaced with Herwig as the baseline MC sample. Using different MC samples may change the acceptance because the kinematics and the number of particles in the final state may differ.

We checked the possible effects from the generator, the parton shower and the hadronization modeling, the ISR and FSR modeling and the PDF modeling. We basically take the difference between the samples which are simulated with the same setting except the modeling which we want to examine. The detail for each systematic source is described in the following.

- *Uncertainty from the generator choice*

Figure 7.11 shows the acceptance at each selection step in $t\bar{t}$ MC generated by the MC@NLO and POWHEG generator. One can see the significant difference at the requirement of two leptons

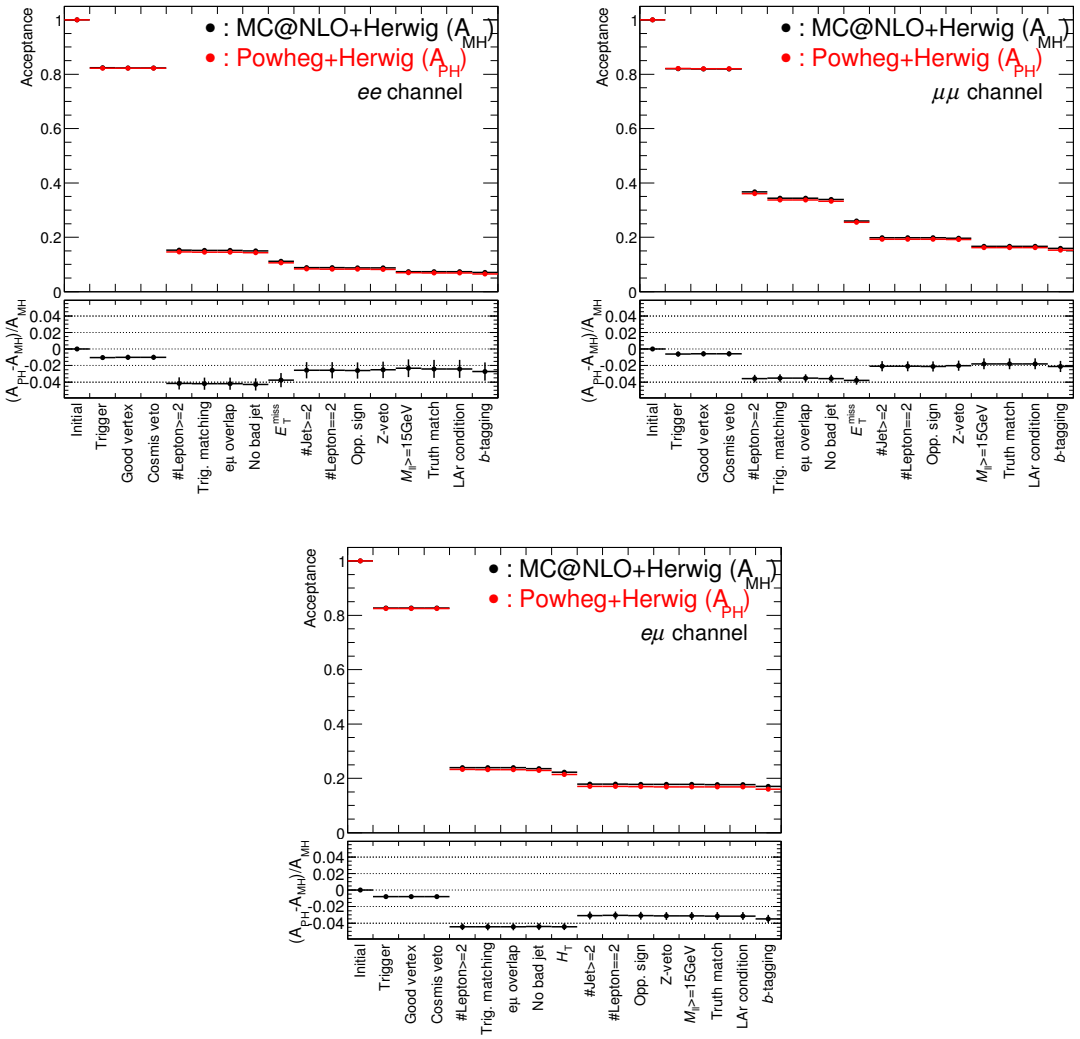


Figure 7.11: The acceptance at each selection step for the MC sample generated with the MC@NLO generator and the POWHEG generator for the ee (top left), the $\mu\mu$ (top right) and the $e\mu$ (bottom) channel. Bottom part of each plot shows the relative acceptance difference between the two samples.

and two jets. The leptons simulated by POWHEG have a low probability to be selected than the ones by MC@NLO. This effect comes from the convolution of many sources, *e.g.* the lepton P_{T} and η distribution. The other feature is that POWHEG produces more jets in the final state as shown at the left plots in Figure 7.12 to 7.14. The acceptance gain at the two jet requirement

partly cancels the loss of the acceptance due to the lepton selection. In the end, the estimated uncertainty from the generator choice is ±2.7 %, ±2.1 % and ±3.5 % for the ee, the $\mu\mu$ and the $e\mu$ channel, respectively.

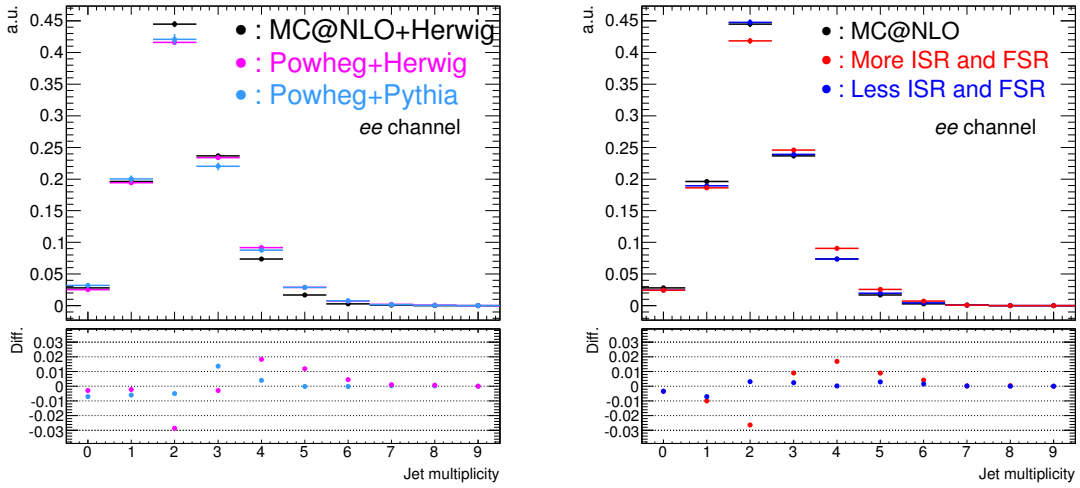


Figure 7.12: Distributions of jet multiplicity after requiring two selected electrons for various MC samples. Bottom plots shows the difference between the samples of interest to estimate the systematic uncertainty, *i.e.* (Powheg+Herwig)-(MC@NLO+Herwig) in magenta, (Powheg+Herwig)-(Powheg+Pythia) in light blue, (More ISR/FSR)-(MC@NLO) in red, (Less ISR/FSR)-(MC@NLO) in blue.

- *Uncertainty from the parton shower and the hadronization modeling*

Figure 7.15 shows the acceptance at each selection step in the $t\bar{t}$ sample generated by Powheg+Herwig or Powheg+Pythia comparing the modeling of the parton shower and the hadronization. We see more accepted electrons and less accepted muons in the sample using Herwig. This behavior can be explained as follows. The left figures in Figure 7.16 to 7.18 show the number of reconstructed tracks after requiring the two selected leptons in the samples with Herwig and Pythia. In the Herwig sample, there are less tracks than the Pythia sample. This causes the acceptance gain of the isolated lepton selection. The isolation selection for muon is tuned to be less sensitive to the number of tracks compared to the one for electrons, leading to the smaller gain of isolated muons. Besides, we see more jets in the Herwig sample, as seen in the left figures in Figure 7.12 to 7.14. This causes to select less muons because the probability to survive the overlap removal between jets and muons gets lower. Therefore, the electron (muon) acceptance becomes larger (smaller) in total. In the end, the estimated uncertainty from the parton shower modeling is ±4.4 %, ±2.2 % and ±2.6 % for the ee, the $\mu\mu$ and the $e\mu$ channel, respectively.

- *Uncertainty from the ISR/FSR modeling*

Figure 7.19 shows the acceptance at each selection step in the $t\bar{t}$ sample generated with increased or decreased ISR/FSR. In these plots, we see a significant difference at the requirement of two leptons. This can be explained by the following mechanism. The distributions of the number of reconstructed tracks after requiring two selected leptons are shown in the right on

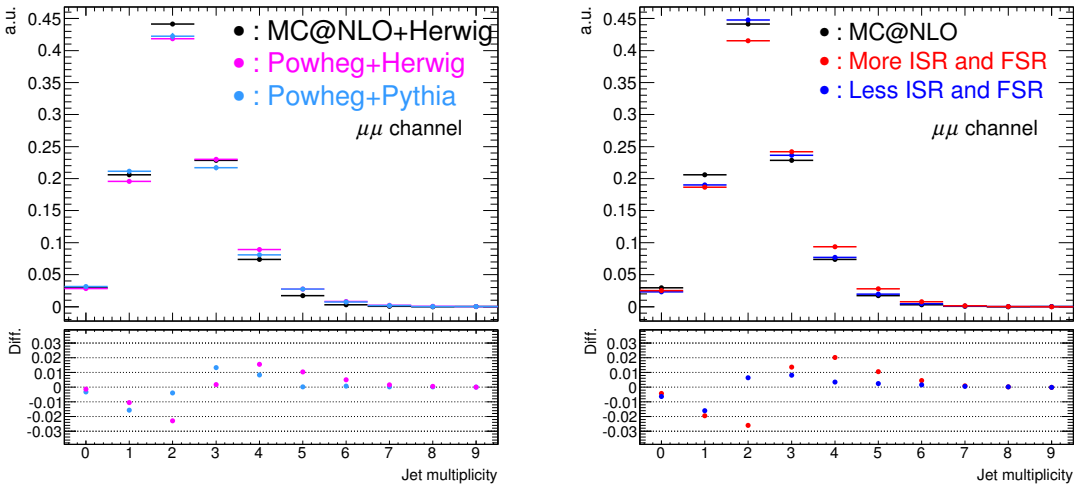


Figure 7.13: Distributions of the jet multiplicity after requiring two selected muons for various MC samples. Bottom plots shows the difference between the samples of interest to estimate the systematic uncertainty, *i.e.* (POWHEG+HERWIG)-(MC@NLO+HERWIG) in magenta, (POWHEG+HERWIG)-(POWHEG+PYTHIA) in light blue, (More ISR/FSR)-(MC@NLO) in red, (Less ISR/FSR)-(MC@NLO) in blue.

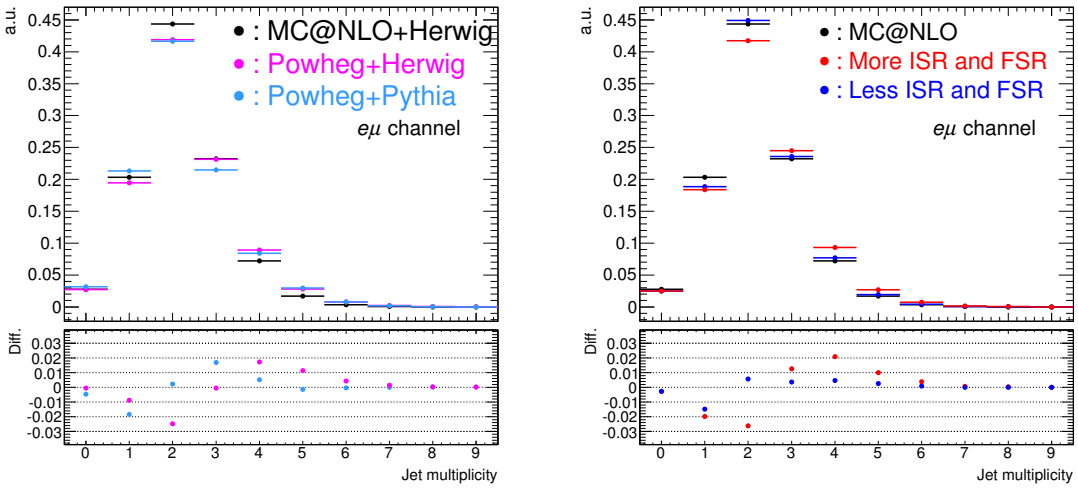


Figure 7.14: Distributions of the jet multiplicity after requiring a selected electron and a selected muon for various MC samples. Bottom plots shows the difference between the samples of interest to estimate the systematic uncertainty, *i.e.* (POWHEG+HERWIG)-(MC@NLO+HERWIG) in magenta, (POWHEG+HERWIG)-(POWHEG+PYTHIA) in light blue, (More ISR/FSR)-(MC@NLO) in red, (Less ISR/FSR)-(MC@NLO) in blue.

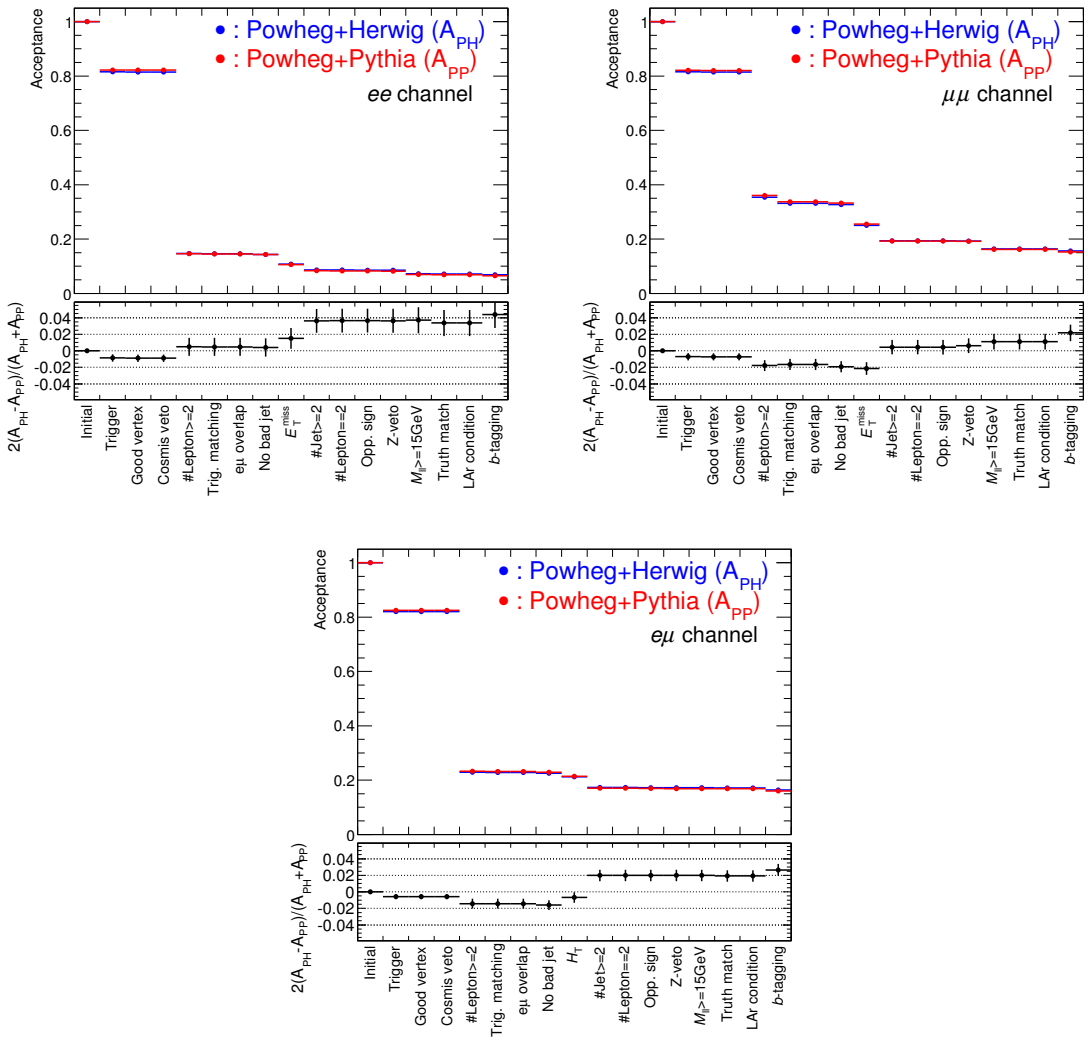


Figure 7.15: The acceptance at each selection step for the MC sample generated with the POWHEG generator interfaced with PYTHIA and HERWIG for the parton shower modeling for the ee (top left), the $\mu\mu$ (top right) and the $e\mu$ (bottom) channel. Bottom part of each plot shows the relative acceptance difference between two samples.

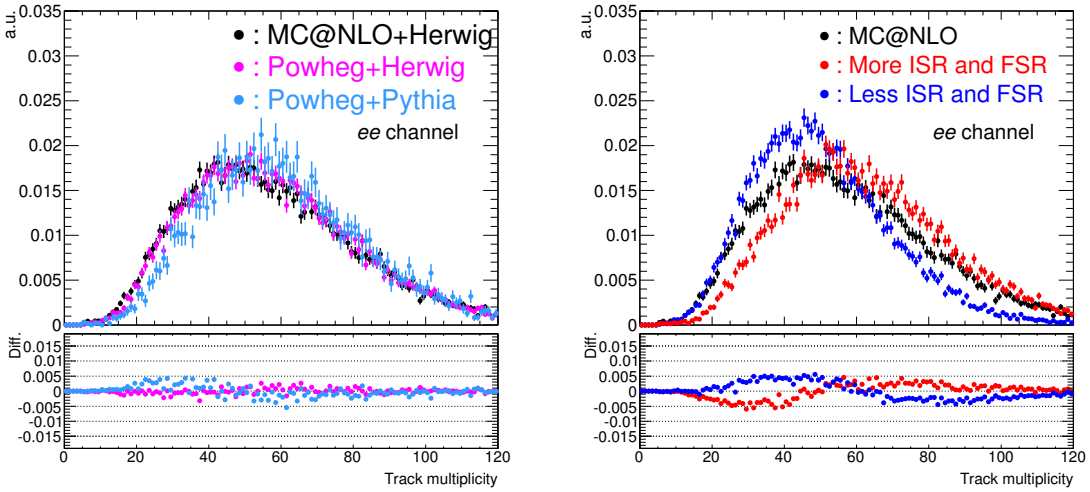


Figure 7.16: Distributions of the track multiplicity after requiring two selected electrons for various MC samples. Bottom plots shows the difference between the samples of interest to estimate the systematic uncertainty, *i.e.* (POWHEG+HERWIG)-(MC@NLO+HERWIG) in magenta, (POWHEG+HERWIG)-(POWHEG+PYTHIA) in light blue, (More ISR/FSR)-(MC@NLO) in red, (Less ISR/FSR)-(MC@NLO) in blue.

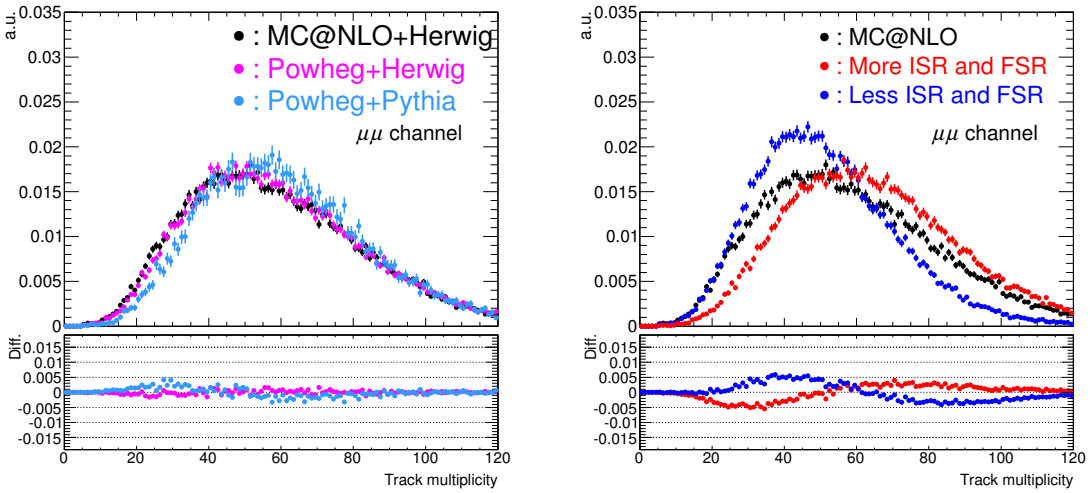


Figure 7.17: Distributions of the track multiplicity after requiring two selected muons for various MC samples. Bottom plots shows the difference between the samples of interest to estimate the systematic uncertainty, *i.e.* (POWHEG+HERWIG)-(MC@NLO+HERWIG) in magenta, (POWHEG+HERWIG)-(POWHEG+PYTHIA) in light blue, (Sample with more ISR/FSR)-(MC@NLO) in red, (Sample with less ISR/FSR)-(MC@NLO) in blue.

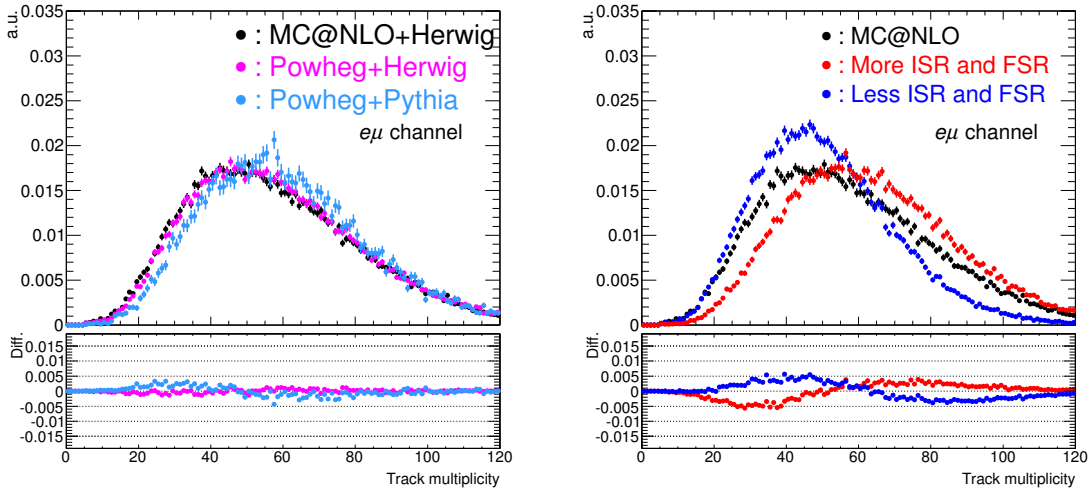


Figure 7.18: Distributions of the track multiplicity after requiring a selected electron and a selected muon for various MC samples. Bottom plots shows the difference between the samples of interest to estimate the systematic uncertainty, *i.e.* (POWHEG+HERWIG)-(MC@NLO+HERWIG) in magenta, (POWHEG+HERWIG)-(POWHEG+PYTHIA) in light blue, (More ISR/FSR)-(MC@NLO) in red, (Less ISR/FSR)-(MC@NLO) in blue.

Figure 7.16 to 7.18. As expected, the increased ISR/FSR produces more particles in the final state. As mentioned above, more tracks decrease the lepton selection efficiency due to the isolation requirement. The right plots in Figure 7.12 to 7.14 show that the number of jets in the samples with increased or decreased ISR/FSR. One can see that there are more jets in the samples with increased ISR/FSR. This causes the acceptance gain at the selection of at least two jets. The total uncertainty on the acceptance from the ISR/FSR modeling is estimated to be ±5.7 %, ±1.3 % and ±3.0 % for the ee, $\mu\mu$ and $e\mu$ channel, respectively.

- *Uncertainty from the PDF modeling*

In order to avoid generating a huge number of samples generated with various PDF parameters, the MC events are re-weighted to mimic that the events are generated with different PDF sets. The re-weighting factor is prepared based on the envelope of error bands from CTEQ66, MSTW08 and NNPDF2.0 PDF sets. The size of the error due to PDF is estimated by repeating the acceptance estimate with the re-weighted sample. The differences from the nominal acceptance are taken as the systematic uncertainty, which are ±2.8 %, ±2.5 % and ±2.2 % for the ee, the $\mu\mu$ and the $e\mu$ channel, respectively.

7.3 Background estimation

This section describes how the background contribution were estimated. Various processes can remain after the event selection even though the dilepton final state is relatively clean compared to the single lepton and the all hadronic final states. The backgrounds are categorized into three types,

- Ones with a fake lepton,
- Ones with a fake $E_{\mathrm{T}}^{\mathrm{miss}}$, and

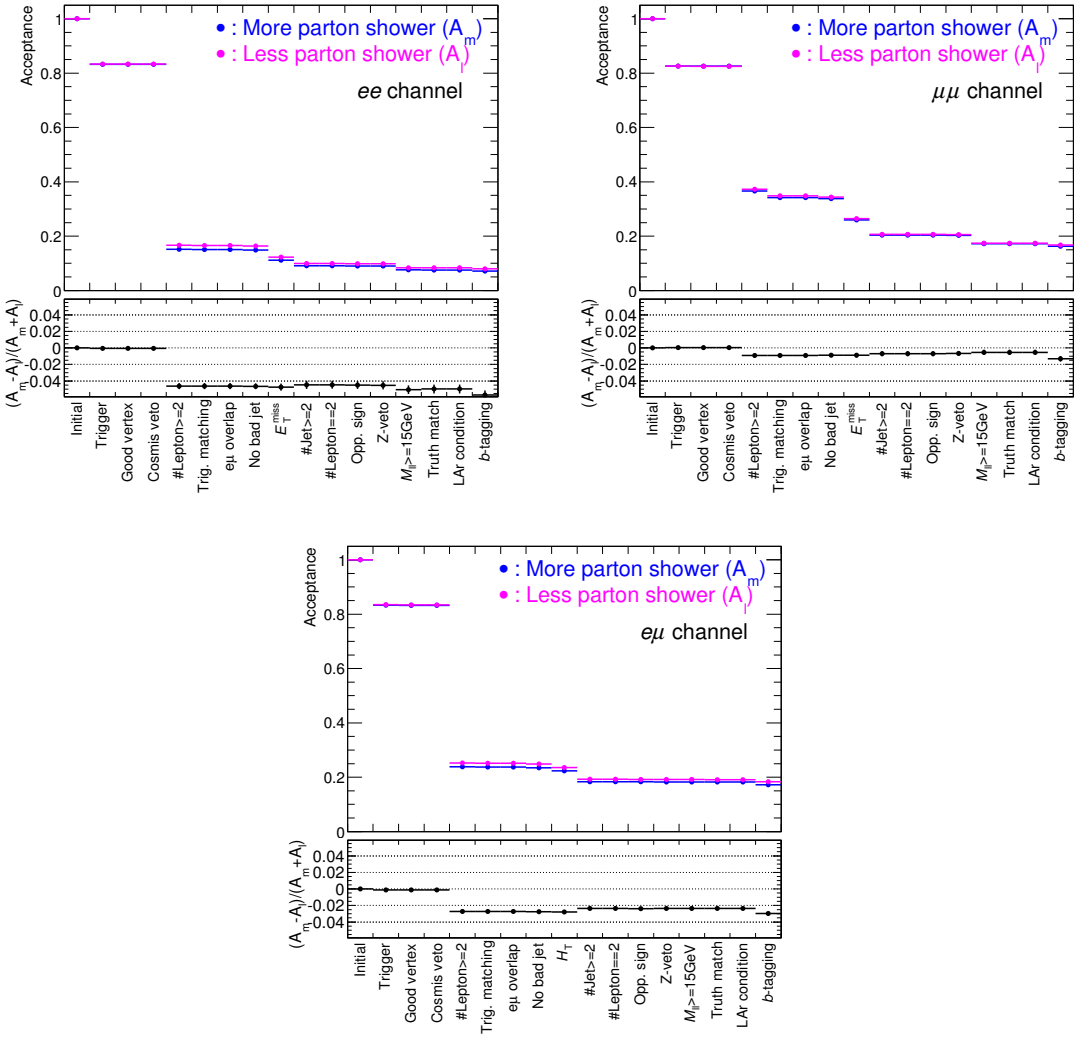


Figure 7.19: The acceptance at each selection step for the MC sample generated with increased or decreased ISR/FSR for the ee (top left), the $\mu\mu$ (top right) and the $e\mu$ (bottom) channel. Bottom part of each plot shows the relative acceptance difference between the two samples.

- Ones with two real charged leptons and real $E_{\mathrm{T}}^{\mathrm{miss}}$ from a neutrino.

The details of the estimation method for each process are described in the sub-sections below.

7.3.1 Fake lepton backgrounds

The selection of dilepton suppresses the QCD multi-jet, W+jets, $t\bar{t}$ single lepton final state and other non-dilepton final states originating from the single top and the di-boson. However, there is still a small contribution from the events with a mis-identified lepton. To estimate the amount of such a contribution, the matrix method, which is used in the measurement of ε_b, is used here as well. The matrix for the dilepton analysis can be written as

$$\begin{pmatrix} N^{\mathrm{tt}} \\ N^{\mathrm{tl}} \\ N^{\mathrm{lt}} \\ N^{\mathrm{ll}} \end{pmatrix} = \begin{pmatrix} r_1 r_2 & r_1 f_2 & f_1 r_2 & f_1 f_2 \\ r_1(1-r_2) & r_1(1-f_2) & f_1(1-r_2) & f_1(1-f_2) \\ (1-r_1)r_2 & (1-r_1)f_2 & (1-f_1)r_2 & (1-f_1)f_2 \\ (1-r_1)(1-r_2) & (1-r_1)(1-f_2) & (1-f_1)(1-r_2) & (1-f_1)(1-f_2) \end{pmatrix} \begin{pmatrix} N_{\mathrm{rr}}^{\mathrm{ll}} \\ N_{\mathrm{rf}}^{\mathrm{ll}} \\ N_{\mathrm{fr}}^{\mathrm{ll}} \\ N_{\mathrm{ff}}^{\mathrm{ll}} \end{pmatrix},$$

where N^{tt} (N^{ll}) is the number of events including two tight (loose) leptons, N^{tl} (N^{lt}) is the number of events that the first lepton passes the tight (loose) lepton criteria and the second one passes the loose (tight) lepton criteria. $N_{\mathrm{rr}}^{\mathrm{ll}}$, $N_{\mathrm{rf}}^{\mathrm{ll}}$, $N_{\mathrm{fr}}^{\mathrm{ll}}$, $N_{\mathrm{ff}}^{\mathrm{ll}}$ are the numbers of events which have two loose lepton candidates. The subscripts, rr, rf, fr, ff, indicate that the two identified leptons are two real leptons (rr), real and fake lepton (rf), fake and real lepton (fr) and two fake leptons (ff), respectively. The efficiency of the n-th real (fake) loose lepton passing the tight lepton criteria is denoted as r_n (f_n), and defined as

$$r = \varepsilon_{\mathrm{real}} = \frac{N_{\mathrm{real}}^{\mathrm{tight}}}{N_{\mathrm{real}}^{\mathrm{loose}}}, \quad f = \varepsilon_{\mathrm{fake}} = \frac{N_{\mathrm{fake}}^{\mathrm{tight}}}{N_{\mathrm{fake}}^{\mathrm{loose}}}.$$

The number of events which have at least one fake tight lepton is obtained by inverting the matrix as

$$\begin{aligned} N_{\mathrm{fake}}^{\mathrm{tt}} &= N_{\mathrm{rf}}^{\mathrm{tt}} + N_{\mathrm{fr}}^{\mathrm{tt}} + N_{\mathrm{ff}}^{\mathrm{tt}} \\ &= r_1 f_2 N_{\mathrm{rf}}^{\mathrm{ll}} + f_1 r_2 N_{\mathrm{fr}}^{\mathrm{ll}} + f_1 f_2 N_{\mathrm{ff}}^{\mathrm{ll}} \\ &= -\alpha r_1 f_2[(1-f_1)(1-r_2)N^{\mathrm{tt}} - (1-f_1)r_2 N^{\mathrm{tl}} - f_1(1-r_2)N^{\mathrm{lt}} + f_1 r_2 N^{\mathrm{ll}}] \\ &\quad -\alpha f_1 r_2[(1-r_1)(1-f_2)N^{\mathrm{tt}} - (1-r_1)f_2 N^{\mathrm{tl}} - r_1(1-f_2)N^{\mathrm{lt}} + r_1 f_2 N^{\mathrm{ll}}] \\ &\quad +\alpha f_1 f_2[(1-r_1)(1-r_2)N^{\mathrm{tt}} - (1-r_1)r_2 N^{\mathrm{tl}} - r_1(1-r_2)N^{\mathrm{lt}} + r_1 r_2 N^{\mathrm{ll}}], \end{aligned} \tag{7.3}$$

where

$$\alpha = \frac{1}{(r_1 - f_1)(r_2 - f_2)}.$$

The parametrization of the efficiency of real and fake leptons is the same as the one used in the ε_b measurement. By putting the measured efficiency into Equation (7.3), we can obtain the number of events with a fake lepton from data by counting $N^{\mathrm{tt}}, N^{\mathrm{tl}}, N^{\mathrm{lt}}$ and N^{ll}. The expected event yield with the fake lepton is computed as 33, 65 and 89 for the ee, the $\mu\mu$ and the $e\mu$ channels, respectively.

Systematic uncertainty on the fake lepton estimate

In order to estimate the systematic uncertainty due to the parametrization of real and fake lepton efficiency, we compare the fake lepton event yields with the one obtained by the previous

result based on 0.7 fb^{-1} of data just by scaling it up by 4.7/0.7. The relative differences between the current estimate and the scaled one from the previous results are 20 % for the ee channel, 30 % for the $\mu\mu$ channel and 20 % for the $e\mu$ channel, which are considered as the systematic uncertainties. In addition, we find that the fake lepton efficiency, $f_{1,2}$, may change from ∼20 % to ∼30 % by using the fake electron control sample where there is a photon conversion vertex around the fake electron candidate. We repeat the analysis using this fake efficiency, and take the half of the differences from the nominal result as the additional systematic uncertainty. These uncertainties are added in quadrature. In the end, we assigned an uncertainty of 50 % for the ee channel, 30 % for the $\mu\mu$ channel and 40 % for the $e\mu$ channel.

7.3.2 The events with Z/γ^* which decays into ee or $\mu\mu$

The Z/γ^* production is the dominant background source for the ee and $\mu\mu$ channel. It does not have real $E_{\mathrm{T}}^{\mathrm{miss}}$ in its nature, while the events are required to have large $E_{\mathrm{T}}^{\mathrm{miss}}$. This implies that the events from Z/γ^* remaining after the selections are caused by the mis-measurement of $E_{\mathrm{T}}^{\mathrm{miss}}$. Because of the difficulty of simulating the mis-modeling of $E_{\mathrm{T}}^{\mathrm{miss}}$, this background is estimated by a data-driven way.

To estimate the number of Z/γ^* events, the number of events in a control region is scaled to the signal region as

$$(\text{Expected } Z/\gamma^* \text{ yields}) = (\text{Data(CR)} - \text{MC}_{\text{other}}(\text{CR})) \times \frac{\text{MC}_{\text{Z}/\gamma^*}(\text{SR})}{\text{MC}_{Z/\gamma^*}(\text{CR})}, \tag{7.4}$$

where 'Data(CR)' is the number of observed data in the control region, 'MC_{other}(CR)' is the number of the expected events from the non-Z/γ^* processes in the control region, '$\text{MC}_{\text{Z}/\gamma^*}$(SR)' and '$\text{MC}_{Z/\gamma^*}$(CR)' are the number of events from Z/γ^* estimated by MC.

The control region is defined to be 81 GeV $< M_{\ell\ell} <$ 101 GeV and $E_{\mathrm{T}}^{\mathrm{miss}} > 30$ GeV. Other selections are the same as the signal region. The distributions of $E_{\mathrm{T}}^{\mathrm{miss}}$ and $M_{\ell\ell}$ of data for ee and $\mu\mu$ channels are shown in Figure 7.20. The term 'MC_{other}(CR)' includes $t\bar{t} \to \ell\ell\nu\nu bb$,

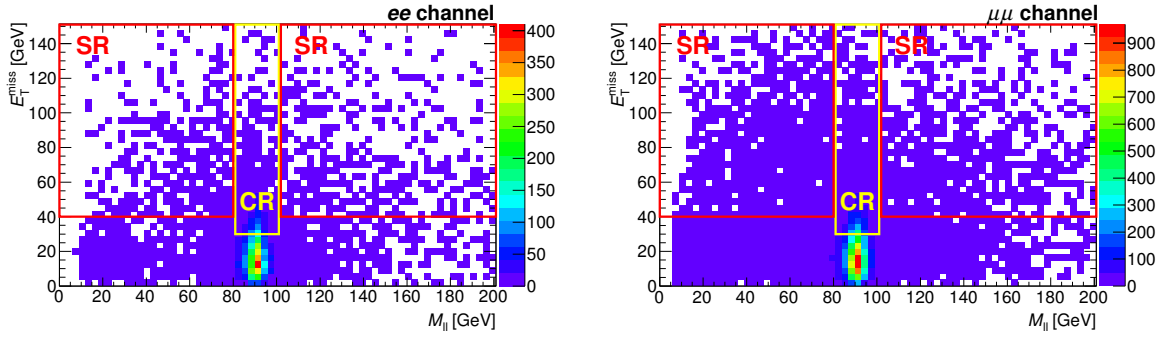


Figure 7.20: The distributions of data on $E_{\mathrm{T}}^{\mathrm{miss}}$ and $M_{\ell\ell}$ plane for the ee (left) and the $\mu\mu$ (right) channel. The control region (CR) and the signal region (SR) is indicated by the yellow and red box, respectively.

$Z/\gamma^* \to \tau\tau$, the di-boson production, the single top production and the events containing the fake lepton. The contamination of the fake lepton events in the control region is estimated by the matrix method described in the previous section. The expected number of events in each region is summarized in Table 7.6. Inserting the numbers in the table into Equation (7.4), we obtain the expected number of events from Z/γ^* events to be 48.0 for the ee and 191.5 for the $\mu\mu$ channel.

Table 7.6: The number of observed events and the expected events by MC. 'Di-boson' includes $WW/WZ/ZZ$ processes. 'Single top' means the Wt process.

		Z/γ^* sources		Other background sources (CR)					
channel	$Data$(CR)	MC(CR)	MC(SR)	$t\bar{t}$	$Z/\gamma^* \to \tau\tau$	Fake lepton	Di-boson	Single top	Total
ee	1145	1045.4	57.4	176.5	0.1	52.6	34.6	6.8	270.7
$\mu\mu$	3430	2593.6	172.7	422.5	1.4	39.6	74.5	16.1	554.1

Systematic uncertainties

We also estimate the amount of Z/γ^* events by using MC to compare how precisely we estimate the Z/γ^* background by the data-driven method. Here, we check the uncertainties for both methods as shown in Table 7.7 and 7.8. The total uncertainty by the data-driven method

Table 7.7: Yields and uncertainties for the $Z/\gamma^* \to ee$ estimate

	Monte Carlo	Data-Driven
Estimated yields	57.4	48.0
	$\delta N_{\mathrm{MC}}/N_{\mathrm{MC}}$	$\delta N_{\mathrm{DD}}/N_{\mathrm{DD}}$
Data statistics	+0.0 / −0.0	+3.9 / −3.9
MC statistics	+8.1 / −8.1	+8.5 / −8.5
Luminosity	+1.8 / −1.8	+0.0 / −0.0
Theory	+34.2 / −34.2	+0.0 / −0.0
CR definition	+0.0 / −0.0	+5.0 / −5.0
Jet energy scale	+24.2 / −8.8	+14.5 / −19.1
Jet energy resolution	+58.4 / −58.4	+21.9 / −21.9
Jet reco. efficiency	+0.0 / −0.0	+0.2 / −0.2
Jet vertex fraction	+0.0 / −0.5	+3.0 / −1.2
Missing E_T	+11.5 / −11.5	+11.1 / −11.1
El. energy scale	+6.5 / −6.5	+1.7 / −1.7
El. energy resolution	+8.3 / −8.3	+2.0 / −2.0
El. reco. efficiency	+7.4 / −7.2	+7.6 / −7.0
El. trig. efficiency	+5.5 / −5.3	+5.6 / −4.9
b-tagging efficiency	+1.6 / −1.6	+2.0 / −1.4
c-tagging efficiency	+1.1 / −3.4	+3.8 / −0.0
l-tagging efficiency	+4.6 / −7.0	+8.8 / −4.3
Total systematics	+74.8 / −71.5	+33.6 / −34.4

ranges 30-35 %, while the one for the MC-based estimate ranges 60-75 %. The relatively small uncertainty in the data-driven method comes from the fact that the uncertainties related to efficiency or resolution are cancelled by taking the ratio between the signal and the control region. In addition, there is no theoretical uncertainty for the cross section of the Z/γ^* process in the data-driven method. The details of how to estimate each uncertainty are described in the following.

Table 7.8: Yields and uncertainties for the $Z/\gamma^* \to \mu\mu$ estimate

	Monte Carlo	Data-Driven
Estimated yields	172.7	191.5
	$\delta N_{\mathrm{MC}}/N_{\mathrm{MC}}$	$\delta N_{\mathrm{DD}}/N_{\mathrm{DD}}$
Data statistics	+0.0 / −0.0	+2.0 / −2.0
MC statistics	+5.6 / −5.6	+5.8 / −5.8
Luminosity	+1.8 / −1.8	+0.0 / −0.0
Theory	+34.2 / −34.2	+0.0 / −0.0
CR definition	+0.0 / −0.0	+5.0 / −5.0
Jet energy scale	+18.5 / −7.3	+10.7 / −17.8
Jet energy resolution	+48.2 / −48.2	+23.4 / −23.4
Jet reco. efficiency	+0.0 / −0.0	+0.1 / −0.1
Jet vertex fraction	+2.0 / −2.4	+2.4 / −1.7
Missing E_T	+10.0 / −10.0	+9.2 / −9.2
Mu. energy scale	+0.9 / −0.9	+0.4 / −0.4
Mu. energy resolution	+2.0 / −2.0	+0.1 / −0.1
Mu. reco. efficiency	+1.6 / −1.6	+2.0 / −1.8
Mu. trig. efficiency	+1.4 / −3.8	+5.0 / −1.7
b-tagging efficiency	+0.6 / −0.6	+1.9 / −1.6
c-tagging efficiency	+0.3 / −2.8	+3.5 / −0.2
l-tagging efficiency	+4.6 / −7.3	+8.3 / −4.3
Total systematics	+63.3 / −61.4	+30.5 / −32.3

- Uncertainties by the energy scale/resolution and the efficiency

The uncertainties from leptons, jets, $E_{\mathrm{T}}^{\mathrm{miss}}$ and the b-tagging are evaluated by varying the energy or efficiency with the procedure same as the one used in the ε_b measurement described in Section 6.11. During this procedure, unexpectedly large or asymmetric uncertainty sometimes appears due to a statistical fluctuation because of the lack of remaining non-$t\bar{t}$ events. However, we can almost neglect this effect because the final precision is determined by the uncertainty from jets, especially from the jet energy resolution which makes the largest effect. Therefore, we only explain how the jet related uncertainty affects the Z/γ^* estimate, which is important to understand the behavior of the Z/γ^* background.

The remaining number of Z/γ^* events with large $E_{\mathrm{T}}^{\mathrm{miss}}$ is sensitive to the modeling of $E_{\mathrm{T}}^{\mathrm{miss}}$ resolution, because there is no real $E_{\mathrm{T}}^{\mathrm{miss}}$. Figure 7.21 shows the $E_{\mathrm{T}}^{\mathrm{miss}}$ distribution in the Z/γ^*+jets MC sample with different JES and the jet energy resolution. The event selection is the same as the one to create Figure 7.20 but omitting the b-tagging selection to see the shape with large statistics. JES or the jet energy resolution directly affects the $E_{\mathrm{T}}^{\mathrm{miss}}$ shape. On top of that, the slope around $E_{\mathrm{T}}^{\mathrm{miss}} \sim 30$ GeV is steep. These two are the main reasons why there is large, ∼50 %, uncertainty on the MC-based Z/γ^* estimate due to the jet energy resolution. On the other hand, by introducing the data-driven method, we can significantly reduce this uncertainty, because the variation of the numbers of events in the signal and the control region does not change the right side of Equation (7.4) as they are cancelled out. The uncertainty is reduced to ~ 20 % from ~ 50 %.

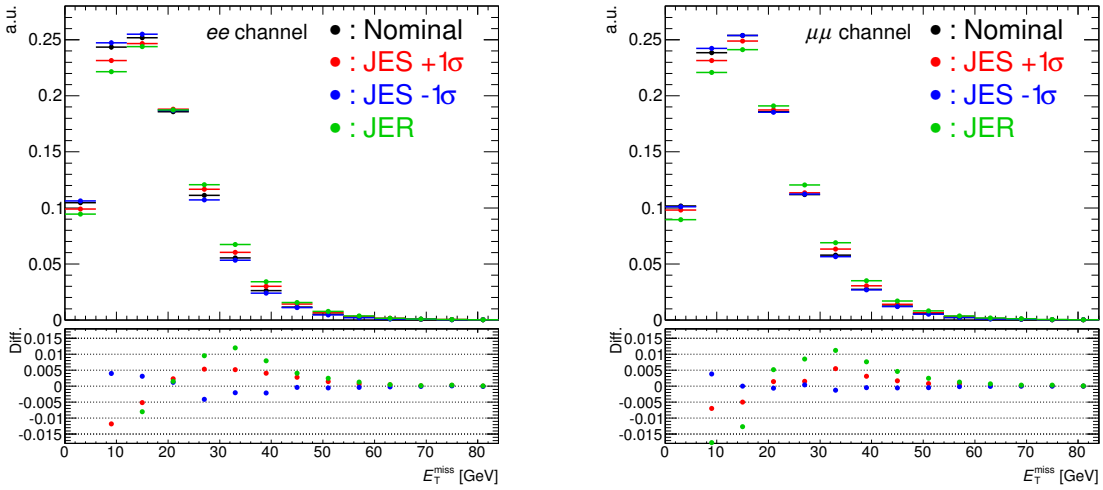


Figure 7.21: The distributions of $E_{\mathrm{T}}^{\mathrm{miss}}$ for the Z+2jets in the ee (left) and the $\mu\mu$ channel with MC samples. The black, red, blue and green histograms show the one with the nominal jet calibration (Nominal), with the JES scaled up and down (JES $\pm1\sigma$) and with the smeared jet energy (JER), respectively. The bottom plots show the difference from the nominal for the case of JES $\pm1\sigma$ and JER with the same color convention.

- *Uncertainty only in the data-driven method*

We check the dependence of the estimated Z/γ^* events on the definition of the control region. The relative difference between the nominal result and the one with various $E_{\mathrm{T}}^{\mathrm{miss}}$ cut values to define the control region are plotted in Figure 7.22. The events typically have the $E_{\mathrm{T}}^{\mathrm{miss}}$ resolution of 10 GeV as shown in Figure 5.16. Here, we change the cut value on $E_{\mathrm{T}}^{\mathrm{miss}}$ from 20 GeV to 40 GeV corresponding to ±10 GeV from the nominal definition of the control region. In the end, we assign ±5 % of the uncertainty by the definition of the control region since the maximum difference from the nominal result is approximately 5 %.

- *Uncertainty only in the MC-based method*

The uncertainties of the luminosity measurement and the cross section calculation affect only the MC based estimation. The luminosity measurement described at Section 4.1.1 has the uncertainty of 1.8 %. Because the mis-measurement of the integrated luminosity linearly changes the expected amount of Z/γ^* events, we assign 1.8 % of uncertainty due to the luminosity measurement.

The uncertainty of the cross section calculation also changes the expected amount of Z/γ^* events linearly. The inclusive production cross section of Z/γ^*+jets is well understood theoretically, having an uncertainty of only 4 %. However, the cross section of Z/γ^* with two or more partons is more difficult to calculate. To estimate the size of the uncertainty from such processes, we follow the procedure described below.

It is known that the ratio of the cross sections for the Z/γ^* with additional n partons and $(n+1)$ partons, $\sigma^{n+1}_{Z/\gamma^*}/\sigma^{n}_{Z/\gamma^*}$, is approximately constant [101]. We check how wide the spread of $\sigma^{n+1}_{Z/\gamma^*}/\sigma^{n}_{Z/\gamma^*}$ is among $n=0$ to 4 in the expected cross section calculated by the MC generator. We obtain 24 % as the maximum difference from the mean value, and added this 24 % uncertainty per additional parton in quadrature to the uncertainty of the inclusive cross

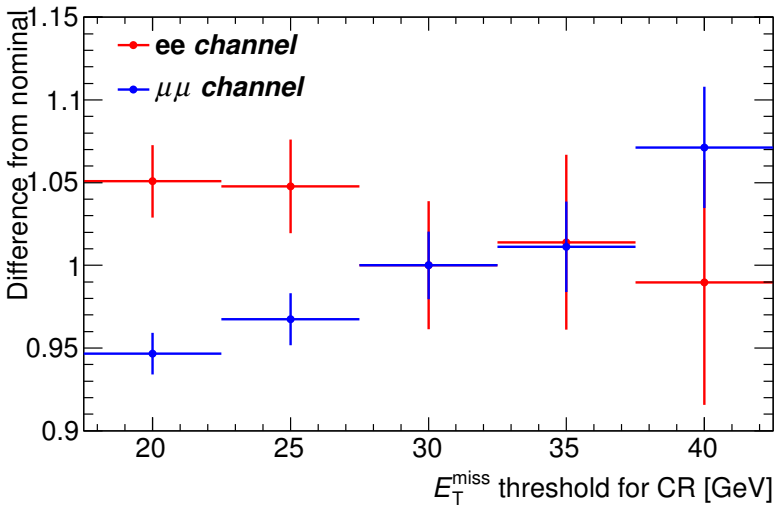


Figure 7.22: The CR dependence of the number of estimated events of Z+jet events. The ratio to the one with the nominal CR definition is plotted.

section. For the dominant process, the Z/γ^* with two partons, the uncertainty corresponds to 34 %. This is the second largest uncertainty in the MC-based estimates.

7.3.3 Other backgrounds

The contributions from $Z(\rightarrow \tau\tau)$+jets, WW, ZZ, WZ and Wt are estimated by using MC. The corrections to reproduce real data, described in Section 7.1.2, are applied to the MC samples. Tables 7.9, 7.10 and 7.11 summarize the expected yields and the systematic uncertainties for the ee, the $\mu\mu$ and the $e\mu$ channels, respectively. Typically, there is an uncertainty of 40 % for $Z/\gamma^* \rightarrow \tau\tau$, 25 % for the di-boson, and 10-20 % for the single top estimate. The details of systematic uncertainty are discussed below.

The luminosity and the theoretical cross section

As discussed in Section 7.3.2, we assign the $\pm$1.8 % uncertainty of the luminosity measurement as the uncertainty of the expected yields.

The theoretical uncertainty of the cross section for $Z/\gamma^* \rightarrow \tau\tau$ and di-boson process is derived by exactly the same method used in the MC-based Z/γ^* estimate described in the previous section. For the $Z/\gamma^* \rightarrow \tau\tau$ process, the size of the uncertainty is evaluated as $\sim$ 34 %, similar to the $Z/\gamma^* \rightarrow ee/\mu\mu$ estimate, since the dominant process comes from Z/γ^* with two jets. On the other hand, for the di-boson events, the size of the uncertainty is estimated to be approximately $\pm$18 %. This is because the di-boson events contain some $WZ/ZZ \rightarrow \ell\ell qq$ events which do not have an additional parton. Therefore, the theoretical uncertainty is smaller than the one for $Z/\gamma^* \rightarrow \tau\tau$. The theoretical uncertainty of the single top production, derived from [75], is $+7.4/-7.7$ % which is dominated by the uncertainty from PDFs. These uncertainties from the cross section calculation is the largest uncertainty for all three processes.

Table 7.9: Yields and the systematic uncertainty of the backgrounds in the *ee* channel which are estimated using MC.

	$Z/\gamma^* \to \tau\tau$	Di-boson	Single top
Yields	9.3 ± 3.8	10.9 ± 1.5	37.0 ± 5.7
	$\delta N/N$ [%]	$\delta N/N$ [%]	$\delta N/N$ [%]
Luminosity	+1.8 / −1.8	+1.8 / −1.8	+1.8 / −1.8
MC statistics	+15.0 / −15.0	+9.4 / −9.4	+9.4 / −9.4
Jet energy scale	+14.7 / −5.1	+1.2 / −5.2	+9.3 / −7.2
Jet energy resolution	+3.6 / −3.6	+2.1 / −2.1	+2.1 / −2.1
Jet reco. efficiency	+0.0 / −0.0	+0.7 / −0.7	+0.0 / −0.0
Jet vertex fraction	+1.1 / −1.1	+0.8 / −0.9	+0.9 / −1.1
Missing Et uncertainty	+1.3 / −1.3	+0.4 / −0.4	+1.6 / −1.6
El. energy scale	+9.3 / −9.3	+0.3 / −0.3	+0.0 / −0.0
El. energy resolution	+7.9 / −7.9	+1.2 / −1.2	+0.2 / −0.2
El. reco. efficiency	+4.4 / −4.3	+6.0 / −5.8	+5.0 / −4.9
El. trig. efficiency	+2.9 / −2.9	+4.0 / −3.9	+3.6 / −3.5
b-tagging efficiency	+0.7 / −0.7	+0.1 / −0.2	+4.6 / −4.8
c-tagging efficiency	+0.6 / −3.3	+1.9 / −2.1	+0.2 / −0.2
l-tagging efficiency	+7.8 / −7.7	+7.1 / −7.2	+0.4 / −0.4
Heavy flavor fraction	+4.5 / −1.7	+11.0 / −4.2	+0.0 / −0.0
Theoretical cross section	+32.8 / −32.8	+19.6 /−19.6	+7.4 / −7.7
Total uncertainty	+42.3 / −39.9	+26.6 /−25.1	+17.2 /−16.3

Table 7.10: Yields and the systematic uncertainty of the backgrounds in the $\mu\mu$ channel which are estimated using MC.

	$Z/\gamma^* \to \tau\tau$	Di-boson	Single top
Yields	31 ± 12	24.2 ± 3.8	90 ± 12
	$\delta N/N$ [%]	$\delta N/N$ [%]	$\delta N/N$ [%]
Luminosity	+1.8 / −1.8	+1.8 / −1.8	+1.8 / −1.8
MC statistics	+5.9 / −5.9	+4.9 / −4.9	+4.9 / −4.9
Jet energy scale	+18.1 / −16.0	+9.1 / −7.7	+5.5 / −5.2
Jet energy resolution	+2.0 / −2.0	+6.9 / −6.9	+0.0 / −0.0
Jet reco. efficiency	+0.0 / −0.0	+0.3 / −0.3	+0.0 / −0.0
Jet vertex fraction	+1.3 / −1.3	+1.3 / −1.3	+0.9 / −1.0
Missing Et uncertainty	+0.4 / −0.4	+0.9 / −0.9	+0.7 / −0.7
Mu. energy scale	+1.5 / −1.5	+0.2 / −0.2	+0.1 / −0.1
Mu. energy resolution	+0.5 / −0.5	+0.0 / −0.0	+0.1 / −0.1
Mu. reco. efficiency	+2.2 / −0.8	+1.6 / −1.6	+1.6 / −1.6
Mu. trig. efficiency	+2.7 / −2.0	+2.9 / −2.8	+3.0 / −2.9
b-tagging efficiency	+1.1 / −1.2	+0.3 / −0.3	+5.4 / −6.0
c-tagging efficiency	+1.9 / −0.7	+1.8 / −1.9	+0.0 / −0.0
l-tagging efficiency	+6.6 / −6.7	+7.0 / −7.1	+0.1 / −0.1
Heavy flavor fraction	+22.4 / −8.5	+20.4 / −7.8	+0.0 / −0.0
Theoretical cross section	+30.3 / −30.3	+16.3 /−16.3	+7.4 / −7.7
Total uncertainty	+43.0 / −36.6	+30.0 /−22.9	+12.3 /−12.6

Uncertainties from leptons, jets and $E_{\mathrm{T}}^{\mathrm{miss}}$

Systematic uncertainties related to leptons, jets and $E_{\mathrm{T}}^{\mathrm{miss}}$ are estimated by repeating the yield estimate using the various MC samples, which is obtained by the same method to estimate the systematic uncertainty for the signal acceptance. Some uncertainties, especially for the $Z/\gamma^* \to \tau\tau$ in the ee channel, tend to be large or sometimes very asymmetric, because of the statistical fluctuation as seen in the $Z/\gamma^* \to ee/\mu\mu$ estimate. This implies that the uncertainty may be overestimated. However, this does not affect the final precision, because the total uncertainty is completely dominated by the cross section calculation.

b-tagging

The Z/γ^* events with light-jets are the dominant background even after requiring at least one b-tagged jet because we use the loose requirement to gain high efficiency, resulting in a low rejection power for light-jets. Therefore, the uncertainty from the b-tagging fake rate for the light-jets largely contributes to the uncertainty. In the di-boson events, there are not only light-jets as in the Z/γ^* events but also c-jets from the W boson decay. Therefore, the b-tagging fake rate for the c-jets gives a visible effect. In the single top event, there is one b-jet from the top quark decay, and less likely an additional b-jet. Therefore, the uncertainty from the b-tagging efficiency for the real b-jets gives the largest uncertainty. The size of the uncertainty is slightly larger than the one for the signal acceptance, because the mechanism to reduce the systematics described in Section 7.2 does not work here.

Table 7.11: Yields and the systematic uncertainty of the backgrounds in the $e\mu$ channel which are estimated using MC.

	$Z/\gamma^* \to \tau\tau$	Di-boson	Single top
Yields	61 ± 23	54.7 ± 8.3	192 ± 24
	$\delta N/N$ [%]	$\delta N/N$ [%]	$\delta N/N$ [%]
Luminosity	+1.8 / −1.8	+1.8 / −1.8	+1.8 / −1.8
MC statistics	+3.7 / −3.7	+2.8 / −2.8	+2.8 / −2.8
Jet energy scale	+11.3 / −9.4	+9.3 / −8.3	+3.9 / −5.3
Jet energy resolution	+5.4 / −5.4	+2.0 / −2.0	+0.3 / −0.3
Jet reco. efficiency	+1.2 / −1.2	+0.1 / −0.1	+0.0 / −0.0
Jet vertex fraction	+0.9 / −1.1	+0.9 / −1.1	+0.9 / −1.1
El. energy scale	+2.0 / −2.0	+0.1 / −0.1	+0.2 / −0.2
El. energy resolution	+1.1 / −1.1	+0.3 / −0.3	+0.2 / −0.2
El. reco. efficiency	+3.4 / −3.4	+3.7 / −3.7	+2.6 / −2.6
El. trig. efficiency	+3.6 / −2.4	+2.4 / −2.4	+1.8 / −1.8
Mu. energy scale	+1.7 / −1.7	+0.1 / −0.1	+0.0 / −0.0
Mu. energy resolution	+1.4 / −1.4	+0.0 / −0.0	+0.0 / −0.0
Mu. reco. efficiency	+2.4 / −1.3	+0.8 / −0.8	+0.8 / −0.8
Mu. trig. efficiency	+0.0 / −0.6	+0.0 / −0.0	+0.0 / −0.0
b-tagging efficiency	+1.7 / −0.7	+0.5 / −0.5	+4.4 / −5.1
c-tagging efficiency	+0.8 / −2.0	+1.9 / −1.9	+0.0 / −0.0
l-tagging efficiency	+6.3 / −6.4	+7.4 / −7.5	+0.2 / −0.2
Heavy flavor fraction	+17.6 / −6.7	+10.7 / −4.1	+0.0 / −0.0
Theoretical cross section	+34.6 / −34.6	+17.0 /−17.0	+7.4 / −7.7
Total uncertainty	+42.0 / −38.1	+24.1 /−21.6	+10.4 /−11.5

Uncertainty from the heavy flavor fraction

To estimate the uncertainty from the heavy flavor fraction in the $Z/\gamma^* \to \tau\tau$ and the di-boson events, we re-estimate the yields by varying its fraction with the same method used in the ε_b measurement described in Section 6.11. The heavy flavor fraction is approximately doubled or reduced to a half where the variation is based on the W+b-jets measurement [100]. Here, we assume the fraction of the heavy flavor jets associated with the W and Z boson is approximately the same. The size of the uncertainty on the yield is estimated to be about +10 % to +20 % and −5 % to −10 %, typically. Much smaller uncertainty is seen in the ee channel, which we think is caused by a statistical fluctuation as seen in the $Z/\gamma^* \to ee/\mu\mu$ estimate.

7.4 Validation of background estimation

To validate the background estimation, some control regions are defined. In those control regions, we compare the expected yield and the distribution with data. Three background sources, $Z/\gamma^* \to ee/\mu\mu$, the fake lepton events, and the $Z/\gamma^* \to \tau\tau$ are considered here. For the backgrounds from the di-boson and single top, it is difficult to define the control region with high purity. Therefore, we just trust the expected yields and the distribution.

$Z/\gamma^* \to ee/\mu\mu$ backgrounds

The events passing all the selections but zero b-tagged jets are used as the $Z/\gamma^* \to ee/\mu\mu$ control sample which has large fake $E_{\mathrm{T}}^{\mathrm{miss}}$. In this region, the purity of the $Z/\gamma^* \to ee/\mu\mu$ is estimated as approximately 50 %. Figure 7.23 shows the distribution of P_T of the leading and the second leading lepton and the invariant mass of the dilepton system. The amount of the events and the shape are well described within the uncertainty. Figure 7.24 shows jet multiplicity, jet P_T and H_T distribution. The distribution of jet multiplicity in the ee channel has small data excess in the second and the fifth bins. This excess results in a discrepancy in the low jet P_T region. Besides, the H_T distribution shows small data excess at the low H_T region. For the $\mu\mu$ channel, we can see that the jet P_T in MC is systematically harder than the one in data, although the difference is within the uncertainty. All these facts mentioned above leads to a small mis-modeling of $E_{\mathrm{T}}^{\mathrm{miss}}$ which we observe in the simulation.

In general the expectations are in good agreement with data. The systematic uncertainty well covers the small discrepancy.

Fake lepton backgrounds

Fake leptons typically come from the mis-identification of jets, resulting in no correlation in charge of the selected two leptons. On top of that, the final state with the same sign isolated leptons is rare in the standard model. Therefore, the events with the same sign lepton pair satisfying all the other event selection are chosen to define the fake lepton control region.

Figure 7.25 and 7.26 show the distributions of the lepton kinematics, $E_{\mathrm{T}}^{\mathrm{miss}}$, H_T, jet multiplicity and b-tagged jet multiplicity in the fake lepton control region. Due to the low statistics, all three channels are combined together. As shown in the plots, the fake lepton background is enhanced, and dominates the control region. In all the plots, it seems that we systematically overestimate the fake lepton contribution. However, the estimate is still within the systematic uncertainty.

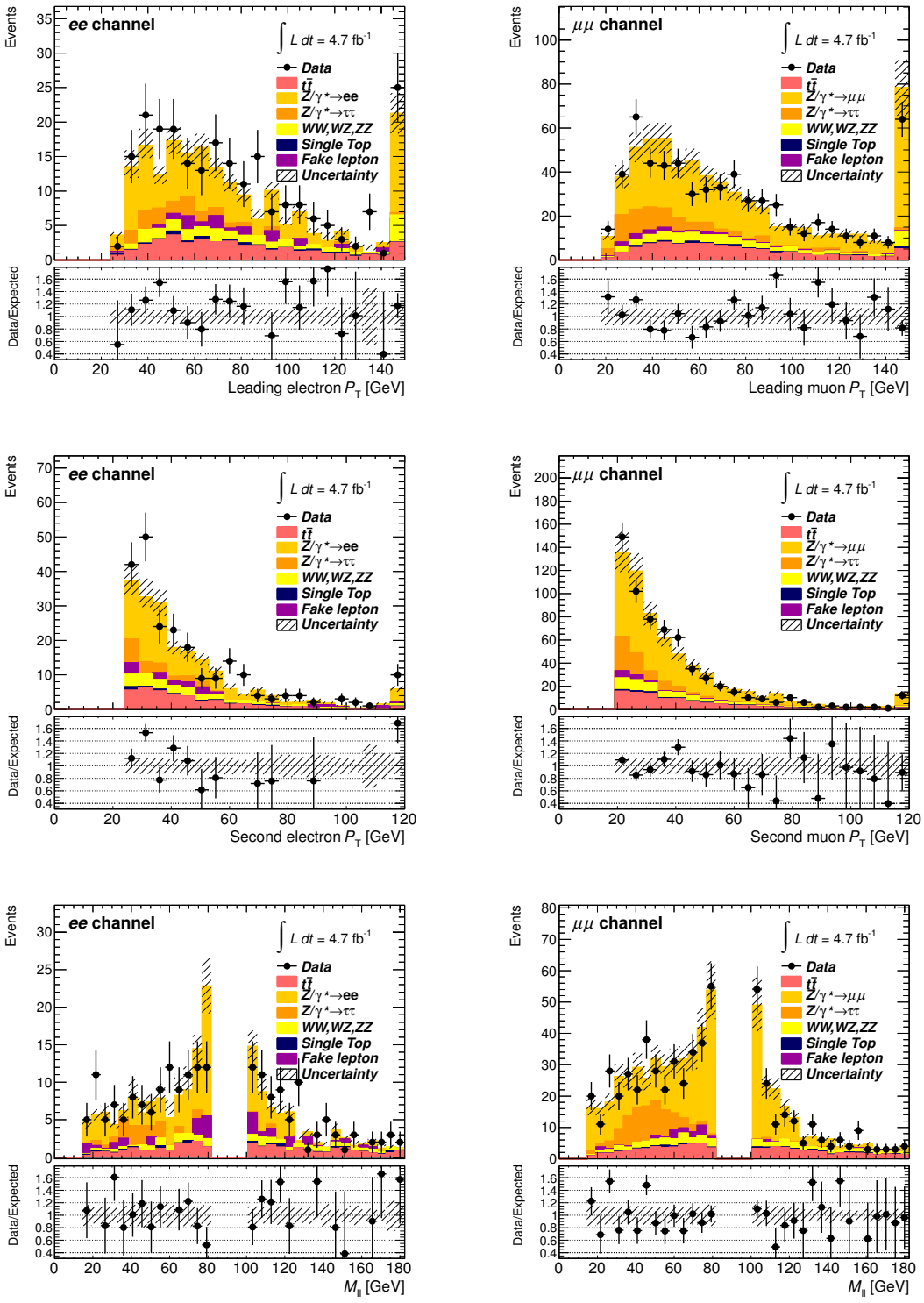


Figure 7.23: Top, middle and bottom plots show P_{T} of the leading and the second leading lepton and the invariant mass of dilepton, respectively, in the Z/γ^* control region. Left (right) shows the one for the ee ($\mu\mu$) channel. The last bin includes the overflow events. The uncertainties indicated here include the uncertainties from the MC statistics and the one related to the normalization of the distribution such as the theoretical uncertainty. The bottom part in each plot shows the ratio between data and the expectation.

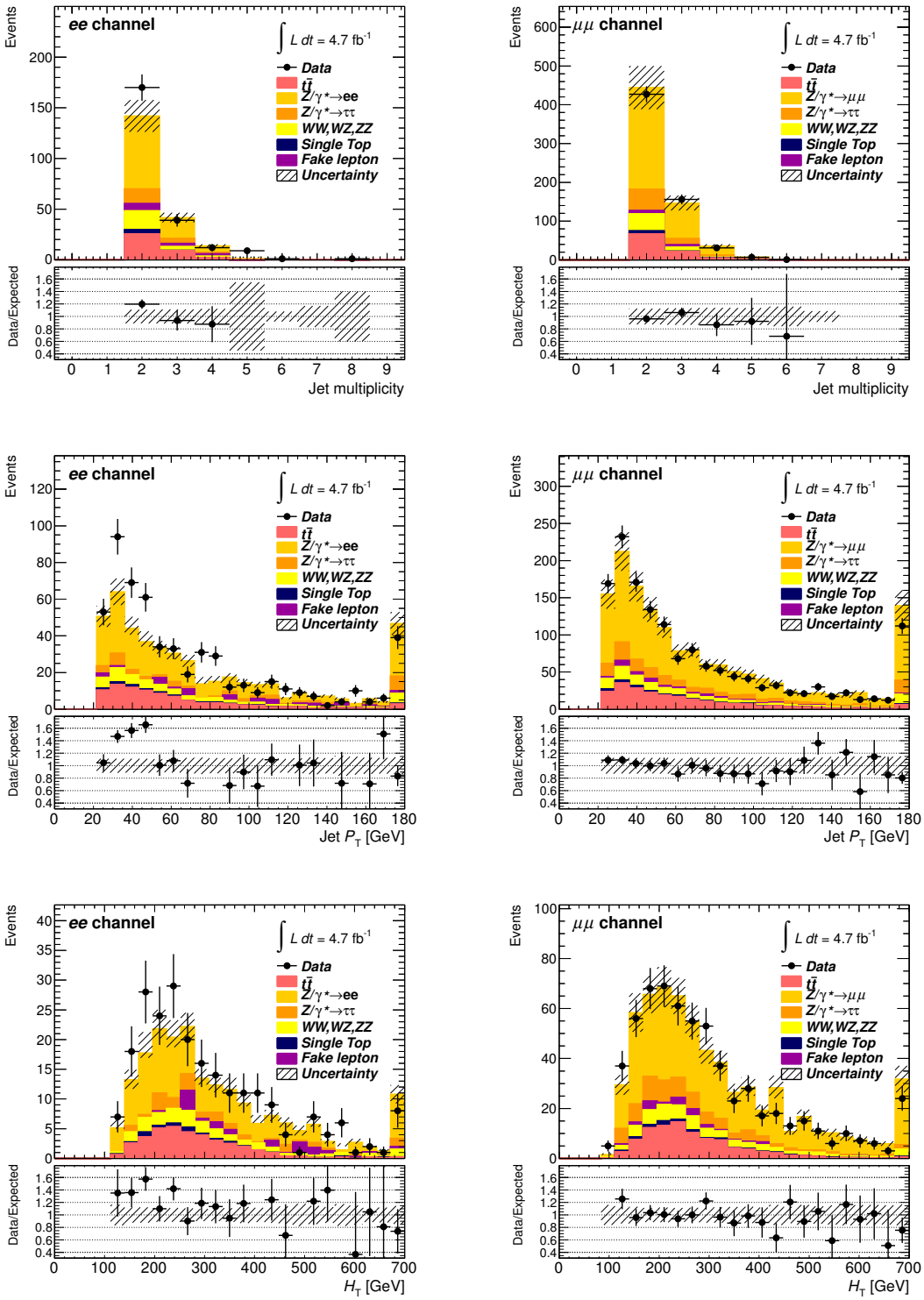


Figure 7.24: Top, middle and bottom plots show the jet multiplicity, the P_{T} of jets and the H_T distribution, respectively, in the Z/γ^* control region. Left (right) shows the one for the ee ($\mu\mu$) channel. The last bin includes the overflow events. The uncertainties indicated here include the uncertainties from the MC statistics and the one related to the normalization of the distribution such as the theoretical uncertainty. The bottom part in each plot shows the ratio between data and the expectation.

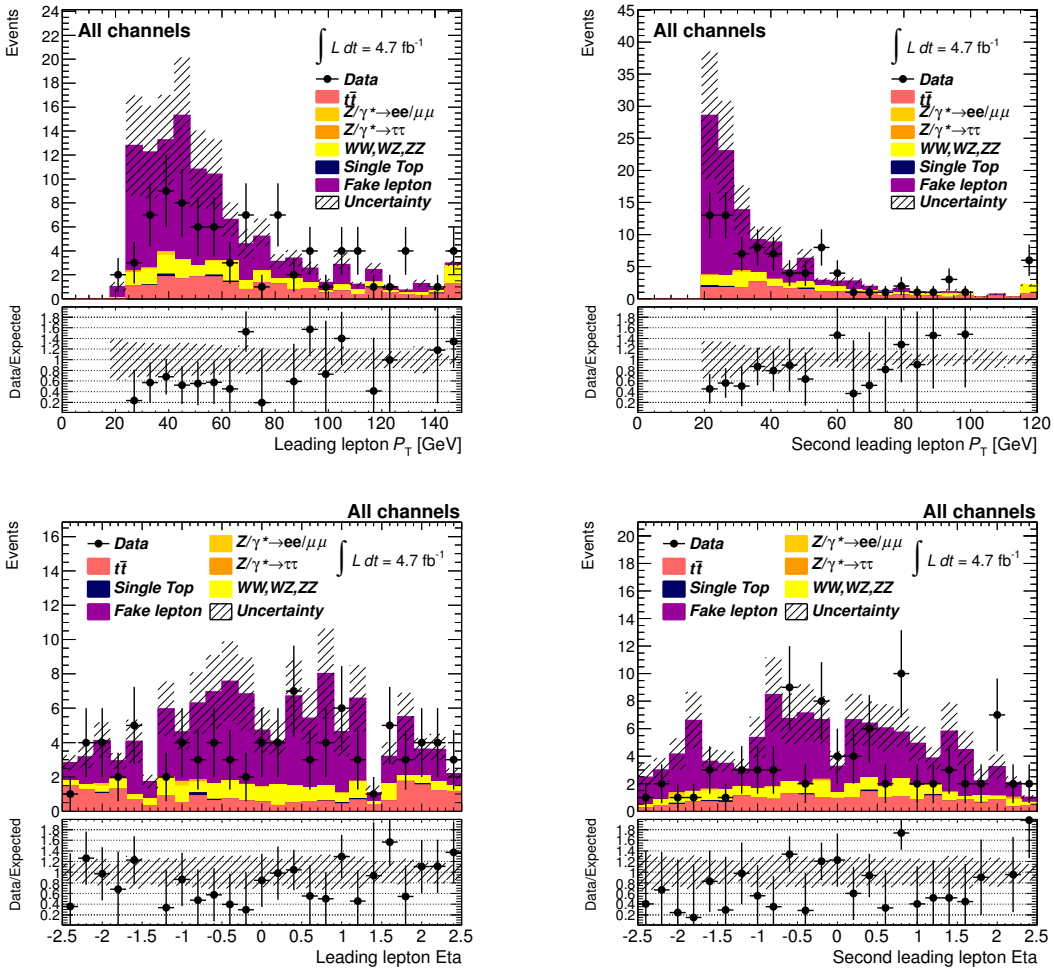


Figure 7.25: The lepton kinematics in the fake lepton control region. Top (Bottom) two figures show the P_T (η) for the leading lepton on the left and the second leading lepton on the right. The last bin for the lepton P_T includes the overflow events. The uncertainties indicated in figures include the uncertainty from the MC statistics, the theoretical cross section uncertainty, and the fake lepton estimate. The bottom part in each plot shows the ratio between data and the expectation.

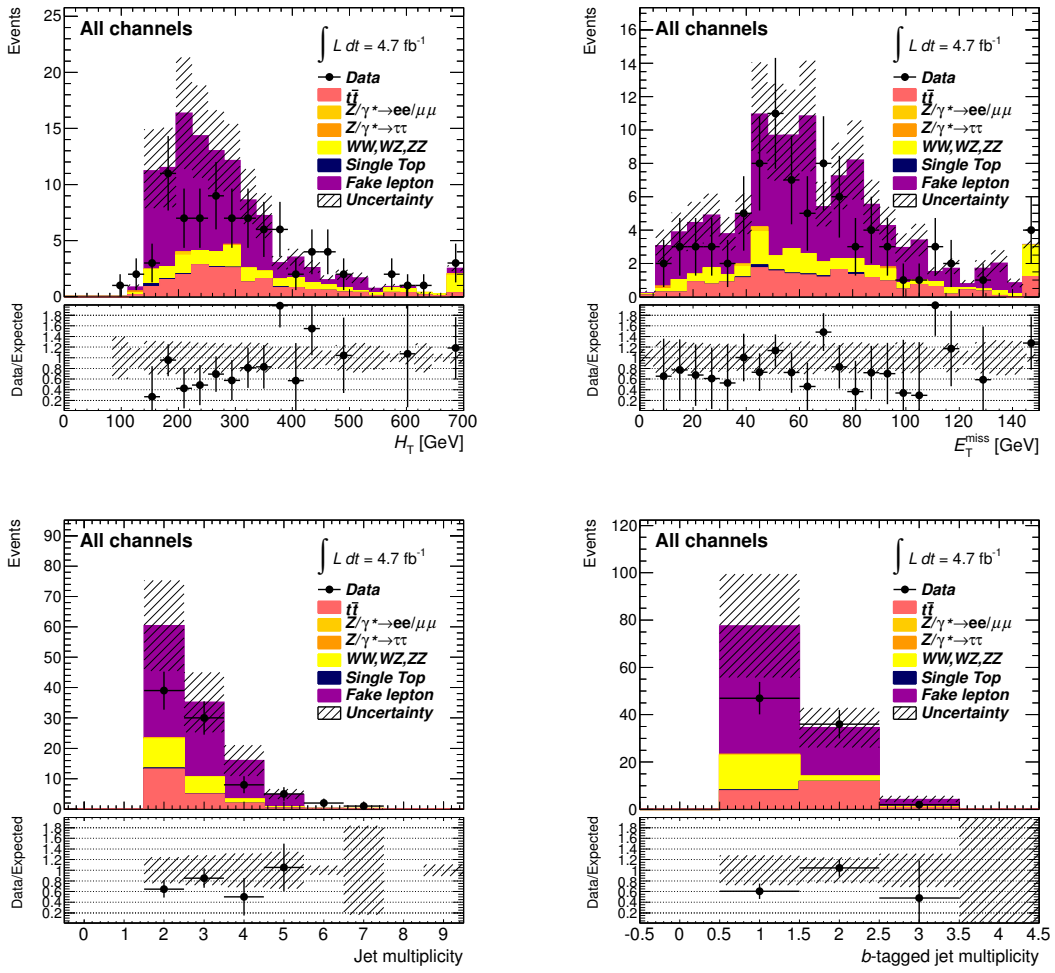


Figure 7.26: The top left (right) figure show the $E_{\mathrm{T}}^{\mathrm{miss}}$ (H_T), and the bottom figures show the jet multiplicity and the b-tagged jet multiplicity. The last bin in each plot includes the overflow events. The uncertainties indicated in figures include the uncertainty from the MC statistics, the theoretical cross section uncertainty, and the fake lepton estimate. The bottom part in each plot shows the ratio between data and the expectation.

$Z \to \tau\tau$ backgrounds

To validate the MC based estimate of $Z/\gamma^* \to \tau\tau$, some distributions in the $e\mu$ channel just after the requirement of two leptons are checked. In the standard model, the final state with one isolated electron and one isolated muon appears typically via the final state with two W bosons or the leptonic decay of tau leptons. The cross section times the branching ratio of $Z/\gamma^* \to \tau\tau \to e\mu +$ neutrinos and $t\bar{t} \to e\mu\nu\nu bb$ are on the same order of magnitude. Therefore, the $Z/\gamma^* \to \tau\tau$ events can be visible in the events with the electron and muon when no cuts to reject $Z/\gamma^* \to \tau\tau$ are applied.

Figure 7.27 shows the lepton P_T, the invariant mass of the dilepton, and the b-tagged jet multiplicity after requiring the event to have one electron and one muon with more than one jets. The requirement on the number of jets are added to make the final state close to the signal region. We can see a significant contribution at the low lepton P_T region, the region in 40 GeV $< M_{\ell\ell} <$ 80 GeV and the zero b-tagged jet bin. In the invariant mass distribution, the peak is shifted from M_Z due to the loss of the energy by neutrinos from tau lepton decays. Both the amount and the shape of $Z/\gamma^* \to \tau\tau$ are well modeled by the MC simulation, and the small discrepancy is well covered by the systematic uncertainty.

7.5 Signal region

The expected and the observed yields for each channel after applying all the event selections are summarized in Table 7.12. The numbers of observed events in data are 960, 2613 and 4813 for the ee, the $\mu\mu$ and the $e\mu$ channel, respectively, while 958 ± 117, 2480 ± 260 and 4650 ± 520 events are expected in each channel. The observed numbers of events are in good agreement with the expectations. The leading sources of the background are Z/γ^* events for the ee and the $\mu\mu$ channel, and the single top events for the $e\mu$ channel.

Table 7.12: The predicted and the observed numbers of events for each final state. The uncertainties include statistic and systematic uncertainties. The word '(DD)' indicates that the contribution is estimated by the data-driven method.

	Yields(ee)	Yields($\mu\mu$)	Yields($e\mu$)
$Z/\gamma^*(\to ee/\mu\mu)$+jets (DD)	$(4.8 \pm 1.6) \times 10^1$	$(1.91 \pm 0.58) \times 10^2$	-
$Z/\gamma^*(\to \tau\tau)$+jets	$(9.3 \pm 3.8) \times 10^0$	$(3.1 \pm 1.2) \times 10^1$	$(6.1 \pm 2.3) \times 10^1$
Di-boson	$(1.09 \pm 0.15) \times 10^1$	$(2.42 \pm 0.38) \times 10^1$	$(5.47 \pm 0.83) \times 10^1$
Single top	$(3.70 \pm 0.57) \times 10^1$	$(9.0 \pm 1.2) \times 10^1$	$(1.92 \pm 0.24) \times 10^2$
Fake lepton (DD)	$(3.3 \pm 1.6) \times 10^1$	$(6.5 \pm 2.0) \times 10^1$	$(8.9 \pm 3.5) \times 10^1$
Total backgrounds	$(1.38 \pm 0.24) \times 10^2$	$(4.02 \pm 0.64) \times 10^2$	$(3.96 \pm 0.49) \times 10^2$
$t\bar{t}$ signal	$(8.20 \pm 1.14) \times 10^2$	$(2.07 \pm 0.25) \times 10^3$	$(4.25 \pm 0.51) \times 10^3$
Total expected	$(9.58 \pm 1.17) \times 10^2$	$(2.48 \pm 0.26) \times 10^3$	$(4.65 \pm 0.52) \times 10^3$
Observed data	960	2613	4813

The plots in the signal region are shown in Figure 7.28 to 7.32. Figure 7.28 shows the lepton kinematics. The $E_{\mathrm{T}}^{\mathrm{miss}}$ and the H_{T} distribution are shown in Figure 7.29. The number of jets and the number of b-tagged jets are shown in Figure 7.30. P_T of all the selected jets and the leading jet are shown in Figure 7.31 and ones for the second and the third jets in Figure 7.32. One can see that the selections with $E_{\mathrm{T}}^{\mathrm{miss}}$ and the b-tagging suppress background. In all the plots, the expected shapes are consistent with the one in data within the uncertainty. However,

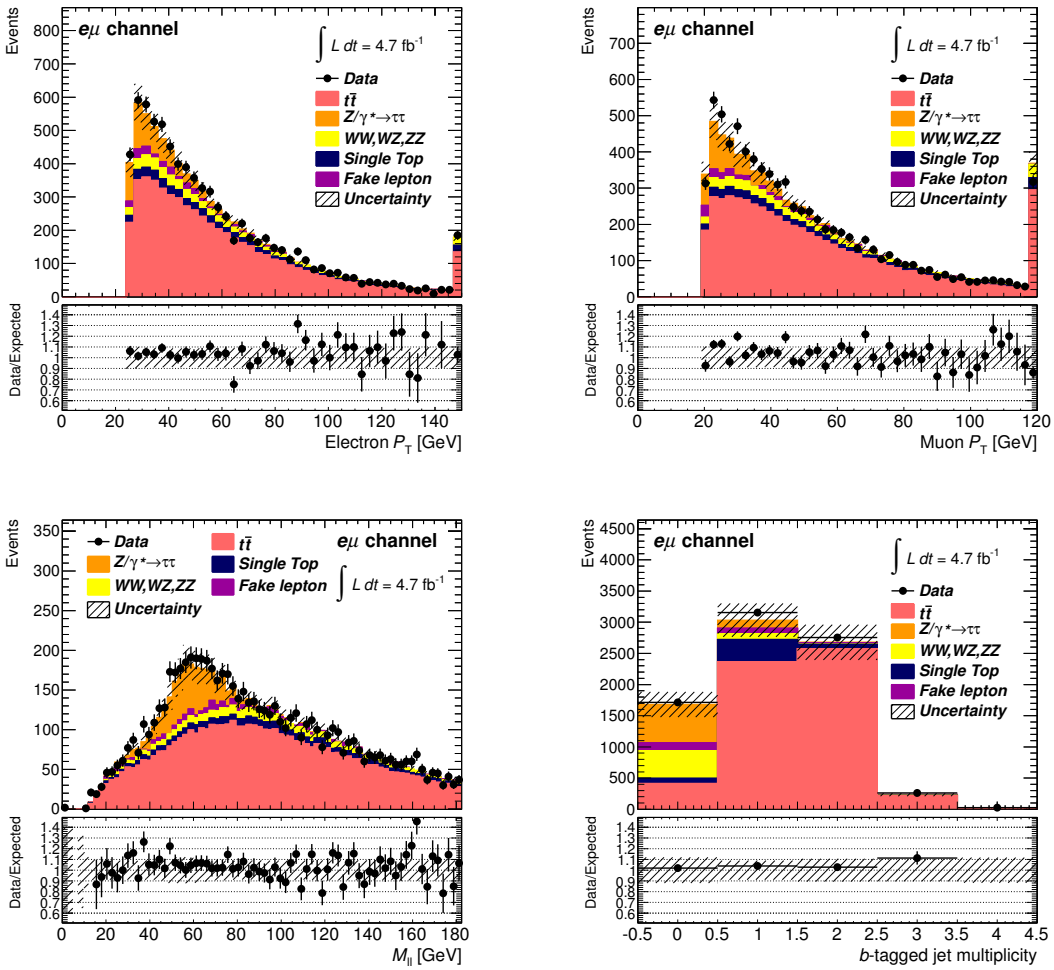


Figure 7.27: The electron and muon P_T (top left and right), the invariant mass of the dilepton system, $M_{\ell\ell}$,(bottom left) and the b-tagged jet multiplicity in the $e\mu$ event with one or more jets. The last bin for the lepton P_T includes the overflow events. The uncertainties indicated in figures include the uncertainty from the MC statistics, the theoretical uncertainty, and the fake lepton estimate. The bottom part in each plot shows the ratio between data and the expectation.

we see some points where mis-modeling may exist in the MC simulation, although the impact to the final result of the $\sigma_{t\bar{t}}$ measurement is small or negligible because they are well covered by the uncertainty due to JES, the b-tagging, the signal modeling.

- Systematic excess in low lepton P_T region in the $e\mu$ channel

We can see in Figure 7.28 a systematic excess at the low lepton P_T region in the $e\mu$ channel. We think this is caused by the background mis-modeling because of the fact that no such discrepancy is observed in the ee and the $\mu\mu$ channel. If the P_{T} spectrum of the $t\bar{t}$ signal was not modeled properly, a discrepancy should be observed in all these channels. On the other hand, the background mis-modeling can affect the expectation for each channel separately because the background composition is different among the three channels.

- Modeling of additional jet in the $t\bar{t}$ sample

In the jet multiplicity distribution in Figure 7.30, we can see that the discrepancy between data and the expectation gets larger in all the channels as the number of jets increases. MC@NLO MC used as the $t\bar{t}$ modeling here is the NLO generator, and hence one additional jet is explicitly generated at the matrix element level. Additional jets are generated by parton showers and fragmentation, which is difficult to model. With the current tuning, MC@NLO tends to generate less additional jets. We estimate the impact to the $\sigma_{t\bar{t}}$ measurement to be less than 1 %. The impact is not significant because the fraction of events with high jet multiplicity is small compared to the total number of events observed in the signal region.

- Modeling of jet P_T

The systematic excess can be seen in low jet P_T region for the inclusive jet sample in Figure 7.31. The lack of the additional jets in MC as presented above makes this discrepancy. The P_T distributions for the first to the third leading jets in Figure 7.31 and Figure 7.32 show good agreements between data and the expectations because those jets are most likely produced at the generator level by the matrix element calculation.

7.6 Cross section measurement

The cross section is obtained by using a likelihood fit. The likelihood is calculated based on the probability of observing N^{obs} events when N^{exp} events are expected. On top of that, to take the effect of systematic uncertainties, some of which are correlated between channels, the corrections are applied to the likelihood. The likelihood function used in the fitting is

$$L(\sigma_{t\bar{t}}, \mathcal{L}, \vec{\alpha}) = \mathcal{G}(\mathcal{L}_0|\mathcal{L}, \sigma_{\mathcal{L}}) \prod_{i\in\{ee,\mu\mu,e\mu\}} \mathcal{P}(N_i^{\mathrm{obs}}|N_{i,tot}^{\mathrm{exp}}(\vec{\alpha})) \prod_{j\in\mathrm{syst}} \mathcal{G}_j(0|\alpha_j, 1). \tag{7.5}$$

The first term $\mathcal{G}(\mathcal{L}_0|\mathcal{L}, \delta_{\mathcal{L}})$ represents a probability related to the integrated luminosity $\mathcal{L}$ with a Gaussian assumption. The central value of the integrated luminosity is given as $\mathcal{L}_0$ with its uncertainty $\sigma_{\mathcal{L}}$. The probability of observing N_i^{obs} events in each final state i with given numbers of expected events, $N_{i,tot}^{\mathrm{exp}}$, is modeled by a Poisson distribution. The systematic variation of $N_{i,tot}^{\mathrm{exp}}$ caused by each systematic source is modeled by the Gaussian distribution $\mathcal{G}_j$ for the associated nuisance parameter α_j. The variation of the systematic source by ± 1 standard deviation is represented by $\alpha_j = \pm 1$. The cross section $\sigma_{t\bar{t}}$ is left as a free parameter of

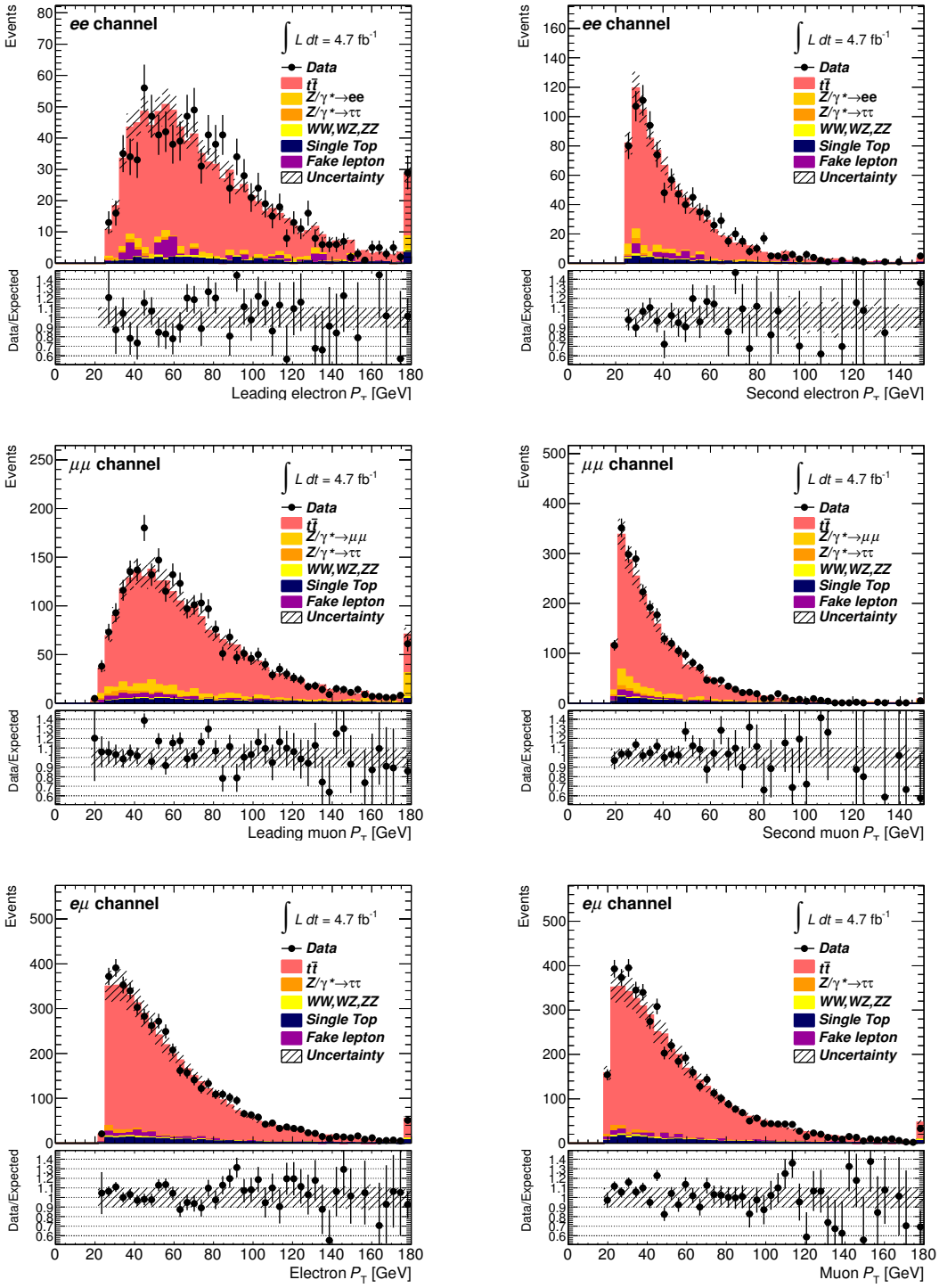


Figure 7.28: Lepton kinematics for ee (top), $\mu\mu$ (middle) and $e\mu$ (bottom) channels. For the ee and $\mu\mu$ channel, the left plots show the P_{T} of the leading lepton, and the right shows the one for second lepton. For the $e\mu$ channel, the P_{T} of electron is on left and the one for muon is on right. The last bin includes the overflow events. The uncertainty band includes the MC statistics and uncertainties related to the MC normalization.

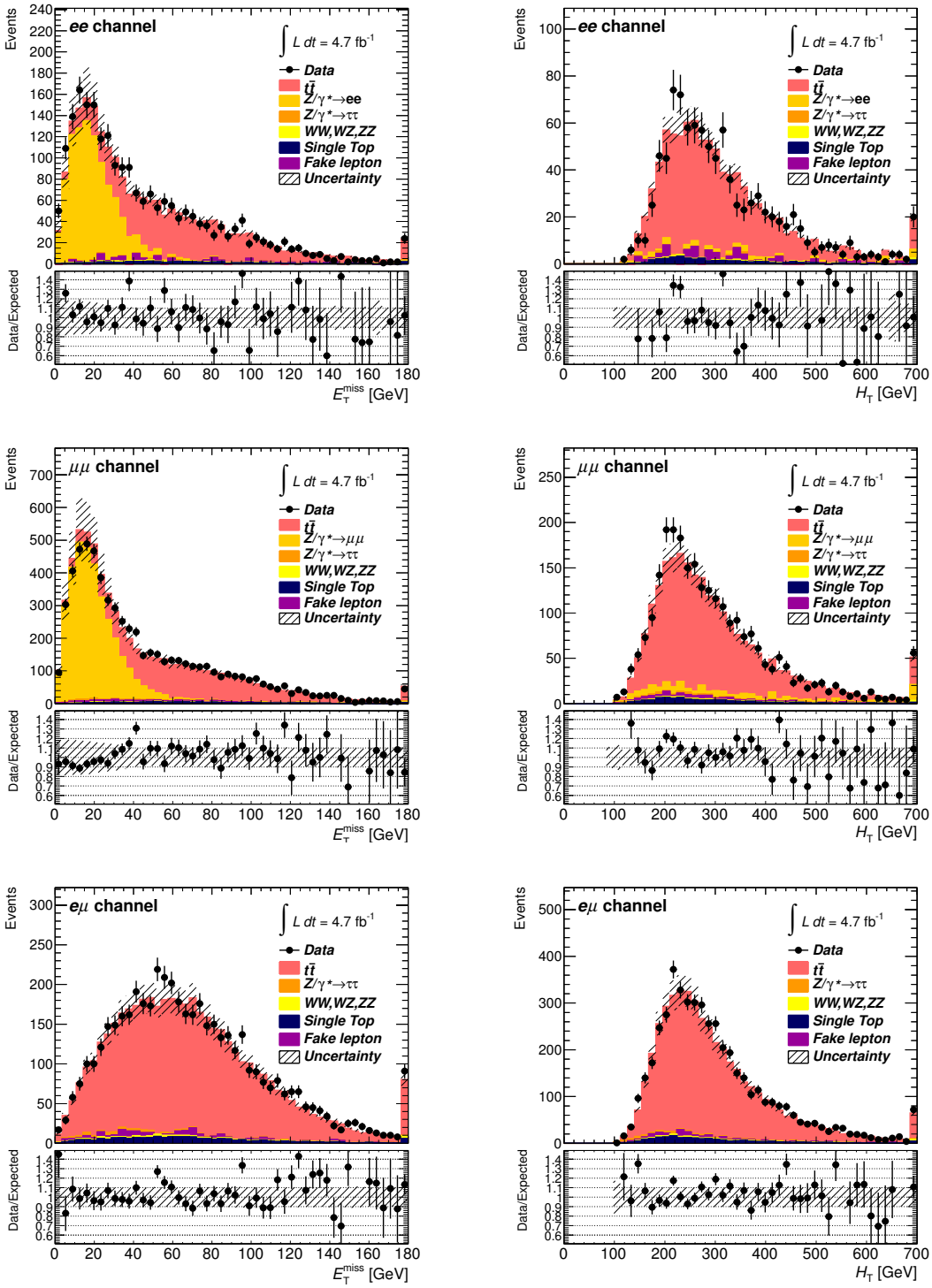


Figure 7.29: Top, middle and bottom plots are for ee, $\mu\mu$ and $e\mu$ channels. $E_{\mathrm{T}}^{\mathrm{miss}}$ distributions are on the left, and H_{T} on the right. In the $E_{\mathrm{T}}^{\mathrm{miss}}$ plots for the ee and $\mu\mu$ channel, $E_{\mathrm{T}}^{\mathrm{miss}}$ selection is omitted for the illustration purpose. The similar treatment is applied for the H_{T} plot for the $e\mu$ channel. The last bin includes the overflow events. The uncertainty band includes the MC statistics and uncertainties related to the MC normalization.

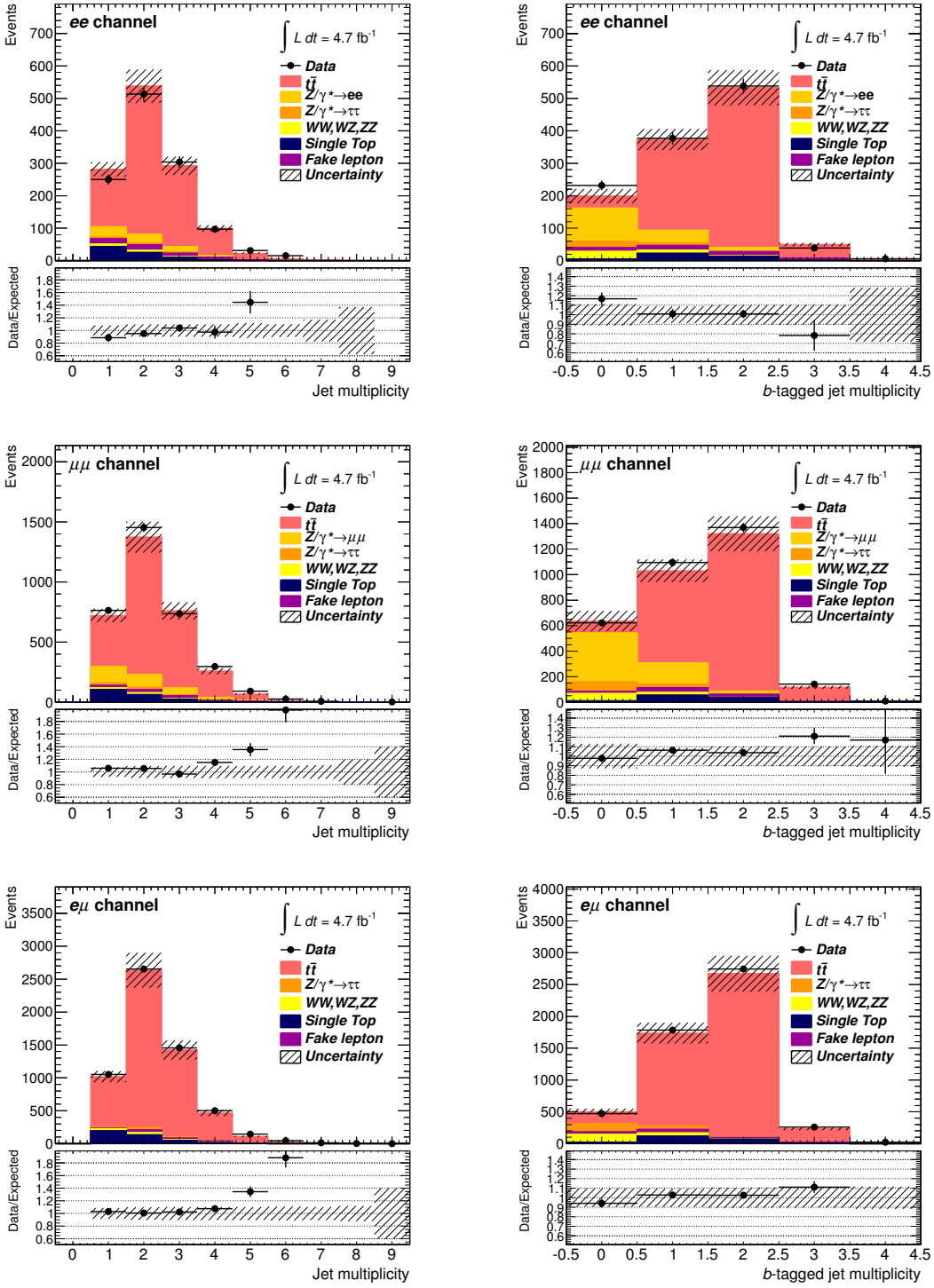


Figure 7.30: Top, middle and bottom plots are for ee, $\mu\mu$ and $e\mu$ channels. The left plots shows the number of jets after all selections but the number of jet cut. The right plots show the b-tagged jet multiplicity distribution before requiring the b-tagging selection. The uncertainty band includes the MC statistics and uncertainties related to the MC normalization.

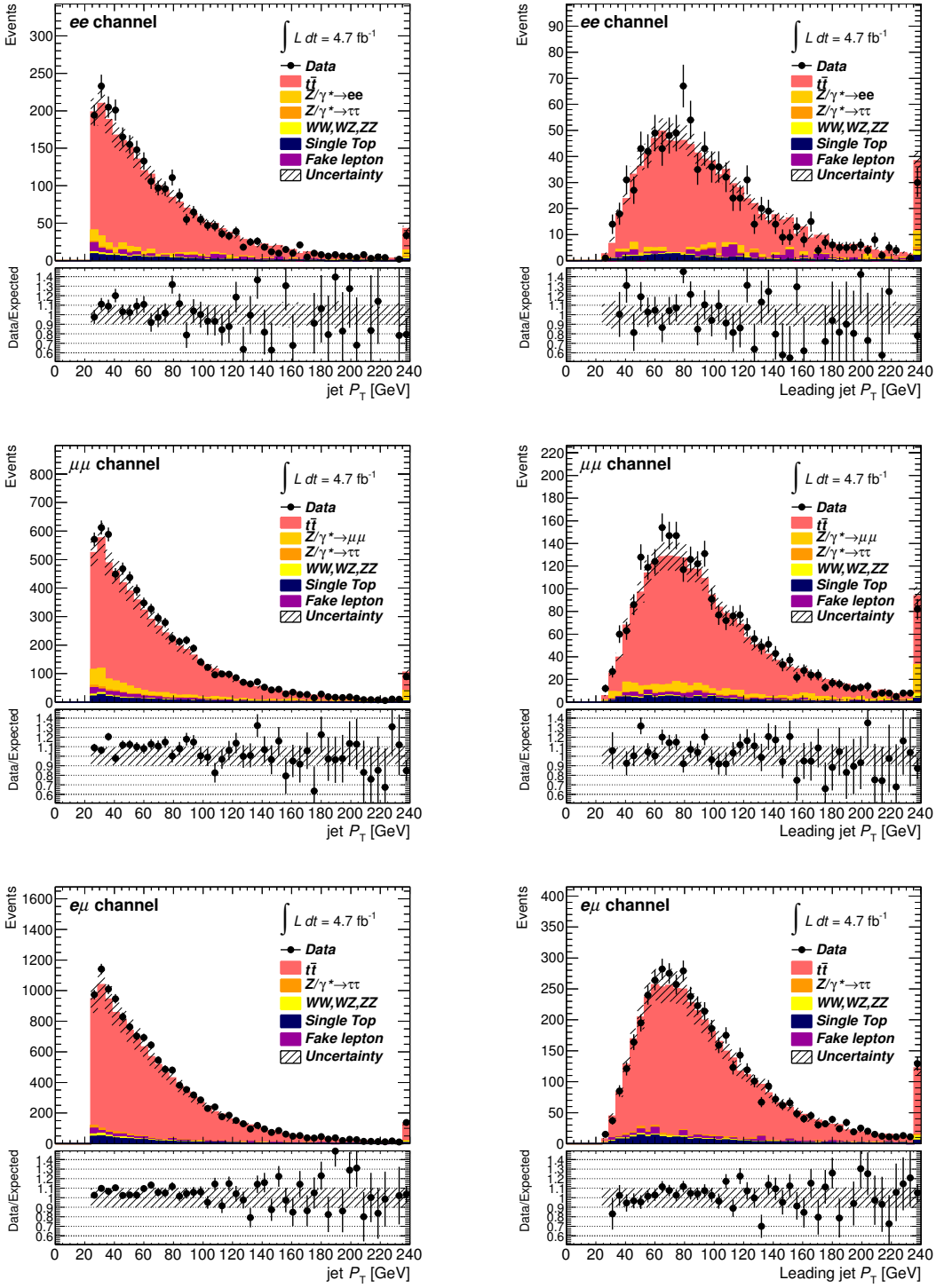


Figure 7.31: Top, middle and bottom plots are for ee, $\mu\mu$ and $e\mu$ channels. Jet P_{T} distributions for all the selected jets are on the left, and the one for the leading jet on the right. The last bin includes the overflow events. The uncertainty band includes the MC statistics and uncertainties related to the MC normalization.

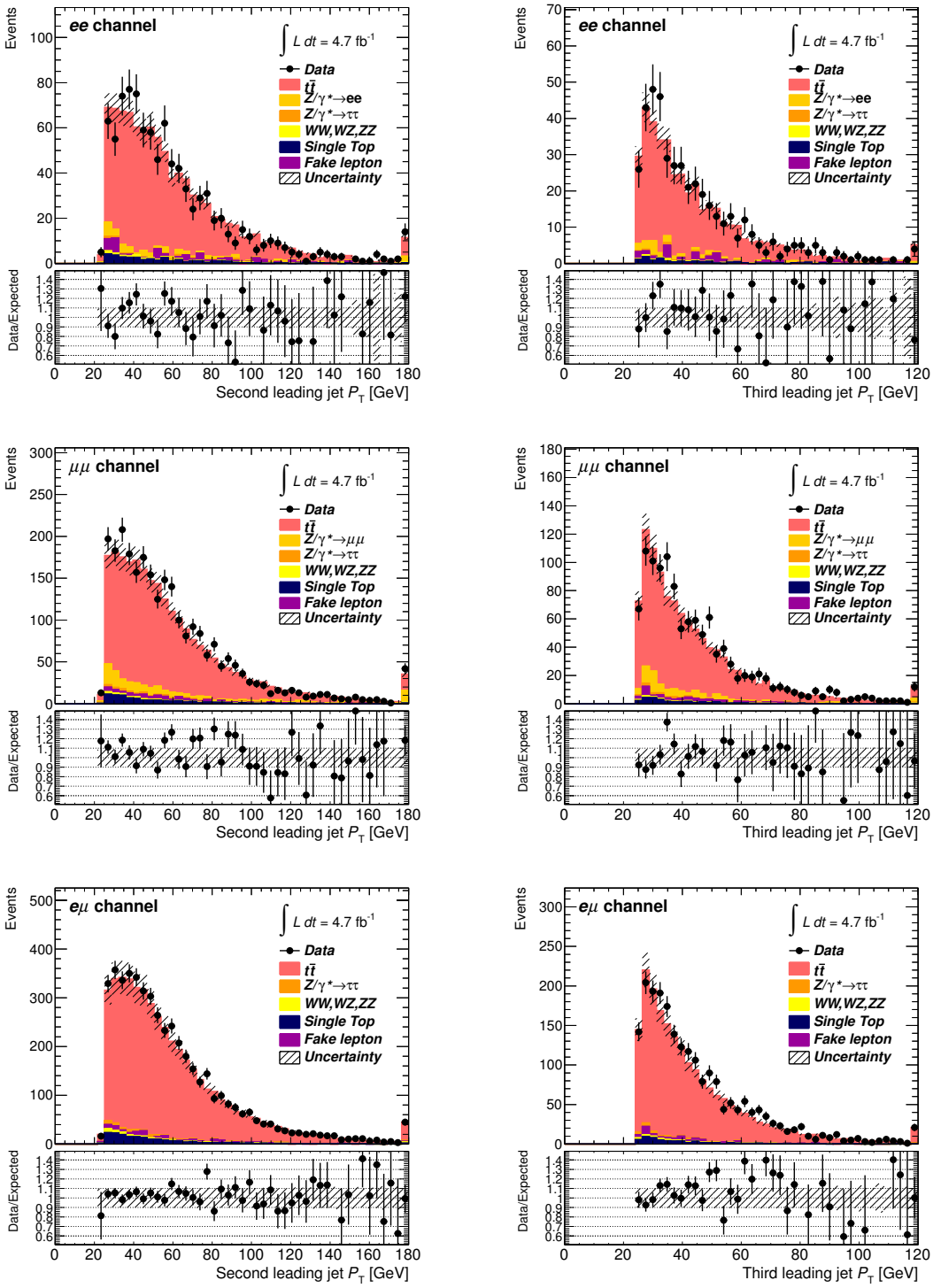


Figure 7.32: Top, middle and bottom plots are for ee, $\mu\mu$ and $e\mu$ channels. Jet P_{T} distributions for the second (third) leading jet are on the left (right). The last bin includes the overflow events. The uncertainty band includes the MC statistics and uncertainties related to the MC normalization.

the likelihood fitting. In addition, the central value of α_j is adjusted during fitting to find a maximum likelihood. Each measurement is based on the likelihood ratio denoted as

$$\lambda(\sigma_{t\bar{t}}) = \frac{L(\sigma_{t\bar{t}}, \hat{\hat{\mathcal{L}}}, \hat{\hat{\alpha}}_j)}{L(\hat{\sigma}_{t\bar{t}}, \hat{\mathcal{L}}, \hat{\alpha}_j)}. \tag{7.6}$$

In the above equation, $\hat{\sigma}_{t\bar{t}}$, $\hat{\mathcal{L}}$ and $\hat{\alpha}_j$ denote the maximum likelihood estimate of all parameters. The parameters $\hat{\hat{\mathcal{L}}}$ and $\hat{\hat{\alpha}}_j$ are the conditional maximum likelihood estimates of L and α_j keeping $\sigma_{t\bar{t}}$ fixed. Resulting cross section inferred from the likelihood ratio is validated by an ensemble test to be unbiased. In addition, it is confirmed that the variance of $\hat{\sigma}_{t\bar{t}}$ is consistent with the curvature of the likelihood at its minimum. Therefore, the 68 % confidence interval is derived from the value of $\sigma_{t\bar{t}}$ which gives $-2\log\lambda(\sigma_{t\bar{t}}) = 1$. Figure 7.33 shows $-2\log\lambda(\sigma_{t\bar{t}})$ as a function of $\sigma_{t\bar{t}}/\sigma_{t\bar{t}}^{\mathrm{Theory}}$.

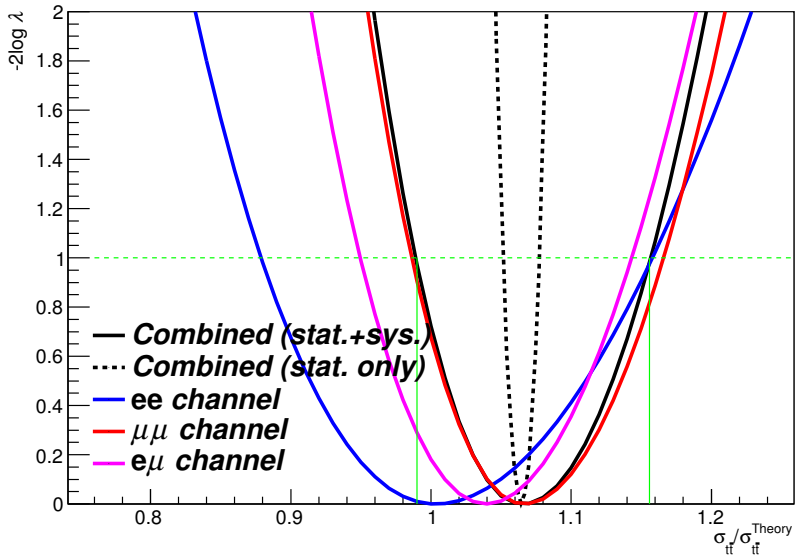


Figure 7.33: Twice of negative log likelihood ratio as a function of $\sigma_{t\bar{t}}/\sigma_{t\bar{t}}^{\mathrm{Theory}}$. The black solid (dotted) line shows the combined result considering the statistic and the systematic uncertainties (only the statistic uncertainty). The likelihood ratio for the ee, the $\mu\mu$ and the $e\mu$ channels are in blue, red and magenta line, respectively. The green line shows $-2\log\lambda = 1$ which corresponds to the one standard deviation for the combined result.

Table 7.13 and Figure 7.34 summarizes the measured cross sections in each channel and the combination of all three channels. They are consistent with each other. The combined result gives $177 \pm 2^{+14}_{-11} \pm 3$ pb. This result is close to the one obtained in the $\mu\mu$ channel, $178 \pm 4^{+15}_{-11} \pm 3$ pb, although the $e\mu$ channel has the highest statistics. This is caused by the fact the precision of this measurement is dominated by the systematic uncertainty which has a correlation among the channels and the muon related uncertainty is much smaller than the one related to electron.

Table 7.14 summarizes the estimated size of the uncertainty on the cross section measurement. The main uncertainty sources are JES and the b-tagging efficiency. This reflects the fact that the signal acceptance estimate is the dominant source of the uncertainty because of the high signal-to-background ratio. In the end, the precision of $+8.7/-7.1$ % for the combined result is achieved.

Table 7.13: The measured cross sections in each dilepton channel, and the combination of all three channels.

Channel	$\sigma_{t\bar{t}}$ [pb] (stat.,syst.,lumi.)
ee	$167 \pm 6^{+25}_{-19} \pm 3$
$\mu\mu$	$178 \pm 4^{+15}_{-11} \pm 3$
$e\mu$	$173 \pm 3^{+16}_{-14} \pm 3$
Combined	$177 \pm 2^{+14}_{-11} \pm 3$

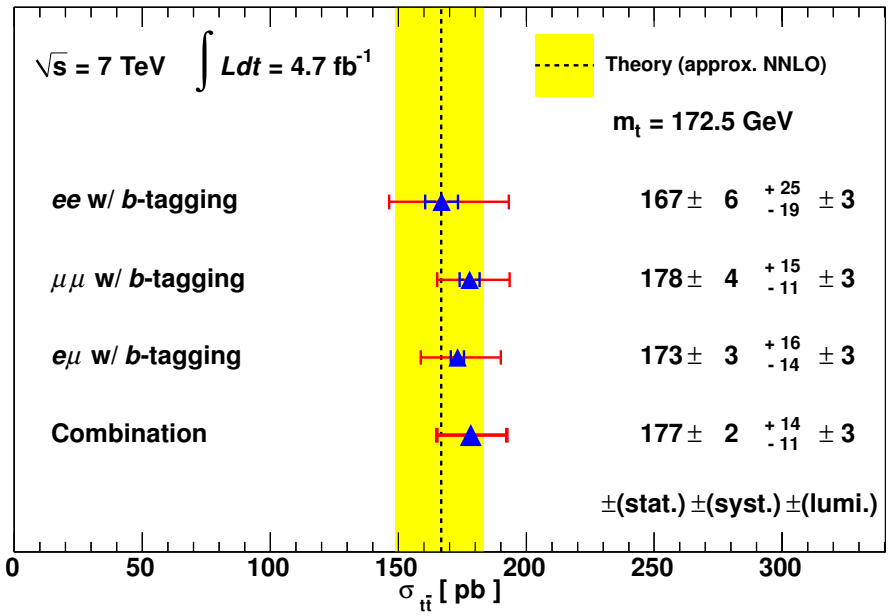


Figure 7.34: Measured production cross section of $t\bar{t}$. The yellow band shows a theoretical prediction.

Table 7.14: The summary of the uncertainty for the cross section measurement.

	ee	$\mu\mu$	$e\mu$	Combined
Uncertainty source	$\delta\sigma_{t\bar{t}}/\sigma_{t\bar{t}}$[%]	$\delta\sigma_{t\bar{t}}/\sigma_{t\bar{t}}$[%]	$\delta\sigma_{t\bar{t}}/\sigma_{t\bar{t}}$[%]	$\delta\sigma_{t\bar{t}}/\sigma_{t\bar{t}}$[%]
Data statistics	+3.8 / −3.8	+2.3 / −2.3	+1.6 / −1.6	+1.2 / −1.2
Luminosity	+1.9 / −1.9	+1.9 / −1.9	+1.9 / −1.9	+1.9 / −1.9
MC statistics	+1.4 / −1.4	+1.0 / −1.0	+0.6 / −0.6	+0.5 / −0.5
Jet energy scale	+3.9 / −3.9	+3.4 / −1.5	+3.1 / −2.4	+3.1 / −1.6
Jet energy resolution	+1.6 / −1.6	+2.7 / −2.7	+0.8 / −0.8	+1.1 / −1.1
Jet reconstruction efficiency	+0.0 / −0.0	+0.0 / −0.0	+0.0 / −0.0	+0.0 / −0.0
El./Mu. energy scale	+0.5 / −0.5	+0.3 / −0.3	+0.3 / −0.3	+0.3 / −0.3
El./Mu. energy resolution	+0.0 / −0.0	+0.0 / −0.0	+0.1 / −0.1	+0.0 / −0.0
El./Mu. trig./reco efficiency	+7.5 / −6.4	+3.2 / −3.2	+3.9 / −3.9	+2.6 / −2.6
Missing transverse energy	+0.8 / −0.8	+1.0 / −1.0	+0.0 / −0.0	+0.3 / −0.3
Z/γ^* estimation	+0.4 / −0.4	+0.5 / −0.5	+0.0 / −0.0	+0.0 / −0.0
Fake lepton estimation	+2.1 / −2.1	+0.9 / −0.9	+0.8 / −0.8	+0.6 / −0.6
b-tagging efficiency	+4.9 / −3.1	+4.6 / −3.4	+4.8 / −3.7	+4.7 / −3.9
b-tagging fake rate (c-jet)	+0.0 / −0.0	+0.0 / −0.0	+0.1 / −0.1	+0.0 / −0.0
b-tagging fake rate (light-jet)	+0.0 / −0.0	+0.3 / −0.3	+0.3 / −0.3	+0.0 / −0.0
Generator	+3.0 / −3.0	+2.1 / −2.1	+3.7 / −3.7	+2.8 / −2.8
Parton shower modeling	+4.5 / −4.5	+2.1 / −2.1	+2.6 / −2.6	+2.4 / −2.4
Initial/final state radiation	+7.4 / −6.0	+1.4 / −1.4	+3.3 / −3.3	+2.0 / −2.0
Parton distribution function	+2.8 / −2.8	+2.5 / −2.5	+2.2 / −2.2	+2.3 / −2.3
Heavy flavor fraction	+0.3 / −0.3	+0.4 / −0.4	+0.3 / −0.3	+0.3 / −0.3
σ_{theory} for BG	+0.6 / −0.6	+0.6 / −0.6	+0.6 / −0.6	+0.6 / −0.6
All systematics but luminosity	+14.9 / −11.6	+8.9 / −6.9	+9.8 / −8.2	+8.3 / −6.8
All systematics	+15.2 / −11.5	+9.1 / −7.1	+10.1 / −8.3	+8.6 / −7.0
Total uncertainty	+15.7 / −12.1	+9.4 / −7.5	+10.2 / −8.5	+8.7 / −7.1

Chapter 8

Discussion

We have presented the analysis of the $\sigma_{t\bar{t}}$ measurement. In this section, we will discuss our result, the theoretical prediction and the possible improvements. The knowledge on the top quarks obtained through this analysis, which would make an impact on the future physics program in LHC, is also presented.

Comparison with the theoretical prediction

Comparing the measured cross sections with the approximate NNLO prediction by the HATHOR program, $\sigma_{t\bar{t}}^{\mathrm{Theory}} = 166.78\ ^{+4.68}_{-9.26}$ (scale) $^{+5.12}_{-4.93}$ (m_t) $^{+15.80}_{-15.09}$ (PDF) pb, all the final states show systematically higher cross sections, but they are still consistent with the prediction.

We achieved the ± 8 % precision in the combined channel. Our measurement is already more precise than the theoretical prediction. To find the phenomenon of beyond the standard model in the $\sigma_{t\bar{t}}$ measurement, more precise prediction is needed. The current prediction is limited by the uncertainty from PDFs and the factorization and renormalization scales. The more precise measurement of PDFs in the LHC experiments would help to improve the theoretical prediction. By using the MCFM program, the uncertainty from the factorization and renormalization scales is estimated as 50 % at the LO calculation and 30 % at the NLO calculation. At the approximate NNLO calculation, the size of the uncertainty is about 5 % as described above. Therefore, the exact NNLO or further NNNLO calculation would be more insensitive to these scales and would give a precise prediction.

Precision of measurement

The main sources of the systematic uncertainty of this analysis are JES and b-tagging. We think that there is still a room to reduce the uncertainty from them. As discussed in Section 7.1.1, the selection threshold of $E_{\mathrm{T}}^{\mathrm{miss}}$, H_{T}, etc. are optimized to minimize these uncertainties. However, other possibilities to reduce the uncertainty were not considered. For example, the acceptance variation due to JES would be reduced by changing the requirement on the number of jets from at least two to at least one. This is because the second leading jet is more sensitive to the JES shift as P_{T} of the second leading jets is populated around the jet P_{T} threshold of 25 GeV as shown in Figure 7.32. For the b-tagging uncertainty, the precision of the ε_b measurement can be improved by combining our results with other measurements.

In general, the systematic uncertainty is often stemmed from the statistic nature, *e.g.* the precision of lepton efficiency measurement is limited by statistics. Therefore, the precision of the measurement which is limited by the systematic uncertainty can be improved by accumulating more statistics. However, it is not the case for the uncertainty from the $t\bar{t}$ modeling which makes a dominant contribution in this analysis. This means that the most part of the systematic

uncertainty is no longer of the statistic nature. To achieve further precision, we have to better understand the kinematics of $t\bar{t}$ production.

During the systematic study, we found that the jet multiplicity, for example, depends on MC generators and the parton shower modeling. This kind of low energy activity is difficult to calculate theoretically, and thus experimental input is needed. Further studies such as differential cross section for jet multiplicity, P_{T}, and η will help to improve the $t\bar{t}$ modeling. Currently, the ATLAS and the CMS experiments perform such studies but still have a large uncertainty, typically 20 % or more. More precise measurements are expected in future by using the full statistics taken in 2012.

Comparison with the different analysis method and the different final states performed in ATLAS and CMS

Figure 8.1 summarizes $\sigma_{t\bar{t}}$ measured by various analysis methods and final states in the ATLAS and the CMS experiments with $\sqrt{s} = 7$ TeV. Both experiments have performed the measurement

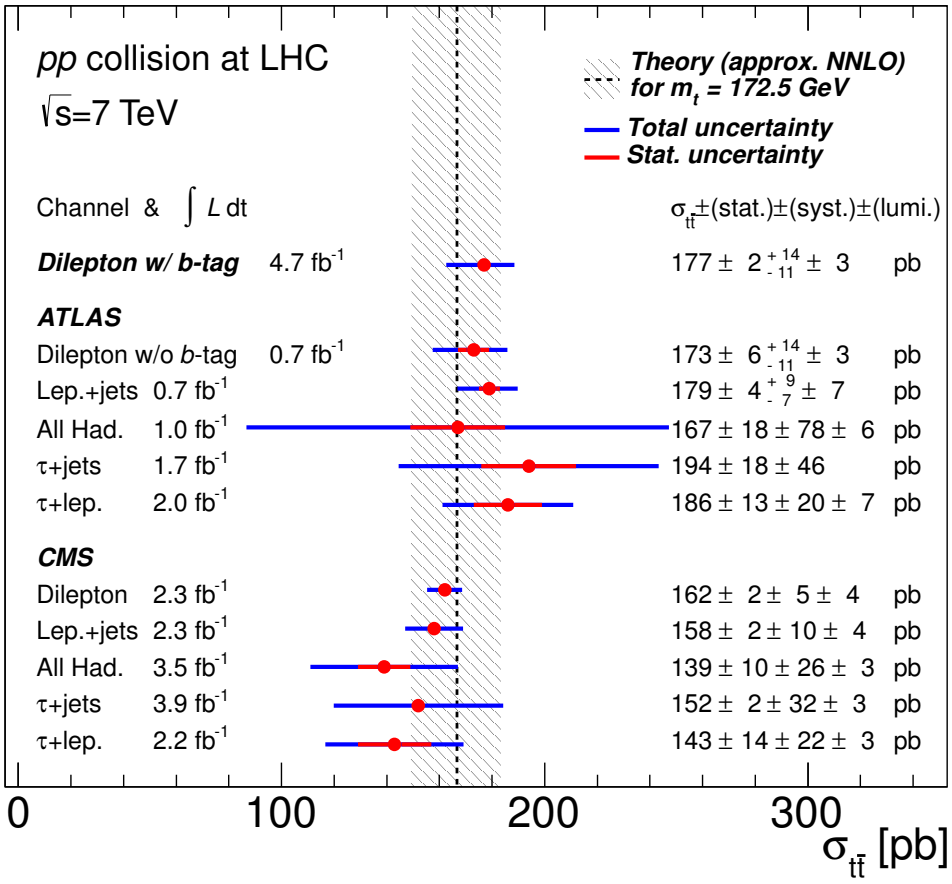


Figure 8.1: Measured cross sections with various final states performed at ATLAS and CMS. Values are referred from the references of [21, 22, 23, 24, 25, 26].

in the dilepton, lepton+jets, all-hadronic, $t\bar{t} \to \tau\nu bqqb$ (called τ+jets) and $t\bar{t} \to \tau\nu b\ell\nu b$ (called τ+lepton) final states. All the results are consistent with the theoretical calculation. This implies that the top quark decays as the standard model predicts.

The precision of all the measurements is systematically limited, although the whole statistics taken with $\sqrt{s} = 7$ TeV is not used except the measurement presented in this thesis. However, it will be improved by using whole statistics, in the tau+lepton and all-hadronic channel in ATLAS for example, because the part of systematic uncertainty comes from the statistic nature as mentioned above.

In the dilepton final state, ATLAS has performed the cut-based counting analysis with and without using b-tagging, while CMS has been performing the analysis utilizing likelihood with jet multiplicity and b-tagged jet multiplicity as its input. At ATLAS, the precision of the result with b-tagging presented in this thesis is $+8.7/-7.1$ %, while the one without b-tagging is $+9.0/-7.5$ %. For CMS, the precision is ± 4.4 %.

The measurements with and without b-tagging in ATLAS have similar size of the uncertainty, but the main source of the uncertainty is different. The analysis without b-tagging is more sensitive to JES and the jet energy resolution because of the relatively lower signal-to-background ratio compared to the one with b-tagging due to the sizable contamination from the Z/γ^* events. The CMS experiment measured $\sigma_{t\bar{t}}$ most precisely in the dilepton final state. The main difference from ATLAS is that their measurement relies on the shape of some distributions. By using the shapes, the analysis becomes relatively insensitive to JES and the $t\bar{t}$ modeling which are the dominant uncertainty sources in ATLAS. This feature can be used in ATLAS as well to further reduce the systematic uncertainty.

Comparing the result obtained by ATLAS with CMS, we can see that the central values of all the measurements in ATLAS are higher than the theoretical prediction, and the other way in CMS, although they all are still in agreement with the theory. It is difficult to explain this feature by statistics because all the statistically independent channels show the same tendency within the group, and the contrast against the other group. Therefore, this fact implies that there is a detector bias. For instance, there might be a possibility that the ATLAS (CMS) experiment is underestimating (overestimating) the signal acceptance.

Dependence on center-of-mass energy

Figure 8.2 shows the expected and the measured cross section as a function of the center-of-mass energy of pp or $p\bar{p}$. Currently, $t\bar{t}$ is observed at pp or $p\bar{p}$ collisions with $\sqrt{s} = 1.8$, 1.96, 7, and 8 TeV. It is found that not only the measurement at 7 TeV but also all the measurements are consistent with the theoretical prediction. The perturbative QCD prediction with the approximately NNLO precision works up to $\sqrt{s} = 8$ TeV.

The top quark pole mass

In Section 1.3, we mentioned that the top quark pole mass, m_t^{pole}, can be extracted by the measured $\sigma_{t\bar{t}}$. Here, we demonstrate the extraction of m_t^{pole} from $\sigma_{t\bar{t}}$ obtained in our measurement.

Figure 8.3 shows the dependence of $\sigma_{t\bar{t}}$ on m_t^{pole} for the theoretical calculations and the measured cross section. The theoretical calculations in approximate NNLO including soft gluon resummations as a function of the pole mass, which is well defined by the renormalization scheme, have been performed in the references [102, 103, 104]. All the theoretical cross sections are parametrized with:

$$\sigma_{t\bar{t}}(m_t) = \frac{1}{{m_t}^4}\left(a + b(m_t - 170) + c(m_t - 170)^2 + d(m_t - 170)^3\right) \text{ pb } (\mathrm{m_t} \text{ in GeV}).$$

The four parameters, a to d, are extracted by fitting a function to the theoretical calculation. The measured $\sigma_{t\bar{t}}$ is shown in circle with its uncertainty at $m_t^{\mathrm{pole}} = 172.5$ GeV. In addition, the

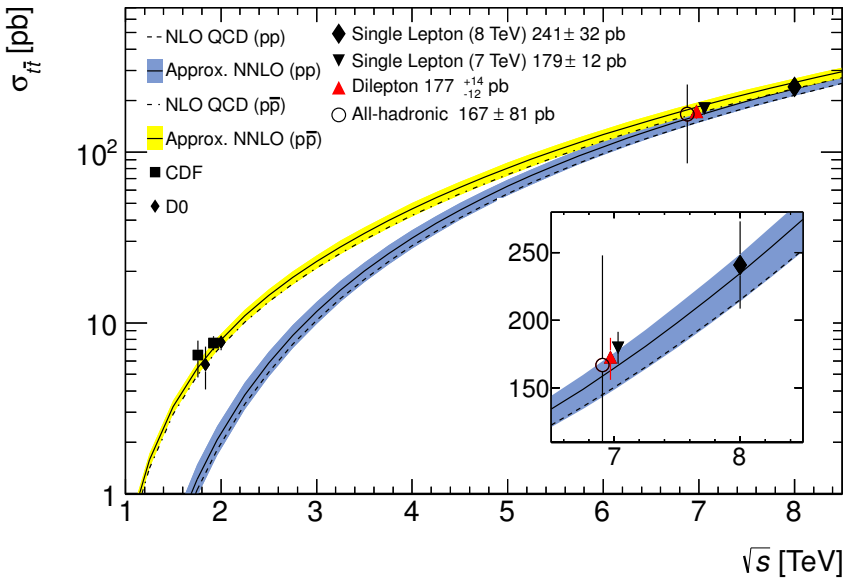


Figure 8.2: Measured cross sections at various center-of-mass energies are indicated with their uncertainties. Our measurement presented in this thesis is shown in the red triangle. The expected production cross section as a function of $\sqrt{s}$ is also shown. The data points at 1.8, 1.96 and 7 TeV are slightly offset horizontally for the illustration purpose.

dependence of the measured $\sigma_{t\bar{t}}$ on $m_t^{\rm pole}$ is obtained from the analysis performed in the ATLAS experiment [105]. The dependence is evaluated by using the MC samples with various assumptions of m_t. The experimental cross section is parametrized using a third order polynomial function:

$$\sigma_{t\bar{t}}(m_t) = a + b(m_t - 170) + c(m_t - 170)^2 + d(m_t - 170)^3 \text{ pb } (\text{m}_\text{t} \text{ in GeV}),$$

and is shown in band with considering the measured uncertainty.

We extracted $m_t^{\rm pole}$ by

$$f(m_t) \propto \int f_{\rm theory}(\sigma|m_t) \cdot f_{\rm experiment}(\sigma|m_t) d\sigma,$$

where $f_{\rm theory}$ ($f_{\rm theory}$) is the theoretical (experimental) probability density function with assuming gaussian centered on the theoretical prediction (experimental measurement) with the uncertainty as its width. The maximum value of this likelihood function determines the extracted $m_t^{\rm pole}$, and the 68 % area from the maximum is considered as the uncertainty of the measurement. The calculated likelihood is shown in Figure 8.4.

The extracted $m_t^{\rm pole}$ for each theoretical calculation is:

$$\begin{aligned} m_t &= 170.9^{+6.0}_{-4.1} \text{ GeV (Kidonakis)}, \\ m_t &= 170.7^{+5.5}_{-6.0} \text{ GeV (Moch and Uwer), and} \\ m_t &= 166.8 \pm 5.8 \text{ GeV (NLO + NNLL)}. \end{aligned}$$

The difference between the results is small. This implies that $m_t^{\rm pole}$ which cannot be extracted by the direct measurement is successfully obtained by the measured cross section with small

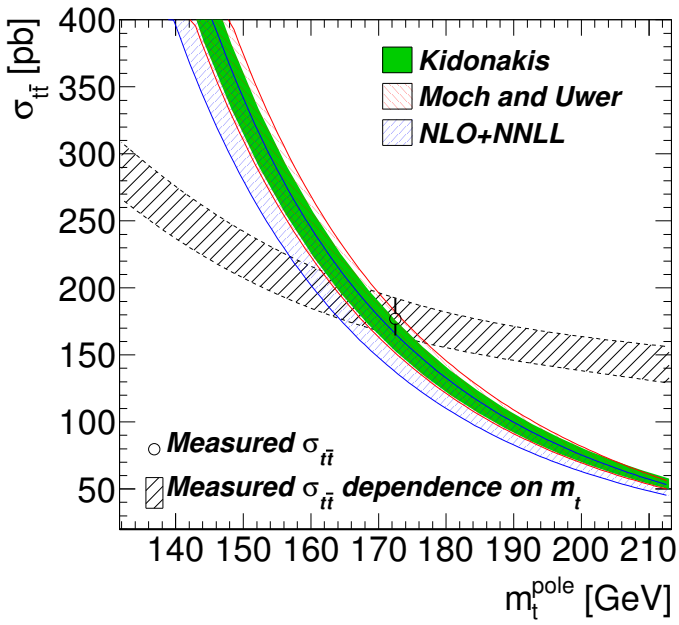


Figure 8.3: The dependence of the theoretically calculated and the measured cross sections on the top quark pole mass. Theoretical calculations of [102, 103, 104] are labeled with 'Kidonakis', 'Moch and Uwer' and 'NLO+NNLL' in the legend, respectively.

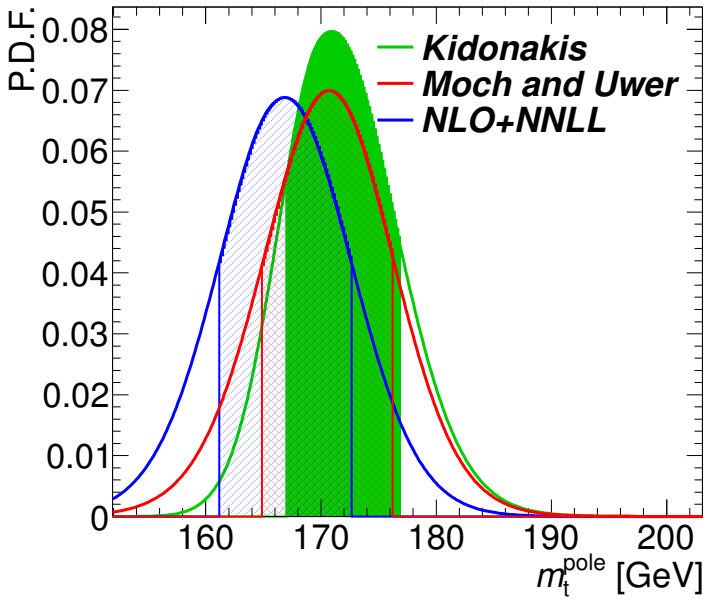


Figure 8.4: Probability density function as a function of the top quark mass. The filled or hatched area in each distribution indicates the 68 % interval from the maximum.

theoretical uncertainty. The combined value of experimental and theoretical uncertainties for each calculation is approximately 3 %. Once more precise experimental measurement and theoretical calculation are achieved by the method discussed at the beginning of this chapter, it is possible to determine m_t^{pole} with higher precision.

The top quarks for future analyses

In this analysis, the measurement of b-tagging efficiency using $t\bar{t}$ events is performed. It is confirmed that this method works with a reasonable precision. Currently, the baseline method to measure ε_b in the ATLAS experiment requires a muon inside the jet, and hence introduces a sample bias to the measurement. By using the method performed in this thesis, we can measure the b-tagging efficiency with a non-biased b-jet coming from top quark decay. On top of that, the b-jets from the top quark have high transverse momentum which is close to the one expected in the decay of Higgs boson or other non-discovered heavy particles. Therefore, measuring b-tagging efficiency with $t\bar{t}$ events would be preferred and applicable for all the future ATLAS physics program using final state with b-jets.

Chapter 9

Conclusion

We performed a precise measurement of $\sigma_{t\bar{t}}$ in pp collisions with the center-of-mass energy of 7 TeV in dilepton final states. One of the features of this analysis is a very high signal-to-background ratio compared to other $\sigma_{t\bar{t}}$ measurements performed in the ATLAS experiment thanks to the requirement of two leptons and the b-tagged jets. The b-tagging efficiency is measured using $t\bar{t}$ events in the single lepton final state. This idea is unique and the first trial to cancel the b-jet kinematic dependence of the b-tagging efficiency.

Using all the available 7 TeV collision data taken in 2011, $\int \mathcal{L}dt = 4.7$ fb^{-1}, we measured $\sigma_{t\bar{t}}$ to be

$$\begin{aligned}
\sigma_{t\bar{t}} &= 167 \pm 6(\text{stat.})^{+25}_{-19}(\text{syst.}) \pm 3(\text{lumi.}) \text{ pb} \quad (ee), \\
\sigma_{t\bar{t}} &= 178 \pm 4(\text{stat.})^{+15}_{-11}(\text{syst.}) \pm 3(\text{lumi.}) \text{ pb} \quad (\mu\mu), \\
\sigma_{t\bar{t}} &= 173 \pm 3(\text{stat.})^{+16}_{-14}(\text{syst.}) \pm 3(\text{lumi.}) \text{ pb} \quad (e\mu) \quad \text{and} \\
\sigma_{t\bar{t}} &= 177 \pm 2(\text{stat.})^{+14}_{-11}(\text{syst.}) \pm 3(\text{lumi.}) \text{ pb} \quad (\text{combined}).
\end{aligned}$$

These are consistent with each other and with the approximate NNLO prediction. This is the most precise measurement of $\sigma_{t\bar{t}}$ using the dilepton final states in the ATLAS experiment.

We confirm that the perturbative QCD works at the TeV scale and the top quark decays as in the standard model. In addition, the behavior of the ATLAS detector and the top quark pair production are well understood through this analysis, and hence we are ready for precise property measurements and new physics searches.

We deduced the top quark pole mass from the measured cross section. The pole mass is an important parameter used in theoretical calculations, and cannot be obtained by direct top quark mass measurements performed in Tevatron and LHC. We used three theoretical calculations to extract the mass and obtained:

$$\begin{aligned}
m_t &= 170.9^{+6.0}_{-4.1} \text{ GeV (based on [103])}, \\
m_t &= 170.7^{+5.5}_{-6.0} \text{ GeV (based on [102])}, \text{ and} \\
m_t &= 166.8 \pm 5.8 \text{ GeV (based on [104])}.
\end{aligned}$$

All these values are consistent with the mass of 172.5 GeV commonly used in the calculations, but slightly lower. Further improvement of precision can make a large impact on all theoretical predictions, and precision measurements that rely on the top quark mass.

Acknowledgment

First of all, I would like to express my gratitude to my supervisor, Kazunori Hanagaki, for giving me a great opportunity for the research in the ATLAS experiment. His support and guidance always encouraged me and lead me. Without them, I could not make my research. I am really lucky and I really enjoyed being his student. I am grateful for the help of Prof. Taku Yamanaka, who gave me a wonderful environment to learn what a particle physicist is all about. He always shows group members how to study by doing it himself.

I would also like to extend my appreciation to the ATLAS Collaboration. They have been working very hard to prepare the great detector and to achieve the superb detector performance, and gave me a good chance to perform the physics analysis at the frontier. I would like to express special thanks to people who worked on the top working group, especially M. Cristinziani, A. Loginov, D.B. Ta, T.M. Liss. In addition to the ATLAS people, I would like to give thanks to the LHC people since my analysis is completely based on their effort.

My deepest appreciation goes to the Osaka ATLAS group, J. Lee, H. Otono, K. Uchida, T. Meguro, T. Takagi, W. Okamura, J. Uchida, M. Endo, S. Higashino, J.J. Teoh, R. Tsuji, N. Ishijima, M. Watanabe. I have greatly benefited from discussion with them. Especially, I really thank W. Okamura, who I spent very long time with at CERN, office and the apartment in CROZET. Discussion about physics and other silly talks have become a good memory now.

I have stayed at CERN for the past four years. I would like to express my deepest gratitude to people who I met there. Fortunately, there are many colleagues at the same Ph.D. year, Y. Azuma, G. Akimoto, T. Domae, K. Kessoku, H. Yamaguchi, T. Yamanaka, Y. Suzuki, T. Kanno, S. Hasegawa, M. King, T. Hayakawa and T. Meguro. We discussed physics, and also many other topics happily. I am happy I met many people from various institutes.

My heartfelt appreciation goes to all the office mates of 301-1-007, A. Bitadze, A. Kastanas, G. Christian, B. Wynne, M. Yamada, J. Hendrik, B. O'brien, M. Cerv, J. Jentzsch, S. Al-kilani, who have created an excellent atmosphere for my life at CERN.

I received generous support from the ATLAS Japan Top group with Nagoya and KEK people. Dr. Y. Okumura and Prof. M. Tomoto always gave me very good advice and suggestions. Prof. J. Tojo helped me for the research work on not only analysis but also SCT. I am deeply grateful to all of group members.

My special thanks go to all the KOTO members in Osaka University. Especially, I really thank my best friend, J.W. Lee, who spent with me more than a decade since we entered Osaka University. I would also like to express my appreciation to Dr. E. Iwai for his mentorship about computing and physics and friendship. I learned the basics of programing, networking and Apple/Mac from discussion with him. I owe great thanks to the secretaries, A. Kamei and K. Kawahara, for their kindness and friendship.

Finally, I would like to thank my family, Ken, Masami and Rie, for supporting my research life, even though we were far apart when I was stationed at CERN.

Minoru Hirose
May 2013

Bibliography

[1] The ATLAS Collaboration, *'Observation of a new particle in the search for the Standard Model Higgs boson with the ATLAS detector at the LHC'*, Phys. Lett. B **716** 1 (2012).

[2] The CMS Collaboration, *'Observation of a new boson at a mass of 125 GeV with the CMS experiment at the LHC'*, Phys. Lett. B **716** 1 (2012).

[3] S. P. Martin, *'A Supersymmetry Primer'*, arXiv:9709356 [hep-ph].

[4] R. Ellis, W. Stirling, and B. Webber, *'QCD and collider physics'* (Cambridge university press, 1996).

[5] N. Kidonakis, and R. Vogt, *'The theoretical top quark cross section at the Tevatron and the LHC'*, Phys. Rev. D **78** 074005 (2008).

[6] G. Altarelli and G. Parisi, *'ASYMPTOTIC FREEDOM IN PARTON LANGUAGE'*, Nucl. Phys. B **126** 298 (1977).

[7] M. Aliev *et al.*, *'HATHOR : HAdronic Top and Heavy quarks crOss section calculatoR'*, Comput. Phys. Commun. **182** (2011) 1034-1046.

[8] A. D. Martin *et al.*, *'Parton distributions for the LHC'*, Eur. Phys. J. C **63** 189-285 (2009).

[9] A. D. Martin *et al.*, *'Uncertainties on α_s in global PDF analyses and implications for predicted hadronic cross sections'*, Eur. Phys. J. C **64** 653-680 (2009).

[10] M. Cacciari *et al.*, *'Top-pair production at hadron colliders with next-to-next-to-leading logarithmic soft-gluon resummation'*, arXiv:1111.5869 [hep-ph].

[11] M. Czakon, and A. Mitov, *'Top++: a program for the calculation of the top-pair cross-section at hadron colliders'*, arXiv:1112.5675 [hep-ph].

[12] The CKMfitter group, *'Preliminary results as of Moriond 2012'*, http://ckmfitter.in2p3.fr/www/results/plots_moriond12/ckm_res_moriond12.html

[13] CDF and DØ Collaborations, *'Combination of the top-quark mass measurements from the Tevatron collider'*, Phys. Rev. D **86** 092003 (2012).

[14] The ATLAS and CMS Collaboration, *'Combination of ATLAS and CMS results on the mass of the top quark using up to 4.9* fb^{-1} *of data'*, ATLAS-CONF-2012-095, https://cds.cern.ch/record/1460441

[15] S. W. Herb *et al.*, *'Observation of a Dimuon Resonance at 9.5 GeV in 400 GeV Proton-Nucleus Collisions'*, Phys. Rev. Lett. **39** 252 (1977).

[16] CDF Collaboration, *'Observation of top quark production in $p\bar{p}$ collisions'*, Phys. Rev. Lett. **74** 2626 (1995).

[17] DØ Collaboration, *'Observation of the Top Quark'*, Phys. Rev. Lett. **74** 2632 (1995).

[18] DØ and CDF collaborations, *'Combination of the $t\bar{t}$ production cross section measurements from the Tevatron Collider'*, DØ Note 6363-CONF.

[19] The ATLAS Collaboration, *'Measurement of the top quark-pair production cross section with ATLAS in pp collisions at $\sqrt{s}$=7 TeV'*, Eur. Phys. J. C **71** 1577 (2011).

[20] The CMS Collaboration, *'First Measurement of the Cross Section for Top-Quark Pair Production in Proton-Proton Collisions at $\sqrt{s}$ = 7 TeV'*, Phys. Lett. B **695** 5 (2011).

[21] The ATLAS Collaboration, *'ATLAS Physics Summary Plots'*, https://twiki.cern.ch/twiki/bin/view/AtlasPublic/CombinedSummaryPlots

[22] The CMS Collaboration, *'Measurement of the $t\bar{t}$ production cross section in the dilepton channel in pp collisions at $\sqrt{s}$ = 7 TeV'*, J. High Energy Phys. 11 (2012) 067.

[23] The CMS Collaboration, *'Measurement of the $t\bar{t}$ production cross section in pp collisions at $\sqrt{s}$ = 7 TeV with lepton + jets final states'*, Phys. Lett. B **720** 83 (2013).

[24] The CMS Collaboration, *'Measurement of the $t\bar{t}$ production cross section in the all-jet final state in pp collisions at $\sqrt{s}$ = 7 TeV'*, CMS-TOP-11-007, arXiv:1302.0508 [hep-ex].

[25] The CMS Collaboration, *'Measurement of the $t\bar{t}$ production cross section in the τ+jets channel in pp collisions at $\sqrt{s}$ = 7 TeV'*, CMS-TOP-11-004, Submitted to Eur. Phys. J. C, arXiv:1301.5755 [hep-ex].

[26] The CMS Collaboration, *'Measurement of the $t\bar{t}$ production cross section in pp collisions at $\sqrt{s}$ = 7 TeV in dilepton final states containing a τ'*, CMS-TOP-11-006, Submitted to Phys. Rev. D, arXiv:1203.6810 [hep-ex].

[27] L. Evans and P. Bryant, *'LHC Machine'*, JINST **3** (2008) S08001.

[28] Y. Ajima *et al.*, *'The MQXA quadrupoles for the LHC low-beta insertions'*, Nucl. Instrum. Meth. A **550** 3 (2005).

[29] *'LEP Design Report'*, CERN-LEP/84-01 (1984); CERN-AC/96-01 (LEP2) (1996).

[30] *'Design report Tevatron'*, fermilab-design-1982-01 (1982).

[31] F. E. Mills, *'Status of the Fermilab antiproton source'*, Nucl. Instrum. Meth. A **271** 1 (1988).

[32] CERN, in web page of *'The CERN accelerator complex'*, https://espace.cern.ch/acc-tec-sector/default.aspx

[33] R. Scrivens *et al.*, *'Overview of the status and developments on preliminary ion sources at CERN'*, CERN-ATS-2011-172 (2011), https://cdsweb.cern.ch/record/1382102

[34] CERN, *'The Linac 2 Pre-Injector'*, CERN-EX-0804060 04, https://cdsweb.cern.ch/record/1157734

[35] E. Lyndon *et al.*, *'The PS complex as proton pre-injector for the LHC : design and implementation report'* CERN-2000-003 (2000), https://cdsweb.cern.ch/record/449242

[36] P. Collier *et al.*, *'The SPS as injector for LHC - Conceptual Design'*, CERN-SL-97-07-DI (1997).

[37] Computer generated image of the whole ATLAS detector, CERN-GE-0803012 01, https://cdsweb.cern.ch/record/1095924

[38] The ATLAS Collaboration, *'ATLAS Muon Spectrometer Technical Design Report'*, CERN/LHCC 97-22 (1997).

[39] The ATLAS Collaboration, *'ATLAS Inner Detector Technical Design Report'*, CERN/LHCC 97-16 (1997).

[40] Computer generated image of the ATLAS inner detector, CERN-GE-0803014 01, https://cdsweb.cern.ch/record/1095926

[41] The ATLAS Collaboration, *'The ATLAS Experiment at the CERN Large Hadron Collider'*, JINST **3** (2008) S08003.

[42] A 3D model of the pixel detector and it's framework, CERN-GE-0803013 02, http://cds.cern.ch/record/1095925.

[43] The ATLAS Collaboration, in web page of *'Public Pixel Tracker Plots for Collision Data'*, https://twiki.cern.ch/twiki/bin/view/AtlasPublic/PixelPublicResults

[44] The ATLAS Collaboration, *'ATLAS silicon microstrip detector system (SCT)'*, Nucl. Instrum. Meth. A **511** 58 (2003).

[45] The ATLAS Collaboration, *'Engineering design of the ATLAS SCT'*, 0-TB-0049-177-01.

[46] The ATLAS Collaboration, in web page of *'The SCT public results'*, https://twiki.cern.ch/twiki/bin/view/AtlasPublic/SCTPublicResults

[47] The ATLAS Collaboration, in web page of *'Public TRT Plots for Collision Data'*, https://twiki.cern.ch/twiki/bin/view/AtlasPublic/TRTPublicResults

[48] Computer Generated image of the ATLAS calorimeter, CERN-GE-0803015, http://cdsweb.cern.ch/record/1095927

[49] Image of the ATLAS LAr EM calorimeter, CERN-EX-9308048_09, http://cdsweb.cern.ch/record/39737

[50] The ATLAS Collaboration, *'ATLAS calorimeter performance Technical Design Report'*, CERN/LHCC/96-040 (1996).

[51] The ATLAS Collaboration, *'ATLAS Forward Detectors for Luminosity Measurement and Monitoring'*, CERN/LHCC/2004-010 (2004).

[52] The ATLAS Collaboration, *'ATLAS Luminosity Public Results'*, https://twiki.cern.ch/twiki/bin/view/AtlasPublic/LuminosityPublicResults

[53] The ATLAS Collaboration, *The ATLAS data quality defect database system'*, Eur. Phys. J. C **72** 1960 (2012).

[54] S. van der Meer, *'Calibration of the effective beam height in the ISR'*, CERN-ISR-PO-68-31 (1968).

[55] The ATLAS Collaboration, *'Improved Luminosity Determination in pp Collisions at* $\sqrt{s}$ *= 7 TeV using the ATLAS Detector at the LHC'*, ATLAS-CONF-2012-080, http://cdsweb.cern.ch/record/1460392

[56] GEANT4 Collaboration, S. Agostinelli *et al.*, *'GEANT4: A simulation toolkit'*, Nucl. Instrum. Meth. A **506** 250 (2003).

[57] The ATLAS Collaboration, *'The simulation principle and performance of the ATLAS fast calorimeter simulation FastCaloSim'*, ATL-PHYS-PUB-2010-013, https://cdsweb.cern.ch/record/1300517

[58] T. Sjostrand, S. Mrenna and P. Skands, *'PYTHIA 6.4 physics and manual'*, J. High Energy Phys. 05 (2006) 026.

[59] G. Corcella *et al.*, *'HERWIG 6.5 release note'*, arXiv:0210213 [hep-ph].

[60] The ATLAS Collaboration, *New ATLAS event generator tunes to 2010 data*, ATL-PHYS-PUB-2011-008, https://cdsweb.cern.ch/record/1345343

[61] The ATLAS Collaboration, *ATLAS tunes of PYTHIA6 and Pythia 8 for MC11*, ATL-PHYS-PUB-2011-009, https://cdsweb.cern.ch/record/1363300

[62] Particle Data Group, *'Review of particle physics'*, Phys. Rev. D **86** 010001 (2012).

[63] S. Frixione and B. R. Webber, *'Matching NLO QCD computations and parton shower simulations'*, J. High Energy Phys. 06 (2002) 029.

[64] S. Frixione, P. Nason and B. R. Webber, *'Matching NLO QCD and parton showers in heavy flavor production'*, J. High Energy Phys. 08 (2003) 007.

[65] H.-L. Lai *et al.*, *'New parton distributions for collider physics'*, Phys. Rev. D **82** 074024 (2010).

[66] M. L. Mangano, M. Moretti, F. Piccinini, R. Pittau and A.D. Polosa, *'ALPGEN, a generator for hard multiparton processes in hadronic collisions'*, J. High Energy Phys. 07 (2003) 001.

[67] J. Pumplin, D. Stump, J. Huston, H. Lai, P.M. Nadolsky and W. Tung, *'New generation of parton distributions with uncertainties from global QCD analysis'*, J. High Energy Phys. 07 (2002) 012.

[68] M. L. Mangano, M. Moretti, and R. Pittau, *'Multijet matrix elements and shower evolution in hadronic collisions:* $Wb\bar{b}$ *+ n jets as a case study'*, Nucl. Phys. B **632** 1-3 (2002).

[69] S. Frixione, E. Laenen, P. Motylinski and B. R. Webber, *'Single-top production in MC@NLO'*, J. High Energy Phys. 03 (2006) 092.

[70] S. Frixione, E. Laenen, P. Motylinski, B. R. Webber and C. D. White, *'Single-top hadroproduction in association with a W boson'*, J. High Energy Phys. 07 (2008) 029.

[71] B. P. Kersevan and E. Richter-Was, *'The Monte Carlo event generator AcerMC version 2.0 with interfaces to PYTHIA 6.2 and HERWIG 6.5'*, arXiv:0405247 [hep-ph].

[72] The Les Houches Accord PDF Interface, http://lhapdf.hepforge.org/

[73] N. Kidonakis, *'Next-to-next-to-leading logarithm resummation for s-channel single top quark production'*, Phys. Rev. D **81** 054028 (2010).

[74] N. Kidonakis, *'Next-to-next-to-leading-order collinear and soft gluon corrections for t-channel single top quark production'*, Phys. Rev. D **83** 091503(R) (2011).

[75] N. Kidonakis, *'Two-loop soft anomalous dimensions for single top quark associated production with a W^- or H^-'*, Phys. Rev. D **82** 054018 (2010).

[76] J. M. Campbell and R. K. Ellis, *'An Update on vector boson pair production at hadron colliders'*, Phys. Rev. D **60** 113006 (1999).

[77] P. Nason, B. Webber, *'Next-to-Leading-Order Event Generators'*, arXiv:1202.1251 [hep-ph].

[78] R. Frühwirth, *'Application of Kalman filtering to track and vertex fitting'*, Nucl. Instrum. Meth. A **262** 2-3 (1987).

[79] D. Wicke, *'A New Algorithm For Solving Track Ambiguities'*, DELPHI 98-163, PROG 236 TRACK 92 (1998).

[80] R. O. Duda, P. E. Hart, *'Use of the Hough Transform to Detect Lines and Curves in Pictures'*, Commun. Ass. Comput. **15** 11-15 (1972).

[81] R. Frühwirth, W. Waltenberger, P. Vanlaer, *'Adaptive Vertex Fitting'*, J. Phys. G **34** (2007) N343.

[82] The ATLAS Collaboration, *'Observation of inclusive electrons in the ATLAS experiment at $\sqrt{s}$=7 TeV'*, ATLAS-CONF-2010-073, http://cdsweb.cern.ch/record/1281364/

[83] The ATLAS Collaboration, *'Electron performance measurements with the ATLAS detector using the 2010 LHC proton-proton collision data'*, Eur. Phys. J. C **72** 1909 (2012).

[84] W. Lampl *et al.*, *'Calorimeter Clustering Algorithms: Description and Performance'*, Tech. Rep. ATL-LARG-PUB-2008-002, http://cdsweb.cern.ch/record/1099735

[85] M. Cacciari, G. P. Salam and G. Soyez, *The anti-k_t jet clustering algorithm*, J. High Energy Phys. 04 (2008) 063.

[86] The ATLAS Collaboration, *'Probing the measurement of jet energies with the ATLAS detector using photon+jet events in proton-proton collisions at $\sqrt{s}$ = 7 TeV'* ATLAS-CONF-2012-063, http://cdsweb.cern.ch/record/1459528

[87] The ATLAS Collaboration, *'Probing the measurement of jet energies with the ATLAS detector using Z+jet events from proton-proton collisions at $\sqrt{s}$ = 7 TeV'* ATLAS-CONF-2012-053, http://cdsweb.cern.ch/record/1452641

[88] The ATLAS Collaboration, *'Track-Jet Reconstruction and Performance'*, ATL-PHYS-INT-2010-040, https://cdsweb.cern.ch/record/1259686

[89] The ATLAS Collaboration, *'Performance of Missing Transverse Momentum Reconstruction in ATLAS with 2011 Proton-Proton Collisions at $\sqrt{s}$ = 7 TeV'*, ATLAS-CONF-2012-101, https://cdsweb.cern.ch/record/1463915

[90] The ATLAS Collaboration, *'Performance of Impact Parameter-Based b-tagging Algorithms with the ATLAS Detector using Proton-Proton Collisions at $\sqrt{s}$ = 7 TeV'*, ATLAS-CONF-2010-091, https://cds.cern.ch/record/1299106

[91] G. Piacquadio, C. Weiser, *'A new inclusive secondary vertex algorithm for b-jet tagging in ATLAS'*, J. Phys. Conf. Ser **119** 032032 (2008).

[92] The SLD Collaboration, *'Time dependent B0(s) - anti-B0(s) mixing using inclusive and semileptonic B decays at SLD'*, SLAC-PUB-8225.

[93] The ATLAS Collaboration, *'Calibrating the b-Tag Efficiency and Mistag Rate in 35* pb^{-1} *of Data with the ATLAS Detector'*, ATLAS-CONF-2011-089, https://cds.cern.ch/record/1356198

[94] The ATLAS Collaboration, *'b-jet tagging calibration on c-jets containing D^{*+} mesons'*, ATLAS-CONF-2012-039, http://cdsweb.cern.ch/record/1435193

[95] The ATLAS Collaboration, *'Measurement of the top quark pair production cross section in pp collisions at $\sqrt{s}$ = 7 TeV in dilepton final states with ATLAS'*, Phys. Lett. B **707** 5 (2012).

[96] The ATLAS Collaboration, *'Measurement of the cross section for top-quark pair production in pp collisions at $\sqrt{s}$ = 7 TeV with the ATLAS detector using final states with two high-pT leptons'*, J. High Energy Phys. 1205 (2012) 059.

[97] The ATLAS Collaboration, *'Measurement of the b-tag Efficiency in a Sample of Jets Containing Muons with 5* fb^{-1} *of Data from the ATLAS Detector*, ATLAS-CONF-2012-043, https://cdsweb.cern.ch/record/1435197

[98] A. D. Martin *et al.*, *'Parton distributions for the LHC'*, Eur. Phys. J. C **63** 2 (2009).

[99] The ATLAS Collaboration, *'Measurement of the $t\bar{t}$ production cross-section in pp collisions at $\sqrt{s}$ = 7 TeV using kinematic information of lepton+jets events'*, ATLAS-CONF-2011-121, http://cds.cern.ch/record/1376413

[100] The ATLAS Collaboration, *'Measurement of the cross section for the production of a W boson in association with b-jets in pp collisions at $\sqrt{s}$= 7 TeV with the ATLAS detector'*, Phys. Lett. B **707** 5 (2012).

[101] F. A. Berends, W. T. Giele1 and H. Kuijf, *'Multijet production in W, Z events at $p\bar{p}$ colliders'*, Phys. Lett. B **224** 1-2 (1989).

[102] U. Langenfeld, S. Moch and P. Uwer, *'Measuring the running top-quark mass'*, Phys. Rev. D **80** 054009 (2009).

[103] N. Kidonakis, *'Next-to-next-to-leading soft-gluon corrections for the top quark cross section and transverse momentum distribution'*, Phys. Rev. D **82** 114030 (2010).

[104] V. Ahrensa *et. al.*, *'Renormalization-Group Improved Predictions for Top-Quark Pair Production at Hadron Colliders'*, arXiv:1003.5827 [hep-ph].

[105] The ATLAS Collaboration, *'Determination of the Top-Quark Mass from the $t\bar{t}$ Cross Section Measurement in pp Collisions at $\sqrt{s}$ = 7 TeV with the ATLAS detector'*, ATLAS-CONF-2011-054, http://cds.cern.ch/record/1342551